Atom interferometry: experiments with electromagnetic interactions and design of a Bose Einsteincondensate setup.

Boris Decamps

To cite this version:

Boris Decamps. Atom interferometry: experiments with electromagnetic interactions and design of a Bose Einsteincondensate setup.. Quantum Physics [quant-ph]. Universite Toulouse III Paul Sabatier, 2016. English. NNT : . tel-01447591

HAL Id: tel-01447591

https://hal.science/tel-01447591

Submitted on 27 Jan 2017

THÈSE

En vue de l'obtention du

DOCTORAT DE L'UNIVERSITÉ DE TOULOUSE

Délivré par :

Université Toulouse 3 Paul Sabatier (UT3 Paul Sabatier)

Présentée et soutenue par :
Boris DÉCAMPS
le mardi 22 novembre 2016

Titre :

Atom interferometry: experiments with electromagnetic interactions and design of a Bose Einstein condensate setup.

École doctorale et discipline ou spécialité :
ED SDM : Physique de la matière - CO090

Unité de recherche :
Laboratoire Collisions Agrégats Réactivité (UMR 5589)

Directeur/trice(s) de Thèse :

David GUERY-ODELIN et Matthias BÜCHNER

Jury :
Carlo RIZZO - Président du jury
David GUERY-ODELIN - Directeur de thèse
Matthias BÜCHNER - Co-directeur de thèse
Christoph WESTBROOK - Rapporteur
Frank PEREIRA DOS SANTOS - Rapporteur
Philipp TREUTLEIN - Examinateur
Caroline CHAMPENOIS - Examinatrice

Dedicated to my environment

CONTENTS

LIST OF FIGURES

LIST OF TABLES

INTRODUCTION

> She felt... how life, from being made up of little separate incidents which one lived one by one, became curled and whole like a wave which bore one up with it and threw one down with it, there, with a dash on the beach.
>
> Virginia Woolf, To the Lighthouse

Waves exhibit conceptual and mathematical properties that make them ideal tools to describe a continuously growing list of physical phenomena (mechanical, acoustical, electromagnetic, gravitational,...). Particularly striking with visible electromagnetic waves, their superposition property leads to one of their most prominent features: Interferences.

OPTICAL INTERFERENCES

The first observations of interferences patterns, known as Newton's Rings (see Fig. 1), were reported by R. Boyle and R. Hooke in the 17^{th} century. The successive high and low intensity regions are either constructive or destructive superposition of two coherent (i.e having a fixed phase relationship) waves. These patterns offer contrasted signal and can be used to measure small perturbations on the scale of an optical wavelength. Optical interferometers thrived partly because of this high sensitivity. Another reason is that interferometers allow to test fundamental properties of electromagnetic waves. From the famous experiments of Fizeau (1851) on the aether-drag hypothesis or of Michelson & Morley (1886) on the speed of light in different inertial frames to the very recent (2016) gravitational waves detection performed by the LIGO interferometer, optical interferometers have provided and still provide extremely sensitive experimental tests to physical theories.

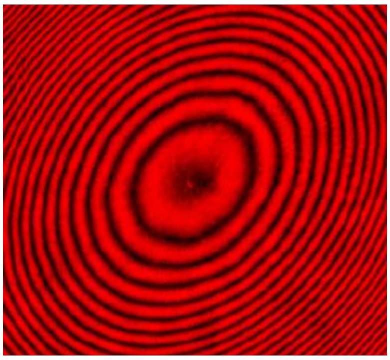

Figure 1
Newton's Rings created by a convex lens illuminated by laser light.
Photo licensed under CC BY-SA 3.0

An interferometer can be described (see Fig. 2) by two different paths which are coherently recombined. For light the two paths can either represent two coherent sources (wavefront splitting in Young's double slit), two wavevector directions (am-

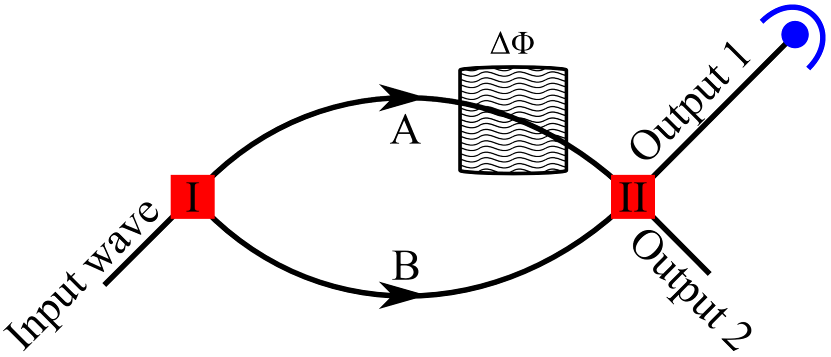

Figure 2: General scheme of an interferometer setup.

plitude splitting for Michelson interferometer) or two polarization states (internal state splitting such as Fresnel-Arago interferometers). For these interferometers, the coherent splitting elements (I and II) are respectively mechanical slits, air-glass interfaces and birefringent materials. The optical intensity at one outputs depends on the relative phase $\Delta\Phi$ between the two paths. For example, the most common origin of phase shift is due to different optical paths (either due to the lengths or refractive indices). But one can also think of topological phases (such as the Pancharatnam phase) which are independent of the exact trajectories.

MATTER WAVES INTERFERENCES

In 1924, the de-Broglie hypothesis extended the realm of waves to massive particles. Indeed, the essence of particle-wave duality lies in the de-Broglie wavelength, λ_{dB}, associated to any particle with momentum p:

$$\lambda_{dB} = \frac{h}{p} \simeq \frac{h}{mv}$$

where h is Plank's constant and, in the non-relativistic limit, m is the mass and v the classical velocity. This hypothesis was successfully demonstrated for the first time in 1927 when C. Davisson and H. Germer diffracted an electron beam on a metallic crystal [1]. Shortly after, this demonstration was extended to helium atoms by I. Estermann and O. Stern [2]. In addition to providing a strong argument in favor of quantum mechanics, this duality opened a new paradigm to particle physics: atom-optics. Indeed, both electromagnetic and matter waves obey the Helmholtz equation:

$$\nabla^2 u + k^2 u = 0 \tag{1}$$

where $k^2 = 2mE/\hbar^2$ for matter waves and $k^2 = E^2/\left(\hbar^2 c^2\right)$ for electromagnetic waves. This analogy has some important limits as the vacuum is dispersive for matter waves while the classical electromagnetic theory is linear in vacuum. Still, matter-wave interferometers are complementary tools to study different particles interactions as well as their inner structure.

Matter-wave interferometers

The first matter-wave interferometers were realized with electrons (Marton *et al.* 1952 [3], Möllenstedt and Düker 1955 [4]) and benefited from the diffraction by thin crystals and from the development of the electron biprism. Electron interferometers have given rise to the field of electron holography which now probes the atomic structure down to the single atom resolution and offers the possibility to map magnetic and electric fields. Also, electron interferometers were the first tools to demonstrate fundamental properties such as the Aharonov-Bohm effect [5], [6] or the antibunching effect resulting from the Pauli's exclusion principle for Fermions. The recent report by Hasselbach *et al.* [7] reviews electron interferometery in details.

The first neutron interferometer (H. Rauch *et al.* 1974 [8]) was developed thanks to the so-called "Perfect silicon crystal". These interferometers demonstrated many physical features such as Berry's phase and the magnetic Josephson effect (see Rauch's book [9]).

Marton's electron and Rauch's neutron interferometers had spatially separated arms with a geometry similar to the optical Mach Zehnder interferometer. This geometry is very simple which makes it one of the most popular geometries in the field of interferometers.

Mach Zehnder geometry

The Mach Zehnder interferometer is inspired by the optical interferometer, represented on Fig. 3 developed at the end of the 19th century by L. Mach and L. Zehnder. This type of interferometers splits the wave amplitude into two spatially separated paths that travels through distinct environments. The two paths are called the interferometer arms. After reflection on mirrors, the two waves are recombined on a second beam splitter. The two outputs of the second beam splitter exhibits complementary signals which oscillates as a function of the differential phase $\Delta\Phi$ acquired between the two arms. Experimentally, this setup allows to control $\Delta\Phi$ with macroscopic objects which interact separately with each arms.

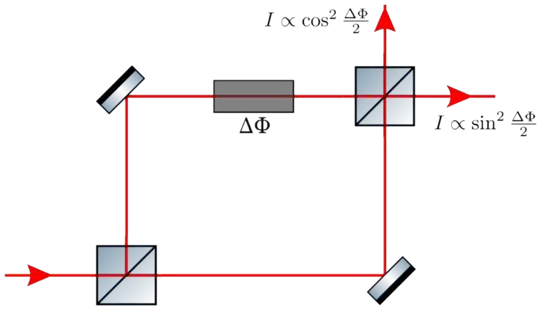

Figure 3
Optical Mach Zehnder interferometer relying on two beam splitters and two mirrors.

Neutron and electron specificities

Electron are relatively simple to produce but, due to the very large Coulomb interaction, a large flux requires high energy ($> 10\,keV$) electrons. Low energy neutrons are produced by nuclear reactors which are not common and the available flux is weak.

Atom waves on the contrary do not experience such long range interactions and can be produced by simpler setups. Additionally, the atom coherent manipulation techniques developed in the mid 80's, with the advent of laser sources, paved the way to atom interferometers. These interferometers provided additional physical features compared to the previous matter wave interferometers:

- Most of the neutrons and electrons interferometers operated in the strict regime of self interference (i.e only a single particle is present at any given time in the interferometer region). This was either due to the naturally low fluxes or to the strong interaction between electrons that produced unwanted phase shifts. Atoms do not suffer from this restriction and many particles effects (such as squeezing) are even being investigated to be used in atom interferometry.
- The variety of atomic internal states offered new opportunities that were not accessible to electrons and neutrons[1]. In particular, atoms offer the possibility to combine specific features such as polarizability or magnetic moments. Also, their interaction with the environment can be resonantly increased or specifically suppressed which allows to tune the interferometric phase accurately.

Atom interferometers were demonstrated for the first time[2] in 1991 and has become a major research field in fundamental physics.

ATOM INTERFEROMETRY

Reviewing the complete field of atom interferometry is a wide endeavor which was undertaken in four reviews [11]–[14] and two books [15], [16]. Some of the general features of these complex experiments will be described in this section, with particular emphasis on the ones applied to Toulouse's interferometers.

1991: a prolific year

In 1991, four different groups published atom interferometer fringes:

- O. Carnal and J. Mlynek [17] used a metastable He beam in a Young's double slit experiment.

---

[1] With the exception of spin state.

[2] Ramsey's spectroscopy of atoms and molecules pre-existed these interferometers and is, per say, an atom interferometer with internal state labelling [10] (similar to polarization interferometers in optics). But the absence of diffracting structures usually excludes them from being considered as the first atom interferometers.

- D. Pritchard *et al.* [18] developed a Mach Zehnder atom interferometer with Na.
- M. Kasevich and S. Chu [19] used a cold Na source to measure the local gravitational acceleration using a Mach Zehnder interferometer.
- Ch. J. Bordé and J. Helmcke *et al.* [20] measured the Sagnac phase with a saturated absorption Ramsey fringes on a Ca beam.

These interferometer schemes (Mach Zehnder, Young's slits, and Ramsey), diffraction elements (mechanical structures for the first two and laser gratings for the last two) and atomic sources (thermal beams or cold clouds) were already very diversified. But many more atom interferometers have been developed since.

Interferometer types

Atom interferometry exhibits many different conceptual schemes. One of the most popular scheme recombines atom waves having different external momentum states to produce interferences patterns. This type of interferometers is well represented by the Mach Zehnder geometry ([18], [19], [21]–[33]) which explicitly shows the momentum difference with a physical spatial separation. Combining this type of geometry with internal state dependent interferometric arms results in Ramsey-Bordé interferometers ([20], [34]–[45]).

In addition to these two schemes, one can mention some specific apparatus which are listed as atom interferometers. For example, Talbot Lau interferometers[3] ([47], [48]) consist in the near-field recombination of the multiple point sources produced by a first grating. Higher interference signal intensities can generally be obtained in these interferometers as a spatially incoherent atomic beam can be used as a source. Also, internal state labeling interferometers, such as the Ramsey separated oscillatory field method [49] or the spin echo technique ([50], [51]) can be viewed as atom waves interfering in the internal state subspace. These setups were developed for spectroscopy and lead to the onset of atomic clocks. Another technique is the temporal counterpart of spatial fringes and is usually denoted as interferometers in the time domain ([52]–[55]). Finally, a particular case of interferometers which confine the atoms [56] during the interferometric time appeared with the development of cold atoms trapping in particular with atom chips ([26], [57], [58])

Diffracting processes

The atom-optic tools to coherently produce superpositions of atom waves can also be listed into general categories such as mechanical (absorbing) structures which have been mostly used at the birth of atom interferometry and light gratings which are one of the most widely spread tool. Light gratings can either endorse the role of phase

---

[3] The C_{60} cluster interferometer developed in M. Arndt group[46] is a notable Talbot-Lau interferometer. This research group demonstrated the possibility to use more and more massive objects in matter waves interferometers.

gratings, absorbing gratings or both. Among the optical diffraction regime, one distinguishes diffraction which do not change the internal state (Kapitza-Dirac, Bragg and Raman-Nath scattering, described in Chap 1) from the diffraction process addressing different internal states (Raman). In every cases, the diffraction process produces atom momentum states separated by integer multiples of the photon wavevector k_L. However, with the advent of ultra cold sources such as Bose Einstein Condensates (BECs), techniques highly velocity selective such as Bloch oscillations [59] or multiple Bragg diffraction were applied to interferometry with ultra cold atoms. Similarly, simultaneous dual species interferometers involve more complex schemes such as four wave double Raman diffraction [60]. In addition to these techniques, some methods such as longitudinal Stern-Gerlach magnets which entangle the momentum state to its internal state with magnetic field gradients, diffraction in time processes which relied on evanescent wave reflection or time dependent potentials (as developed in Chap 2) were used to produce interferometers in the time domain.

Atom source

Another criteria can be used to classify atom interferometers: their atom source. Initially, the large majority of atom interferometers relied on either thermal (effusive, supersonic) or cold beams which produced modest atomic flux and required efficient detection techniques. This is the reason why the first atom interferometers were developed either with alkali atoms or with metastable noble gas atoms. With the development of cold atoms, a new type of interferometers based on laser cooled gases flourished due to the very long interaction time which improves the interferometer sensitivity. The use of BECs for atom interferometry was initially set aside as preliminary experiments demonstrated the prejudicial impact of atom-atom interactions. However, the possibility to use BECs squeezed states [49] or extremelly small velocity distribution for large spatial separations [61] renewed the interest in these sources.

Table 1 gives an overview of the previously cited interferometers. It is not a comprehensive list of all experiments that can be cited in the domain of atom interferometry but it shows how cold atoms, with the clear example of Rubidium atoms, represent a very large fraction of current atom interferometers. It also points out the recent development of dual species atom interferometers which, apart from the initial demonstration of M. Weitz *et al.* [62], appeared after 2013.

---

5 This is the only available value about their initial cloud temperature.
6 Kapitza-Dirac.
7 More specifically, Velocity Selective Raman Transitions (VSRT) which filters the initial cloud momentum distribution.

Species	Source	Diffraction	Group	Reference
H*	Thermal beam	Stern-Gerlach	J. Baudon	[63]
	Cold beam	Photon echo	T. Hänsch	[39]
He*	Thermal beam	Mechanical	O. Carnal and J. Mylnek	[17]
	Cold beam	Mechanical slits	J. P. Toennies	[64]
^{3}He	Cold beam	Stern-Gerlach	U. Spinola	[50]
Li	Thermal beam	Spin echo	R. Grimm	[51]
	Thermal beam	Bragg	J. Vigué	[24]
Ne*	Thermal beam	Bragg	S. A. Lee	[22]
Na	Thermal beam	Mechanical	D. E. Pritchard	[18]
	Cold atoms (30 µK)	Raman	M. Kasevich and S. Chu	[19]
	BEC	Kapitza-Dirac	W. D. Phillips	[48]
	Thermal beam	Mechanical	A. D. Cronin	[25]
Mg	Thermal beam	Ramsey	W. Ertmer	[34]
Ar*	Thermal beam	Kapitza Dirac	E. M. Rasel	[21]
K	Cold beam	Mechanical	S. Li	[47]
Ca	Thermal beam	Ramsey	C. J. Bordé and F. Riehle	[20]
	Thermal beam	Ramsey	N. Ito	[35]
^{85}Rb	Thermal beam	Ramsey	A. Weis	[36]
	Cold atoms	Time modulation	T. Sleator and B. Dubettsky	[53]
	Cold atoms	Photon echo	A. Kumarakrishnan	[55]
^{87}Rb	Cold atoms	Evanescent wave	A. Aspect	[54]
	BEC	Bragg	T. Kuga	[23]
	BEC	Double well potential	J. Schmiedmayer	[65]
	BEC	Bragg, confined	S. Wu	[26]
	Cold atoms	Temporal KD[5], confined	M. Prentiss	[57]
	Cold atoms (8 µK)	Raman[6]	W. Ertmer	[40]
	Cold atoms (3 µK)	Bloch oscillations	F. Biraben	[59]
	BEC	Ramsey	M. Oberthaler	[49]
	BEC	Bragg	N. P. Robins	[28]
	BEC (0.004 µK)	Multi-Bragg	M. Kasevich	[61]
	Cold atoms (2 µK)	Raman, confined	F. P. D. Santos	[56]
	BEC	Ramsey, confined	P. Treutlein	[58]
	Cold atoms (1.8 µK)	Raman	A. Bresson	[30]
	Cold atoms (0.3 µK)	Raman	J. Luo	[31]
	Cold atoms (3 µK)	Raman	A. Peters	[32]
	Cold atoms (4 µK)	Raman	G. M. Tino	[33]
	Cold atoms (30 µK[4])	Raman	Z. Zhou	[44]
Sr	Cold atoms (1.2 µK)	Bragg	G. M. Tino	[66]
Cs	Cold beam	Evanescent wave	J. Dalibard	[52]
	Thermal beam	Raman	M. Kasevich	[37]
	Cold atoms (1.5 µK)	Raman	S. Chu	[38]
	Cold atoms(1.2 µK)	Raman	A. Landragin	[41]
(^{85}Rb/^{87}Rb)	Cold atoms(6 µK)	Raman-Nath	M. Weitz	[62]
	Cold atoms(1 µK)	Raman	A. Bresson	[42]
	BEC	Bragg	N. P. Robins	[67]
	Cold atoms(6 µK)	Raman	M. Zhan	[68]
(^{39}K/^{87}Rb)	Cold atoms (30 µK)	Raman	E. M. Rasel	[43]
(^{40}K/^{87}Rb)	Cold atoms (20/3 µK)	Raman	P. Bouyer and A. Landragin	[45]
(^{87}Sr,^{88}Sr)	Cold atoms (1 µK)	Confined atoms	G. M. Tino	[69]

Table 1

Selected atom interferometers listed by atomic species. The variety of diffraction techniques as well as the advent of cold atom sources are emphasized by the difference between the smallest atoms (first quarter of the table) and the large number of Rubidium cold sources.

PRECISION MEASUREMENTS

From proof of principle apparatuses, atom interferometers rapidly focused towards precision measurement setups. For twenty years, they have demonstrated their extreme sensitivity and high accuracy on a large panel of effects. The interferometer phase is indeed a combination of external potential effects, of the atomic trajectory in the interferometer and its internal state wavefunction evolution. These effects can be investigated for themselves or can be used to access fundamental physical properties and to put new theories to the test.

Interaction phase shifts

Interest in atom interferometers mainly arises from their high sensitivity to external perturbations. For example, in the framework of first order perturbation theory, an external static potential U modifies an atom wave wavevector, k_0 in free space, according to the energy conservation:

$$\frac{\hbar^2 k_0^2}{2m} = \frac{\hbar^2 k_p^2}{2m} + U$$

where k_p is the perturbed wave vector in the interaction region. The perturbative assumption, $U \ll \hbar^2 k_0^2\,(2m)$ allows to give an approximate expression for k_p:

$$k_p \simeq k_0 - \frac{mU}{\hbar^2 k_0}$$

Therefore, the phase shift induced by the external potential can be expressed as:

$$\phi_p = \int (k_p - k_0)\, ds = -\int \frac{U}{\hbar v} ds = -\int \frac{U}{\hbar} dt \qquad (2)$$

where we have neglected the trajectory deviation induced by the perturbation and used the fact that v is the atom group velocity which is related to the atom path s via $ds/dt = v$, where t is the propagation time. For example, a constant perturbation applied for 100 µs measured with a sensitivity on the interferometer phase of 10 $mrad$ allows to probe potentials of $U = 6 \times 10^{-14}$ eV which, compared to the atomic kinetic energy (of the order of a few meV for thermal atoms) shows a relative sensitivity of 10^{11}.

Depending on the origin of the perturbation potential, information on the atomic structure and interactions are measurable with interferometry. For example :

- The interaction with an electromagnetic field leads to the measurement of both DC or AC electric polarizability [70], [71] (see Chap. 4).

- The presence of a gas on the interferometer arm induces phase shifts and collisions via the van der Waals interactions which can be described as an effective index of refraction and measured with interferometry [72], [73].
- The atom interaction with surfaces probes the Casimir-Polder potential [74], [75].

Inertial effects

Another important sources of phase shift in an atom interferometer are inertial effects. Indeed, eq. (2) clearly shows that the phase depends on the atomic trajectory in the interferometer. As a result, accelerometers and gyrometers were developed and proved to be extremely accurate tools sensitive, at $1\,s$, at the $4 \times 10^{-8}\,m/s^2$ [31] and $10^{-8}\,rad/s$ level. These interferometers measure at the single atom level gravitational accelerations [19], [76], gravity gradients [77] and rotations [37], [41]. The sensitivity of these interferometers scales proportionally with the separated arms momentum difference k_{eff} and as the square of the interferometer duration T. Progresses towards higher sensitivities includes larger momentum separations [61] and larger T with either large apparatus, micro-gravity environments [27], [78] or even spatial missions [79].

Topological phases

Besides atomic physics applications and inertial sensors, the sensitivity to the wavefuntion's phase was used to demonstrate the existence of non-dynamical phases. Aharonov-Bohm, Aharonov-Casher and Berry phases are some examples of the non-dynamical phases that are acquired by the atomic wavefuntion. They respectively correspond to the situation when the two paths enclose a region of different vector potentials (for a charged particle), of different electric field (for a magnetic dipole) or when the atomic states performs certain cyclic transformations (see Chap. 3). This type of phases can only be detected by interferometers as they do not result from an energy difference (i.e a force) which changes the atom trajectory.

Fundamental constants measurements

The high sensitivity to inertial effects was used to perform additional measurements of the gravitational constant $\mathcal{G}$. The relative uncertainty on this constant was of 150 ppm in the CODATA 2002 and resulted from a large discrepancy between reported measurements. An additional measurement using atom interferometry [33] helped to identify systematic effects as it is conceptually different with single atoms interactions. Also, using the integer number of photons transferred to atoms with light pulses, the fine structure constant α was recently measured with high accuracy through its relationship with the h/m ratio [59].

Fundamental tests

Finally interferometers are sensitive tools to probe for new physics. Among the fundamental studies performed with atom interferometry, one can think of the wide range of decoherence experiments which were undertaken. Different processes were investigated such as the coupling to the environment or the internal state dependent interferometric paths. Some atom interferometers are dedicated to the test of the Weak Equivalence Principle [43], [80], to the investigation of predicted deviation from standard gravity [81], [82] or to test the matter neutrality (see Chap. 5).

THESIS OUTLINE

In this context of atom interferometry, my work in Toulouse's group contributes both to the initial, and now fading, impulse of atomic beam interferometers and to the newest field of ultra cold atom sources for precision measurement. Indeed, during my three years P.h.D thesis, I worked on the lithium beam interferometer which was developed in Toulouse near 2000. I contributed to experiments on atom wave beats, on topological phases, on precision measurements and on fundamental decoherence tests. In parallel, I participated to the development of a new dual species BEC interferometer which extends the atom interferometry research in Toulouse to new topics such as matter neutrality.

As a result this thesis will be split into two parts:

Experiments with electromagnetic interactions:

The first part is dedicated to the experiments we did on the Lithium beam interferometer which will be described in Chap. 1. Then, each of the following chapters will focus on one experiment which are, in order of appearance:

- **Chap 2**: A modulation in time experiment with a versatile Kerr modulator used to detect both homodyne and heterodyne atomic beat signals.
- **Chap 3**: A new Pancharatnam dephasor which imprints a geometrical phase of light on the interferometric signal to scan the atomic fringes.
- **Chap 4**: The first experimental measurement of ^{7}Li, $^2S_{1/2}\,|F=2, m_F=2\rangle$ "tune-out" wavelength at which its dynamical polarizability vanishes.

Design of a Bose Einstein Condensate setup:

The second part of this thesis concerns the development of a new experimental apparatus relying on a dual-species BEC source. The objectives and theoretical developments required for the proper scaling of this setup will be described in Chap 5. Both dual species BEC production and transport challenges will be addressed as well as some new theoretical discussions on multi-pulses Mach Zehnder interferometers. Then, a much more detailed chapter will describe the experimental setup (vacuum system, laser sources, magnetic fields,...) and show how its performances fit with our requirements. Finally, the last chapter will focus on the first atomic signals obtained with this setup.

Part I

Experiments with electromagnetic interactions

1 LITHIUM BEAM INTERFEROMETER

Contents

The atom interferometer developed in Toulouse in the late 90's was designed to investigate various dephasing interactions in a spatially separated interferometer. To maximize the interferometer fringe visibility and the atomic flux, the atom diffraction operates in the first Bragg order. The interferometric arms are produced in the Mach Zehnder geometry with light gratings. These gratings are optical lattices which produce a coherent superposition of identical internal states with different momenta. In this configuration, the choice of the Lithium atom, the lightest of alkali atoms, leads to the large spatial arm separation of $100\,\mu\mathrm{m}$ in an interferometer $1.2\,\mathrm{m}$ long.

A 100 μm microscopic separation was enough to control separately the interaction on each of the two interferometric arms and was put to great use for multiple investigations:

1. The magnetic field gradients influence on the total interferometric signal resulting from incoherent sum of interference signals due to different magnetic sublevels [83].
2. The measurement of the lithium electric polarizability with the lowest uncertainty achieved up to now [71].
3. The measurement of the real and imaginary parts of the refractive index of several noble gases for lithium matter waves [73].
4. The measurement of Van der Waals interaction between lithium and silicon nitride gratings[1] [75].
5. The first measurement of the topological phase predicted by He, McKellar and Wilkens and the test of its independence with the wave group velocity [84].

This chapter gives a general description of this atom interferometer with particular focus on the experimental details necessary to the analysis of the experiments described in the following chapters.

The general setup is schematized on Fig.4. It consists in four regions and five vacuum chambers. The first three chambers contain the lithium oven and collimating slits as a very narrow atomic beam is needed to separate spatially the two interferometric arms. They make up the lithium source which will be described in Sec. 1.1. Then, I will summarize briefly the different regimes of atom diffraction with an optical lattice and focus on Bragg diffraction. The principal elements of our laser system used for atom diffraction and some of its main characteristics will conclude the description of the interferometric chamber. Finally, I will describe the Langmuir-Taylor detector used to measure the output signal of our atom interferometer. The general expression of the detected interferometric signal as well as the critical experimental parameters which influence the phase measurement performance will be presented.

1.1 VACUUM SYSTEM AND LITHIUM SOURCE

The performances of an interferometer highly depend on its source quality. For optical interferometers, light sources can be described in terms of monochromaticity and luminance. Monochromaticity ensures the homogeneity of the phase shift acquired by the different spectral components of the light which ultimately limits the interferometer sensitivity. The luminance characterizes the photon flux per unit area and solid angle and is a conserved quantity when the light travels through a non absorbing medium. The interferometric signal depends on the incident luminance,

---

[1] Which are similar to the absorbing gratings used by Keith *et al.* [18] in their Sodium interferometer

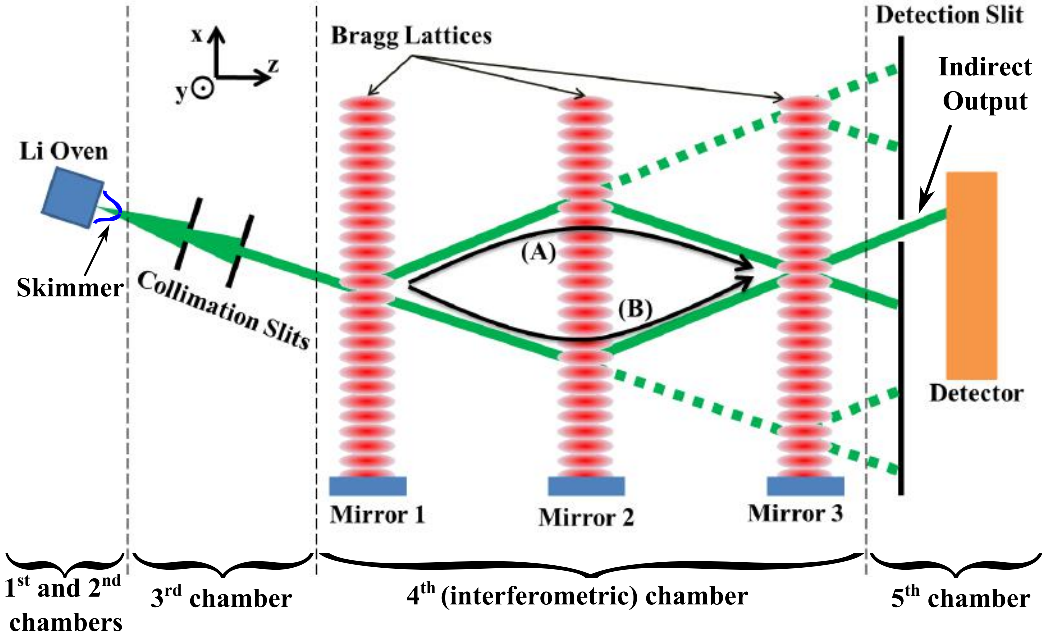

Figure 4: Schematic representation of our Mach-Zehnder lithium interferometer. Four distinct regions separate the lithium source, the collimation slits, the interferometer itself and the detection.

the efficiency of coherent superposition (i.e the visibility) and detector characteristics. These quantities are directly linked to the interferometer phase sensitivity as will be discussed in Sec. 1.3.2. Similarly, an atom interferometer source can be described in terms of brilliance[2] and monochromaticity, which from the de Broglie relation is directly related to the atomic velocity distribution. The characterization of our atomic beam is thoroughly described in A. Miffre's thesis [85] and only the main results will be presented here. But before describing our lithium source, we need to give a few details about the vacuum system.

1.1.1 Vacuum system

The scheme described on Fig. 4 is enclosed in five vacuum chambers represented on Fig. 5. The first two chambers contain the lithium oven. They are pumped by two oil diffusion pumps and are separated by a differential pumping stage. The highest gas load comes from the supersonic beam which is why the pump with highest speed (Varian VHS 400, $8000\,\mathrm{L\,s^{-1}}$) is used there. A pressure below $5 \times 10^{-4}\,\mathrm{mbar}$ is typical of this first chamber. The second chamber is used as a differential vacuum chamber, with a pressure of the order of $3 \times 10^{-6}\,\mathrm{mbar}$ when the lithium beam is under operation. It also serves to characterize the lithium atomic beam by laser induced fluorescence. A differential pumping stage separates the lithium oven from the collimation region with a $1\,\mathrm{mm}$ diameter skimmer. Just after the skimmer, optical pumping of the lithium beam in a single hyperfine-Zeeman F, m_F sublevel was implemented for some experiments. Afterwards, the collimation chambers and interferometric chambers are

---

[2] This quantity corresponds to the atomic flux per unit area and solid angle

respectively pumped by one oil diffusion pump from Edwards and two Varian VHS 1200, fitted with water cooled baffles, so that the pressure in these chambers is typically 5×10^{-7} mbar, independently of the operation of the atomic beam. Finally the detection chamber is pumped by a turbo molecular pump (TMP) which allowed to reach ultra high vacuum pressure necessary to minimize stray signal on the hot wire detector (described in Sec 1.3.1). The residual pressure is a few 10^{-9} mbar when this chamber is isolated by a gate valve and about 10^{-8} mbar when the valve is opened.

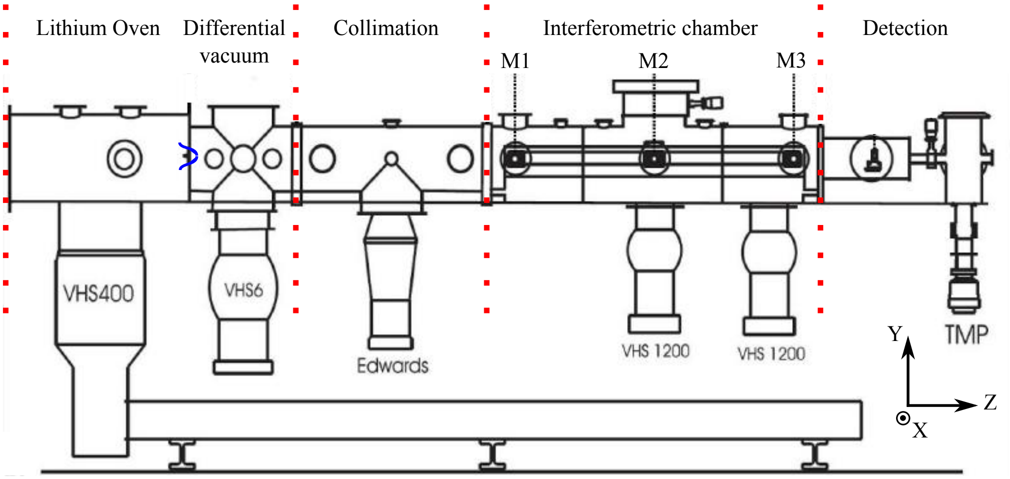

Figure 5: Main elements of the vacuum system. The four main regions are delimited by the red dotted lines and the three Bragg mirrors are indicated. The six vacuum pumps are labeled by their manufacturer or acronym.

Low pressure in the interferometric chamber is mandatory because collisions with the background gas deflect the atoms which attenuates the mean atomic intensity. One can also think of coherence loss but for light atoms such as lithium atoms, a background collision almost always results in an atomic trajectory which is not detected and therefore does not contribute to the interferometric signal. A rough estimate of the acceptable background pressure consists in imposing a mean free path ten times larger than the interferometer length which corresponds approximately to a pressure of 3×10^{-7} mbar at room temperature. Therefore, the vacuum performances of this system are acceptable to prevent the background gas from limiting our interferometer performances.

1.1.2 Supersonic lithium beam

The lithium beam is produced by a supersonic expansion of a carrier gas (which is always a noble gas and is Argon in all the experiments described in this thesis) mixed with a small amount of lithium. The rare gas pressure is usually 325 mbar. The lithium pressure is about 0.5 mbar, equal to the vapor pressure of lithium at a temperature near 700 °C, while the expansion velocity is fixed by the temperature (780 °C) of the oven front part.

The numerous collisions occurring during the expansion keep the expanding gas in a local thermal equilibrium while the internal enthalpy is transformed into kinetic energy. As the density decreases rapidly, the collision rate becomes too small and the thermal equilibrium ceases to be maintained. The atoms of the beam can be described by a Maxwellian distribution for their longitudinal velocity with a terminal temperature T which is very low. The theory of this cooling effect has been developed by Toennies and Winkelmann [86] and by Beijerinck and Verster [87]. Moreover in the case of the expansion of a gas mixture, the terminal temperature is different for the carrier gas and for the seeded gas. Our research group has developed the theory of this effect, in the limit of infinite dilution of the seeded gas [88], [89]. The supersonic beam carries a high atomic flux which can be described, far from the nozzle, by the longitudinal velocity distribution:

$$P\left(v_{||}\right) = \frac{S_{||}}{\bar{u}\sqrt{\pi}} e^{-\left(\frac{S_{||}\left(v_{||}-\bar{u}\right)}{\bar{u}}\right)^2} \tag{3}$$

where $S_{||}$ is a parameter called the parallel speed ratio which characterizes the distribution's width and $\bar{u}$ is the mean longitudinal velocity which depends on the square ratio of the oven temperature over the carrier mass[3]. For the purpose of this work, $S_{||}$ will be close to 8 and $\bar{u}$ will be of the order of $1060(10)\,\mathrm{m\,s^{-1}}$.

1.1.3 Collimation

There are three main mechanical elements which collimate the previously described atom beam: the skimmer and two slits

The skimmer consists in a $1\,\mathrm{mm}$ diameter hole near the apex of a cone which is aligned with the oven nozzle. It selects the highest intensity part of the beam and reduces the gas load, due to the Argon stream, in the collimation and interferometric chambers. The collimation of the lithium beam is done by two narrow rectangular slits[4], separated by $0.78\,\mathrm{m}$. The slit position can be tuned under vacuum with a $\mu\mathrm{m}$ sensitivity which is necessary to optimize the lithium beam intensity. As we will see in the next section, Bragg diffraction is highly selective in the atomic incidence angle and the collimation is mandatory to prevent undiffracted atoms from reaching the detection region. Also, having a small divergence ensures a spatial separation between the two interferometric paths in the interferometer region and between its two outputs. In practice, we used $18\,\mu\mathrm{m}$ wide slits which corresponds to an atomic beam divergence (angular aperture of $46\,\mu\mathrm{rad}$) smaller than the Bragg diffraction angle. The resulting beam brilliance is approximately 2×10^{20} $\mathrm{atoms/(sm^2sr)}$.

---

[3] This was of great practical use when different mean velocity were necessary because changing the carrier gas (with either a lighter element, Neon, of a heavier one, Krypton) and keeping the oven temperature constant allowed to work with different velocities.

[4] We use a set of slits with different widths, nanolithographied on a silicon wafer.

1.2 DIFFRACTION PROCESS

As mentioned in the introduction, various diffraction techniques have been employed in atom interferometry. In this section, we will focus on the atom diffraction induced by a monochromatic standing wave. We note however that moving lattices produced by the superposition of different counter-propagating frequencies have also been extensively used with Raman diffraction which diffracts into different internal states. More recently, Bloch oscillations have also been used but we will leave this discussion to the description of the new interferometer in the second part of this thesis.

1.2.1 Atom diffraction by a standing light wave

The interaction of the electromagnetic field with an atom can be completely treated in the formalism of second quantization (see for example [90]). In a situation when the number of photons in a given mode is large and when the internal state atom wavefunction is localized on a distance small compared to the optical wavelength, it reduces to the electric dipole approximation. In this approximation, the electric field amplitude and polarization are treated classically and the coupling to the atomic electronic cloud is expressed in the interaction Hamiltonian:

$$\hat{H}_{int} = -\hat{\vec{d}} \cdot \vec{E}\left(\hat{\vec{r}}, t\right) \tag{4}$$

where $\vec{d}$ is the atomic electric dipole moment and $\vec{E}\left(\vec{r}, t\right)$ is the total electric field. The hat on the position vector is used to emphasize the classical treatment of the field compared to the quantum treatment of $\vec{r}$, the atom center of mass.

The following treatment of atom-light interaction in the dipole approximation has been extensively described in original papers [91], [92] and only main arguments will be presented here.

Optical lattice

Let us now consider the interaction between an atom and a particular electric field consisting in two counter propagating electric fields of identical amplitudes and polarizations. The resulting field is called an optical lattice because of its periodic structure in space. The subsequent total Hamiltonian is:

$$\hat{H} = \hat{H}_0 + \frac{\hat{\vec{p}}^2}{2m} - \frac{\hat{\vec{d}} \cdot \vec{E}\left(\vec{r}\right)}{2}\left(e^{i[\omega t - \vec{k}_L \cdot \hat{\vec{r}} + \phi(\vec{r}_0)]} + e^{-i[\omega t - \vec{k}_L \cdot \hat{\vec{r}} + \phi(\vec{r}_0)]}\right) \tag{5}$$

where $\hat{H}_0$ is the atomic Hamiltonian, m is the atomic mass and $\left\{\omega, \vec{k}_L\right\}$ are respectively the electric field's frequency, wavevector and , $\phi\left(\vec{r}_0\right)$ is the reference phase of the lattice which depends on a given position $\vec{r}_0$ such as a retro-reflecting mirror position for example.

In a two internal states picture, this Hamiltonian couples atomic states of different momenta separated by integer numbers of $\vec{k}_L$. However, when we assume that the laser detuning $\delta := \omega - \omega_0$, where ω_0 is the internal state resonance frequency, is large compared to :

- Γ, the excited state linewitdh
- $\omega_D := \hbar\vec{k} \cdot \vec{k}_L / m$, the Doppler frequency (where $\vec{k}$ is the atomic momentum)
- $\omega_{rec} := \hbar k_L^2 / (2m)$, the atomic recoil frequency

It is possible to adiabatically eliminate the excited state population which remains marginally populated under the atom-light interaction. This results, in the rotating wave approximation which neglects terms oscillating faster than δ, in the following interaction Hamiltonian:

$$\hat{H}_{eff} = \frac{\hat{\vec{p}}^2}{2m} + \hbar\Omega_{eff}(\vec{r}) \cos^2\left(\vec{k}_L \cdot \vec{r}\right) \tag{6}$$

This Hamiltonian only acts on the external motional states of the ground-state. It can be interpreted as a spatial potential lattice with amplitude $\Omega_{eff} = \Omega_0^2(\vec{r}) / (2\delta)$, where $\Omega_0(\vec{r}) := -\langle e| \hat{\vec{d}} \cdot \vec{E}(\vec{r}) |g\rangle / \hbar$ is the single photon Rabi frequency. This effective interaction energy, as called light shift, emphasizes the parallel between atom optics and classical optics for which periodic structures in matter play a similar role.

Now that we have the appropriate theoretical tools, we are going to discuss two particular applications of this Hamiltonian which correspond to short and large interaction times: the Kapitza-Dirac and Bragg regimes.

1.2.2 Kapitza-Dirac regime

This interaction regime owes its name to the theoretically similar situation of an electron beam diffracted by a standing wave of light, discussed by Kapitza and Dirac in 1933 [93]. This regime corresponds to short interaction times t_{int} with an intense optical lattice during which the atom dynamic is neglected [94]. The simplest situation in which this occurs is when an atom beam intersects orthogonally a standing light wave as schematized on Fig. 6a. An initial plane wave with well defined momentum $k_{z,0}$ along z becomes, after the interaction:

$$|\Psi(q,\tau)\rangle = \sum_{n=-\infty}^{\infty} J_n(2q\tau)|2n\rangle \tag{7}$$

where $J_n(\cdot)$ is the Bessel function of the first kind, $|2n\rangle$ is the momentum state in the lattice direction $2nk_L$, $q = \Omega_{eff}/(4\omega_{rec})$ is the dimensionless potential amplitude and $\tau = \omega_{rec} t_{int}$ is the dimensionless interaction time[5]. This corresponds to a trans-

---

[5] The validity of this approximation corresponds to $\tau < 1/(4\sqrt{q})$ [95]

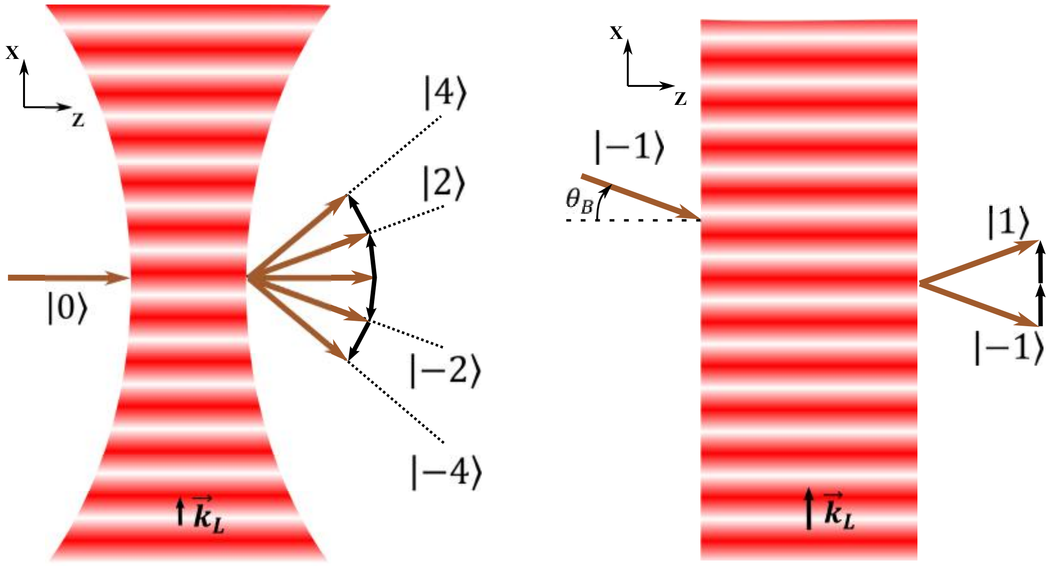

(a) Kapitza-Dirac regime **(b)** First order Bragg diffraction

Figure 6: **(a)** Kapitza-Dirac interaction with an orthogonal standing wave. The incident atom wave is diffracted into several momentum components due to the lattice wave vector distribution. The angular distribution has been exaggerated for visual clarity. **(b)** When the atom beam angle of incidence fulfills the Bragg condition, the transmitted atom wave corresponds to a superposition of two momentum states separated by $2\vec{k}_L$. Only the first order Bragg diffraction is represented here.

mitted wave in a superposition of transverse momentum states $k_x = 2nk_L$ which, from energy conservation, have a longitudinal component $k_{z,n} = \sqrt{k_{z,0}^2 - (2nk_L)^2}$.

Physically, this process corresponds to the absorption and stimulated emission of multiple photons with an angular distribution of momentum directions. On sees that in this regime, the population in the diffracted states cannot be evenly distributed between two states (atom Beam-Splitter) or completely transferred to a single momentum state (atom Mirror). The Bragg diffraction regime is much better suited for separated arms interferometry.

1.2.3 Bragg regime

When the optical potential is shallow, $q < 1$, and the interaction time is large, $\tau > 1$, the Hamiltonian (6) couples two momentum states separated by $2n$ photon momenta when the incident plane wave fulfills the n^{th} order Bragg condition[6]:

$$\sin(\theta_B) = \frac{n\lambda_{dB}}{\lambda} \tag{8}$$

---

[6] This condition results from energy and momentum conservation only.

This condition is represented on Fig. 6b for the first order Bragg diffraction ($n = 1$). The transmitted state is in a coherent superposition [83] of momentum states $|-1\rangle$ and $|1\rangle$:

$$|\Psi(\tau)\rangle = \left[\cos(q\tau)|-1\rangle - ie^{i\phi(\vec{r}_0)}\sin(q\tau)|1\rangle\right] \tag{9}$$

where we included the lattice phase $\phi(\vec{r}_0) = \vec{k}_L \cdot \vec{r}_0$, which was assumed to be zero at $\vec{r} = \vec{0}$ in eq. (6) but needs to be taken into account in the general case as it is imprinted on the diffracted state. Also, by tuning the argument of the sine and cosine functions, one can create an output state in either a momentum superposition $1/\sqrt{2}\left(|-1\rangle - ie^{i\phi(\vec{r}_0)}|1\rangle\right)$ which corresponds to an atom beam splitter or an output state in the opposite momentum state which corresponds to an atomic mirror[7].

Velocity selectivity

To realize an atom beam splitter, the transit time has to be equal to $2\pi/\Omega_{eff}$. However, as discussed in the Sec. 1.1, our atom beam has a velocity distribution with an approximately 20 % full width at half maximum. Therefore, the diffraction amplitudes are also distributed around a mean value corresponding to the interaction time of the mean velocity. In practice, we use optical lattices with a top hat intensity distribution with a diameter $D = 8\,\text{mm}$. In this situation, the mean interaction time $\bar{\tau}$ corresponding to the mean velocity atomic wave is:

$$\bar{\tau} = \frac{D}{\bar{u}} \tag{10}$$

In our case, $\bar{\tau}$ corresponds to $7\,\mu s$. The diffraction sensitivity to the interaction time distribution is maximum in the atom splitter for which the transmitted state coefficient is approximately linear in the interaction time. The atom beam velocity spread results in a population imbalance of approximately 20 % between the two outputs[8]. However, in the symmetric configuration of a Mach-Zehnder interferometer, this asymmetry compensates between the first and the last Bragg diffraction gratings and the two interfering waves have similar or equal amplitudes. The interferometer visibility should therefore be very close to 1 as it decreases slowly (see eq. (16) and [83]) with the amplitudes imbalance:

$$\mathcal{V} = \frac{2\sqrt{\rho}}{1+\rho}$$

where ρ is the intensity ratio of the two interfering waves. For a diffraction imbalance as large as 20 %, the theoretical maximum visibility is still larger than 0.97.

---

[7] These transformations are usually denoted by $\pi/2$ and π pulses respectively which relates to the value of $q\tau$.

[8] This means that instead of having a perfect 50/50 beam splitter, the relative population at the output is 60/40 for atoms having a velocity 12 % smaller than the mean velocity.

Bragg angle

The Bragg condition eq. (8) corresponds, in our interferometer, to an incident angle of 87 $\mathrm{\mu rad}$. Due to the finite lattice width, the direction of the absorbed and emitted photons is not perfectly defined. Their components along the propagation direction are zero with an uncertainty of the order of $\Delta k_L \sim 1/D$ where D is the diameter of the lattice beam. Therefore, the angular acceptance (FWHM) of the Bragg diffraction can be estimated with:

$$\delta\theta = \frac{\Delta k_L}{k_L} = \frac{\lambda_L}{2\pi D}$$

For our experimental parameters, it corresponds to $14\,\mathrm{\mu rad} \sim \theta_B/6$. This small acceptance angle is one reason why drastic collimation was necessary to remove undiffracted atom waves from the transmitted beam.

Internal state selectivity

The theoretical model of eq. (6) assumed an ideal two-level atom which needs to be extended in the case of ^{7}Li internal structure. Three effects need to be taken into account when considering Bragg diffraction on our lithium beam.

1. The fine splitting of the excited state is not negligible compared to the laser detuning δ which increases the effective coupling between different momentum states by allowing different intermediate excited states. The resulting two photon Rabi frequency becomes:

   $$\Omega_R = \frac{\Omega_0^2}{2}\left[\frac{1}{\delta_{1/2}} + \frac{2}{\delta_{3/2}}\right]$$

   where $\delta_{1/2}$ ($\delta_{3/2}$) is the detuning from the D_1 line $^2S_{1/2} \rightarrow {}^2P_{1/2}$ (resp. D_2 line $^2S_{1/2} \rightarrow {}^2P_{3/2}$) transition and the factor of 2 comes from the dipole transition term which is $\sqrt{2}$ stronger for D_2 than for D_1.

2. The hyperfine splitting of the ground state is not small compared to the detuning of the Bragg laser[9]. Hence when lithium atoms are equally distributed among the ground state sublevels, which is initially the case at the output of the lithium source, they experience different Rabi frequencies due to their different detunings. In practice, ^{7}Li has two hyperfine sublevels $F = 1$ and $F = 2$ sepa-

---

[9] Only the ratio of the laser power (proportional to Ω_0^2) over the detuning determines the two photon Rabi frequency. Thus for a given available laser power, the detuning, chosen as large as possible to minimize spontaneous emission due to the excited level population, has a maximum value of the order of 3.5 GHz with our laser system (see Sec 1.2.4).

rated by $\Delta_{HFS}/(2\pi) = 803.5\,\mathrm{MHz}$. If the laser detuning is defined with respect to the $F = 2$ state, the Rabi frequency of the $F = 1$ state will be:

$$\Omega_R^{F=1} = \frac{\Omega_0^2}{2}\left[\frac{1}{\delta_{1/2}+\Delta_{HFS}} + \frac{2}{\delta_{3/2}+\Delta_{HFS}}\right]$$

It is therefore not possible to realize simultaneously atom splitters and perfect atom mirrors for the two sublevels.

3. The presence of ^{6}Li (7.5 % of natural abudance) in our lithium beam does not hinder the interferometer performances as the 10 GHz isotopic shift of ^{6}Li $^2S_{1/2}$ level leads to a much higher detuning which reduces the diffraction efficiency for this isotope.

Let us now describe the laser system used in our interferometer as the available laser power limits our laser detuning.

1.2.4 Laser setup

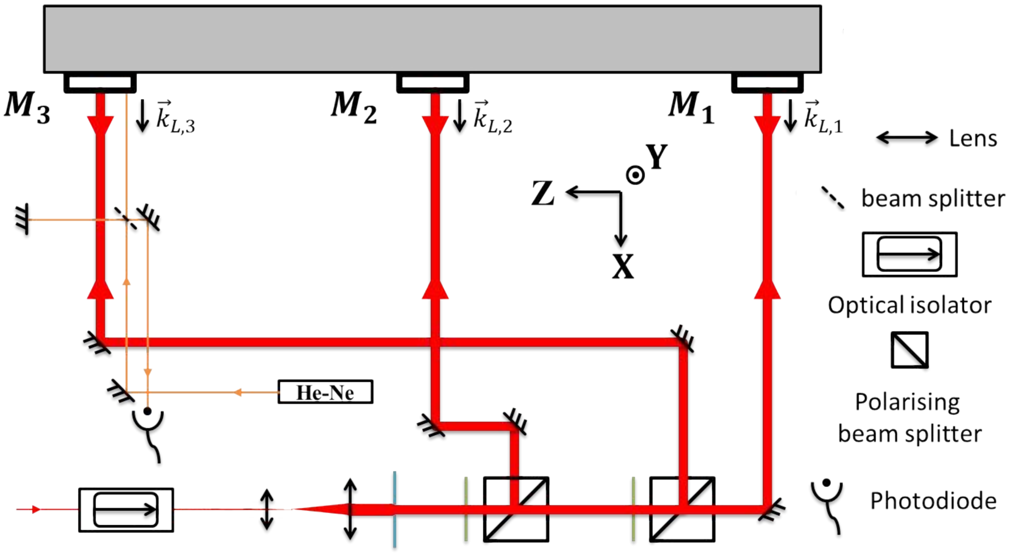

Figure 7: Schematic representation of the optical and mechanical setup used to produce three Bragg lattices. The optical bench is represented from above and the atom beam travels from the right to the left.

The light source is a dye laser developed by Biraben *et al.*[96]. It converts 5 W of laser light at 532 nm produced by a diode-pumped solid state laser (Verdi) manufactured by Coherent® into, after a double stage optical isolator, approximately 400 mW of laser light at 671 nm. Its wavelength is measured with a home-made wavemeter which compares it to the wavelength of a thermally stabilized Helium-Neon laser. The wavelength reading has an accuracy of 10^{-4} nm which corresponds to 70 MHz at 671 nm. Finally, a Hansch-Couillaud [97] locking scheme is implemented with a thermally stabilized external cavity to control the Bragg detuning in the MHz range.

The majority of the available power is then shaped into a larger beam with a radius of $\sim 8\,\mathrm{mm}$ which homogeneous part is diaphragmed with a blade iris into a flatter intensity profile 8 mm diameter. A set of polarization cubes and half wave plates distributes the resulting power to the three Bragg lattices as schematized in Fig. 7. The three retro reflecting mirrors are glued on optical mounts fixed on a 1.4 m long aluminum alloy beam. Each mount rotations around the $\vec{Z}$ and $\vec{Y}$ directions[10] are controlled by piezoelectric-actuators to superpose the reflected beam on the incident beam. Indeed, the lattice wave-vector of a retro-reflected setup is orthogonal to the mirror surface with progressive fringes parallel to it (see Sec. 1.3.2 for a discussion on the effect of the wavevector difference between incident and reflected beam). Additionally, to scan the interferometric phase which depends (see eq. (9) and eq. (15)) on the lattice phase, the third Bragg mirror can be translated along the $\vec{X}$ direction on a full course of 10 λ_L with an accuracy of $\lambda_L/1000$. In practice, to limit the non-linearity of the actuator, the mirror was translated in its central region over 1 λ_L to scan the atom fringes.

As mentioned above, the interaction time with the Bragg standing wave corresponds to a transit time near 7 µs. To perform a Bragg mirror, we have an available power of approximately 40 mW in the second Bragg lattice which gives us a maximum detuning $\delta_{3/2}/(2\pi) = 3.5\,\mathrm{GHz}$. This limits the interference signal mainly via two effects:

- The spontaneous emission rate during the π pulse is given by the excited population times the spontaneous emission rate :

  $$\Gamma_{spon} \simeq \frac{\Gamma}{2} \frac{\Omega_0^2}{\delta_{3/2}^2}$$

  where we have used the two level atom (D2 line) picture for simplicity. This quantity leads to atom losses because a spontaneously emitted photon has a dipolar radiation diagram which almost always results in the deviation from the Bragg condition. Therefore, we can evaluate this loss as $\Gamma_{spon}\tau \sim 0.3\,\%$ for the maximum detuning possible. Summed over the three Bragg pulses, this leads to 1 % loss in the transmitted atomic flux.

- The different diffraction efficiencies due to the hyperfine splitting[11] leads to an imbalance between the detected atoms in the $F = 2$ manifold and in the $F = 1$ manifold. This has to be taken into account when the interferometric phase depends on the sublevel (in particular in Chap 4 where the optical potential depends on the orbital momentum projection on the quantization axis).

---

[10] The rotation along $\vec{Y}$ was adjusted to optimize the Bragg diffraction at each lattice and the rotation around $\vec{Z}$ was optimized mainly on the third grating by maximizing the interferometric visibility.

[11] Note that in our case, the detuning is not very large compared to the hyperfine splitting, which is approximately 1/4 of the total detuning.

To quantify this, we distinguish the proportion $P(F)$ of detected atoms in the interferometer output by its deviation from equiprobability:

$$P(F) = \begin{cases} \frac{1+5\chi}{8} & F = 1 \\ \frac{1-3\chi}{8} & F = 2 \end{cases} \qquad (11)$$

where χ is a parameter between $-1/5$ and $1/3$. A detailled analysis described in S. Lepoutre's thesis [98] shows that with this value of detuning, χ is of the order of -0.06. Which means that almost 75 % of the detected atoms are in the $F = 2$ state.

Now that the Bragg diffraction parameters have been defined, let us describe the detector used to count the atom number on an interferometric output before giving some useful expression of the total interferometric signal.

1.3 ATOMIC SIGNAL

The schematized interferometer setup of Fig. 4 shows how the Mach Zehnder interferometer produces, when the Bragg pulses are not perfect, multiple closed interferometers in addition to the principal one (the continuous green line diamond). In order to select the desired interferometer output a detection slit of 50 µm width[12] is micropositioned 0.4 m after the third laser standing wave. It prevents other interferometer arms from entering the detection chamber (5^{th} Chamber) where a hot wire detector counts the transmitted atomic flux.

1.3.1 Hot wire detector

This hot wire detector consists in a rhenium ribbon (30 µm × 760 µm cross section) heated to approximatelly 1500 K. It relies on the principle developped by Langmuir in 1925 [99] and demonstrated by Taylor [100] a few years later. A complete description and characterization of this system can be found in R. Delhuille thesis [101] and in [102].

The principle of this detector relies on the ionization of the lithium atoms adsorbed on the oxidized rhenium surface. This ion evaporation from the surface is a probabilistic event which can be characterized by an exponential distribution. The residence time of the lithium ion on the wire surface follows the probability $P(t_{res}) \propto \exp(-t_{res}/\tau)$ with the characteristic time τ given by:

$$\tau = \tau_0 e^{\frac{E_{ads}}{k_B T}} \qquad (12)$$

---

[12] Which corresponds to the geometric size of the lithium beam at the detector position.

where $\tau_0 \sim 10^{-13}$ s is of the order of the ionic vibrational period close to the surface[13], $E_{ads} \sim 2.95\,\mathrm{eV}$ is the adsorption energy of the lithium ion and T is the wire temperature which was chosen as a trade-off between detection efficiency and dynamic[14]. In our case, $\tau \sim 200\,\mu\mathrm{s}$ with a large uncertainty. The ionized atom is then focused with an electrostatic lens on a channeltron which produces with a high probability an electronic pulse at each impact. These pulses are then processed with a counter interfaced with the acquisition panel. The overall detection efficiency is estimated to 30 %.

1.3.2 Interferometric signal

The detected atomic signal at the indirect output is the coherent sum of the two atomic waves in the diffracted state $|1\rangle$ which followed paths (A) and (B) as schematized on Fig 4. These two paths interacted with the three Bragg lattices. From eq. (9), it is straightforward to decompose each trajectory into elementary diffraction processes which transform the momentum state $|\pm1\rangle$ into the superposition:

$$|\pm1\rangle \longrightarrow \left[e^{i\phi^{\pm}(\vec{r}_i)}\alpha_i^{\pm}(1)\,|1\rangle + ie^{i\phi^{\mp}(\vec{r}_i)}\alpha_i^{\pm}(-1)\,|-1\rangle\right]$$

In this expression, we have separated the diffraction phases from the diffraction amplitudes:

$$\begin{cases} \alpha_i^{\pm}(\pm1) = \cos(q_i\tau_i) \\ \alpha_i^{\pm}(\mp1) = \sin(q_i\tau_i) \end{cases}$$

where the subscript i denotes the parameter of the i^{th} lattice. These coefficients can be collected for the two paths under consideration and lead to the following amplitudes of the $|1\rangle$ output state:

$$\begin{aligned} a_A &= \alpha_1^{-}(1)\,\alpha_2^{+}(-1)\,\alpha_3^{-}(1)\,e^{i\left[-\vec{k}_{L,1}\cdot(\vec{r}-\vec{r}_1)+\vec{k}_{L,2}\cdot(\vec{r}-\vec{r}_2)-\vec{k}_{L,3}\cdot(\vec{r}-\vec{r}_3)-\frac{3\pi}{2}\right]} \\ a_B &= \alpha_1^{-}(-1)\,\alpha_2^{-}(1)\,\alpha_3^{+}(1)\,e^{i\left[-\vec{k}_{L,2}\cdot(\vec{r}-\vec{r}_2)-\frac{\pi}{2}\right)} \end{aligned}$$

where $\vec{r}_i$ is a reference position which depends on the i^{th} mirror position. When the diffraction processes are perfect, the amplitudes $|a_A|$ and $|a_B|$ are identical, but in the general case, the atomic intensity per unit area is:

$$\tilde{I} = |a_A + a_B|^2 = \tilde{I}_0\left[1 - \tilde{\mathcal{V}}\cos\left(\delta\vec{k}\cdot\vec{r} + \phi_d\right)\right] \tag{13}$$

---

[13] The measured values available in the literature [102] are scattered due to the absolute temperature determination.

[14] Increasing the temperature clearly reduced the ionization time but also reduces the lithium ionization probability because the oxide coverage decreases [102].

where the vector $\delta\vec{k}$:

$$\delta\vec{k} = \vec{k}_{L,1} - 2\vec{k}_{L,2} + \vec{k}_{L,3} \tag{14}$$

is a wavevector difference representing the superposition of the interferometer paths. The phase ϕ_d is the diffraction phase which only depends on the lattices reference phases. Its general form is:

$$\phi_d = \vec{k}_{L,1} \cdot \vec{r}_1 - 2\vec{k}_{L,2} \cdot \vec{r}_2 + \vec{k}_{L,3} \cdot \vec{r}_3 \tag{15}$$

The parameter $\tilde{\mathcal{V}}$ corresponds to the fringes visibility and is defined by:

$$\tilde{\mathcal{V}} = \frac{2\,|a_A|\,|a_B|}{|a_A|^2 + |a_B|^2} \tag{16}$$

and the mean intensity per unit area is $\tilde{I}_0 = |a_A|^2 + |a_B|^2$.

The detected interference signal is the integration of all the transmitted atomic flux by the detection slit:

$$\begin{aligned} I &= \int_{slit} \tilde{I}_0 \left[1 + \tilde{\mathcal{V}} \cos\left(\delta\vec{k} \cdot \vec{r} + \phi_d\right)\right] d^2\vec{r} \\ &= I_0 \left[1 + \mathcal{V} \cos\left(\phi_d\right)\right] \end{aligned} \tag{17}$$

where the reference position vector $\vec{r}$ extends over the detection slit which is approximately $50\,\mu m = 74\,\lambda_L$! wide in the $\vec{X}$ direction and $1\,mm = 1500\,\lambda_L$!! high in the $\vec{Y}$ direction. To reduce the spatial differential phase shifts between these detected signals, $\phi_{spatial} = \delta\vec{k} \cdot \vec{r}$, $\delta\vec{k}$ has to be as parallel as possible to $\vec{Z}$. Because the $\vec{X}$ components of the wavevector are already highly constrained by the simultaneous Bragg conditions[15] this wavevector difference mainly reduce to the $\vec{Y}$ projections. This component is minimized by rotating the second mirror around the $\vec{Z}$ axis until the highest visibility is obtained.

To scan the interferometric fringes, one can either add a controlled interaction on the atomic paths which usually results in an additional phase ϕ_{int} in the cosine argument or one can change the laser diffraction phase by changing the position of one mirror which acts as a reference frame for the lattice phase. This can be done by translating the retroreflection mirror of the 3^{rd} Bragg lattice which changes the

---

[15] The differential component on the $\vec{X}$ direction is necessary much smaller than $\theta_B k_L$ which results in a negligible spatial phase shift of $5\,mrad$ (for a factor of $1/10$).

corresponding phase reference Φ_i by an amount proportional to the displacement induced along the $\vec{X}$ direction mainly, $\delta\vec{x}$:

$$\delta\Phi_3 = 2\vec{k}_{L,3} \cdot \delta\vec{x} \tag{18}$$

This phase scan was continuously measured in order to reduce the number of parameters used to fit the interferometric fringes.

Optical Michelson interferometer

This measurement was performed with an optical Michelson interferometer which uses the third Bragg mirror as a retroreflecting mirror. It is represented on Fig.7 and consists in a Helium-Neon laser at 633 nm split under vacuum, retro-reflected on M3 and interfering after the beam splitter with another reference arm . The optical interference fringes are detected outside vacuum on a photodiode. The detected fringes are a function of the path difference between the two arms which depends on the third mirror displacement $\delta\vec{x}\,(V)$:

$$\delta\Phi_{Michelson}\,(V) = 2\vec{k}_{He-Ne} \cdot \delta\vec{x}\,(V) \tag{19}$$

where $\vec{k}_{He-Ne}$ is the wavevector of the He-Ne induced lattice and V is the voltage applied to the piezoelectric actuator. The Michelson interferometer arm was positioned below the atomic beam and does not interact with it. Due to non-linearities, the mirror displacement $\delta\vec{x}\,(V)$ is expressed as a polynomial of order 3 in V in order to fit accurately the fringe signal of the Michelson interferometer $\Phi_{Michelson}\,(V)$. Apart from a constant phase shift, the diffraction phase can be expressed by:

$$\phi_d\,(V) = K\delta\Phi_{Michelson}\,(V) + \phi_{d,0} \tag{20}$$

where K is a constant coefficient equal to $k_{L,3}/k_{He-Ne} \sim 0.94$ which depends on the projection of the He-Ne wavevector on the lattice wavevector. The phase $\phi_{d,0}$ should be constant if the X position of the mirrors were perfectly stable in time. However because of thermal distortion of the mirror support it is slowly drifting in time (see Fig. 8b). A typical atomic fringe as a function of the detected Michelson phase is represented on Fig. 8a with the corresponding fitting coefficients.

Additional phase shifts

It is usual to group the different phases that are either part of the diffraction phase or from other sources into some generic denominations that allow to discuss each effect separately.

1. **Lattice phase**: This corresponds to the phase difference of the two interfering laser beam forming the Bragg lattice. In our case, because the coherence length

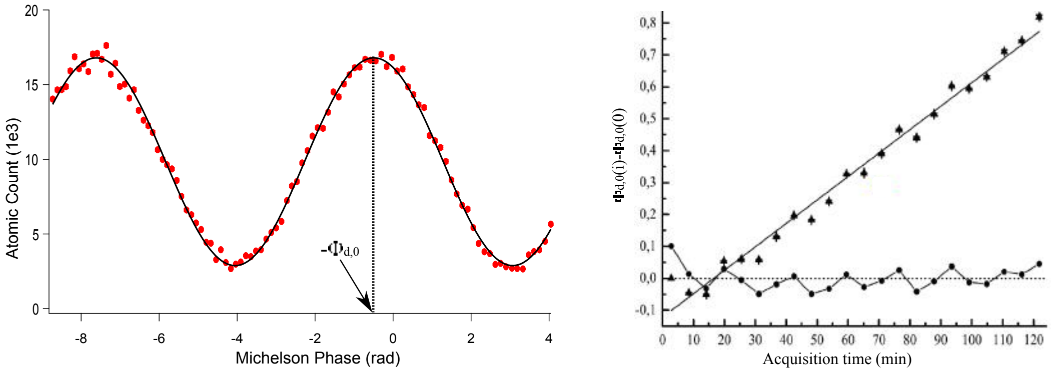

(a) Interferometric signal **(b)** Diffration phase drift

Figure 8: **(a)** Interferometric signal during a 100 s scan. Each points corresponds to a 1 s integration of the detected atoms. The black line is a result of a fit with eq. (17) which gives $I_0 = 9.8 \times 10^3$ atom/s , a visibility $\mathcal{V}$ of 71 %, $K = 0.88$ and $\phi_{d,0} = 0.4$ rad (see eq. (20)). For this recording, the atomic flux was quite low compared to an optimal configuration.
(b) Drift of the diffraction phase reference $\phi_{d,0}$ minus its initial value during a 2 h period. The graph is adapted from A. Miffre thesis [85]. The stars correspond to the measured mean phases during 5 min scanning periods and indicates a linear drift of 7.4(2) mrad/min. The residual of the linear fit is represented at the bottom with circles. A clear oscillation correlated to the temperature of water-cooled baffles used for the two VHS 1200 oil diffusion pumps is visible. Indeed, the period of this oscillations is close to 20 min which corresponds to the period of the water cooler used for the pumps.

of the dye laser is much larger than the path length difference between the Bragg lattices, it can be treated as zero. But when the laser frequencies come from different sources, their differential phase fluctuations needs to be taken into account. Also, when the reflected beam acquires a differential phase shift (such as the Pancharatnam phase in Chap. 3) this needs to be accounted for.

2. **Sagnac phase**: This phase is due to the global lattices rotations during the interferometer inducing a different laser phase probed by the two paths. Its general form is

$$\phi_{Sagnac} = 2m\vec{\Omega} \cdot \vec{A}/\hbar \tag{21}$$

where $\vec{\Omega}$ is the angular rotation speed and $\vec{A}$ is the interferometer's enclosed area. In our interferometer, the area is parallel to the floor which gives a projection coefficient $\sin(\lambda_{Toulouse})$, where $\lambda_{Toulouse}$ is the laboratory's latitude. It corresponds to 640 mrad [103].

3. **Zeeman phase**: The phase difference between the two paths depends on the integrated atomic energy along each paths. When a non zero magnetic field is

experienced by each arm, the atomic ground state first order Zeeman shift leads to a differential phase between different Zeeman sublevels:

$$\phi_{Zeeman}\left(F, m_F\right) = -\frac{\mu_B m_F g_F}{\hbar} \int \left\|\vec{B}\left(t\right)\right\| dt \tag{22}$$

where μ_B is Bohr's magnetic moment and g_F is the hyperfine level landé factor. This phase vanishes when the field is homogeneous but, when a magnetic field gradient exists bewteen the two arms, a differential Zeeman phase shift has to be included in the interferometric phase. This is discussed in details in [89]. As an order of magnitude, one can estimate the effect of a constant gradient orthogonal to the propagation direction. With a $20\,\mathrm{mG/mm}$ gradient, the differential phase between the two paths will be approximately π. This constraining condition shows how the magnetic environment needs to be controlled for $m_F \neq 0$ atomic states.

4. **Interaction phase**: This phase, denoted ϕ_{int} includes any kind of induced phase shift between the two paths.

1.3.3 Fringe visibility

The total interferometric signal is an incoherent superposition of:

- Different hyperfine component contributions, with varying populations $P\left(F\right)$ (see eq. (11)), and phases (see eq. (22)).
- Different velocity components in the atomic beam, with different diffraction amplitudes $\cos\left[\Omega_{eff}\tau\left(\nu\right)\right]$ (see eq. (9)) and dispersive phases.
- Different spatially distributed signals with different phases and possible overlap between interferometric outputs.

Therefore, it is a useful simplification to collect these effects into the expression:

$$I = I_0\left[1 + \mathcal{V}e^{-\frac{\left\langle\phi^2\right\rangle}{2}}\cos\left(\phi_m\right)\right] \tag{23}$$

where $\left\langle\phi^2\right\rangle$ is the variance of the mean phase ϕ_m. This expression captures the interferometric signal behavior when all the differential phase effects on the incoherent components are small compared to the mean phase[16]. This model shows that to get the highest visibility, implying the highest phase sensitivity, one should keep the phase variance on each path to a minimum. It also tells us that a visibility change

---

[16] This expression also assumes a Gaussian distribution of the total phases which is a typical assumption in term of noise sources and can be acceptable for the velocity dependent phases. Yet it is far from being justified for the different Zeeman populations or for spontaneous emission processes. However, it is still instructive for the aforementioned effects.

informs us on the phase spread on each path (as is used for the optical pumping characterization used in Chap 4).

1.3.4 Phase sensitivity

When a small interaction phase shift $\delta\phi_{int}$ is added to the diffraction phase, it is convenient to keep the later constant and close to $\pi/2$ to have the highest phase sensitivity of the interferometric signal. In this situation, the atom intensity is approximately linear in the interaction phase: $I(\delta\phi_{int}) \sim I_0 + I_0 \mathcal{V} \delta\phi_{int}$. From this expression we can estimate the smallest phase shift measurable by considering that all noise sources are below the fundamental Poissonian noise induced by the discrete atomic count. The phase sensitivity σ_ϕ, defined as the ratio of the 1σ statistical phase deviation per square unit of frequency[17], is:

$$\sigma_{\phi,count} = \frac{1}{\mathcal{V}\sqrt{I_0}} \tag{24}$$

which is around $7\,\mathrm{mrad}/\sqrt{\mathrm{Hz}}$ for our interferometer used at its highest performance ($\mathcal{V} = 80\,\%$ and $I_0 = 3 \times 10^4\,\mathrm{atoms/s}$). Usually, we do not use this kind of measurement process and prefer to scan a few fringes to get rid of drifts as described previously. The resulting phase sensitivity is in this case $\sqrt{2}$ larger $\sigma_{\phi,count} \sim 10\,\mathrm{mrad}/\sqrt{\mathrm{Hz}}$. In addition to this fundamental phase noise, additional perturbations (such as vibrations of the mirror support) can induce phase fluctuations. This is discussed in details in [104] were the main source of phase noise, the Sagnac[18] noise, was identified and accounted for most of the visibility reduction of eq. 23. This noise has a vanishing average value and its effect is already taken into account in eq. (24) which uses the measured fringe visibility.

Phase drift

When the Michelson phase is used as a reference for the diffraction phase, a constant term $\phi_{d,0}$ was used to link the two quantities. In practice, this term was subject to a rather large drift of a few $7.4(2)\,\mathrm{mrad/min}$ when measured by A. Miffre [85]. This is represented on Fig. 8b where this "constant" phase is plotted as a function of the acquisition duration. This drift was highly correlated to temperature drifts of the mirror supports induced by the steady increase of the setup temperature during the day. This is the reason why we mainly used a measurement procedure which acquired simultaneously the diffraction phase without additional interaction phase which was used as a reference. Details on this procedure are given in Chap. 4 Sec. 4.3. It resulted in a factor of two larger phase noise $\sigma_{\phi,count} \sim 20\,\mathrm{mrad}/\sqrt{\mathrm{Hz}}$ which

---

[17] In other words, $\langle \phi^2 \rangle = \sigma^2_{\phi,count} 1/T_{acq}$ where T_{acq} is the phase acquisition time.

[18] Called hence because it can be expressed as an effective rotation of the mirrors position during the interferometer which leads to a phase shift proportional to the angular velocity and the enclosed interferometer area

allowed to measure phases with a 1 mrad statistical uncertainty in less than an hour of operation, depending on the interferometer performances.

1.4 CONCLUSION

In this chapter, we have described the lithium interferometer developed in Toulouse. The characteristics and performances of its three main components, the lithium source, the diffraction lattices and the hot wire detector, were discussed. In addition, some theoretical aspects of the diffraction process were described which will be useful in the second part of this thesis. Emphasis was made on the interferometric signal which involves many effects, such as Zeeman shifts and vibrational noise, implicitly included in the simple expression:

$$I = I_0 \left[1 + \mathcal{V} \cos\left(\phi_0 + \phi_d + \phi_{int}\right)\right] \tag{25}$$

where we have collected in ϕ_0 all additional phase shifts and have used a global visibility resulting from differential diffraction efficiency and phase dispersion. With this description, we should have all the tools necessary to describe the first part of my work during these three years which were:

- **Chap 2**: The demonstration and characterization of a Kerr modulator for atom interferometry.
- **Chap 3**: The development of a new tool for continuously phase shifting an atom interferometer phase, the Pancharatnam phase shifter
- **Chap 4**: The measurement of ^{7}Li, $\left|2S_{1/2}, F = 2, m_F = 2\right\rangle$ 'tune-out' wavelength, at which its polarizability vanishes.

2 KERR MODULATOR FOR MATTER WAVES

Contents

In this chapter, we describe a phase modulator for atom-waves, which is the perfect atom-optics analogue of the Kerr modulator for light waves [105]. The Kerr effect is the variation of a medium's refractive index produced by the application of an electric field. The variation is quadratic in the electric field amplitude for a large variety of media and this effect has been used to modulate the phase of light waves. This modulation induces frequency side-bands in the spectrum which can be detected via wave-beating. We implemented the equivalent of this side-bands homodyne and heterodyne detection in our interferometer by modulating the refractive index of the atom waves. We briefly present the concept of electrical wave modulation, its extension to matter waves and summarize the experiments which already produced phase modulation of atom waves. Then, developing a theoretical model, we derive the modulation amplitudes that we can expect from our experiment. Finally, we describe in more details our phase modulator and compare the obtained spectra with our model.

2.1 WAVE MODULATION

2.1.1 Classical phenomenon

Wave beating is ubiquitous in physics [106]. It was discovered with acoustic waves and extended to electromagnetic waves, from radio-frequencies to the laser domains. It simply relies on the superposition of multiple waves oscillating at different frequencies. For electromagnetic waves it can be written, in the simpler case of two fields along the same polarization axis, as: $E_{tot} = E_1 e^{i\omega_1 t} + E_2 e^{i(\omega_2 t+\phi)} + C.C.$, where E_1 and E_2 ere the fields amplitudes, ω_1 and ω_2 their frequencies and ϕ is a phase shift. Simple algebra yields a total intensity, $\langle I_{tot}(t)\rangle = I_1 + I_2 + \sqrt{I_1 I_2}\cos\left[(\omega_1 - \omega_2)t - \phi\right]$, where I_1 and I_2 are the respective intensities of the two fields. This expression assumes that the detector bandwidth is higher than the frequency difference: $|\omega_1 - \omega_2|$ but lower than ω_1 and ω_2. The sum of two waves of different frequencies thus induces an intensity modulation, called a beat note, which is a signature of this difference averaged by the detector. This effect is commonly used for frequency comparison especially since the advent of the frequency comb [107]. The generation of waves oscillating at different frequencies from a single-frequency source is commonly done for electro-magnetic waves. For example, by modulating the electric field's amplitude. The resulting field is $E_{AM} = E_c e^{i\omega_c t}\left[1 + M\cos(\omega_m t + \phi)\right]$, where ω_c and ω_m are the carrier and modulation frequencies, M is the modulation amplitude and ϕ is the modulation phase. One can express the total electric field as a superposition of three frequencies[1]:

$$E_{AM} = E_c \left\{ e^{i\omega_c t} + \frac{M}{2}\left[e^{i(\omega_c+\omega_m)t+i\phi} + e^{i(\omega_c-\omega_m)t-i\phi}\right]\right\}$$

and the intensity reads:

$$I_{AM}(t) = I_c\left[1 + \frac{M^2}{2} + 2M\cos(\omega_m t + \phi) + \frac{M^2}{2}\cos(2\omega_m t + 2\phi)\right]$$

displaying frequencies at the modulation frequency and its first harmonic. This method is useful for extracting a signal from a noisy low frequency environment[2] because it can be synchronously mixed with the modulating signal and purified of modulation harmonics. This is called homodyne detection and is used in communication protocols or spectroscopy [110] in many different configurations: multiplexing, amplitude modulation, frequency modulation or phase modulation. The latter consists in modulating directly the electromagnetic wave's phase to generate side-bands at the modulation frequency harmonics:

---

[1] When the modulation frequency is much smaller than the carrier frequency, the additional frequencies appearing in the spectrum are usually called side-bands.

[2] Which can be due to low frequency intensity noise or electrical background noise see [108], [109].

$$\begin{aligned} E_{PM} &= E_0 e^{i(\omega t + \phi_m \sin(\omega_m t))} \\ &= E_0 \sum_{p=-\infty}^{+\infty} J_p(\phi_m)\, e^{i(\omega + p\omega_m)t} \end{aligned} \tag{26}$$

Where $J_p(\cdot)$ is the Bessel function of the first kind. To produce this phase modulation, one can modulate the refractive index n of the medium in which the wave propagates with an additional electric field $E(t)$. A second order expansion of the refractive index modulation leads to:

$$n(t) = n_0 + n_1 E(t) + n_2 E(t)^2$$

where n_1 and n_2 are in fact tensors of rank 1 and 2 respectively if the medium is a crystal. The linear term $n_1 E(t)$ is the Pockels effect and exists only in non-centro-symmetric crystals[3]. The quadratic term $n_2 E(t)^2$ is the Kerr effect and corresponds to the self interaction between the induced electric dipoles in the medium and the applied electric field.

These wave modulation techniques essentially rely on the superposition principle and on the wave description of electrical fields, which motivated us to extend it to atoms. But let us first present how this can, and has been, done with matter waves.

2.1.2 Quantum extension

Following the description of Sec. 1.2, producing different frequency components in an atom wave requires to create a coherent[4] superposition of different energy states. Diffraction is a general technique which describes the interaction of an incident plane wave $|\mathbf{k}_i, \Omega_i\rangle$ ($\hbar\mathbf{k}_i$: momentum, $\hbar\Omega_i$: energy) with a perturbation periodic in space and time. This interaction can transfer p quanta of momentum $\hbar\kappa$ and energy $\hbar\omega$, thus producing a superposition of plane waves $|\mathbf{k}_i + p\kappa, \Omega_i + p\omega\rangle$.

Contrary to electromagnetic waves, the vacuum is dispersive for matter waves, which limits the range of detectable modulation frequencies. The dispersion relation being $\hbar\omega = \frac{\hbar^2 k^2}{2m} + mc^2$ in a non-relativistic description of matter waves, where m is the particle's mass and k its wave-vector. The phase velocity is $v_\varphi = \left(v_g^2 + c^2\right)/v_g$, where v_g is the wave's group velocity. Clearly v_φ is always greater than c ! This quantity does not describe any physical observable and the only relevant quantity is v_g which corresponds, for an atom, to its classical velocity. The dispersion of the propagation delay between the modulation region and the detector can wash out the phases between the different energy states. The average value of the propagation delay is given by $\tau_{prop} = D/v_g$ where D is the distance between the diffraction region and the detection region. Its dispersion leads to a maximum modulation frequency:

---

[3] For example Lithium Niobate (LN) partially doped with magnesium oxyde and Potassium titanyl phosphate (KTP) are commonly used in Electro-Optic Modulators (EOM).

[4] This ensures that the differential phase between different frequency components does not blur the beating signal

$$\begin{aligned}\omega_{max,p}/(2\pi) &= \frac{1}{\Delta\tau_c} \\ &= \frac{v_g^2}{D\Delta v_g}\end{aligned} \tag{27}$$

which corresponds to a phase spreading of $1\,\mathrm{rad}$ between the carrier and the sideband. The resulting "decoherence" can however be circumvented by heterodyne detection of the matter wave sidebands whose frequency difference is smaller than $\omega_{max,p}/(2\pi)$. Another typical frequency of matter waves is the frequency width of the source. This frequency gives an idea of the lowest detectable modulation frequency which does not require homodyne techniques for longitudinal modulation. For an atom wave of mean longitudinal velocity v_g and of width Δv, the longitudinal coherence length is $l_c := \lambda_{dB} v_g/\Delta v_g$ which, expressed in frequency unit, gives a minimum modulation frequency:

$$\begin{aligned}\omega_{min,s}/(2\pi) &= \frac{m v_g \Delta v_g}{\hbar} \\ &= \frac{\Omega_g}{2\pi}\frac{2\Delta v_g}{v_g}\end{aligned} \tag{28}$$

where $\Omega_g/(2\pi) = E_{kin}/h$ is the wave mean kinetic energy (in frequency unit). The minimum modulation frequency is thus a fraction of the wave frequency. Orders of magnitude of these two frequencies are listed in Tab. 2.

Matter wave	$v_g(m/s)$	$\Delta v_g(m/s)$	$D(m)$	$\omega_{min,s}/(2\pi)$	$\omega_{max,p}/(2\pi)$
Electron beam	10^8	100	1	10 THz	100 THz
Thermal atom beam	1000	100	1	1 THz	10 kHz
Cold neutron beam	10	0.1	1	1 MHz	1 kHz
Cold atom wave	1	10^{-4}	10^{-2}	10 kHz	10 kHz

Table 2: Maximum modulation frequencies for different type of matter wave experiments (^{7}Li was taken as a reference atom). The electron matter wave combines a small velocity width and a high mean velocity which results in a high maximum modulation frequency. For thermal atom beam and cold neutron beams, the propagation dispersion limits the possible modulation frequencies at a few kHz. For cold atom experiments, both frequencies are of the same order of magnitude.

The production of coherent superposition of different kinetic energies quantum states has already been demonstrated with electrons, neutrons and atoms using various techniques:

Acoustic wave diffraction

In 1987, Hamilton *et al.*[111] used surface acoustic waves to diffract a grazing incident neutron beam. They observed the direction of reflections on a quartz substrate which was excited by electrodes transducers producing surface waves. The first order of diffraction peaks are clearly resolved. This technique was latter on extended to atomic waves on vibrating "surfaces" [52], [112].

Evanescent wave diffraction

In 1995, Dalibard's group [52], [113] used a repulsive evanescent wave on the surface of a prism, produced by an internally totally reflected laser beam, to create a superposition of different kinetic energy states by modulating ($\sim 1\,\text{MHz}$) the intensity of the evanescent wave. They showed the appearance of different kinetic energy states in their time of flight signal. The year after, they used a similar configuration to create a series of temporal slits of controlled length and delay. An incident atom wave, freely falling orthogonal to the surface could be absorbed (reflected) depending on their arrival time on the "atom mirror" and whether the laser was turned Off (On). Chopping the atom beam with these temporal slits resulted in temporal interference signal, which proved the coherence between the different side-bands. The interference signal from [113] is presented on Fig 9a.

Bragg diffraction with modulated potential

The same year, Zeilinger's group [114] experimentally demonstrated that an amplitude modulated standing light wave produces "dynamic" Bragg scattering of an incident metastable Ar beam which incident angle was detuned from the Bragg angle. Indeed, modulating the light grating intensity produced frequency side-bands that matched the recoil frequency and restored diffraction. This phenomena is easily understood in the atomic rest frame. For example, if the incident angle is higher than the Bragg angle $\theta = \theta_B + \Delta\theta > \theta_B$, the intensity modulation in the rest frame of the atoms is higher than the recoil frequency. Therefore, adding a frequency modulation co-propagating with the atoms reduced the frequency of the intensity modulation. This effect restores energy conservation and diffraction. The produced side-bands are detected by spatial filtering of the transmitted atomic beam, as shown on Fig 9b. They verified the coherence of the diffracted beams by probing the atomic interference pattern with an absorbing grating. The transmitted intensity revealed the beat notes oscillating at the modulation frequency which could be phase-shifted by shifting the phase of the Bragg beam intensity modulation.

Time-dependent Zeeman interaction

In 1995, Werner's group [115] applied a time dependent Zeeman splitting between two spin states on one arm of their Mach-Zehnder neutron interferometer. They observed the Fourier spectrum of their interference signal to extract the amplitudes of the two spin states for different numbers of absorbed or emitted photons. These numbers correspond to different side-bands in their energy spectrum. This method was also used by Pritchard's group to investigate coherences in a supersonic Na beam and to rephase its different longitudinal components [116], [117].

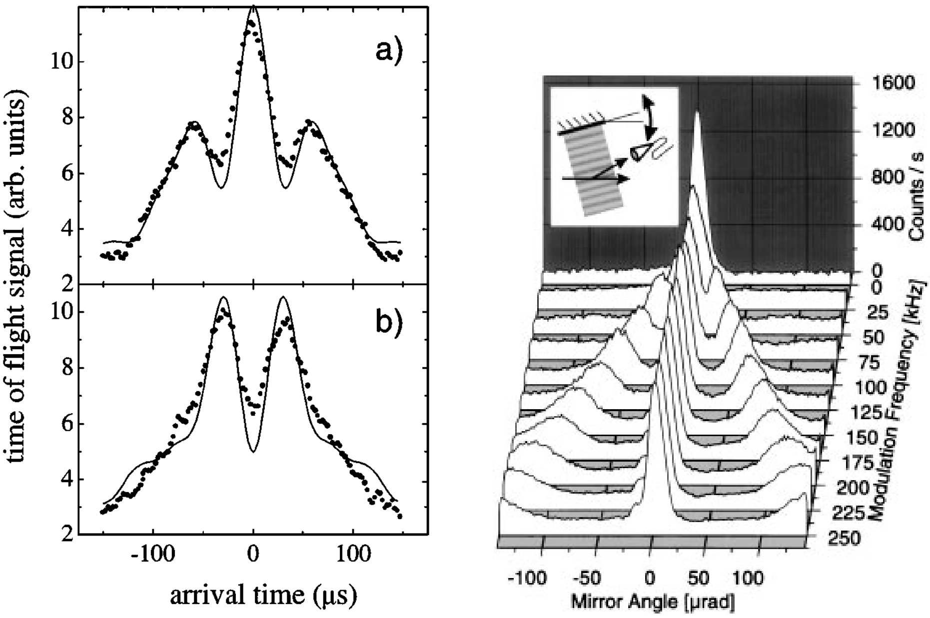

(a) Time interference

(b) Bragg diffraction

Figure 9: Figures from Dalibard's experiment on evanescent mirrors temporal slits [113], and from Zeilinger's experiment on "dynamic" Bragg scattering [114].
(a): Interference pattern obtained in the temporal Young's slits experiment displaying constructive (destructive) in the top (bottom) panel. The phase shift was induced by changing the evanescent wave strength.
(b): Intensity of diffracted atoms as a function of their incident angle for different intensity modulation frequencies. The central peak corresponds to the 'static' Bragg diffraction peak centered at $\Delta\theta = 0$ while the wings corresponds to the 'dynamic' Bragg diffraction peaks which appears for symmetric angle due to the symmetric side-bands generated by the modulation

Atom laser modes

In 2002, Aspect's group [118] used the continuous out-coupling from a Rubidium condensate (known as the atom-laser) to demonstrate the possibility to mode-lock the freely falling exiting waves. In practice, they frequency modulated the out-coupling RF to produce coherent energy side-bands that interfered into short coherent pulses of atoms. A similar setup had been used a few years before by Bloch *et al.*[119] to measure the spatial correlation function in a condensate. The principle of the experiment was to use slightly different RF frequencies which, due to the gravitational potential, out-coupled atoms from different height in the condensate. In this situation, the two freely-falling waves interfered and the visibility of the pattern was a signature of the spatial coherence in the condensate.

Rotating grating diffraction

In 2003, Frank *et al.*[120], sent a neutron beam on a rotating silicon grating acting as a phase modulator via a real index of refraction. They analysed the energy spectrum of the diffracted beam and detected energy side-bands. Due to the small neutron mass and velocity ($4.5\,\mathrm{m\,s^{-1}}$), the kinetic frequency is relatively small and its spread is relatively narrow ($E_{kin}/h \simeq 25\,\mathrm{MHz}$ and $\omega_{min,s} \simeq 1\,\mathrm{MHz}$). Because the frequency of the phase grating could be as high as 1.7 MHz, they were able to clearly resolve side-bands in the energy spectrum.

Modulation in time

Side-bands generation had already been convincingly demonstrated with neutrons, electrons and atoms. The coherence properties of diffraction in time process have been clearly shown for various techniques such as :

- Intensity modulation of a light grating.
- Zeeman interaction with an oscillating magnetic field.
- Modulated out-coupling from a Bose Einstein Condensate
- Modulation of an effective refractive index

The phase modulator we developed aimed at resolving the generated energy side-bands via heterodyne wave-beatings in order to quantitatively compare the diffraction in time experiments to theory (diffraction amplitudes and phases). This technique is very general and applicable to a wide range of interferometers and can be used as a tool for heterodyne measurements of high frequency phase shifts.

2.2 THEORETICAL DESCRIPTION

2.2.1 Naïve description of the phase modulation

We consider the description of an atom of mass μ propagating freely in the $+z$ direction. At time $t = 0$ the atom enters a region, localized in space, in which its potential energy depends on an external oscillating parameter. Semi-classically, we can describe this atom with an initial wavepacket having a group velocity v_i localized in space at the position $z(t) = v_i t$. Because the potential is constant in the transverse direction on a scale which is much larger than the de Broglie wavelength $\lambda_{DB} = \frac{h}{\mu v_i} \sim 53\,\text{pm}$ we can neglect the transverse dynamics and reduce our study to a one-dimensional Schrödinger equation:

$$i\hbar\frac{\partial\Psi}{\partial t} = \left[-\frac{\hbar^2}{2\mu}\frac{\partial^2}{\partial z^2} + U(z(t))\right]\Psi$$

Because of the linearity of this equation, we can simplify our study to the case of a single initial plane wave $|k_i, \Omega_i\rangle$ (initial wave-vector k_i and energy $E_i = \hbar\Omega_i$). Analytically, because of the relation between space and time $z(t) = v_i t$, the spatially localized interaction potential can be described by a purely time dependent potential which is schematized on Fig. 10:

$$U(t) = \begin{cases} 0 \quad \text{if} \quad t \notin \left[-\frac{L}{2v_i}, \frac{L}{2v_i}\right] \\ U_0 + U_M\cos(\omega t) \quad \text{for} \quad t \in \left[-\frac{L}{2v_i}, \frac{L}{2v_i}\right] \end{cases} \tag{29}$$

In the static approximation, when the oscillation frequency ω is much lower than the inverse of the transit time $\frac{2\pi}{\tau}$, the problem simplifies to the rectangular potential barrier treated in any introductory course on quantum mechanics [121]. The transmitted plane wave, in the weak potential approximation, is equal to the incoming wave phase shifted by $\phi(t) = -\Delta kL = -\frac{U_0(t)k_i L}{2E_i} = -\frac{U_0(t)\tau}{\hbar}$. where Δk is the wave-number difference between the interaction region and free space, $U_0(t)$ is the height of the potential perturbation during the interaction. In this situation, energy is a conserved quantity and no side-bands can be created. This result is exactly the first order perturbation phase shift demonstrated by [122] which states that the phase shift accumulated by a plane wave in presence of a stationary perturbation $U(z)$ can be expressed as :

$$\phi = -\frac{1}{\hbar}\int_{\Gamma_{cl}^{(0)}} U(z(t))\,dt \tag{30}$$

where $\Gamma_{cl}^{(0)}$ is the unperturbed classical path of the particle. The time dependence here is only fortuitous and comes from the propagation of the plane wave. However, if one extends naïvely this expression to our time dependent potential (discarding

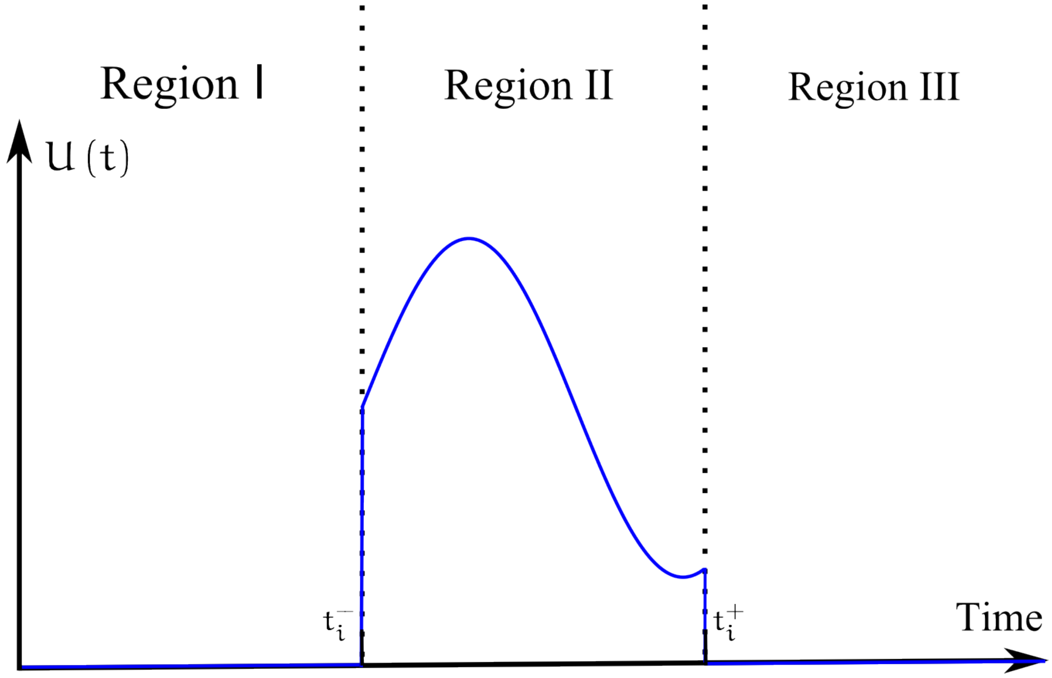

Figure 10: Interaction region: We are interested in a time dependent, localized potential, acting on a propagating atom wavefunction. Because of the propagation, the spatially restricted potential appears as purely time dependent, which starts at $t_i^- = -\frac{L}{2v_i}$ and ends at $t_i^+ = \frac{L}{2v_i}$. The reference time being taken at the center of the interaction region. Here, $v_i = \frac{\hbar k_i}{\mu}$ is the atoms classical velocity associated with $|k_i, \Omega_i\rangle$ and L is the spatial length of the interaction region.

the constant step potential U_0 for simplicity), the resulting phase shift would be, for a plane wave of wave-vector $k_i = \frac{m v_i}{\hbar}$:

$$\phi(t) = -\frac{2U_M}{\hbar\omega} \sin\left(\frac{\omega L}{2v_i}\right) \cos(\omega t) \tag{31}$$

and the resulting transmitted wave $|\Psi_t\rangle = |\Psi_i\rangle\, e^{i\phi(t)}$ is[5]:

$$|\Psi_t\rangle = A_i \sum_{p=-\infty}^{+\infty} (-i)^p J_p(\phi_m)\, e^{i(p\omega+\Omega_i)t} |k_i, \Omega_i\rangle \tag{32}$$

The time dependent phase shift in this expression can be interpreted as a coherent superposition of different energy states $|k_p, \Omega_i + p\omega\rangle$, where $k_p = \sqrt{\frac{\hbar}{2\mu}(\Omega_i + p\omega)}$, diffracted by the potential and coincides with the expression we get by considering the phase diffraction eq. (26) of an optical field by a Kerr cell. This cannot be obtained in a time independent approximation which conserves the atom wave energy. In the next section, we will demonstrate rigorously that this description of the transmitted state is correct.

---

[5] Using the Anger-Jacobi expansion [123] for $e^{-iz\cos(u)} = \sum_{n=-\infty}^{+\infty} (-i)^n J_n(z)\, e^{inu}$.

2.2.2 Diffraction in time

Due to the fact that the maximum potential height in our experiment is of the order of a millionth of the incoming wave's kinetic energy, we will completely neglect the reflected wave in our treatment[6]. In addition, the modulation frequency $\omega < (2\pi)30\,\mathrm{kHz}$ is much less than the typical kinetic energy of the atomic beam : $E_i/\hbar \simeq (2\pi)9\,\mathrm{THz}$, which cancels the probability of backward scattering, justifying this approximation.

The problem of diffraction in time has been discussed by Li and Reichl [125] and consists in two sets of infinite number of continuity equations. In our case, due to the hypothesis of negligible reflection, we can obtain a closed form for the transmitted wave. To do so, we will adapt their formalism and use the same Floquet approach.

Floquet expansion

Separating the atomic propagation into three regions, the free space propagation regions (I and III) and the interaction region (II), one can solve the Schrödinger equation in each region and combine the resulting expressions. As the freely propagating solution are well known, we will focus on the interaction region. When the oscillating potential $U(t)$ is periodic in time of period $T = \frac{2\pi}{\omega}$, the Floquet theorem states that the solutions to the Schrödinger equation in the region II can be written in the form:

$$\Psi_F^{II}(z,t) = e^{-iE_F t/\hbar}\phi(z,t)$$

where E_F is the Floquet eigen-energy and $\phi(z,t)$ is an unknown periodic function of period T. Due to the homogeneity of the potential, finding the solution in region II reduces to solving the separable Schrödinger equation [126]:

$$\left(E_F + \frac{\hbar^2}{2\mu}\frac{\partial^2}{\partial z^2}\right)\phi(z,t) = \left(U(t) - i\hbar\frac{\partial}{\partial t}\right)\phi(z,t)$$

which have solutions of the form $\phi(z,t) = g(z)f(t)$. Denoting E the separation constant, one get the un-coupled set of equations:

$$-\frac{\hbar^2}{2\mu}\frac{d^2 g(z)}{dz^2} + U_0 g(z) = E g(z) \qquad (33)$$

$$i\hbar\frac{df(t)}{dt} - U_M\cos(\omega t)f(t) = (E - E_F)f(t) \qquad (34)$$

---

[6] In a step potential, for low amplitude, the reflection coefficient reduces to $\left(\frac{U_0+U_M}{E_i}\right)^2$ which is in our situation negligible. Furthermore, the distance over which our potential rises is large $\sim 1\,\mathrm{mm}$ [124] which does not change significantly over one atomic wavelength (54 pm) and this circumstances further reduces the reflection probability.

Solving eq. (34) and using the periodicity of f allows us to specify the separation constant $E = E_F + m\hbar\omega$ for a given $m \in \mathbb{Z}$. Therefore, for each $m \in \mathbb{Z}$ the two equations (33) and (34) admit solutions labeled by m:

$$\begin{aligned} f_m(t) &= f_m(0)\, e^{-\frac{i}{\hbar}\left[m\hbar\omega t + \frac{U_M}{\omega}\sin(\omega t)\right]} \\ g_m(z) &= g_m(0)\, e^{i q_m z} \end{aligned}$$

where $q_m = \pm\sqrt{\frac{2\mu}{\hbar}\left(E_F + m\hbar\omega - U_0\right)}$ is the wave-vector inside the diffraction region. We can collect these solutions in a compact form for the general solution in region II:

$$\Psi^{II}(z,t) = \sum_{m,n=-\infty}^{+\infty} a_m J_n\left(\frac{U_M}{\hbar\omega}\right) e^{i\left(q_m z - [\Omega_F + (m+n)\omega]t\right)} \tag{35}$$

where $\Omega_F = \frac{E_F}{\hbar}$ is the Floquet frequency and a_m is a constant coefficient.

Continuity equations

The single incoming wave $|k_i, \Omega_i\rangle$ in region (I) and the transmitted wave in region (III) can be expressed as:

$$\begin{aligned} \Psi^{I}(z,t) &= A_i e^{i(k_i z - \Omega_i t)} \\ \Psi^{III}(z,t) &= \sum_{p=-\infty}^{+\infty} A_p e^{i(k_p z - \Omega_p t)} \end{aligned}$$

where, for the time being, $(k_p, \Omega_p)_{p\in\mathbb{Z}}$ (wave-vector, energy) is an arbitrary basis set for freely propagating waves. Equating the wavefunctions at the borders:

(a) $\Psi^{I}\left(-\frac{L}{2}, t\right) = \Psi^{II}\left(-\frac{L}{2}, t\right) \forall t$

(b) $\Psi^{II}\left(\frac{L}{2}, t\right) = \Psi^{III}\left(\frac{L}{2}, t\right) \forall t$

induces a convenient choice for Ω_F (which was defined modulo ω): $\Omega_F = \Omega_i$ and shows that the only non-zero elements of the basis for the third region are defined by energies $\Omega_p = \Omega_i + p\omega$ and their associated wave-vectors. Now, one can extract from these continuity equations the following infinite set of equations:

$$\sum_{m=-\infty}^{\infty} a_m J_{-m}\left(\frac{U_M}{\hbar\omega}\right) e^{-i\frac{q_m L}{2}} = A_i e^{-i\frac{k_i L}{2}} \tag{36}$$

$$\sum_{m=-\infty}^{\infty} a_m J_{n-m}\left(\frac{U_M}{\hbar\omega}\right) e^{-i\frac{q_m L}{2}} = 0 \quad \forall n \in \mathbb{Z}^* \tag{37}$$

$$\sum_{m=-\infty}^{\infty} a_m J_{p-m}\left(\frac{U_M}{\hbar\omega}\right) e^{i\frac{q_m L}{2}} = A_p e^{i\frac{k_p L}{2}} \quad \forall p \in \mathbb{Z} \tag{38}$$

To solve eq. (36) and eq. (37), we need to use the property of Bessel's functions:

$$J_n(u+v) = \sum_{m=-\infty}^{\infty} J_m(v)\, J_{n-m}(u)$$

which, reduces to[7]:

$$\delta_{n0} = \sum_{m=-\infty}^{\infty} J_{-m}(u)\, J_{n-m}(u) \tag{39}$$

where δ_{n0} is the Kronecker delta. From the similarity between eq. (36), eq. (37) and eq. (39), we can directly extract that one solution (and thus the only one by unicity of the solution of a linear differential equation with well defined boundary conditions) satisfies:

$$\frac{a_m}{A_i} e^{i\frac{(k_i-q_m)L}{2}} = J_{-m}\left(\frac{U_M}{\hbar\omega}\right)$$

Replacing the resulting expression for the a_m coefficients in eq. (38) we get the renormalized diffracted amplitudes:

$$\frac{A_p}{A_i} = \sum_{m=-\infty}^{\infty} J_{-m}\left(\frac{U_M}{\hbar\omega}\right) J_{p-m}\left(\frac{U_M}{\hbar\omega}\right) e^{i\frac{(2q_m-k_i-k_p)L}{2}} \tag{40}$$

Approximation

To describe further the diffraction amplitudes, one can expand to first order[8] the phase appearing in the sum eq. (40):

$$\begin{aligned} k_p &\simeq k_i\left(1+\frac{p\omega}{2\Omega_i}\right) \\ q_m &\simeq k_i\left(1+\frac{m\omega}{2\Omega_i}-\frac{U_0}{2\hbar\Omega_i}\right) \end{aligned}$$

collecting identical terms and factorizing terms independent of the summation index m, we obtain the following diffraction amplitude:

$$\frac{A_p}{A_i} = e^{-i\frac{U_0 L}{\hbar v_i}} e^{-i\frac{p\phi}{2}} (-1)^p \sum_{m=-\infty}^{\infty} J_m\left(\frac{U_M}{\hbar\omega}\right) J_{m-p}\left(\frac{U_M}{\hbar\omega}\right) e^{im\phi}$$

---

[7] It simply follows from parity properties and the specific choice of $v = -u$, recalling that $J_n(0) = \delta_{n0}$

[8] It is again justified by the height of the potential step compared to the initial energy $(\omega, U_0/\hbar) \ll \Omega_i$

where $\phi = \frac{\omega L}{v_i}$. In this expression, one directly recognizes the phase shift due the constant potential U_0 which is identical for all terms. We can simplify it by using the Graf's generalization [127] of the Bessel's sum rule eq. (39):

$$\begin{aligned} J_\nu(\varpi)\exp(i\nu\chi) &= \sum_{m=-\infty}^{\infty} J_{\nu+m}(u) J_m(v)\exp(im\alpha) \\ \varpi &= \sqrt{u^2+v^2-2uv\cos\alpha} \\ u - v\cos\alpha &= \varpi\cos\chi \\ v\sin\alpha &= \varpi\sin\chi \end{aligned} \tag{41}$$

where, for $(u,v) \in \mathbb{R}^{+,*}$ and $\alpha \in [0,\pi]$, ϖ and χ are real and positive. According to [127], the validity condition $|ve^{\pm i\alpha}| < |u|$ can be removed for $\nu \in \mathbb{Z}$ which is our case. Substituting $\alpha = \phi$, $\chi = \frac{\pi-\phi}{2}$ and $\varpi = 2\frac{U_M}{\hbar\omega}\sin\left(\frac{\phi}{2}\right)$, one gets a simple expression for the diffracted amplitude:

$$\frac{A_p}{A_i} = e^{-i\frac{U_0 L}{\hbar v_i}}(-i)^p J_p\left(2\frac{U_M}{\hbar\omega}\sin\left(\frac{\phi}{2}\right)\right) \tag{42}$$

This expression is equal to the static approach of eq. (31). Indeed, our hypothesis of a small potential completely justifies the first order WKB approximation in which only the phase of our wavefunction is affected by the potential.

2.2.3 Technical implementation

Now that we have a solid description of diffraction in time processes, let's focus on the interferometric signal that we can detect and on the significant quantities that we can derive to test our model.

Electric potential and static polarisability

To produce an homogeneous oscillating potential that leads to significant time diffraction, one needs to maximize[9] the argument of Bessel function in eq. (42). In this argument, three parameters can be, in principle, adjusted independently: the potential height U_M, the modulation frequency ω and the length[10] of the interaction region L. It is easier to distinguish between two frequency domains:

1. $\frac{\omega L}{v_i} \ll 1 \Leftrightarrow \omega \ll \omega_{tr} = (2\pi)\frac{v_i}{L}$: for low frequency compared to the inverse of the transit time in the interaction region, the argument of Bessel's function is independent of frequency and is maximum for large potential and long inter-

---

[9] To produce a pth harmonic, $2\frac{U_M}{\hbar\omega}\sin\left(\frac{\omega L}{2v_i}\right)$ has to be of order $p+1$ which roughly corresponds to the Bessel's first maximum.

[10] It is possible to also change the mean group velocity of our atomic beam v_i by changing the beam's seeding gas, but only the ratio L/v_i appears in the argument so L and v_i are not independent parameters.

action region. Note that the frequency range over which this approximation is valid decreases with L

2. $\frac{\omega L}{v_i} \gg 1 \Leftrightarrow \omega \gg \omega_{tr} = (2\pi)\frac{v_i}{L}$: for high frequency compared to ω_{tr}, one should maximize the potential height and choose an interaction length $L = \frac{v_i \pi}{2\omega}$ to be at the maximum of the sinus function. However, one should be careful that the velocity distribution does not wash out this maximum. In mathematical terms, $\frac{1}{2}\frac{\partial^2}{\partial v_i^2}\left[\sin\left(\frac{\omega L}{v_i}\right)\right]\Delta v_i^2 = \left(\frac{\pi \Delta v_i}{2 v_i}\right)^2 \ll 1$. This reduces to $\frac{\Delta v_i}{v_i} < \frac{2}{\pi}$, which is verified in our case.

We opted for the first domain which has the advantages of allowing longer interaction lengths for which homogeneous potentials with sharp edges (compared to the total length of the interaction region) were easier to implement. Also we wanted first to observe modulation frequencies lower than our detection bandwidth ~ 1 kHz which is limited by Langmuir Taylor detector. Moreover, the two electrodes separated by one ground plate setup developed by S. Lepoutre [84] produced both a good electric field homogeneity and a long interaction region. This type of Kerr modulator had already been used to compensate the phase spreading induced by the atomic velocity distribution [128] or to measure the mean velocity of an atomic beam [129].

The principle of this interaction cell is to polarize the atom electronic cloud with an electric field. By doing so, the induced electric dipole moment is proportional to the electric field in the low frequency, low field limit[11]:

$$\langle \vec{p} \rangle_T = \alpha_0 \vec{E}$$

where $\vec{p} = \sum_i q_i \vec{r}_i$ is total electronic dipole moment, where i indexes each electron, the time average $\langle\rangle_T$ is taken over a time long compared to electronic dynamics, α_0 is the static electrical polarizability, and $\vec{E}$ is the electric field. In turn, the interaction of this induced dipole moment with the electric field shifts the ground state atomic energy level by:

$$U(\vec{r},t) = -2\pi\epsilon_0 \alpha |\vec{E}(\vec{r},t)|^2 \tag{43}$$

where we have used the polarizability volume $\alpha = \frac{\alpha_0}{4\pi\epsilon_0}$. To produce a well controlled electric field on each path of the interferometer we use, as can be seen on Fig. 11, two capacitors separated by a thin aluminium foil, called "septum" by Pritchard's group which developed it initially [70], acting as a common ground. We apply, on each of the capacitors, a small oscillating electric potential $V_1 \in [0, 15]$ V combined with a high

---

[11] More details on this effect will be given in Chap. 4.

static one $V_0 \sim 800\,\text{V}$ to enhance the oscillating term. The electric field magnitude can therefore be written:

$$|\vec{E}_{tot}(z,t)|^2 = \frac{1}{d_{eff}}\left\{V_0^2 + 2V_0V_1\cos(\omega t) + [V_1\cos(\omega t)]^2\right\} \quad z \in \left[-\frac{L}{2}, \frac{L}{2}\right] \tag{44}$$

where d_{eff} is an effective distance between the electrodes depending only on the geometry of the capacitors. Because the oscillating potential is small compared to the static one, we can neglect[12]the last term oscillating at 2ω. The resulting potential experienced by each arms of the interferometer can therefore be expressed by:

$$U^{\alpha}(t) = U_{0,\alpha} + U_{1,\alpha}\cos(\omega_{\alpha}t) \tag{45}$$

where α denotes the two paths A and B. Because we detect the interference term between the two paths, we chose the constant potentials to be equals $U_{0,A} = U_0 = U_{0,B}$. And used symmetrical modulation amplitudes to simplify the analysis $U_{1,A} = -U_{1,B} = U_1$. Depending on the goal of the experiment, to detect the p^{th} harmonic, we chose either identical modulation frequencies $\omega_A = \omega_B = \omega$, when $p\frac{2\pi}{\omega}$ was much higher than the detection time ($\sim 1\,\text{ms}$) allowing us the directly detect the modulation or slightly different frequencies $\omega_A - \omega_B = \omega$ to perform heterodyne detection. This slightly different frequencies configuration allowed us to measure the beating of the diffracted signals when the modulation frequency was too high for our detector.

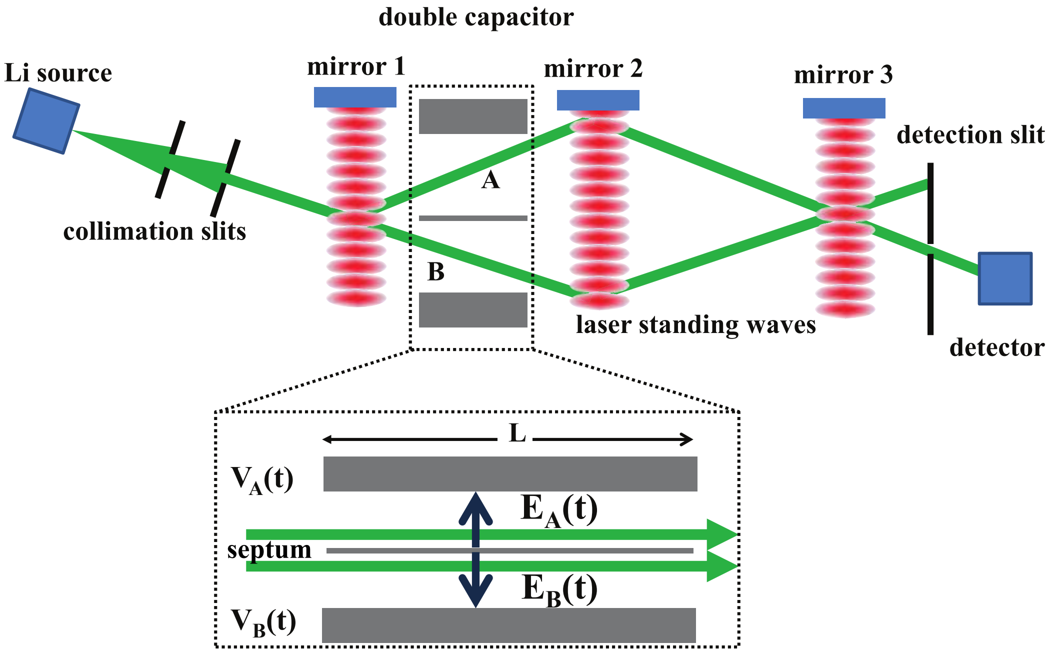

Figure 11: Schematic representation of the interferometer and its interaction region. The two paths A and B are separated by approximately $100\,\mu\text{m}$ and the length of the interaction region is approximately $48\,\text{mm}$.

---

[12] The amplitude of the corresponding phase shift is less than 1 % of the main phase shift.

From eq. (42) we can write the atomic state at the position of the detector as:

$$\left|\Psi_{\mathrm{arrival}}^{\alpha}\left(\nu_{i},t\right)\right\rangle = A_{i}^{\alpha}e^{i\left(\mp\frac{\phi_{d}}{2}-\frac{U_{0}L}{\hbar\nu_{i}}\right)}\sum_{p=-\infty}^{\infty} i^{p}J_{p}\left(\phi_{m}^{\alpha}\right)e^{i\left(k_{p}^{\alpha}(z_{d}-z_{c})-\Omega_{p}t\right)}\left|k_{p}^{\alpha},\Omega_{p}^{\alpha}\right\rangle$$

where we have included the differential phase due to diffraction ϕ_d [its sign is $-$ $(+)$ for path A (B)], $\phi_m^\alpha = -\frac{2U_{1,\alpha}}{\hbar\omega_\alpha}\sin\left(\frac{\omega_\alpha L}{2\nu_i}\right)$, $k_p^\alpha \simeq k_i + \frac{k_i p\omega_\alpha}{2\Omega_i}$ and $\Omega_p \simeq \Omega_i^\alpha + p\omega_\alpha$. The travelling distance $z_d - z_c$ corresponds to the position difference between the center of the interaction region and the detection. Because the detector bandwidth is approximately 1 kHz, the interference term between the two paths will not discriminate between the different states $\left|k_p^\alpha,\Omega_p^\alpha\right\rangle_\alpha$, thus we can factorize the last expression into:

$$\begin{aligned}\left|\Psi_{\mathrm{arrival}}^{\alpha}\left(\nu_{i},t\right)\right\rangle &\simeq A_{i}^{\alpha}e^{i\left(\mp\frac{\phi_{d}}{2}-\frac{U_{0}L}{\hbar\nu_{i}}\right)}e^{i\left(k_{i}(z_{d}-z_{c})-\Omega_{i}t\right)}\sum_{p=-\infty}^{\infty} i^{p}J_{p}\left(\phi_{m}^{\alpha}\right)e^{ip\omega_{\alpha}(t-\tau_{\mathrm{prop}})}\left|k_{i},\Omega_{i}\right\rangle\\ &\simeq A_{i}^{\alpha}e^{i\left(\mp\frac{\phi_{d}}{2}-\frac{U_{0}L}{\hbar\nu_{i}}\right)}e^{i\left(k_{i}(z_{d}-z_{c})-\Omega_{i}t\right)}e^{i\phi_{m}^{\alpha}\cos[\omega_{\alpha}(t-\tau_{\mathrm{prop}})]}\left|k_{i},\Omega_{i}\right\rangle\end{aligned}$$

where we have introduced the propagation delay between the detector and the interaction region $\tau_{\mathrm{prop}} = \frac{z_d - z_c}{\nu_i}$. Finally, we get the interference signal which corresponds to the amplitude of the coherent sum of the two states:

$$\begin{aligned}I_{\mathrm{arrival}}(t) &= \left|\left|\Psi_{\mathrm{arrival}}^{A}\left(\nu_{i},t\right)\right\rangle + \left|\Psi_{\mathrm{arrival}}^{B}\left(\nu_{i},t\right)\right\rangle\right|^{2}\\ &= \left|A_{i}^{(A)}\right|^{2} + \left|A_{i}^{(B)}\right|^{2} + 2\,\mathrm{Re}\left(A_{i}^{(A)}A_{i}^{(B)}e^{i(\phi_{d}+\Delta\phi_{m}\cos(\omega(t-\tau_{\mathrm{prop}})))}\right)\\ &= I_{0}\left[1+\mathcal{V}_{0}\cos\left(\phi_{d}+\Delta\phi_{m}\cos\left(\omega\left(t-\tau_{\mathrm{prop}}\right)\right)\right)\right] \qquad (46)\end{aligned}$$

where $\Delta\phi_m = \phi_m^A - \phi_m^B \simeq 2\phi_m^A$, and we have simplified the result for the case of identical modulation frequencies $\omega_A = \omega_B = \omega$. A similar expression for the case of slightly different frequencies, as well as a graphical interpretation of this result, is presented in Sec. 2.2.3 . We have also introduced the average intensity and visibility of the interferometric signals:

$$\begin{aligned}I_{0} &= \left|A_{i}^{(A)}\right|^{2} + \left|A_{i}^{(B)}\right|^{2}\\ \mathcal{V}_{0} &= \frac{2\left|A_{i}^{(A)}\right|\left|A_{i}^{(B)}\right|}{\left|A_{i}^{(A)}\right|^{2} + \left|A_{i}^{(B)}\right|^{2}}\end{aligned}$$

Because the detection time is not instantaneous, there is a slight average ionization delay $\tau_{\mathrm{res}} \simeq 200\,\mu\mathrm{s}$ between the detected amplitude and the arrival amplitude at the detector. The Langmuir-Taylor hot wire detection distribution can be approximated by an exponential function:

$$dP(\tau) = \exp\left(-\tau/\left\langle\tau_{res}\right\rangle\right) d\tau \tag{47}$$

We can combine this effect with τ_{prop} to get a unique mean time delay $\tau(v_i) = \tau_{prop}(v_i) + \tau_{res}$. Moreover, many terms in eq. (46) depend on the atom's initial velocity, with the particular example of the modulation phase $\Delta\phi_m$. Therefore we observe an interferometric intensity averaged over the velocity distribution eq. (3):

$$I_{tot}(t) = \int_0^\infty P(v_i)\, I_0 \left\{1 + \mathcal{V}_0 \cos\left[\phi_d + \Delta\phi_m(v_i)\cos\left[\omega\left(t - \tau(v_i)\right)\right]\right]\right\} dv_i \tag{48}$$

where we have explicitly indicated the velocity dependence of the relevant terms. It is to be noted that the diffraction phase, the mean intensity and the visibility depend on the velocity, but we simply used their mean values in our theoretical model. Indeed, a complete description of the atom interferometer is not relevant in our case because we can completely discriminate the modulation from the wide variety of constant effects such as residual Zeeman phase shifts, velocity dependent diffraction efficiency, Sagnac phase,...

To simplify the analysis of the recorded interferometric signal, it is useful to compute the Fourier transform of eq. (48) in order to extract the phase and amplitude of the modulation harmonics. From the measured Fourier signal:

$$\mathcal{I}(\nu) = \frac{1}{T}\int_0^T I_{tot}\left(t'\right) e^{i\nu t'} dt'$$

we get, according the Shannon's criteria in the limit of long measurement time[13] T a simple expression for the normalized pth harmonic:

$$\frac{\mathcal{I}(\nu = p\omega)}{I_0} = \left[\delta_{0p} + \tilde{\mathcal{V}}(p)\cos\left(\phi_d + \frac{p\pi}{2}\right)\right] \tag{49}$$

where we have defined the complex visibility which takes into account the averaged amplitudes of modulation harmonics:

$$\begin{aligned} \tilde{\mathcal{V}}(p) &= \mathcal{V}_0 \int_0^\infty P(v_i)\, J_p\left(\Delta\phi_m(v_i)\right) e^{-ip\omega\tau(v_i)} dv_i \\ &= \mathcal{V}(p)\, e^{-i\Psi_m(p)} \end{aligned} \tag{50}$$

To be completely coherent, one should take into account explicitly the detection response function into the Fourier transform of the detected signal. In other words,

---

[13] In practice, this condition is verified when $\omega T \gg 1$ which correspond to approximately a minute of recording.

because of the sampling rate, the counting method and the detector's response time, the detected signal consists in the convolution of the interferometric signal with the detection function:

$$I_{\mathrm{measured}}(t) = \int_{-\infty}^{0} f_{\mathrm{detect}}\left(t^{'}\right) I_{\mathrm{tot}}\left(t - t^{'}\right) dt^{'}$$

where f_{detect} represents the measurement method as well as the detector's response. This expression simply leads, in the Fourier domain, to multiply the normalized pth harmonic by the normalized spectral response[14] of our detector:

$$\frac{\mathcal{F}(\nu)}{\mathcal{F}(0)} = H_0\left(\omega_{\mathrm{sample}} - \nu\right) \frac{\omega_{\mathrm{res}}}{1 - e^{-\frac{\omega_{\mathrm{res}}}{\omega_{\mathrm{sample}}}}} \frac{1 - e^{-\frac{\omega_{\mathrm{res}}}{\omega_{\mathrm{sample}}}} e^{i\left(\frac{\nu}{\omega_{\mathrm{sample}}}\right)}}{\omega_{\mathrm{res}} + i\nu}$$

where H_0 denotes the Heaviside step function, ω_{sample} is the sampling rate and $\omega_{\mathrm{res}} = \frac{1}{\tau_{\mathrm{res}}}$ is the ionisation frequency of the hot wire detector. In our experiment, we have $\omega_{\mathrm{res}} \sim 5\,\mathrm{kHz}$, $\omega_{\mathrm{sample}} = 1\,\mathrm{kHz}$ and $\nu \ll \omega_{\mathrm{sample}}$. Thus, the normalized spectral response reduces to:

$$\begin{aligned}\frac{\mathcal{F}(\nu)}{\mathcal{F}(0)} &\simeq e^{i\arctan\left(\frac{-\nu}{\omega_{\mathrm{res}}}\right)} \\ &\sim e^{-i\nu\tau_{\mathrm{res}}}\end{aligned}$$

which is simply the time delay introduced in eq. (48). By doing this approximation, we introduced at most a 1 % error on the measured harmonic amplitude.

Modulation amplitudes

When the modulation frequencies on each paths are identical, the Fourier transform 'Visibility' of the pth harmonic is given by eq. (50). It consists in the Bessel function of order p, with phase $ip\omega\tau(\nu_i)$, averaged over the velocity distribution. This can be decomposed as a sum over n of the product of two Bessel functions (p and $n+p$) as expressed by eq. (41). It can be represented graphically (see Fig 12) by considering the recombination of two frequency combs corresponding to both interferometric paths. When recombined, a partial pth harmonic amplitude corresponds to the product of a tooth from each path exactly separated by $p\omega$. Summing the partial amplitudes over the teeth gives the detected full modulation amplitude.

When using different modulation frequencies on each path, we can either develop the interference signal eq. (46) without the assumption of identical frequencies, collect the terms oscillating at harmonics of $\omega = \omega_A - \omega_B$ and discard the terms oscillating too fast for our detector. Or, we can simply reproduce the same analysis consisting

---

[14] $\mathcal{F}(\nu) = \int_{-\infty}^{\infty} f_{\mathrm{detect}}\left(t^{'}\right) e^{i\nu t^{'}} dt^{'}$

in combining amplitudes (see Fig. 13) resulting in the pth harmonic and we get an harmonic visibility similar to eq.(50) but with a Bessel's argument divided by 2:

$$\tilde{\mathcal{V}}(p) = \mathcal{V}_0 \int_0^{\infty} P(\nu_i) \left[J_p\left(\phi_{m,A}(\nu_i)\right)\right]^2 e^{-ip\omega\tau(\nu_i)} d\nu_i \tag{51}$$

Now that we have a theoretical description of our Kerr modulator, let us describe in more details the performed experiments and their results.

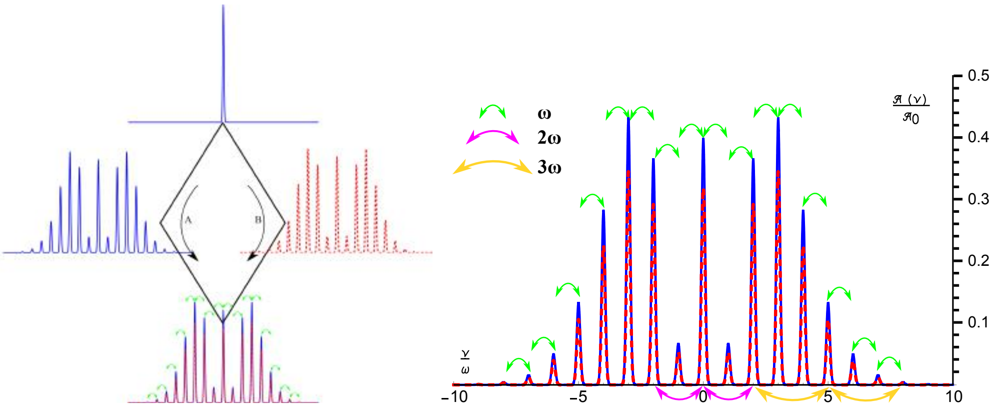

(a) Frequency comb (b) Recombination

Figure 12: Schematic representation of the wave-function amplitudes as a function of frequency, in unit of ω, for identical modulation frequencies at a modulation phase $\Delta\phi_m(u) = 8\,\text{rad}$. The initial state at the top of **(a)** corresponds to a single atom having a well defined velocity which is separated and diffracted identically on two paths (A and B). The superposition of the two outputs leads to **(b)** on which we represented all the products making up the signal at ω (green arrows) and only two products for 2ω (pink) and 3ω (yellow). The width of the frequency distribution has been exaggerated for clarity

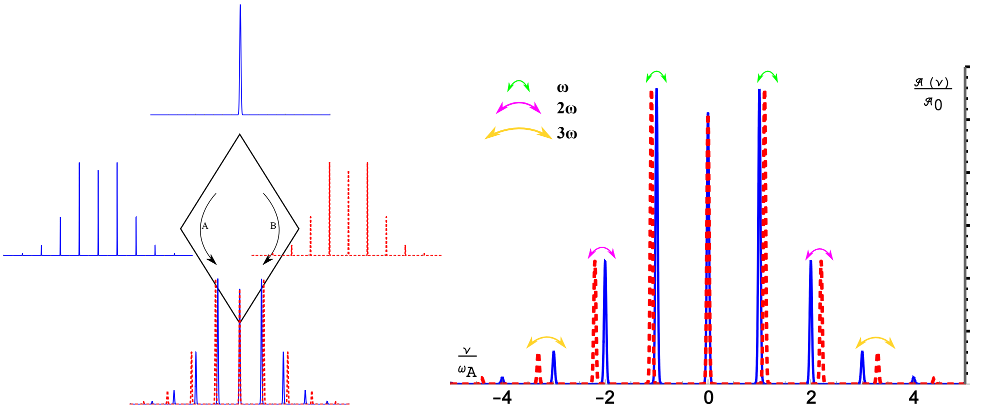

(a) Frequency comb (b) Recombination

Figure 13: Schematic representation of the wave-function amplitudes as a function of frequency, in unit of ω_A, for different modulation frequencies at a modulation phase $\phi_{m,\alpha}(u) = 1.5\,\text{rad}$. The initial state at the top of **(a)** corresponds to a single atom having a well defined velocity which is separated and diffracted on two paths (A and B). The superposition of the two outputs leads to **(b)** on which we represented the products making up the signal at ω (green arrows), at 2ω (pink) and 3ω (yellow). The width of the frequency distribution has been exaggerated for clarity as well as the frequency difference between the two paths which is much smaller than the modulation frequencies.

Atom wave phase modulation

The modulation of an atom wave effective index of refraction produces a superposition of momentum states in the transmitted wave. A complete quantum treatment of a modulation localized in space leads, in the perturbative regime, to diffraction amplitudes (eq. (42)) which agree with the ones inferred from the WKB approximation.

We produce phase modulation in our lithium interferometer by modulating an external electric field which results, via the static polarizability, to the analog of the Kerr effect in optic. If the modulation frequencies are low, we can detect an homodyne beat signal eq. (49) and eq. (50). If the modulation frequencies are large, we detect an heterodyne beat signal given by eq. (51).

2.3 KERR MODULATOR

As already described in Chap. 1, we use an atom interferometer in a Mach-Zehnder configuration with spatially separated arms. For this diffraction-in-time experiment, we used a phase modulator cell based on the electrically induced polarization of lithium atoms in presence of an external electric field. Because the atom's ground state energy dependence is quadratic in the applied field, this situation is similar to the optical Kerr effect. The induced differential phase shift is:

$$\Delta\phi_m(v_i) = -\frac{2U_{1,A}}{\hbar\omega_A}\sin\left(\frac{\omega_A L}{2v_i}\right) + \frac{2U_{1,B}}{\hbar\omega_B}\sin\left(\frac{\omega_B L}{2v_i}\right) \tag{52}$$

Because the modulation frequencies and amplitudes are very similar, this phase shift is approximately given by:

$$\Delta\phi_m(v_i) \simeq 4KV_0V_1\frac{2v_i}{\omega_A L}\sin\left(\frac{\omega_A L}{2v_i}\right) \tag{53}$$

where $K = 4.79 \times 10^{-4}\ \mathrm{rad}/V^2$ was previously determined from DC measurements [130]. Due to the frequency dependence of this phase shift, we can separate two types of experiment:

- The low frequency modulation, for which $\Delta\phi_m(v_i)$ is independent of ω_A and v_i. This corresponds to $\omega_A \ll \frac{2\bar{u}}{\pi L} \simeq (2\pi)\,22\,\mathrm{kHz}$.
- The frequency dependent case, where the transit time in the modulation cell is not negligible compared to the modulation period. In this situation, the modulation amplitude, for constant potentials, exhibits cancellations and revivals as well as velocity spreading.

2.3.1 Low frequency modulation

Interferometric signal

We first apply low identical frequency modulations $\omega/(2\pi) \ll 1\,\text{kHz}$ on both interferometer arms. By changing the modulation potential amplitude, we could produce phase shifts up to $15\,\text{rad}$ and detect up to the 16th modulation harmonics provided that it lays in the detector bandwidth. A typical interferometric signal is presented on Fig 14 for a modulation frequency of $21\,\text{Hz}$. For each frequencies $\omega = (2\pi)\{11, 21, 43, 73, 97, 151\}\,\text{Hz}$, similar interferometric signals were obtained.

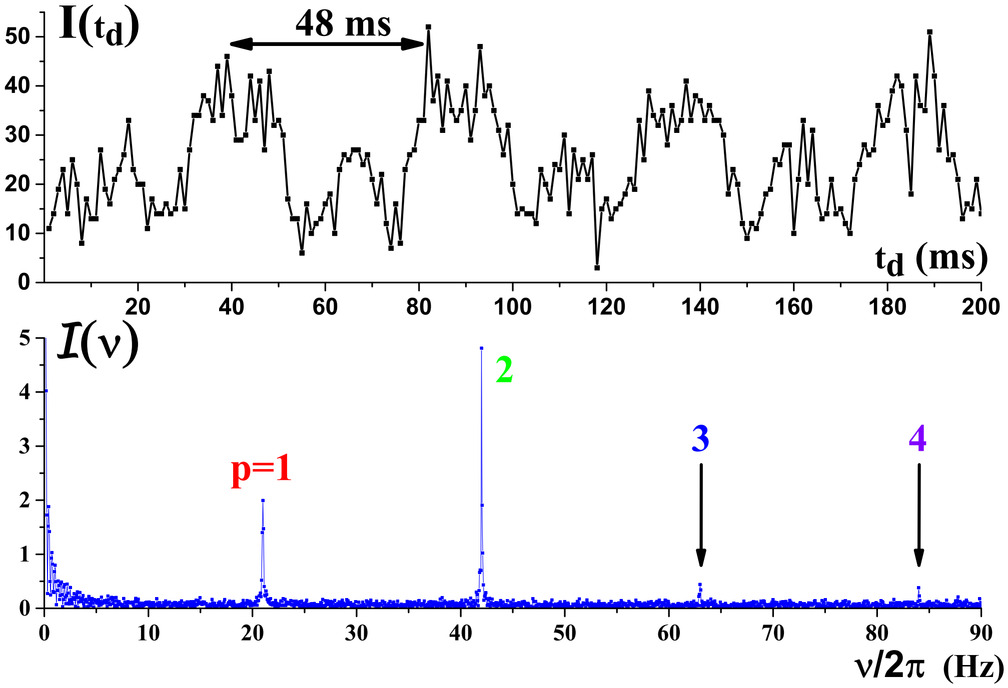

Figure 14: Interferometer signal for a constant phase difference $\Delta\phi_m = 2.7\,\text{rad}$ and a constant diffraction phase $\phi_d \sim -0.5\,\text{rad}$. Top panel: Number of atoms detected per millisecond as a function of time. Bottom panel: Fourier amplitude of a $16.4\,\text{s}$ long recording as a function of frequency. Up to the 4th harmonics is revealed.

Diffraction amplitudes

In order to extract the Fourier amplitude of the $p\text{th}$ modulation harmonic eq. (49), we vary the interferometer phase ϕ_d by slowly moving the position of the third grating mirror with a piezoelectric actuator. The resulting scanning is monitored with a Mach Zehnder optical interferometer which records this mirror's position. As can be seen from eq. (49), the harmonics amplitude oscillates with the interferometric phase. Thus, for each mirror position, a $200\,\text{ms}$ long interferometric signal was recorded and Fourier transformed. An example of the resulting interferometer signal and Fourier signal is represented on Fig 15. Scanning the interferometer phase for approximately a 2π period allowed for a full oscillation of the modulation amplitude. The result of such scans can be seen on Fig 16. Finally, by extrapolating the obtained amplitudes with eq. (49), we extract the modulation "visibility" $\tilde{\mathcal{V}}(p)$ and its phase $\Psi_m(p)$.

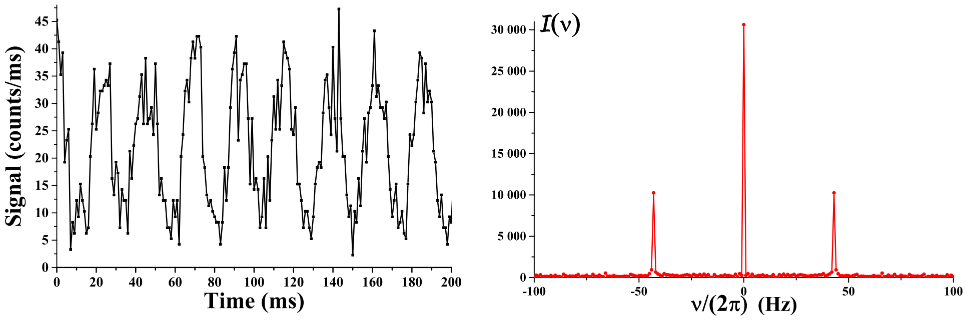

(a) Scan 1

(b) Scan 1

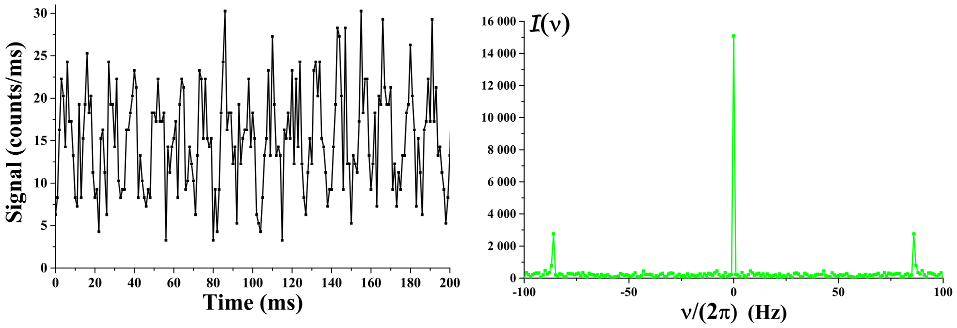

(c) Scan 2

(d) Scan 2

Figure 15: Interferometric signals for two different interferometric phases displaying a maximal first order diffraction (top, $\phi_d = \frac{\pi}{2}$) and a maximal second order diffraction (bottom, $\phi_d = \pi$). The left hand panel represents the direct interferometric signal and the right hand panel shows the corresponding Fourier transform.

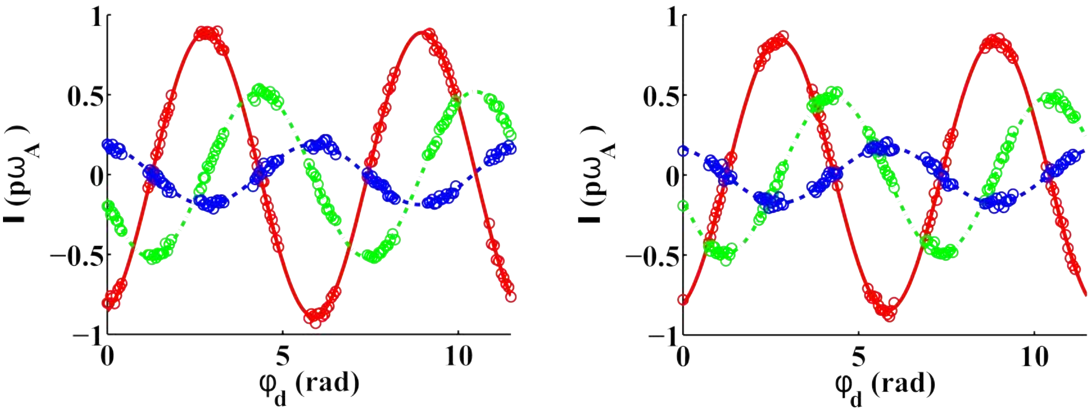

(a) Scan 1

(b) Scan 2

Figure 16: Fourier coefficient of the first three diffraction order (First: solid red, Second :green dotted and Third :blue dashed) as a function of the interferometric phase for two different scans (a), (b). The points correspond to data and the lines to the sinusoidal fits. Note that half of the time, the modulation was turned off to monitor the interferometric phase, its intensity as well as its visibility for proper normalization of the Fourier amplitudes.

Visibility and phase

Knowing the Fourier transform amplitude and phase, relative to $\phi_d + \frac{p\pi}{2}$ for the pth harmonic, it is straightforward to extract the experimental visibility and phases. By varying $\Delta\phi_m$ we observed the appearance, disappearances, inversions and revivals of up to the 16th harmonic, typical for Bessel's functions. Fig. 17 summarizes the obtained visibility and the Fig. 18 shows the phases. There is good agreement between our theoretical model and the experimental data. There was only one free parameter, the ionization delay τ_{res} (eq. (47)), for all fits and it was found to remain constant equal to $\tau_{res} = 290(10)\,\mu s$ which agrees qualitatively with the not well known value of $200\,\mu s$ (see Sec. 1.3.1 eq. (12) and [102]). For the visibility data, the residual uncertainty is smaller than the size of the points and for the phases, the statistical uncertainty corresponding to the quadratic mean of the residual uncertainties of different scans, is represented. The small phase dispersion can be explained by velocity dispersion effects when the diffraction phase is large.

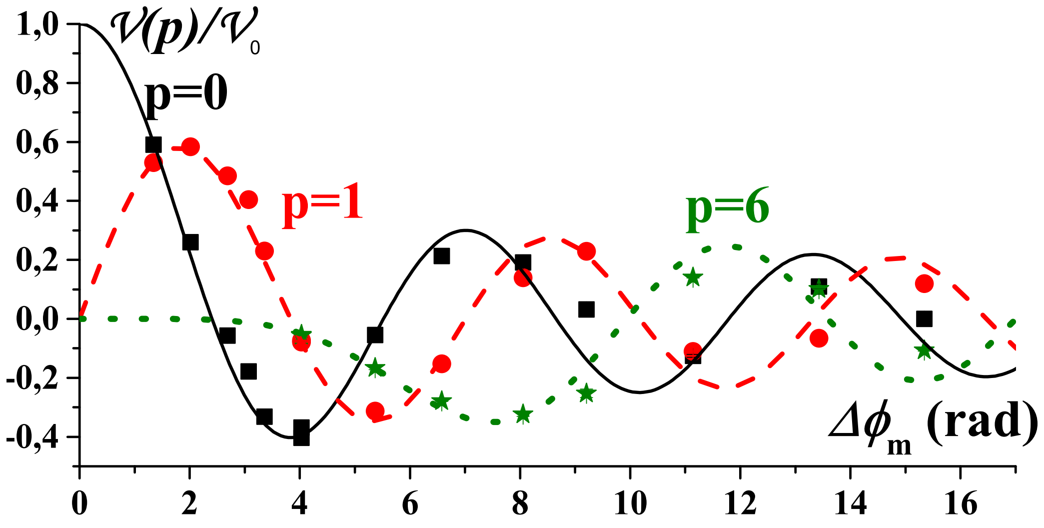

Figure 17: Evolution of the harmonics visibility as a function of the total diffraction phase. The squares (solid line) correspond to $p = 0$, the bullets (dashed line) to $p = 1$ and the stars (dotted line) to $p = 6$. The lines correspond to the theoretical model eq. (50) with no free parameter.

2.3.2 Heterodyne atom wave beats

Confindent that our theoretical model represented well the low frequency domain, we now demonstrate the sinus cardinal behavior of the differential phase shift eq. (53). To do so, we keep the modulation potential constant and change the modulation frequency. In order to maximize the effect, we choose a low frequency differential phase of $6.7\,\mathrm{rad}$ which mainly corresponds to zero, second and fourth harmonics and almost no first and third harmonic as is summarized in Tab. 3. To be able to detect the induced modulation, which had to be of the order of the inverse transit time in the modulation cell $\sim (2\pi)\,22\,\mathrm{kHz}$, we used a heterodyne detection scheme by applying slightly different frequencies on each interferometer's arm. By doing so, we

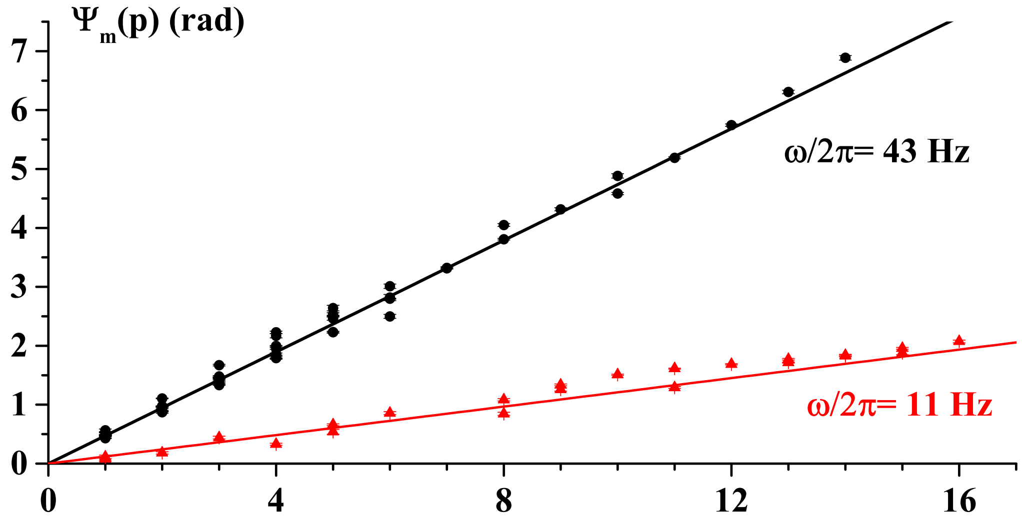

Figure 18: Measured phase $\Psi_m(p)$ as a function of the harmonic order. Two different frequencies were used: 11 and 43 Hz. Different modulations amplitude were needed for the different orders in order to minimize the phase's uncertainty. For some orders, multiple symbols corresponds to multiple modulation amplitudes for which the phase could be extracted. The lines correspond to linear fits which yielded the mean total time delay of 1.65(1) ms from which we could deduce the ionization delay $\tau_{res} = 290(10)\,\mu s$. There is no phase value for the seventh harmonic because we did not, at the time, choose potential configurations for which the seventh harmonic was intense enough at a modulation frequency of 11 Hz.

$\Delta\phi_m(u)$ (rad)	Order 0	Order 1	Order 2	Order 3	Order 4
1	0.765	0.440	0.115	0.020	0.003
3	0.260	0.339	0.486	0.309	0.132
5	0.178	0.328	0.047	0.365	0.392
6.7	0.285	0.095	0.314	0.092	0.231
8	0.172	0.234	0.113	0.291	0.105

Table 3: Harmonics amplitudes for different low frequency mean differential phases. The phase used for atom-wave beating demonstration is highlighted and corresponds to the cancellation of the first and third orders with high zeroth and second orders.

insured that the difference in modulation phase would not be significant while being able to detect the beat notes between the generated side-bands with the same order. In practice, we used a frequency difference $(\omega_B - \omega_A)/(2\pi) = 13$ Hz for which, even at the highest sensitivity frequency of 25 kHz (which corresponds to the maximum of the sinus function in eq. (42)), the difference of modulation phase is less than 7 %. Thus, to a very good approximation, we can use the harmonic amplitudes eq. (51) with $\phi_{m,A}(v_i) = 2KV_0V_1\frac{2v_i}{\omega_A L}\sin\left(\frac{\omega_A L}{2v_i}\right)$.

The Fourier amplitudes are represented on Fig 19. The dependence on the modulation frequency agrees well with our model. In particular, at 22 kHz, an atom going at the mean velocity $\bar{u} = 1050\,\mathrm{m\,s^{-1}}$ spends exactly one period in the phase modulator and its wavefunction in not modulated. The expected decrease of the side-bands amplitude is well observed and the unmodulated visibility $\mathcal{V}(0)/\mathcal{V}_0$ is maximum. The total amplitude is however non-zero due to the atomic beam velocity spread.

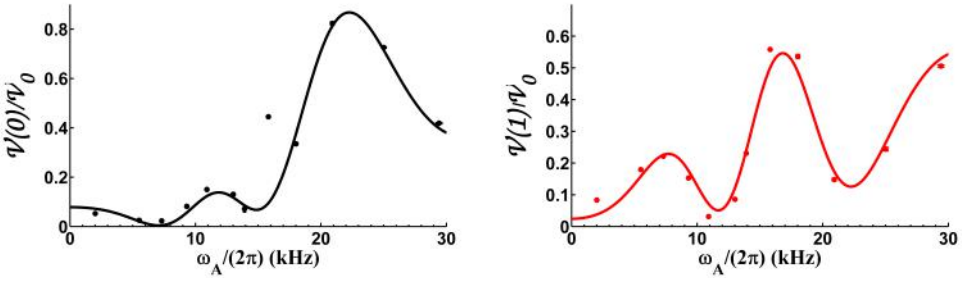

(a) Zeroth Order **(b)** First Order

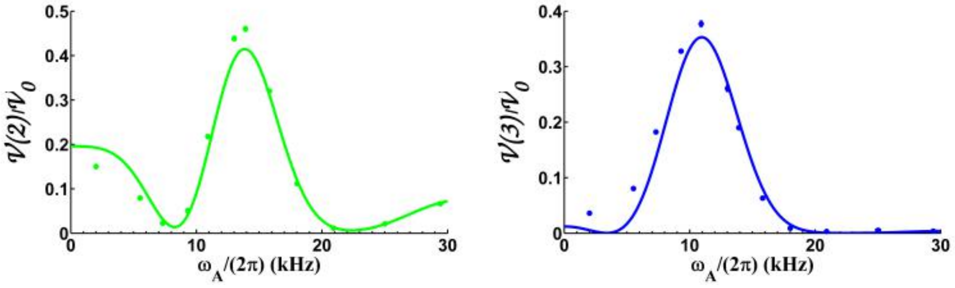

(c) Second Order **(d)** Third Order

Figure 19: Evolution of the harmonics visibility as a function of the modulation frequency: the unmodulated amplitude $\mathcal{V}(0)/\mathcal{V}_0$ as well as the first three harmonics are represented. The points correspond to data and the lines correspond to eq. (50). The unmodulated amplitude increase around 22 kHz corresponds to the zero of the mean velocity modulation amplitude which can be seen on all the harmonics amplitude.

2.3.3 Data transmission

Because of the high degree of similarities between this phase modulator and the modulation techniques used in classical data transmission[15], we used our interferometer as a data transmission line, using a technique similar to phase shift keying (PSK) in what we call the 'Atomic Fax'. We also produced the equivalent of a radio by encoding in our interferometer phase an audio signal which we call the 'Atomic Radio'.

Atomic fax

Because PSK was historically used in modems and is still, in an advanced form, used in wireless protocols and broadcastings, we first implemented a basic data transfer. Basically, PSK consists in encoding on an electromagnetic signal p bit(s) by phase shifting it by a multiple of $\frac{\pi}{2(p-1)}$. In our case, we restricted ourselves to transferring a black and white picture encoded by a list of 1 bit. The protocol simply consisted in phase shifting our interferometer phase by $\Delta\phi_m = \pm\frac{\pi}{2}$. By choosing the appropriate diffraction phase $\phi_d = \frac{\pi}{2}$, the atomic intensity reduced from eq. (46) to:

$$I_{arrival}(t) = I_0\left[1 \pm \mathcal{V}_0\right] \tag{54}$$

---

[15] For example, the commonly AM and FM radio bands or even more the PAL broadcast protocol encoding the color information in the quadrature phase of the intensity signal.

where ± depends on the sign of the 'modulation' phase. Here, no actual modulation was used ($\omega = 0$) in order to get the higher bit rate[16]. Furthermore, by restricting ourselves to 1 bit, we prevented our signal statistics (which is slightly over-Poissonian) from inducing error bits. A typical example of our outputs distribution is represented on Fig. 20 for which 95 934 bits were transmitted and the number of detected atoms each 2 ms were analysed. To prevent transient delays due to our detection or our electrodes, we switch the phase every 5 ms but ignore the first two and the last one in our data analysis. This choice corresponds to the maximum distance between our two counting peaks represented on Fig 20. This analysis gives a robust split number of 90 atoms which separates the number of atoms corresponding to bit 1 and to bit 0. The resulting error between the transmitted file and the initial one is less than 0.1 % for a 200 bits/s transfer and can be mainly attributed to a typical defect of our detector which consists in intense burst of ions lasting a few hundreds of ms induced by rhenium oxydes [101]. The original and faxed files are shown on Fig. 21.

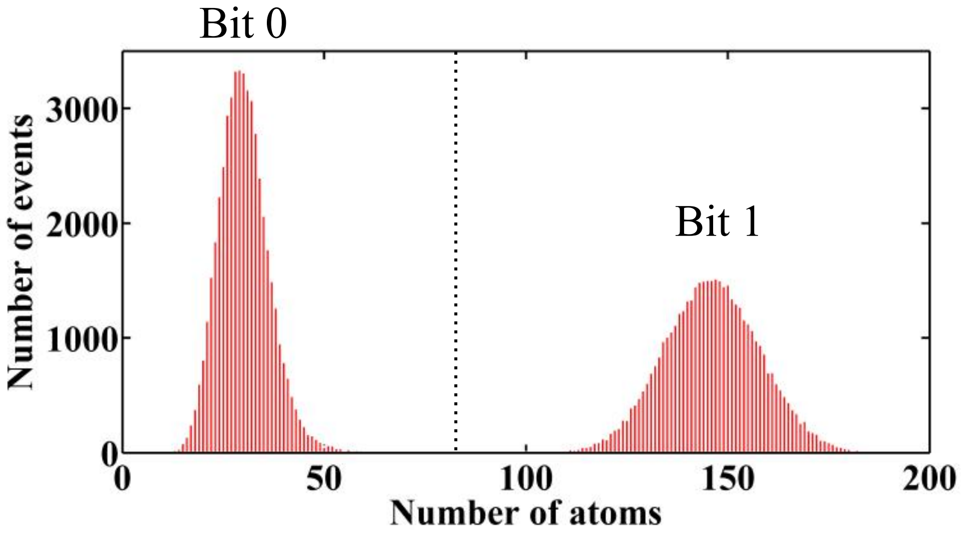

Figure 20: Histogram distribution of one data set. A total of 95 934 bits were counted during 2 ms long recordings. The two states corresponding to bit 0 and bit 1 are well separated by more than 2 FWHM which are slightly larger than the poissonian width to be expected from independent singular events counting. The dashed line between the two peaks corresponds to averaged distance between them, allowing the correct splitting of the two bits.

Atomic radio

This setup transfers slightly more complex signals and we chose an audio file which had the advantage of being already commonly described with its Fourier spectrum. This enhances the parallel between our phase modulator spectrum description and the audio spectrum we wanted to transfer. To implement this radio, we decided to use a modulation amplitude $\Delta\phi_{m,\mathrm{radio}} \sim 0.5\,\mathrm{rad}$ around which the first harmonic amplitude is approximately linear. Moreover, by keeping the diffraction phase constant

---

[16] Detecting a modulation would require approximately a period which itself needs to be of the order of ten times the detection time which leads to a maximum bit rate ~ 100 bit/s, while simply detecting a maximum or a minimum intensity can be done in a few detection times (in practice, we used 5) leading to higher bit rates.


(a) Original file (b) Faxed file

Figure 21: Original and decoded files transferred with our atomic fax. The original picture is a black and white reproduction of a self-portrait wood engraving from an expressionist German artist available at http://www.paboeckstiegel.de/. One clearly sees the high degree of fidelity between the two pictures. A localised error can be seen at the bottom left of the decoded picture corresponding to a well known defect of the atomic detector which produces, randomly, a short burst of the detector (see text), increasing the atomic signal count.

Original file	🔊	Transfered file	🔊

Table 4: A portion of the European anthem, "Ode to Joy", was used as audio data. The original as well as the transmitted one can be compared on this table.

$\phi_d = \frac{\pi}{2}$, the second harmonic was theoretically removed from the interferometric spectrum. Finally the third harmonic was completely negligible with an amplitude approximately 1/100 of the first harmonic amplitude. Therefore, modulating the modulation phase with the audio signal leads to a simple approximate interferometric signal:

$$I_{radio}(t) = I_0 \left\{ 1 + \mathcal{V}(1)\, \Delta\phi_{m,radio} \left(1 + \kappa_1 u_{signal}(t) \right] \right\} \tag{55}$$

where κ_1 represents the slope of the first harmonic amplitude at $\Delta\phi_{m,radio}$ and $u_{signal}(t)$ is the audio file to be transmitted. In practice, we needed to reduce the sampling rate of the audio file by a factor ten to prevent high frequency components of the audio file from being cut-off by our detection. Finally, for simple comparison, the recorded interferometric signal is accelerated ten times and the resulting audio can be compared to the original in Tab. 4.

2.4 CONCLUSION

In this chapter, we reviewed the previous experiments which performed diffraction in time on matter waves and presented our Kerr modulator implemented in our Lithium interferometer. Our modulator has the advantages of being directly applicable to other atomic or electronic separated arms interferometers and to allow the temporal observation of high frequencies modulation via homodyne and heterodyne detection. In addition, a completely analytical model was presented which allowed us to identify the main characteristics of the modulator (its modulation frequency, length and amplitude) that have to be adapted to the interferometer. Finally, we described four different experiments. The first two allowed us to test our model in two different configurations. One was conducted with a low modulation frequency, showing that up to the 16th (limited by our ability to produce higher potentials) harmonic of the modulation was present in our atomic beam and that the amplitude and phase of the different side-bands are well described by our model (Fig. 17 and Fig. 18). The second was aiming at producing the first matter-wave homodyne detection which allowed us to check the high frequency limit of our model by observing disappearances and revivals of the modulation amplitudes (Fig. 19). The last two experiments were conducted in a more pedagogical perspective and consisted in the first atomic fax and radio which convincingly transmitted data with an atomic phase modulator.

Beyond the simple scope of a proof of principle that these experiments provide, they can be pushed farther with higher modulation frequencies and could be extended to practical use in an electron holographic microscope or in a cold atom interferometer.

HIGHER MODULATION FREQUENCIES

For the time being, our homodyne detection of modulated matter waves was limited by both the available frequencies in our Kerr modulator and by the rather large distance between the modulation region and the detector. To circumvent these limits it would be interesting to use two laser beams, far detuned from resonance (to prevent decoherence), and intensity modulated that would create an oscillating potential at much higher frequencies. For example two focused laser beams having $40\,\mu m$ waists would allow modulation frequencies three order of magnitudes larger ($50\,MHz$).

ELECTRON HOLOGRAPHIC MICROSCOPE

As described in [7], a holographic microscope can be thought as a separated arm interferometer. Thus applying on one arm (A) an oscillating electric potential at frequency ω_A, results in a modulated phase shift on that arm $\varphi_A(t)$. If the second arm (B) interacts with a sample excited by a perturbation $U(t) = U_0 \cos(\omega_B t)$, it will acquire a modulated phase shift $\varphi_B(t) = k_i e \delta n_s(t)$, where k_i is the electron wave vector, e is the sample thickness and $\delta n_s(t)$ is the modification of refractive index induced by the perturbation $U(t)$. The recombined interference signal would therefore exhibit a modulation at the frequency difference $\omega = \omega_A - \omega_B$. This heterodyne effect enables to get information on $\delta n_s(t)$. Its phase in particular is related, in the linear response approximation, to the time domain by Fourier transform. This method should make it possible to measure, for example, the sample response time with very high spatial resolution ($\lambda_{DB} \sim 10\,\mathrm{pm}$ for high velocity electron beams) as well as high temporal resolution (limiting modulation frequencies of $\sim 100\,\mathrm{THz}$ see Tab. 2).

3 THE PANCHARATNAM PHASE: A TOOL FOR ATOM OPTICS

Contents

In this chapter, I will present the Pancharatnam phase as a tool for controlling the phase in an atom interferometer. It will consist in a brief introduction on geometric phases, with emphasis on the particular case of the Pancharatnam phase for light waves. I will focus on its description on the Poincaré sphere and some examples of its experimental observation. Next, I will present our experimental apparatus and discuss the technical parameters which modify the total phase of our Pancharatnam phase-shifter. Then, I will present our experimental results and evaluate the effect of the previously described defects on the interferometric signal. Finally, I will consider the use of this type of phase shifter in two different contexts: single species interferometer phase control and dual species simultaneous phase shifting.

3.1 GEOMETRIC PHASES

Geometric phases appear in physical systems of very different nature such as:

- A spin 1/2 precession in a magnetic field.
- A molecular wavefunction evolution in conformation transformations [131].
- Nonlinear dissipative systems [132].
- Enzymatic mechanism [133].

A particularly illustrative example is the interpretation of the Foucault's pendulum precession. This massive pendulum was initially (in 1851) conceived as a proof of Earth's rotation. Its principle relies on the rotation of the pendulum oscillation plane with respect to a local fixed direction (say the North for example). Considering only the Earth rotation around its North/South axis, this precession can be understood by describing the normal to the oscillation plane. The normal is constrained to remain in the local horizontal plane which implies that its instantaneous change is directed towards the Earth center. If the pendulum is not located on the equator, this means that the instantaneous change has non-zero components along the local reference directions which slowly rotates the angle between the normal and the local North direction. After a 2π rotation of the Earth, the normal to the oscillation plane will have a non-trivial angle with its initial direction which corresponds to the geometric phase accumulated during its transport on the sphere. This angle is:

$$\theta_{\mathrm{Foucault}} = 2\pi \sin(\lambda)$$

where λ is the latitude at which the pendulum oscillates. This phase corresponds to the geometric phase acquired by the pendulum during one revolution.

The first part of this section will derive summarily the general expression of the geometric phase and show how, applied to light's polarization trajectories on the Poincaré sphere, it gives the Pancharatnam phase. Experimental verifications of the Pancharatnam phase will then allow us to describe in more details how these abstract trajectories are realized in practice.

3.1.1 Phase in quantum mechanics

The concept of phase in a dynamical system pre-existed the modern generalisation of global invariant in an arbitrary quantum-state space. May it be the observable relative phase between the Earth's and Moon's orbit or the appearance (and disappearance) of harmonics in the superposition spectrum of two waves (acoustic, electromagnetic,...) the phase was a measure of the purely temporal synchronicity between dynamical objects. Its change was a consequence of the system's dynamic. With the advent of quantum mechanics, and matter-wave duality, phase became a dynamical object in itself and was explicitly associated with an eigen state's energy. In particular, it was associated with the system's trajectory as can be seen in the Feynman propagator [134] :

$$\mathcal{K}\left(q',t' \mid q_i,t_i\right) = \int \mathcal{D}q\left(t\right) e^{i\frac{\mathcal{S}[q(t)]}{\hbar}}$$

where $\mathcal{D}q\left(t\right)$ is the functional measure on the path space and $q\left(t\right)$ represents any path starting at $\left(q_i,t_i\right)$ and ending at $\left(q',t'\right)$ and $\mathcal{S}\left[\cdot\right]$ is the system's action:

$$\mathcal{S}\left[q\left(t\right)\right] = \int_{t_i}^{t} \mathcal{L}\left(q\left(t'\right),\dot{q}\left(t'\right)\right) dt'$$

where $\mathcal{L}$ is the Lagrangian. $\mathcal{K}\left(q',t' \mid q_i,t_i\right)$ is the Feynman propagator which determines the quantum state of a system at a later time $t_f > t_i$ and arbitrary position q_f via the convolution:

$$\Psi\left(q_f,t_f\right) = \int \mathcal{K}\left(q',t' \mid q_i,t_i\right) \Psi\left(q_i,t_i\right) dq' dt'$$

In this formulation, the influence of the trajectories energy is clearly emphasized. Indeed, the action being the time integral of the Lagrangian, the weight $e^{i\frac{\mathcal{S}[q(t)]}{\hbar}}$ in the path integral will interfere destructively and cancel the contribution of trajectories which explore energy regions far from the classical trajectory. The classical trajectory corresponds to the action's minimum i.e to the trajectory of minimal integrated energy. This link between dynamic and phase is at the core of quantum mechanics. Let us however be clear about the possible ambiguity regarding the "phase operator" sometimes defined as the natural conjugate of the number operator (Discussion of this operator can be found in the articles by Mandel *et al.*[135]–[137]). Here, the phase is used as a scalar quantity and as such is an equivocal quantity because it is defined modulo 2π. This leads, as we will see in the next section, to a particular class of phases which appears along dynamical trajectories of quantum states: the geometric phase.

3.1.2 Geometric phase derivation

Following closely the kinetic approach of N. Mukunda and R. Simon [138], we will give the general expression of the geometric phase appearing in quantum state transformations. However, the initial descriptions of this effect is attributed to Berry [139], in 1984, who described a particular case of this phase in an adiabatic approximation. Previous work already discussed the appearance, in the Born Oppenheimer approximation, of a global phase factor in the nuclear wave function going around a closed path [131] but did not described its general character. Also, the particular cases of the polarization phase (Pancharatnam, [140]) and the electronic phase in presence of electromagnetic potentials (Ehrenberg and Siday [141] followed by Aharonov and Bohm, [142] whose name were associated to this effect) are particular examples of this general geometric phase.

General definitions

We consider the quantum states of an arbitrary system, denoted ψ, which are normalized: $|\psi| = 1$ [the scalar product between states is denoted by $(.,.)$]. We call $\mathcal{N}_0$ the set of such quantum states. From the normalization condition, we see that when two states differ only by a constant phase: $\psi^{'} = e^{i\alpha}\psi$, where α is a real, they belong to the same equivalent class under the action of $U(1) = \left\{e^{i\alpha},\ \alpha \in \mathbb{R}\right\}$ on $\mathcal{N}_0$. Now, to show the consequences of this property on a transformation in this set, we need to observe how the evolution of a state is characterized. To do so, let us take an arbitrary smooth curve (in the sense that it is a family of states indexed by a continuous parameter, which are differentiably transformed into each others):

$$\mathcal{C}_0 = \{\psi(s)\,|s \in [s_1, s_2] \subset \mathbb{R}\} \tag{56}$$

The dynamic evolution of such a family has to obey:

$$\left(\dot{\psi}(s), \psi(s)\right) + \left(\psi(s), \dot{\psi}(s)\right) = 0 \quad \forall s \in [s_1, s_2]$$

due to the norm conservation. Thus, we have that $\left(\psi(s), \dot{\psi}(s)\right)$ is purely imaginary and as such equals to $i\mathrm{Im}\left[\left(\psi(s), \dot{\psi}(s)\right)\right]$. When we perform a continuous change of phase on $\mathcal{C}_0$ parametrized by the real continuous function α, called a gauge transformation, we obtain a different family in $\mathcal{N}_0$:

$$\mathcal{C'}_0 = \left\{\psi^{'}(s) = e^{i\alpha(s)}\psi(s)\,|s \in [s_1, s_2] \subset \mathbb{R}\right\} \tag{57}$$

From this, it is straightforward to see that

$$\left(\psi^{'}(s), \dot{\psi}^{'}(s)\right) = \left(\psi(s), \dot{\psi}(s)\right) + i\dot{\alpha}(s)$$

which gives, integrated over $[s_1, s_2]$:

$$\begin{aligned}
&\arg\left(\psi'(s_1), \psi'(s_2)\right) - \mathrm{Im}\left[\int_{s_1}^{s_2}\left(\psi'(s), \dot{\psi}'(s)\right) ds\right] \\
&= \arg\left(\psi(s_1), \psi(s_2)\right) + \left(\alpha(s_2) - \alpha(s_1)\right) - \mathrm{Im}\int_{s_1}^{s_2}\left[\left(\psi(s), \dot{\psi}(s)\right) + i\dot{\alpha}(s)\right] ds \\
&= \arg\left(\psi(s_1), \psi(s_2)\right) - \mathrm{Im}\left[\int_{s_1}^{s_2}\left(\psi(s), \dot{\psi}(s)\right) ds\right]
\end{aligned}$$

Therefore this quantity is independent of the gauge transformation and only depends on $\mathcal{C}_0$. Because it is also parametrization invariant (which means that it does not depend on the way the parameter s scans $[s_1, s_2]$, nor does it depend on $[s_1, s_2]$), we can define the geometric phase associated to C_0. C_0 is the projection of $\mathcal{C}_0$ onto the quotient space[1] N_0 of $\mathcal{N}_0$ under the action of $U(1)$. The geometric phase is:

$$\phi_g [C_0] := \arg(\psi(s_1), \psi(s_2)) - \operatorname{Im}\left(\int_{s_1}^{s_2} \left(\psi(s), \dot{\psi}(s)\right) ds\right) \tag{58}$$

This geometric phase can be separated into two parts, which depend on the specific choice of class representative $\mathcal{C}_0$:

- **The total phase:** $\phi_p [\mathcal{C}_0] = \arg(\psi(s_1), \psi(s_2))$
- **The dynamical phase:** $\phi_d [\mathcal{C}_0] = \operatorname{Im}\left(\int_{s_1}^{s_2} \left(\psi(s), \dot{\psi}(s)\right) ds\right)$

Clearly, the total phase represents the phase difference between the initial and final states while the dynamic phase depends on the specific path going from $\psi(s_1)$ to $\psi(s_2)$. An elegant way to classify geometric phases consists in choosing particular representative $\mathcal{C}_0$ of C_0 called a horizontal lift for which geometrical interpretations are easier.

Horizontal lifts

Because the geometric phase does not depend on the choice of curve $\mathcal{C}_0$ representative of C_0, we can find a gauge transformation for which the dynamical phase of $\mathcal{C}_0$ is exactly zero. This can be done by having:

$$\operatorname{Im}\left(\psi(s), \dot{\psi}(s)\right) = 0 \,\forall\, s \in [s_1, s_2]$$

Such a lift is called a horizontal lift. It is unique because the gauge transformation which allows to find this particular representative is completely *determined*[2]. Using this lift, we can express the geometric phase as:

$$\phi_g [C_0] = \arg(\psi(s_1), \psi(s_2)) \tag{59}$$

Therefore, we can visualize geometrically this phase as the phase shift between the initial and final states on the condition that the curve between them is horizontal. Geometrically, this condition is called parallel transport and consists in transforming the state with infinitesimal orthogonal operations. To illustrate it, let us consider the simple case of a two level atom. This system is equivalent to a spin $1/2$ and its evolution can be similarly represented on the Bloch-sphere (see Fig. 22a). For example,

---

[1] This emphasize that this quantity does not depend on the gauge choice because on N_0, all gauges equivalent families have the same projection.

[2] From a general representative $\mathcal{C}_0$, with the gauge transformation $\alpha(s) = -\operatorname{Im}\left(\int_{s_1}^{s} \left(\psi(s'), \dot{\psi}(s')\right) ds'\right)$ we can create this family.

an atomic population only distributed in the lower (resp. higher) state is represented by the South (resp. North) pole. During the parallel transport, the angle (defined in the local tangent plane) between the state's phase (represented by a vector) and the direction of transport has to stay constant. This results in a phase shift between the two extremal quantum states. It can be shown ([143]–[145]) that the resulting phase-shift is equal to half the solid angle subtended by the enclosed area on the sphere.

3.1.3 Pancharatnam phase

To obtain the Pancharatnam phase, we now have to transpose the previous example to the evolution of a polarization state on the Poincaré sphere [146]. The Poincaré sphere is a powerful tool to describe the polarization state of a transverse electromagnetic wave. Because the electric field is orthogonal to the direction of propagation, its polarization can be described by two projections on orthogonal directions and by a phase shift between these two components. Recalling that the electromagnetic field is invariant under a global change of phase, the Poincaré sphere is identical to the Bloch sphere when we identify the two orthogonal polarization states to the two atomic levels. We can therefore apply the previous analysis performed on quantum states to the evolution (see Fig. 22b) of light going through polarization rotators[3]. These perfect rotators perform unitary transformations along great circles on the Poincaré sphere. This ensures that the polarization state follow horizontal lifts on the Poincaré sphere along the path denoted γ. This leads to a total phase shift, purely geometric, called the Pancharatnam phase between polarization states at each path extremity. Its value is also given by half the subtended solid angle which can be expressed [143] as:

$$\phi_{panch}[\gamma] = \arccos\left[\frac{\cos(\theta_{12}/2)^2+\cos(\theta_{23}/2)^2+\cos(\theta_{31}/2)^2-1}{2\cos(\theta_{12}/2)\cos(\theta_{23}/2)\cos(\theta_{31}/2)}\right] \tag{60}$$

where θ_{12}, θ_{23} and θ_{31} denote the angles between the trajectory's vertices in the case of a cyclic transformation[4] performed by three rotators. Note that the Gauss-Bonnet's theorem [147] gives a much more compact expression[5]:

$$\phi_{panch}[\gamma] = \frac{A_1 + A_2 + A_3}{2} - \pi$$

where A_i are the interior angular jumps at the surface vertices.

---

[3] The rotation refered to affects only the polarisation state not actual geometrical rotations.

[4] When the transformation is not cyclic, the final state can be projected onto the initial state which defines the last portion of an artificially cyclic trajectory

[5] This forms clearly emphasize the role of the underlying quotient space which curvature directly impact the resulting formula.

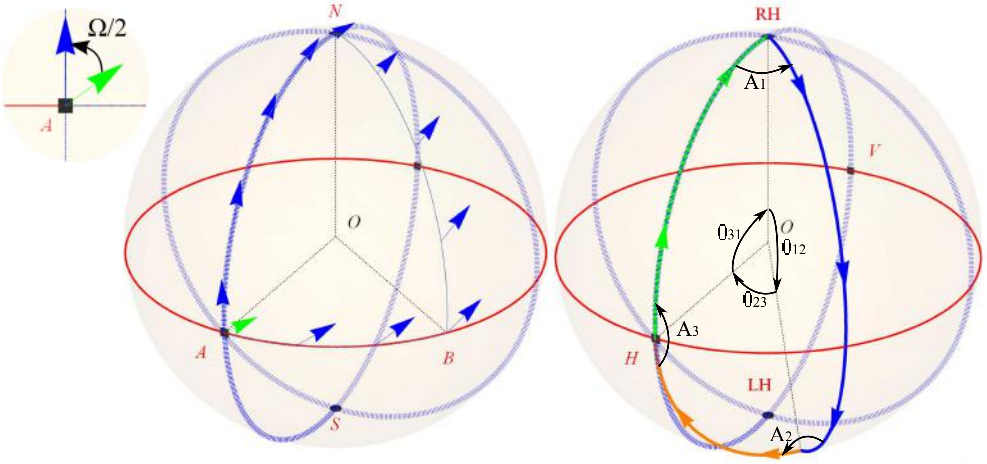

(a) Parallel transport on the Bloch sphere **(b)** Polarization trajectory on the Poincaré sphere

Figure 22: **(a)** Parallel transport of the quantum state of a two level system on the Bloch sphere. The phase of the state is represented by the direction of the blue vector. The poles are denoted by N, S and the equator is represented in red. An initial state is transported from A to pole N, then from N to B and finally brought back to A. The parallel transport keeps the angle between the state's phase and the direction of transport constant. From A to N, this angle is zero while from N to B it is not. The inset shows the phase shift between the initial (blue) and the final (green) state. Ω is the solid oriented angle subtended by the trajectory.
(b) Poincaré sphere displaying the usual orthogonal polarization states: Right Handed (RH) and Left Handed (LH). The Cartesian direction are labelled Horizontal (H) and Vertical (V). O is the center of the sphere. The trajectory γ of a right handed polarization going through three successive rotators is represented in blue, orange and green. The arrows merely represent the direction of evolution. θ_{12}, θ_{23}, θ_{31} correspond to the angles between the radii of the triangle vertices and the angles A_1,A_2 and A_3 are the jumps between the trajectory's vertices.

3.1.4 Experimental demonstrations

The earliest experimental demonstration of a geometric optical phase[6] appears in 1986 [148], [149] when Chiao *et al.* used an helically wounded optical fiber to rotate adiabatically the propagation direction of a linearly polarized laser beam (see Fig. 23a). This purely geometrical evolution rotated the polarization state along a circle which subtends a cone with apex at the origin and apex semi-angle θ. By changing the pitch angle of the helix, they could change θ and scan the Pancharatnam phase which resulted in the rotation of the polarization direction at the output of the fiber (kept parallel to the input).

The following years, experiments using separated arms interferometers [150] demonstrated, by using mirrors which non-adiabatically reversed the light's helicity, that adiabaticity was not necessary. In particular several experiments [151], [152] using a quarter wave plate inside a Michelson interferometer (schematized on Fig.23b) demonstrated a continuous change of the Pancharatnam phase by rotating the wave-

---

[6] Because this experiment does not rotate a polarization state on the Poincaré sphere but a polarization state direction in real space, the resulting phase is not, streactly speaking, a Pancharatnam phase and is usually labelled as a spin redirection phase.

plate. They even produced frequency side-bands in the light's spectrum at twice the rotation frequency of the rotating quarter-wave plate [153].

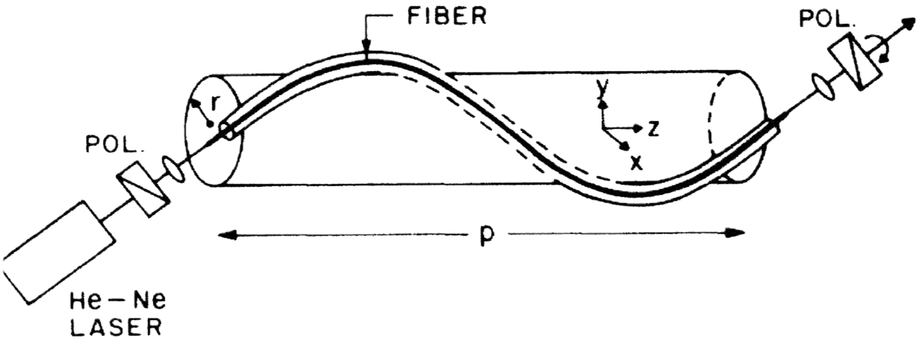

(a) Wound optical fibre set-up

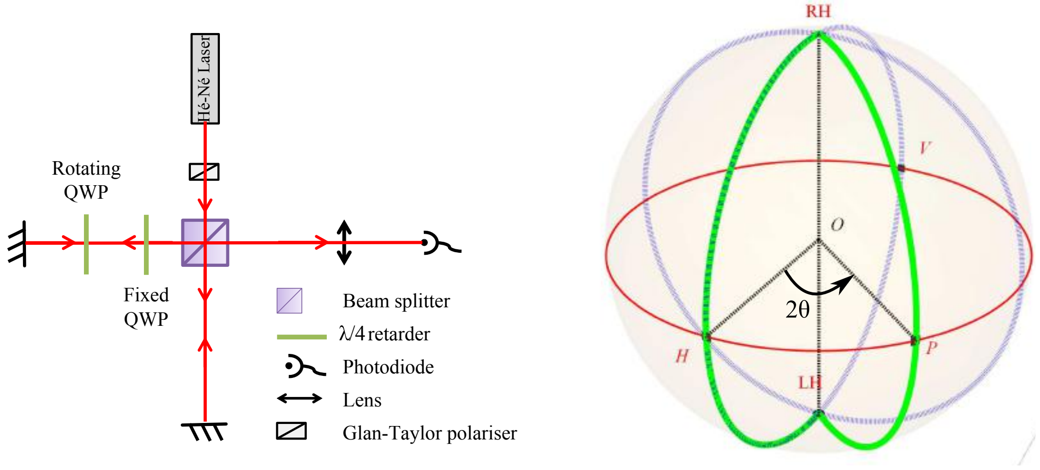

(b) Michelson set-up

(c) Trajectory

Figure 23: **(a)** Experimental set-up from [149]. An optical fiber is wound with a fixed helix pitch and the linear polarisation direction at the fibre's output is measured with a polariser.
(b) Setup used for a continuous scan of the Pancharatnam QWP [152]. The polarized laser beam travels through two quarter-wave plates on one arm of the interferometer. The first one is fixed with fast axis at 45° relative to the incident polarization. The second one can be continuously rotated and its fast axis makes an angle θ with respect to the initial polarization direction.
(c) Corresponding trajectory on the Poincaré sphere. The polarization state goes from horizontal (H) to right handed (RH) in the first quarter-wave plate. Then, depending on the angle θ, returns to linear (P). After retro-reflection on the mirror, it goes from linear (P) to left handed (LH) and finally, returns to its original state (H).

This phase was investigated down to the single photon level [154], [155]. The experiment of Kwiat *et al.*[154] used a coincident detection setup of photon pairs produced by a non-linear crystal (KDP). The lower frequency photon (idler) was directly detected while the other one interfered in a Michelson interferometer similar to the one described on Fig 23b. By reducing the energy acceptance of a filter used to detect the idler photon, they reduced the energy distribution of the signal photons contributing to the interference. When the Michelson interferometer was unbalanced, this lead to the revival of the Pancharatnam fringes visibility. The signal from [154] is represented on Fig. 24.

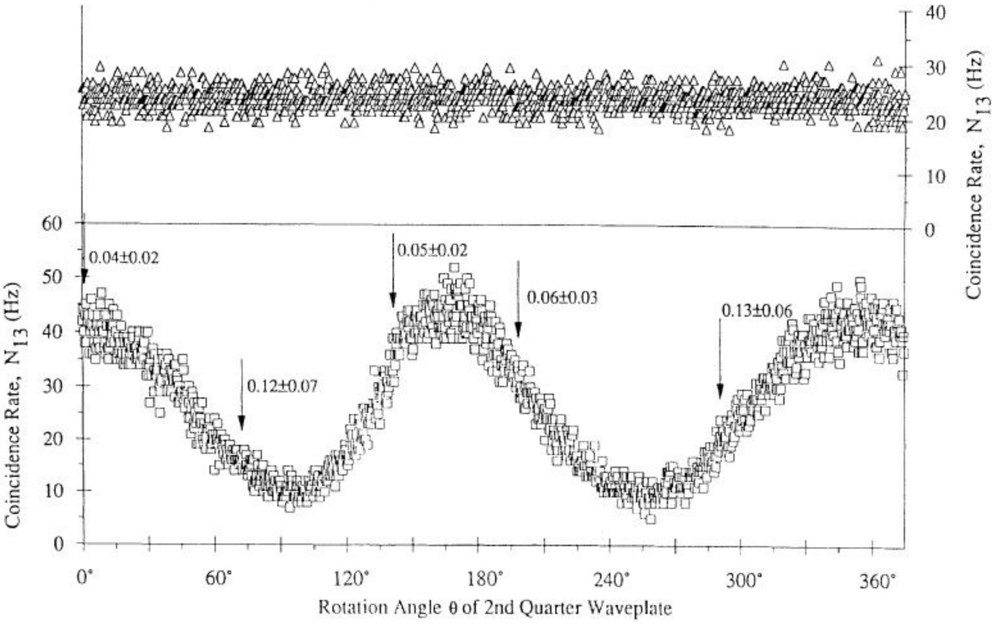

Figure 24: Figure adapted from [154] representing coincident optical interference fringes. The rotation angle of the quarter waveplate scans the Pancharatnam phase. The interference signal top (resp. bottom) corresponds to a broad (resp. narrow) energy filter shows revival of the fringes visibility when the photon distribution is narrow. The arrows indicate the measured triple anticorrelation parameter, ensuring the non-classical state of the detected photons.

Later on, the potential non linear behavior of the Pancharatnam phase was demonstrated using a rotating analyser [156] or initially elliptic polarization states [157]. The distinction between the dynamical part and geometric part was investigated with twisted polarizers and retarders [158] and the case of open transformations, which can lead to singularities, were described in [159].

Finally, I would like to emphasize the wavelength independent property of the Pancharatnam phase which was demonstrated by Hariharan *et al.*[160] in a white-light interferometer. This achromaticity is hard to realize in optics because optical polarization elements have to be achromatic which is not easy. For example, an achromatic phase shifter with a phase deviation of $100\,\mathrm{mrad}$ over the whole visible spectrum was described in [161]. But for atoms imprinting the phase of an optical lattice (as described in Sec. 1.2), part of this phase is achromatic (i.e velocity independent). This property motivated the development of a new atom-optics tool: the Pancharatnam phase shifter described in the next Section.

Geometric phases

Geometric phases are intrinsically related to the system underlying symmetry. For quantum states, the $U(1)$ group leads to a global invariant of homotopic transformations: the Berry's phase. For light waves, the polarization state imprints a geometric phase called the Pancharatnam phase. Its characteristics have been successfully demonstrated in many different setups. In particular, a combination of two quarter wave plates on one arm of a Michelson interferometer (Fig. 23b) allows to scan continuously the Pancharatnam phase.

3.2 THE PANCHARATNAM PHASE-SHIFTER

The interferometric phase shift ϕ_d (see Sec. 1.3.2 eq. (15)) depends, in our Mach Zehnder configuration, on the standing waves phases of each gratings:

$$\phi_d = \Phi_1 + \Phi_3 - 2\Phi_2 \tag{61}$$

where Φ_i denotes the phase of the i^{th} Bragg lattice. To scan this phase, we usually changed, with a piezo actuator, the position of the retro-reflecting mirror of the third Bragg standing wave which modified the spatial reference of Φ_3. A Pancharatnam phase shifter also changes the diffraction phase without displacing the third mirror. It consists in adding a pair of QWP's in between the atom interferometer arms and the retroreflecting mirror. This results in adding to the lattice phase Φ_3 the Pancharatnam phase ϕ_P which can be controlled by the relative orientation of the two QWP's. This type of setup is directly inspired from the Michelson setup (see Fig. 23b) used by Chyba *et al.*[152].

3.2.1 Description of the experimental apparatus

This phase shifter schematized on Fig.25a consists in two quarter wave-plates positioned right between the retro-reflecting mirror and the atom interferometer's arms. We use two zero order quarter wave plates manufactured by Fichou® for the 671 nm wavelength. They are made of two polished quartz plates which optical axis are parallel to their faces. The thickness difference between the two plates is 18.6(2) µm. The two plates are attached by molecular adhesion with their axis crossed. Therefore, they induce a phase shift equal to $\pi/2 \pm \pi/150$ at the nominal temperature of 20 °C . These QWP's were mounted on aluminium rings. The first QWP is glued with Torr Seal® epoxy onto the mechanical support of the second, rotating, QWP. The rotation is driven with an externally rotated cam and a ferrofluid feedthrough located 150 mm above the atom interferometer arms. This choice was motivated by the high sensitivity of the atomic phase to magnetic gradients which prevents the use of electric motors too close to the interferometer. The cam is attached to a nylon worm screw which transmits the rotation to a nylon worm wheel. The wheel is fixed on a 1 ″ diameter vacuum compatible bearing which is attached to the support. The bearing is made of polymer with glass balls in order to exclude ferromagnetic elements close to the atomic beam, at the expense of its guidance stability compared to usual metallic balls bearings. The QWP ring is directly glued onto the wheel. On the other side of the mechanical support, a digital encoder[7] (microE®, MercuryII 6000V) records the angular position of a glass plate attached on the other side of the bearing. This compact (less than 30 mm long) set up has an optical acceptance diameter of approximately 12 mm which is smaller than our Bragg beam diameter of 16 mm. But by adjusting the beam power and the laser detuning, this reduced aperture did not change the performance of our interferometer.

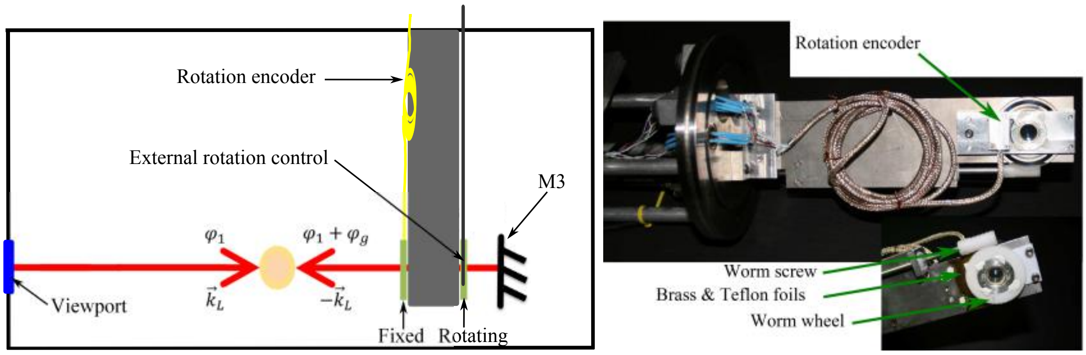

(a) Phase shifter in vacuum **(b)** Realisation

Figure 25: Schematic representation **(a)** and picture **(b)** of the mechanical system introducing two quarter wave plates on the path of the third Bragg beam. The rotation of the second QWP is transmitted via a worm drive with a vacuum compatible rotation worm screw. To minimize and stabilize the tilt between the rotation axis and the QWP's normal, thin foils of brass and Teflon have been fixed bellow the worm wheel. A digital encoder records the angular position of the rotating QWP on the other side of the bearing. The fixed QWP is mounted on the mechanical support of this encoder.

3.2.2 Theoretical Pancharatnam phase shifter

In an ideal setup, each quarter wave plates produces a constant $\frac{\pi}{2}$ phase shift between the two polarization states on the whole laser beam. The incident laser beam is orthogonal to the QWP's, its polarization is perfectly linear and makes an angle of 45° with the ordinary axis of the fixed quarter wave plate (FQWP). In these conditions, the Pancharatnam phase is linear in the angle of rotation of the rotating quarter wave plate (RQWP) and changes by 2π when the RQWP rotates by π. In other word, if ω is the angular speed of the RQWP, the theoretical Pancharatnam phase is[8]:

$$\phi_{P,theo}(t) = 2\omega t \tag{62}$$

---

[7] Its accuracy is specified at 314 μrad with a resolution approximately 4 times higher.

[8] Provided an appropriate choice of the time origin.

3.2.3 Optical fringes

We tested our Pancharatnam phase shifter with the Michelson interferometer implemented on mirror M3 which was initially used to monitor the diffraction phase when it was changed by varying the mirror's position (see Sec 1.3.2). To test our phase shifter, the mirror was fixed and we recorded the optical fringes as well as the RQWP's angle reading on the rotation encoder. Apart from a constant phase ϕ_M proportional to the arm's length difference, the measured intensity detected on one output is expected to be:

$$I(t) = I_0 \{1 + \mathcal{V} \cos [\phi_M + \phi_{P,theo}(t)]\} \tag{63}$$

Where I_0 is the mean intensity and $\mathcal{V}$ is the visibility. We recorded the light intensity directly with a photodiode. The result of a typical 2π revolution of the QWP is represented on Fig. 26. As expected, the interferometric signal presents oscillations at twice the rotation angle frequency and from the different width of the lobes, one can clearly see a modulation of the instantaneous 'frequency' at which the fringes are scanned. Indeed, the modulation effect can be described as an effective time dependent frequency $\omega [1 + u_M \cos(\omega t + \Psi)]$ which oscillates periodically. This impression is confirmed by comparison of two different fitting procedure. The linear one is a fit to a simple sinusoidal evolution

$$f_{linear}(\theta) = \mathrm{off} + \mathrm{amp} * \sin(2\theta + 2\Psi)$$

while the non-linear one includes a modulated frequency:

$$f_{non-linear}(\theta) = \mathrm{off} + \mathrm{amp} * \sin[2\theta + u_M \cos(\theta + \Psi + \Phi) + 2\Psi]$$

where (off, amp, Ψ, u_M and Φ) are the fitting parameters. From the residuals, one sees that some aspect of the difference between our measurement and the theoretical prediction is captured (the residual is clearly lower around $3\,\mathrm{rad}$ and $6\,\mathrm{rad}$) but there remain some periodic behavior that is not accessible to our model. The modulation amplitude resulting from the non-linear fit is $u_M = 0.35\,\mathrm{rad}$.

To understand the origin of this modulation, we must refine our description of the Pancharatnam phase shifter by taking into accounts defects of our apparatus. Of course, due to the periodicity of the system, these defects do not change the total phase after a 2π rotation of the QWP, but they can induce non-linearities in the Pancharatnam phase. We identified three potential sources that we are going to describe successively in the remaining of this section.

3.2.4 Quarter Wave Plate geometry

In a standing light wave, the intensity modulation is a consequence of the interference between two counter-propagating electric fields and as such is highly sensitive to

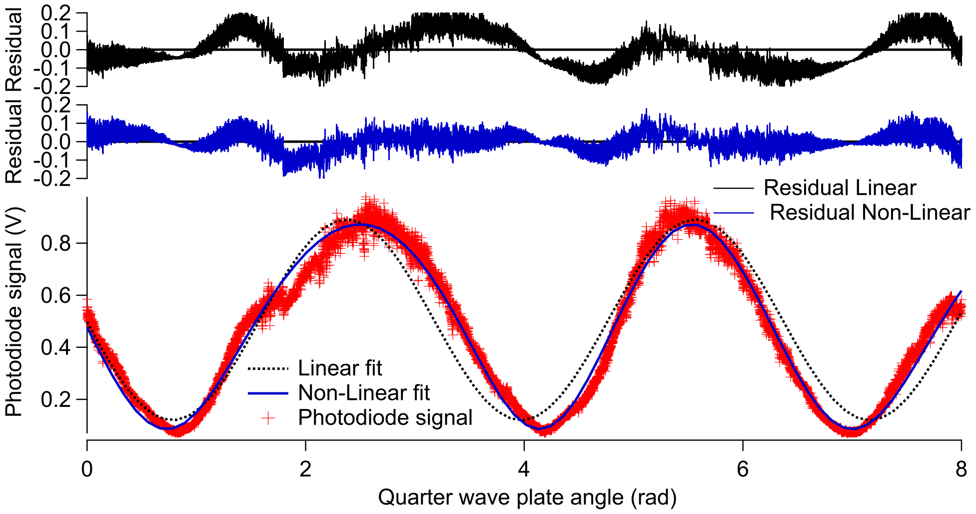

Figure 26: Pancharatnam fringes of the optical interferometer. The photodiode signal (which has been sub-sampled for visual clarity) is proportional to the laser intensity in one output of the Michelson interferometer. A 2π rotation induces two full oscillation periods. The speed at which the fringes are scanned is clearly lower between 1 and 3 rad than between 5 and 7 rad indicating an angular dependence of the instantaneous angular speed. A periodic defects around 2 rad is estimated to come from a periodic slip of the QWP's support on the rotation axis. The result of two fitting functions (see text) are compared.

the wave-front quality. In a standard configuration, the reflected beam wave-front is a combination of both the incoming wave-front and the mirror surface. But with our phase-shifter, two quarter-wave plates contribute to modify the reflected wave-front and, as the light goes back and forth, the effect is doubled. The specification of our quarter wave plates indicates a transmitted wave-front quality of $\frac{\lambda}{10}$ RMS. However, in our interferometer, the part of the laser standing wave interaction with the atoms is a horizontal band of about $3\,mm$ height and $8\,mm$ length which is small compared to the diameter of the QWP's. Thus, we can reasonably expect that the effective wave-front distortion is lower than the one specified. In addition, the mechanical construction of the phase shifter was such that the center of rotation of the RWQP was very close to the center of the mirror M3 but the exact altitude of the atomic interferometer arm is not well known relative to the RQWP's rotation center. Therefore, the rotation can modulate the lattice phase around a mean value close to the Pancharatnam phase due to the additional dynamical[9] laser phase modulation.

To quantify this modulation, we measured the optical path in the quarter wave plate. The method used is adapted from [162] and relies on the Fabry-Perot produced by the parallel faces of the Quartz quarter wave plate. An incident polarized (aligned on a principal axis of the slab) light is completely transmitted when the resonance condition is fulfilled:

$$2ne\cos\left(i_p\right) = p\lambda \quad p \in \mathbf{N}$$

---

[9] The dynamical phase here describes the phase accumulated during the laser propagation which is equal to the integral along the optical path of $\frac{2\pi}{\lambda}n\left(l\right)dl$, where $n\left(l\right)$ is the local index of refraction and dl is the infinitesimal path in real space.

where λ is the light's wavelength, n is the refractive index at this wavelength and for a given polarization direction, e is the slab thickness and i_p is the resonant incident angle. Therefore, by monitoring the reflected light, which displays concentric dark rings whose angular minima are i_p, we can determine the slab thickness variation by measuring the angles $(i_p)_{p\in\mathbf{N}}$. This method is very effective even in the presence of anti-reflection coatings[10] on the quarter wave plates. With pairs of consecutive resonant angles, we measured the fractional part ϵ of p:

$$\begin{aligned}\epsilon &:= \frac{2ne}{\lambda} - \left[\frac{2ne}{\lambda}\right] \\ &= \frac{i_p^2}{i_{p+1}^2 - i_p^2}\end{aligned}$$

where $[]$ is the integer part. The results are displayed on Fig. 27. We found a linear variation on both coordinates, with a maximum excursion of the fractional part of $\Delta\epsilon = 0.43$, for the best QWP among the three produced by Fichou. This linear dependence indicates a prismatic shape of the quarter wave plate. From the difference of thickness over the large diagonal, which is simply given by $\Delta\epsilon\lambda/\bar{n}$ where $\bar{n} \sim 1.548$ [163] is the quartz's mean refractive index at $\lambda = 0.633\,\mathrm{nm}$, we get the prism apex angle:

$$\alpha = \frac{\Delta\epsilon\lambda}{2\sqrt{\Delta X^2 + \Delta Y^2}\bar{n}} \simeq 10\,\mu\mathrm{rad}$$

When the beam is slightly off the rotation axis as is represented on Fig 28a, this prismatic effect leads to modulations of the dynamical phase. The dynamical phase shift corresponds to twice the integrated optical path which, apart from a constant term $\frac{2\pi\bar{n}\bar{e}}{\lambda}$, consists in a modulation :

$$\phi_{dyn1}(t) = \frac{2\pi}{\lambda}(\bar{n} - 1)\,\delta r \alpha \cos(\omega t + \Psi_1)$$

where δr is the distance between the rotation axis and the effective laser region and Ψ_1 is a constant phase which depends on the prism orientation relative to the quarter wave plate axis. We estimate a height difference $\delta r \sim 1\,\mathrm{mm}$ between the QWP rotation center and the interferometer's arms which leads, with this QWP, to a modulation amplitude of $0.19\,\mathrm{rad}$.

---

[10] It was specified better than 0.2 % at 670 nm but we used a slightly different wavelength $\lambda_{He-Ne} = 633\,\mathrm{nm}$ to have more reflected light. A better choice would have been a single frequency laser with a wavelength for which the AR coating have a stronger reflection coefficient but we did not have one at hand.

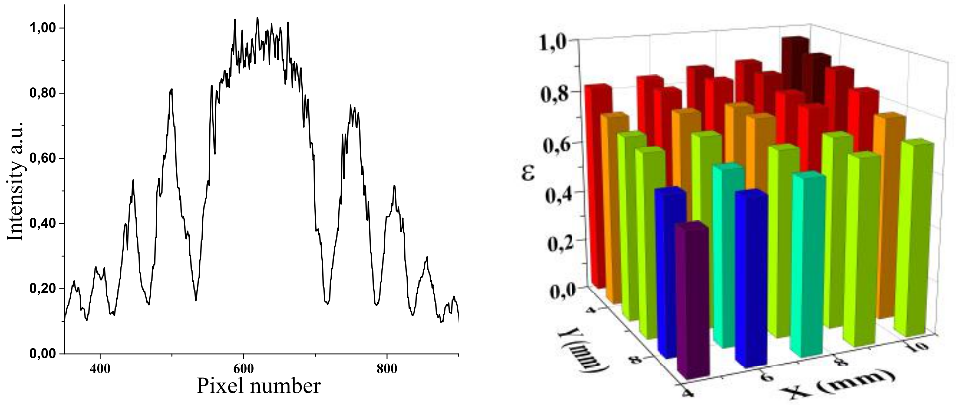

(a) Fabry-Perot Signal **(b)** Fractionnal Part

Figure 27: (a) : Typical CCD signal of the Fabry-Perot measurement. The pixel number is an affine function of the light's angle i. The intensity modulation has a contrast better than 90 % for the first extinction and the rings diameter are measured with a 1 % uncertainty, leading to a fractional part uncertainty of ±2 %
(b): Fractional part for different beam position in a rectangle centred on the disc. The rectangle is 6 mm × 7.5 mm and the fractional part is between 0.52 and 0.95 for this quarter wave plate (see text). The linear dependence on the distance indicates a prismatic slab with vertex angle $\alpha = 10\,\mu\mathrm{rad}$. A schematic representation of the prism is shown on Fig. 28a.

3.2.5 Rotation axis

In addition to the prismatic effect, the axis of the laser beam can be different from the normal to the quarter wave plate which itself can be different from the rotation axis. This is represented on Fig.28c. We will decompose this effect in two parts:

Tilt between the laser beam axis and the QWP

The general formula giving the phase shift ϕ for a light beam going through a birefringent media with an angle of incidence i [164]:

$$\phi = \frac{2\pi e}{\lambda}\left\{n_e\left[1-\left(\frac{\sin^2(\theta)}{n_e^2}+\frac{\cos^2(\theta)}{n_0^2}\right)\sin^2(i)\right]^{1/2} - n_0\left[1-\frac{\sin^2(i)}{n_0^2}\right]^{1/2}\right\}$$

where n_e and n_0 are respectively the extraordinary refractive index and the ordinary refractive index of the crystal, θ is the angle between the plane of incidence and the ordinary axis. To first order in $i \ll 1$ and in $\Delta n = n_e - n_0 \ll n_e, n_0$ this reduces to:

$$\phi_{bi} = \frac{2\pi e\Delta n}{\lambda}\left[1+\frac{i^2}{2}\frac{1-2\cos^2(\theta)}{n_0 n_e}\right] \tag{64}$$

We see that this phase shift will depend on the direction of the ordinary axis θ. For the RQWP, this angle will change with the rotation while for the fixed quarter wave plate (FQWP), it will remain constant. We can however evaluate the order of magnitude of this effect by considering the worst case $\theta \equiv 0\left[\frac{\pi}{2}\right]$. In this case, the optical length will

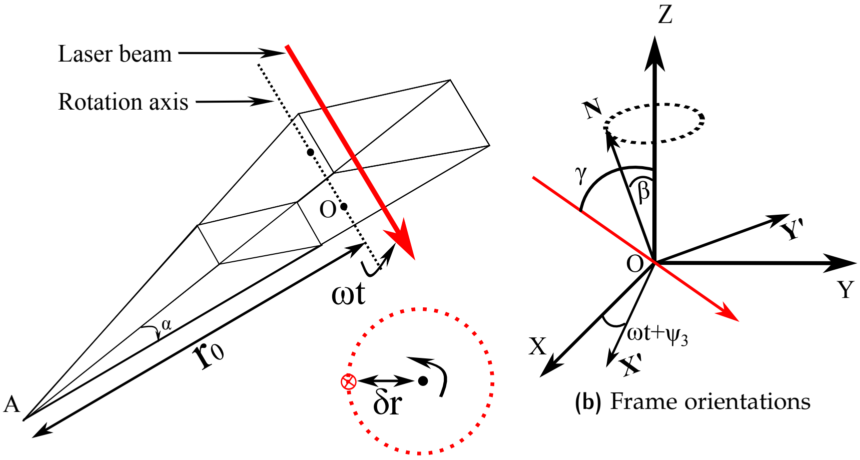

(a) Prismatic slab

(b) Frame orientations

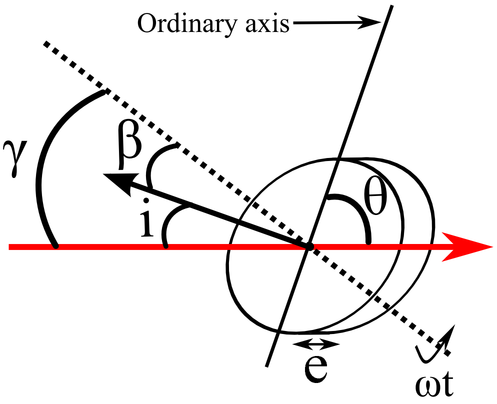

(c) Axes of the crystal slab

Figure 28: **(a)**: Prismatic effect of the rotating quarter wave plate. The laser beam (red) intersects orthogonally the prism which rotates around an axis parallel to its edge going through its center O (dotted line). The distance from the rotation axis is schematized at the bottom right
(b): Orientation of the rotation reference frame (O;X,Y,Z) relatively to the QWP birefringent axis frame (O;**X′**,**Y′**,**N**). The laser beam is not orthogonal to the QWP face and makes a constant angle with the rotation axis.
(c): Schematic representation of the possible alignment defects between the laser beam axis (red), the normal of the quarter wave plate (N) and the rotation axis (dotted line). The three axis are not coplanar !

differ from it's expected value by $\lambda i^2/(4n_0n_e)$ which, for $i \sim 15\,\mathrm{mrad}$, is $\sim \lambda/80000$. This value is about 0.1 % of the specified accuracy of the QWP and is negligible in our case but can become important if the optical length is better controlled (see 3.3.2)

Similarly to the prismatic effect, the dynamical phase will also change due to the incident angle i. The dynamical phase shift induced by a parallel glass slide of width $\bar{e}$ is, in the small angle approximation:

$$\begin{aligned}\phi_{dyn2}(i) &= \frac{2\pi\bar{e}}{\lambda}\left\{\frac{n}{\cos(i/n)} - \frac{\cos(i/n - i)}{\cos(i/n)}\right\}\\ &\simeq \frac{2\pi\bar{e}}{\lambda}\left\{(n-1) + \frac{i^2}{2}\frac{(n-1)}{n}\right\}\end{aligned}$$

where i is the incident angle. Apart from a constant term, we can express the dynamical phase shift as a function of i:

$$\phi_{dyn2}(i) = \frac{2\pi\bar{e}}{\lambda}\frac{(n-1)}{n}i^2$$

where an additional factor 2 due to the double pass configuration has been used. In practice, this dynamical phase shift can account for $0.33\,\mathrm{rad}$ for an incident angle of $15\,\mathrm{mrad}$.

It might seem unrealistic to consider these two effects simultaneously (birefringent effect and dynamical effect) since the latter is orders of magnitudes larger than the former. However, the first effect is not negligible on the Pancharatnam phase when one wants to control its value down to the mrad range as we will see in Sec. 3.2.6 and discuss in Sec. 3.3.2.

Tilt between rotation axis and the QWP's normal

When the rotation axis is not perfectly orthogonal to the quarter wave plate, the normal to the plate precesses around the rotation axis, which dynamically changes i and θ. To determine their evolution, we can use the formalism of rotation matrices which relates the coordinates in the rotating frame $\left(\vec{N}, \vec{X'}, \vec{Y'}\right)$ attached to the QWP, to the coordinates in the fixed frame $\left(\vec{Z}, \vec{X}, \vec{Y}\right)$ as represented on Fig. 28c)). If β is the constant angle between $\vec{N}$ and $\vec{Z}$, and if one direction ($\vec{X'}$) of the QWP is supposed to remain in the $(O; X, Y)$ plane, we get:

$$\begin{pmatrix} \cos(\beta) & 0 & \sin(\beta) \\ \sin(\beta)\sin(\omega t + \Psi_2) & \cos(\omega t + \Psi_2) & -\cos(\beta)\sin(\omega t + \Psi_2) \\ \sin(\beta)\cos(\omega t + \Psi_2) & \sin(\omega t + \Psi_2) & \cos(\beta)\cos(\omega t + \Psi_2) \end{pmatrix}$$

where Ψ_2 is a phase determined by initial conditions and ω is the precession rate. The direction of the normal axis is given by its first row:

$$\vec{N} = \begin{pmatrix} \cos(\beta) \\ \sin(\beta)\sin(\omega t + \Psi_2) \\ \sin(\beta)\cos(\omega t + \Psi_2) \end{pmatrix}$$

thus, if we consider a laser beam contained in the plane $(O; Z, X)$, making an angle γ with $(O; Z)$, its unit direction vector is:

$$\vec{L} = \begin{pmatrix} \cos(\gamma) \\ \sin(\gamma) \\ 0 \end{pmatrix}$$

which simply gives us $i(t)$ from the definition:

$$\cos[i(t)] := \vec{L} \cdot \vec{N} = \cos(\gamma)\cos(\beta) + \sin(\gamma)\sin(\beta)\sin(\omega t + \Psi_2)$$

which reduces, in the limit of small $\beta, \gamma \ll 1$, to:

$$\frac{i^2(t)}{2} = \gamma\beta \sin(\omega t + \Psi_2)$$

To get the expression of $\cos[\theta(t)]$, we need to take into account the fact that the ordinary axis can make an arbitrary angle α with $\vec{X'}$:

$$\begin{aligned} \cos[\theta(t)] &:= \left[\cos(\alpha)\vec{X'} + \sin(\alpha)\vec{Y'}\right] \cdot \vec{L} \\ &= \gamma\cos(\omega t + \Psi_2 - \alpha) + \beta\sin(\alpha) \end{aligned}$$

Recalling eq. (64), the effect of the angle between the ordinary axis and the plane of incidence, proportional to $\cos^2[\theta(t)]$, adds a fourth order contribution to the birefringent phase which will be ignored due to the already small value of the second order term.

3.2.6 Phase retardation

We will now summarize the effective total phase shifts induced by the two QWP on the laser beam. To do so, we will first focus on the birefringent phase shifts which modulate the Pancharatnam phase. Then, we will add the dynamical phase shifts to get the total phase shift imprinted on the lattice.

Birefringent phases

The first QWP is fixed and we didn't investigate its prismatic shape. However, we can use the manufacturer's specification to evaluate the maximum systematic uncertainty on the phase shift:

$$\phi_{FQWP} = \frac{\pi}{2}\left[1 \pm \epsilon_1\right]\left\{1 + \frac{i^2}{2}\frac{1 - 2\cos^2(\theta)}{n_0 n_e}\right\} \simeq \frac{\pi}{2}\left[1 \pm \epsilon_1\right]$$

where ϵ_1 is the FQWP specified accuracy (in our case, $\epsilon_{1,2} < \frac{1}{75}$). The tilt angle ($i \sim 15\,\mathrm{mrad}$) accounts for $\lambda/80000$ which is less than 0.1 % of ϵ_1 and as such negligible. The second QWP combines both the systematic effect and a dynamical tilt which can be expressed as:

$$\phi_{RQWP}(t) = \tfrac{\pi}{4}\left[1 \pm \epsilon_2\right]\left\{1 + \tfrac{\gamma\beta}{n_0 n_e}\sin(\omega t + \Psi_2)\right\} \tag{65}$$

These effects will produce a modulation of the Pancharatnam phase and harmonics of the rotation frequency can appear in the total phase due to the deviation from the ideal trajectory on the Poincaré sphere. This effect might be higher than the previous one because of the difficulty to simultaneously align three axis (rotation, birefringent plate and laser) in vacuum but remains marginal. However, for the sake of the discussion[11], we will give the expression of the Pancharatnam phase which takes into account this modulation

Effect on the Pancharatnam phase

To evaluate the effect of these imperfections on the Pancharatnam phase, one can use eq. (60) which relates the solid angle subtended by a spherical triangle on the sphere. To do so, the simplest way is to decompose the spherical polygon into three spherical triangles. The first one has vertices V_1, V_2 and V_3 which correspond to the initial, FQWP and RQWP polarization states respectively. The second one has vertices V_3, V_4 and V_5 which correspond to the polarization states after the second crossing of the RQWP and the final state (after the second crossing of the FQWP). In this description, the rotators are not perfect which results in an open trajectory on the Poincaré sphere. Hence, the Pancharatnam phase is measured by orthogonal projection of the final state on the initial one. This closes the path and adds a third triangle with vertices V_5,V_1 and V_3. Figure 29 summarizes this subdivision. Doing so, we can express the total solid angle as the sum of the three partial solid angles subtended by each of the spherical triangles. This leads to a page long analytical expression which can be advantageously expended in power series of ϵ_1, ϵ_2 and $\frac{\gamma\beta}{n_0 n_e}$:

---

[11] in addition to the fact that this, to my knowledge, has not been expressed before.

$$
\begin{aligned}
\phi_P(t) \simeq\ & 2\omega t + \left[\pi \sin(2\omega t)(\epsilon_1 + \epsilon_2) - \frac{\pi}{2}\sin(4\omega t)\,\epsilon_1\right] \\
+\ & \frac{3\pi^2}{16}\left(4\sin(2\omega t)\,\epsilon_1\epsilon_2 - \sin(4\omega t)\,\epsilon_1^2\right) \\
+\ & \pi\sin(2\omega t)\left[1 + \epsilon_2 + \frac{3\pi}{4}\epsilon_1\right]\sin(\omega t + \Psi_1)\,\frac{\gamma\beta}{n_0 n_e}
\end{aligned}
\tag{66}
$$

As anticipated, the different defects will mainly modulate the Pancharatnam phase around its linear value $2\omega t$ and will integrate to zero over the whole cycle. In our case, ϵ_i are about three order of magnitudes larger than the tilt modulation which is why we kept only their second order terms in the development. Interestingly, the frequencies at which these modulations occur are distinct which allows to measure them independently. Furthermore, only the first QWP retardance ϵ_1 has a second harmonic component at 4ω which comes from the fact that the FQWP defect is integrated twice when the light goes through the RQWP, while the RQWP defect is only integrated when going back through the RQWP.

Dynamical phases

The two effects inducing changes in the laser dynamical phase can be collected in a total dynamical phase:

$$
\begin{aligned}
\phi_{dyn}(t) &= \phi_{dyn1}(t) + \phi_{dyn2}[i(t)] \\
&= \frac{4\pi(n-1)}{\lambda}\left\{\alpha\delta r\cos(\omega t + \Psi_1) + \bar{e}\frac{\gamma\beta}{n}\sin(\omega t + \Psi_2)\right\}
\end{aligned}
$$

Total phase

The total phase of the reflected laser beam is the sum of the initial phase, a constant dynamic phase and two time-dependent contributions, the dynamical phase $\phi_{dyn}(t)$ and the Pancharatnam phase $\phi_P(t)$.

$$
\phi_d(t) = \phi_0 + \phi_{dyn}(t) + \phi_P(t) \tag{67}
$$

This analysis justifies the non-linear fitting function used for the optical fringes presented at the beginning of this Section. The order of magnitude of the modulation amplitude obtained $u_M = 0.35\,\mathrm{rad}$ compares well with the two dynamical effect estimated[a] at $0.19\,\mathrm{rad}$ (prismatic) and $0.33\,\mathrm{rad}$ (tilt).

---

[a] We did not at the time take particular attention to the angular references which prevented us from having an idea of the phase difference $\Psi_2 - \Psi_1$ which could have allowed us to measure these two effects separately.

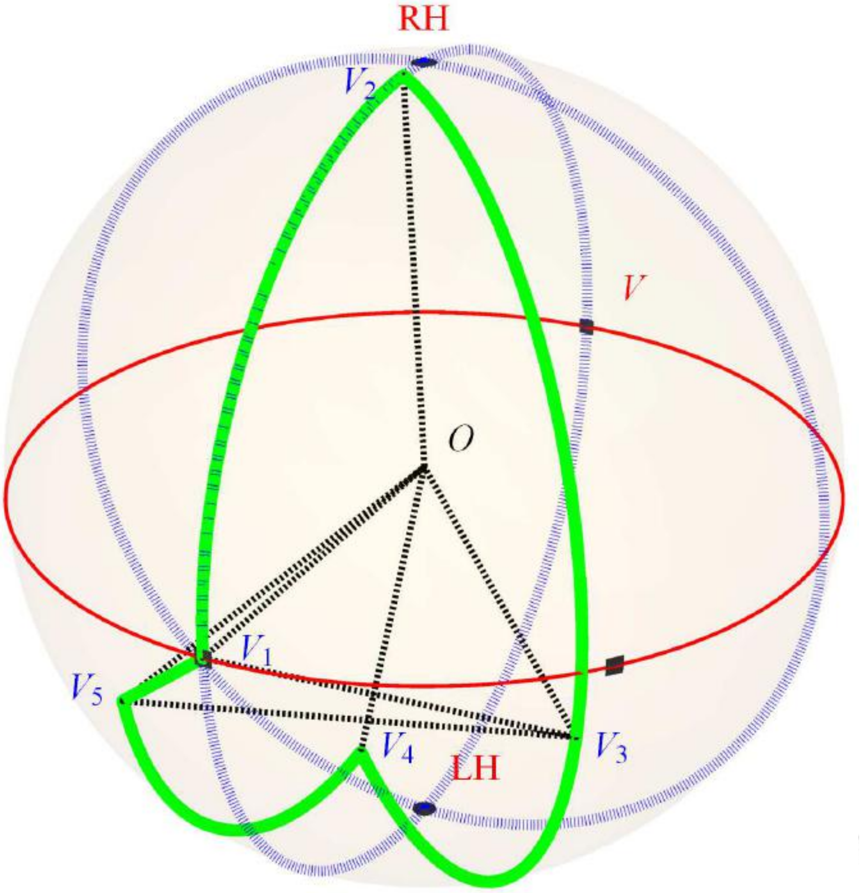

Figure 29: Imperfect trajectory on the Poincaré sphere due to a phase retardance different from $\pi/2$ of the QWP's. The defaults have been exaggerated for the sake of clarity to $\epsilon_1 = -1/15$ and $\epsilon_2 = 1/15$. The 5 vertices used to calculate the subtended solid angle are represented in blue.

3.3 APPLICATION TO ATOM INTERFEROMETRY

.

Now that we have quantitatively described the different parameters which modify the total phase shift produced by this apparatus, let us examine how it was implemented in an atom interferometer and what would be its advantages and its limits for two applications: a continuous phase shifter for a single interferometer and a simultaneous phase shifter for a dual species interferometer.

3.3.1 Atomic fringes swept by the Pancharatnam phase shifter

Once the Pancharatnam phase-shifter was operational, we used it on our atom interferometer to scan the atomic fringes. The result is presented in Fig.30. We obtained fringes with high visibility (72 %) which is similar to the fringes obtained by scanning the phase with mirror M3. Similarly to the optical interferometer, we observed a non linear dependence of the scan frequency which is very well described by the prism and tilt modulation model. The modulation value we obtained from the atom interferometer fringes is $u_M = 0.39(1)\,\mathrm{rad}$, which is consistent with the measurement performed using the optical Michelson interferometer. The slight difference can be attributed to a different combination of the two effects which can differ for the Bragg beam and the Michelson beam. In addition to the phase modulation, the angular deviation of the reflected Bragg beam can have an effect on the atomic diffraction process and we are going to describe them now.

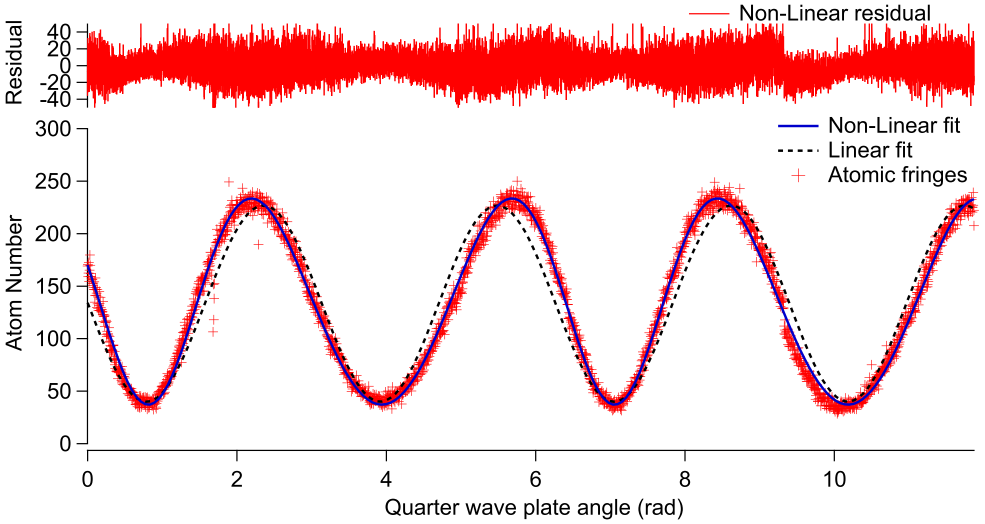

Figure 30: Atomic fringes scanned with the Pancharatnam phase-shifter. The number of atoms at one output of the Mach-Zehnder type interferometer is plotted as a function of the rotating quarter wave plate angle. The atomic period is approximately half the rotation period, as expected. A non-linear modulation is clearly visible in the difference of slope around 4 and 7 rad and is well reproduced by a fitting procedure including a modulation of the instantaneous frequency. For comparison, a linear fitting is also represented, but its residual has not be plotted to emphasize the quality of the non-linear fit. A modulation of the residual amplitude is clearly apparent but can be partly explained by the Poissonian statistic of atomic counting

Interferometer visibility dependence

We have seen that the prismatic shape of the QWP induced a dynamical phase shift. Doing so, we neglected the angular deviation of the reflected beam. This deviation can change the mean wavevector of the third diffraction grating $\vec{k}_3 = \left(\vec{k}_3^i - \vec{k}_3^r\right)/2$, where $\vec{k}_3$ is the laser wavevector and the superscript denote the incident and reflected beams. This changes the spatial superposition of the interferometer arms which degrades the visibility[12] and modulate the interferometric signal. From the angular deviation in a prism under quasi normal incidence $D = (n-1)\,\alpha - n^2\alpha^2 i$ where α is the apex angle and i the angle of incidence, we get the projection of the mean wave-vector on the vertical plane, in the direction orthogonal to the laser beam:

$$k_3^y \simeq \frac{k_L}{2} \sin\left(i_0 + 2\,(n-1)\,\alpha - n^2\alpha^2 i\right) \tag{68}$$

where i_0 is the angle between the two beams without the phase shifter and we have assumed that the fixed QWP plate does not deflect the beam because the interferometer alignment takes into account this deflection. Because, in our interferometer, the visibility depends sharply on the wavevector difference between the three standing waves [83], we can express the visibility $\mathcal{V}$ as a function of the incidence angle:

$$\mathcal{V}(i) = \mathcal{V}_0 \left|\mathrm{sinc}\left[h_D k_L \sin\left(i_0 + 2\,(n-1)\,\alpha - n^2\alpha^2 i\right)\right]\right|$$

where $h_D \sim 3\,\mathrm{mm}$ is the height of the detection region. For example, in a pessimistic assumption, if we consider that the mean visibility we measured, 72 %, is entirely due to i_0 and the constant deviation $2\,(n-1)\,\alpha$ and that the maximum visibility $\mathcal{V}_0$ is closer to 80 %, we can approximate $i_0 \sim 4\,\mu\mathrm{rad}$. With the prism angle value measured in Sec. 3.2.4 and typical values of $i \sim 10\,\mathrm{mrad}$ we find a modulation of the visibility of about 2 % which is not statistically resolved on Fig.30.

3.3.2 Phase control in a single interferometer

The Pancharatnam phase shifter can be used to control the phase shift of an atom interferometer. Indeed, to obtain an accuracy of $1\,\mathrm{mrad}$ on the total phase shift, one would have to control the term $2\omega t$ to at least $0.5\,\mathrm{mrad}$. This means that the angular position of the RQWP has to be controlled with an accuracy better than $0.25\,\mathrm{mrad}$. Additionally, each modulating term of eq. (67) would decrease the accuracy. The main effect on the Pancharatnam phase $\phi_P(t)$ comes from the QWPs' retardances accuracy ϵ_1 and ϵ_2. To keep its modulation amplitude below 10 % of the angular accuracy, ϵ_i have to be better than $\frac{1}{6000}$. This is reachable since recent techniques in retardance measurement have an accuracy better than $\frac{1}{4000}$ [165] or even $\frac{1}{10^4}$ [166]. As for the

---

[12] This is simply due to the fact that the interferometer signal is integrated in the directions orthogonal to the propagation axis. This washes out the fringes if there is a non zero wavevector difference in these directions between the two outputs of the interferometer.

dynamical phase $\phi_{dyn}(t)$, the prismatic angle α and distance from the rotation axis δr have to be simultaneously considered. For a realistic $\delta r \sim 1\,\mathrm{mm}$, the RQWP apex angle is constrained below $0.1\,\mu\mathrm{rad}$ which seems unrealistic. It is therefore necessary to design a rotating mount whose rotation center is precisely adjusted on the atoms. Furthermore, the second part of the dynamical phase depends on the product $\gamma\beta$ and the QWP's thickness $\bar{e}$. Typical values of $0.5\,\mathrm{mrad}$ are easily reachable with a careful alignment which leads to a modulation amplitude of $1.5\,\mathrm{mrad}$. Thus, this effect can be reduced below the desired accuracy with the use of an autocollimator.

This phase shifter can be used to rapidly measure an induced (or offset) phase shift ϕ_{int} in a sequential interferometer. Indeed, switching the interferometric phase ϕ_d by π allows to alternatively measure the interferometric signal around the two highest phase sensitivity regions. To perform these switches, the RQWP needs to be rotated by $\frac{\pi}{2}$ between two cycles. Motorized rotator with high accuracy are commercially available[13] with rotation speed up to $15\pi\,\mathrm{rad/s}$ which would be compatible with a 30 Hz repetition rate.

3.3.3 Dual-species simultaneous phase control

An interesting feature of this phase shifter is its almost perfect independence on spatial coordinates and on wavelength. As long as the QWP's produce an homogeneous phase shift on its aperture, atoms located at different positions in the laser beam will acquire the same phase shift. Similarly, if the trajectories on the Poincaré sphere of the polarization states of two different lasers of different wavelength are identical, the geometric phase shift experienced by the different atomic species interacting with each wavelength will be identical. Several types of such achromatic QWP have been developed based on different principles: combination of two materials having different birefringent dispersion [167] or identical materials with well chosen angle between their principal axes [168], etc [169]. A dual species control relaxes the achromatic condition because it only requires a $\pi/2$ retardance at two well determined wavelengths. QWP's presenting such characteristics can be realized with a combination of two different thickness materials but these wave plates present, on average, higher sensitivity to temperature[14] and to the angle of incidence, which imposes more stringent conditions on alignment.

Description

In dual species experiment, each atom interferometer phase shift is a complex combination of the diffracting laser's phase, of residual Zeeman effect, dynamical phase along the species' specific trajectory and optical shifts including cross-talks. When Bragg's pulses are used, the two standing wave phases can be scanned simultaneously only by controlling the retro-reflecting mirror position. However the mirror

---

[13] The 'HO Series Slotless Motors' of applimotion.inc uses a similar rotation encoder. It is however magnetic but the phase shifter does not have to be close to the atom interferometer arms.

[14] Thermo-optic coefficients at two different wavelength can be different and it needs to be taken into account in the design of the two materials.

is also the reference frame to which the accelerations experienced by the atoms are compared to. Thus, phase shifting by mirror control seems incompatible with vibration reduction and absolute positioning. Furthermore, when the optical wavelength are different, the induced phase shift is not identical for the two species. The Pancharatnam phase-shifter could be used to solve these issues by providing an identical control on the total phase for both species.

Lissajous ellipses

When the signal of interest is the differential phase between the two interferometers, the interferometric signal of one species can be plotted with respect to the signal of the other species to get what is called Lissajous ellipses. To scan this ellipse, it is sufficient to have vibrations on the reflecting mirror which produces common phase shift but can also add non common phase noise. The Pancharatnam dephasor could be used to uniformly scan the ellipse at controlled phase difference, reducing the time needed to acquire an ellipse and the bias [170] induced by this measurement process.

3.4 CONCLUSION

In this chapter, we presented briefly the concept of geometric phase, its independence on the state path in Hilbert space and its application to polarization states of an electromagnetic wave: the Pancharatnam phase. This lead us to present the Pancharatnam phase-shifter we developed for our atom interferometer. Its characterization with an initial optical interferometer showed an additional phase modulation to the theoretical ideal value of $2\omega t$. A finer description of the experimental defects allowed us to point out the main parameters (incidence angle, prismatic shape and birefringence accuracy) which influence the induced phase shift. The measured modulation amplitude of $0.35\,\mathrm{rad}$ was well described by our model. Then, we applied this phase shifter to atom interferometry and recorded interferometric fringes displayed on Fig.30. The interferometric signal did not present higher phase noise compared to the classical method and had the advantage of being unbounded. As expected, a 2π rotation of the RQWP induced a phase shift of 4π. Because of our setup defects, we observe a modulation of the total phase with an amplitude of $0.39\,\mathrm{rad}$, which compares well to the value obtained with the similar arrangement of the optical Michelson interferometer. To reduce this phase modulation, one should first decrease the distance between the rotation axis and the laser region interacting with the atoms. Greater care must also be taken on the orthogonality between the QWP faces and the Bragg laser beams. Finally, the example of two prospective applications was described: the accurate control of an interferometer's phase and a common phase-shifter for dual species Bragg interferometer.

4 LITHIUM TUNE-OUT WAVELENGTH

Contents

In this chapter, I will summarize the AC stark shift experienced by a polarized atom in presence of an external electric field. This will lead me to present the "tune-out wavelength" for which it vanishes. Historically, another particular wavelength: the "magic" wavelength was used as it allows to cancel the differential light shift experienced by two different atomic sublevels. A short description of a theoretical model based on second order perturbation theory will allow us to exhibit and discuss these wavelengths for the particular case of ^{7}Li. These wavelengths are interesting in metrological apparatus as well as in experimental tests of QED calculations which is the reason why a lot of experimental efforts were made recently to measure them accurately. Atom interferometers are well fitted for these measurements which motivated us to implement our own experimental setup. I will present it briefly and focus on the parameters which determine directly our measurement accuracy and sensitivity. Finally, I will present our experimental results which allowed us to measure ^{7}Li "tune-out" wavelength of the $|F = 2, m_F = 2\rangle$ state with an accuracy of a few tens of fm which compares well with other recent experiments. Additionally, the power dependence of the measured stark shift will be discussed and the influence of hyperpolarizability will be subject to a preliminary evaluation.

4.1 TUNE-OUT WAVELENGTH

4.1.1 Electric polarizability of alkali atoms

The spectral response of a particle assembly to an external perturbation has been used in a large variety of domains, providing information on the collective (stress deformation in elasticity theory, phonons dispersion relations in crystals, electrical conductivity in metals) and individual (refractive index of gases, shifting and splitting of spectral lines induced by electric (Stark) and magnetic (Zeeman) effects) behaviors. Dynamic polarizability is the restriction of this method to the electronic cloud response function of an atom or a molecule under an external oscillating electric field. In the classical theory, in presence of an external electric field $\vec{E}$, the induced total dipole moment $\vec{P}$ of the cloud can be expanded in a power series of the instantaneous electric field[1]. This polarization vector represents the electronic cloud's ability to deform under the electric field's influence. The interaction changes the system's energy by an amount δU, which, for a centrally symmetric system is given by:

$$\delta U = -\frac{\alpha(\omega)\left\langle |E|^2 \right\rangle}{2} \tag{69}$$

where $\alpha(\omega)$ is the polarizability and $\left\langle |E|^2 \right\rangle$ is the electric field mean squared amplitude over a period. The simplest system that can be considered is probably the hydrogen atom in an homogeneous electric field. Assuming an electronic density distribution spherically symmetric only displaced from equilibrium by the external field leads [171] to the simple expression of hydrogen's polarizability:

$$\alpha_H^{(1)} = \frac{3}{4} a_0^3$$

where a_0 is Bohr's radius and the polarizability is expressed in its volumic expression which is related to its S.I expression by $\alpha = \alpha_0/(4\pi\epsilon_0)$. This result gives an approximate[2] order of magnitude but calculations from first principles, using quantum mechanics, lead to the exact value of $\frac{9}{2} a_0^3$. For more complex systems, such as atoms or ions, the polarizability can be calculated [172] by considering the dipole approximation Hamiltonian:

$$\hat{H}_{int} = -\sum_i q_i \hat{\vec{E}}(\vec{r}_i, t) \cdot \hat{\vec{r}}_i$$

---

[1] In some systems, such as ferroelectric materials, this polarization vector also depends on the electric field's history due to a spontaneous polarization whose direction depends on the surrounding environment.

[2] It is possible to refine this model by including density deformations.

where $\vec{E}(\vec{r},t) = E_0/2\left[\vec{\epsilon}e^{-i(\omega t-\vec{k}\cdot\vec{r})} + c.c\right]$ is the electric field (amplitude E_0, polarisation $\vec{\epsilon}$ and frequency ω) and $(q_i,\vec{r}_i)$ are respectively the charge and position of each particle. The summation is performed over all the charged particles in the system. When the electric field frequency is far from resonance, this interaction Hamiltonian can be treated as a perturbation of an initial Hamiltonian $\hat{H}_0$ which takes into account the kinetic term as well as the inter particles interaction. Because $\hat{H}_0$ commutes with the parity operator and the interaction Hamiltonian $\hat{H}_{int}$ is uneven, transition coefficients $\left|\langle b|\hat{H}_{int}|a\rangle\right|$ will be non-zero only between states of different parity. Applying the perturbation theory to the total Hamiltonian $\hat{H} = \hat{H}_0 + \hat{H}_{int}$ gives the second order Stark shift [173] of a non degenerate ground state $|a\rangle$:

$$\delta U(\omega) = -\frac{E_0^2}{4\hbar}\sum_b \Re\left(\frac{\left|\langle b|\vec{\epsilon}\cdot\vec{d}|a\rangle\right|^2}{\omega_b-\omega_a-\omega-i\gamma_{ba}/2} + \frac{\left|\langle a|\vec{\epsilon}\cdot\vec{d}|b\rangle\right|^2}{\omega_b-\omega_a+\omega+i\gamma_{ba}/2}\right) \tag{70}$$

where $\Re$ denotes the real part, $\omega_b = E_b/\hbar$ ($\omega_a = E_a/\hbar$) is the eigenstate initial energy in frequency unit, $\gamma_{ba} = (\gamma_a+\gamma_b)/2$ is the mean transition linewidth and $\vec{d} = \sum_i q_i\vec{r}_i$ is the total electric dipole. From eq. (69), it is straightforward to recognize in eq. (70) the scalar dynamical polarizability of neutral atoms $\delta U(\omega) = -\frac{\alpha^{(2)}(\omega)}{4}E_0^2$ where a factor $1/2$ comes from the $\cos(\omega t)^2$ time average.

For Alkali atoms, the electronic shell structure allows to separate the total atomic state into two parts: the core made of a series of closed shells and the single valence electron. When the electric field amplitude ($\sim 10^6\,\mathrm{V\,m^{-1}}$ for 1 *W* laser power focused on a $6\,\mu\mathrm{m}$ waist) is much lower than the inner core electric field ($\sim 10^{12}\,\mathrm{V\,m^{-1}}$), the inner shell frequency dependence is negligible. In this regime, only the valence electron's state contributes to the dynamic polarizability which is developed:

$$\alpha^{(2)}(\omega) \simeq \alpha^{(2)}_{core} + \alpha^{(2)}_v(\omega)$$

where $\alpha^{(2)}_{core}$ denotes the second order constant contribution of the inner shell and $\alpha^{(2)}_v(\omega)$ is the dynamic polarizability which can be decomposed with a formula similar to eq. (70) where the full atomic states are replaced by the electronic state of the valence electron.

4.1.2 Hyperfine coupling

One can develop $\alpha^{(2)}_v(\omega)$ by taking into account the fine and hyperfine coupling of the valence electron with its spin and the nucleus spin. Recalling that the Wigner-Eckart theorem make it possible to factorize matrix element of spherical tensors into two components, one independent of the angular momentum projection and one Clebsch-Gordan coefficient. Also recalling that the electric dipole does not couple to the nuclear spin, it is possible to express the total polarizability as a sum of three tensorial components [173]:

$$\begin{aligned}\alpha^{(2)}_{\nu,n,J,F,m_F}(\omega) &= \Big[\alpha^{(s)}_{n,J,F} - V\cos\chi\frac{m_F}{2F}\alpha^{(\nu)}_{n,J,F} \\ &+ \left(\frac{3\cos^2\xi - 1}{2}\right)\frac{3m_F^2 - F(F+1)}{F(2F-1)}\alpha^{(t)}_{n,J,F,}\Big]\end{aligned} \tag{71}$$

where $\alpha^{(s,\nu,t)}$ are the irreducible scalar (s), vector (ν) and tensor (t) components, implicitely dependent on ω, of the polarisability. With the electromagnetic wave vector $\vec{k}$ and the quantization axis $\vec{e}_B$, the angle χ is defined by $\cos\chi = \left|\vec{k}\cdot\vec{e}_B\right|$, V is the fourth Stokes parameter of the light and characterizes the degree of circular polarisation[3]. And $\cos\xi = \vec{\varepsilon}\cdot\vec{e}_B$ is the projection of the polarisation vector onto the quantization axis. Here, the usual spectroscopic notation have been used with n, the quantum number corresponding to the angular momentum operator $\hat{\vec{L}}$, J corresponds to the fine structure composition $\hat{\vec{J}} = \hat{\vec{L}} + \hat{\vec{S}}$, where $\hat{\vec{S}}$ is the electron's spin and F corresponds to the hyperfine structure $\hat{\vec{F}} = \hat{\vec{J}} + \hat{\vec{I}}$, with $\hat{\vec{I}}$ the nuclear spin. The different irreducible components are given by:

$$\begin{aligned}\alpha^{(s)}_{n,J,F} &= \frac{1}{\sqrt{3(2F+1)}}\,\alpha^{(0)}_{n,J,F} \\ \alpha^{(\nu)}_{n,J,F} &= -\sqrt{\frac{2F}{(F+1)(2F+1)}}\,\alpha^{(1)}_{n,J,F} \\ \alpha^{(T)}_{n,J,F} &= -\sqrt{\frac{2F(2F-1)}{3(F+1)(2F+1)(2F+3)}}\,\alpha^{(2)}_{n,J,F}\end{aligned} \tag{72}$$

with

$$\begin{aligned}\alpha^{(K)}_{n,J,F} &= (-1)^{K+F+1}(2F+1)\sqrt{2K+1} \\ &\sum_{n',J',F'}(-1)^{F'}(2F'+1)\begin{Bmatrix}1 & K & 1\\ F & F' & F\end{Bmatrix}\begin{Bmatrix}F & 1 & F'\\ J' & I & J\end{Bmatrix}^2 \\ &\frac{1}{\hbar}\mathcal{R}e\left(\frac{1}{\omega'-\omega-i\gamma'/2} + \frac{(-1)^K}{\omega'+\omega+i\gamma'/2}\right)\left|< n', J'\|d\|n, J >\right|^2\end{aligned}$$

where $\omega' = \left[E_{n',J',F'} - E_{n,J,F}\right]/\hbar$ is the energy difference between hyperfine states in frequency units and $\gamma' = \left[\gamma_{n',J',F'} + \gamma_{n,J,F}\right]/2$ are the mean linewidths of the coupled levels. $|< n', J'\|d\|n, J >|$ are the irreducible dipole matrix elements. It is interesting to note that, when the hyperfine coupling is taken into account, hyperfine levels of alkali's groundstates, for which $J = \frac{1}{2}$, can have different polarizabilities[4] due to the tensor component which is non-zero as can be seen in the pre-factor of $\alpha^{(T)}$. This comes from the coupling with the nucleus spin which leads to a total spin F eventually different from 0 and $\frac{1}{2}$.

---

[3] In practice, $V\cos\chi = i\left(\vec{\varepsilon}^* \times \vec{\varepsilon}\right)\cdot\vec{e}_B$

[4] This effect is one of the main limit of atomic clock accuracy as is reviewed in [174]

4.1.3 Two particular wavelengths

The energy difference between two hyperfine states of alkali atoms can therefore be expressed with the dynamical polarizability:

$$\begin{aligned}\delta U\left(\omega, E_0, \epsilon, \vec{e}_B\right) \;&=\; \hbar\left(\omega_{n,J,F_1,m_{F_1}} - \omega_{n,J,F_2,m_{F_2}}\right)\\ &\quad - \left(\alpha^{(2)}_{\nu,n,J,F_1,m_{F_1}} - \alpha^{(2)}_{\nu,n,J,F_2,m_{F_2}}\right)\frac{E_0^2}{4}\\ &\quad - \left(\gamma^{(4)}_{\nu,n,J,F_1,m_{F_1}} - \gamma^{(4)}_{\nu,n,J,F_2,m_{F_2}}\right)\frac{E_0^4}{64} \qquad (73)\end{aligned}$$

where we have explicitly indicated the dependence in the electric field parameter only in the energy difference and we have purposely added the hyperpolarizability, usually denoted by γ for later discussion. To reduce the Stark shift induced by the electric field amplitude, one can look for states which have exactly the same polarization. As can be seen from eq. (71), it is automatic when the two states are from the same hyperfine manifold $F_1 = F_2$ and have opposite m_F projections. For this example, the electric field has to be polarized along the quantization axis to ensure that the vector component difference does not contribute to the polarization difference. But it is also possible[5] to use the field frequency as an adjustable parameter which, because of the sign difference in the real part of $\alpha^{(K)}_{n,J,F}$, can either cancel the polarization difference between the two states or the dynamic polarization itself. These two situations correspond respectively to the so-called 'magic' wavelengths and 'tune-out' wavelengths.

Alkali's 'tune-out' wavelength

For the ground states $^2S_{1/2}$ of alkali atoms, it is straightforward to get an estimate of the 'tune-out' wavelength. To do so, let us consider only the first two excited states $^2P_{1/2}$ and $^2P_{3/2}$ contributions in the sum eq. (70). These contributions account for more than 95 % of the total polarizability [175]. Because the fine splitting of the excited states is much larger than the hyperfine splittings and the ground state fine splitting, we will neglect them in this discussion. Additionally, the level linewidths are negligible compared to the detuning $\omega - \omega'$ which simplifies the real part. In the end, the Stark shift of the ground state simplifies to:

$$\delta U = -\frac{E_0^2}{2\hbar}\left[\frac{d_1^2\omega_1}{\omega^2 - \omega_1^2} + \frac{d_2^2\omega_2}{\omega^2 - \omega_2^2}\right] \qquad (74)$$

where ω_i corresponds to the Di line frequency[6] and d_i is the associated dipole transition matrix elements. For alkali atoms the first two exited states corresponds to

---

[5] In particular when specific hyperfine substates are interesting due to their identical first order Zeeman coefficients or low hyper-polarizabilities.

[6] Traditionally, the $^2S_{1/2} \longrightarrow {}^2P_{1/2}$ transition is called D1 line and the $^2S_{1/2} \longrightarrow {}^2P_{3/2}$ transition is called D2 line

$J_1 = 1/2$ and $J_2 = 3/2$ which is why the transition strength ratio between the D2 line and the D1 line is equal to $\sqrt{2J_2+1}/\sqrt{2J_1+1} = \sqrt{2}$. Therefore, eq. (74) simplifies to:

$$\delta U = -\frac{E_0^2 d_1^2}{2\hbar}\left[\frac{\omega_1}{\omega^2-\omega_1^2} + \frac{2\omega_2}{\omega^2-\omega_2^2}\right] \tag{75}$$

To find the 'tune-out' wavelength, i.e the wavelength which cancels the polarizability, one can use the fact that the fine splitting $\Delta_{FS} = \omega_2 - \omega_1$ is much smaller than the optical frequencies ω_i. The solution to $\delta U(\omega) = 0 \, \forall E_0$ can be approximated by:

$$\omega_{tune-out,approx} = \omega_1 + \frac{\Delta_{FS}}{3} \tag{76}$$

which supports a geometrical approach consisting in finding the barycentre between two weights separated by Δ_{FS} with one of them twice as heavy as the first one.

Alkali's 'magic' wavelength

Similarly, one can give an approximate value of the 'magic' wavelength of the two groundstate hyperfine levels, neglecting the hyperfine structure of the excited states. The relative Stark shift between the states $|^2S_{1/2}, F = I - 1/2>$ and $|^2S_{1/2}, F = I + 1/2>$, where I is the nuclear spin, is:

$$\delta U = -\frac{E_0^2 d_1^2}{2\hbar}\left[\frac{\omega_1}{\omega^2-\omega_1^2} + \frac{2\omega_2}{\omega^2-\omega_2^2} - \frac{\omega_3}{\omega^2-\omega_3^2} + \frac{2\omega_4}{\omega^2-\omega_4^2}\right] \tag{77}$$

where $\delta_{HFS} = \omega_3 - \omega_1 = \omega_4 - \omega_2$ is the ground state hyperfine splitting and $\Delta_{FS} = \omega_2 - \omega_1 = \omega_4 - \omega_3$ is the excited states fine splitting. Solving $\delta U(\omega) = 0 \, \forall E_0$ for frequencies far from resonances in between the two D lines one gets the approximate 'magic' wavelength:

$$\omega_{magic,approx} = \omega_1 + \frac{\Delta_{FS}}{3} + \frac{\delta_{HFS}}{2} \tag{78}$$

which again compares well with an intuitive approach. The two 'tune-out' wavelengths for each hyperfine sublevel are separated by δ_{HFS}. If the polarizability of each sublevel has a similar Taylor development around its zero value, the first order terms will cancel each other in eq. (75) and the second order will only be zero precisely in between the two 'tune-out' wavelengths which corresponds to ω_{magic}.

Getting finer analytical expressions which take into account the excited state hyperfine structure and higher excited states becomes rapidly cumbersome. Which is why numerical solutions will now be used to discuss further the value of these wavelengths.

4.1.4 Theoretical calculations

Ab-initio evaluation of the 'tune-out' and 'magic' wavelengths using methods such as configuration interaction, many-body perturbation theory and coupled cluster methods have been extensively studied recently. But it is out of the scope of this chapter to describe these methods (see for example [176] for alkali 'magic' wavelength and [172] for a review of the numerical methods). However, using eq. (71), we were able to calculate accurately the dynamic polarizability of ^{7}Li close to the D lines because the contribution of highly excited state is small[7] compared to the contribution of the 2P states. We were careful to take into account the hyperfine structure, which is about 8 % (resp. 1 %) of the ^{2}P fine structure for the ground (resp. first excited) state. I will present here the obtained spectra and our theoretical evaluation of the 'tune-out' and 'magic' wavelengths for ^{7}Li different groundstate hyperfine levels.

Theoretical and experimental parameters

To calculate the irreducible components $\alpha^{(K)}_{\nu,n,J,F}$ we used:

1. **Irreductible dipole matrix components** $|< n', J' \| d \| n, J >|$ from numerical calculations of Safronova *et al.* [177].
2. **Frequency** ω' **of the hyperfine components of the** D1 **and** D2 **lines** from experimental values of Sansonetti *et al.* [178]
3. **Frequency** ω' **of the transitions toward higher states** from experimental values of Wiese *et al.* [179]. The hyperfine structure is not taken into account for these states whose contribution to the polarizability is small
4. **The transition linewidths for the** D1 **and** D2 **lines** experimentally measured by McAlexander *et al.* [180]

The transition linewidths for the higher excited states are neglected and we completed the scalar polarizability of eq. (71) by a small amount (2.09 au which is in good agreement with the value 2.04(69) au reported by [175]) to account for the small polarizability of the electronic inner shell. This was done by adjusting the zero frequency limit of the dipole polarizability to the experimental value of 164.2 au [71].

Dynamic Polarizability

The calculated polarizability of the two hyperfine levels $|F = 2, m_F = 2 >$ and $|F = 1, m_F = -1 >$ is represented on Fig. 31. The position of "tune-out" and "magic" wavelengths depends on the hyperfine state and on the laser polarization. Different configuration were chosen to discuss the influence of the polarization purity and direction on the "tune-out" wavelength:

---

[7] We have taken into account excited states up the 7P state which shifted the 'tune-out' wavelength by 0.3 MHz which was far below our experimental accuracy and indicated that higher levels would not shift significantly our result.

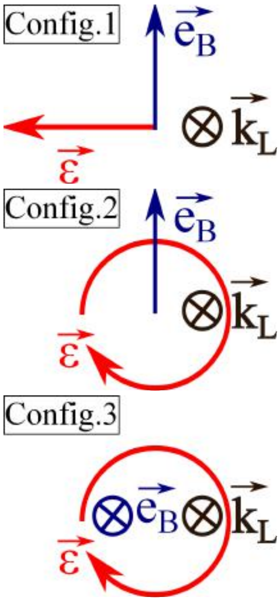

- Config.1: The laser polarization $\vec{\varepsilon}$ is linear and forms with the propagation direction $\vec{k}_L$ and the quantization axis $\vec{e}_B$ an orthogonal trihedral. This corresponds to linear-σ transitions with $V\cos(\chi) = 0$ and $\cos(\xi) = 0$.
- Config.2: The laser polarization is right handed and the propagation direction is orthogonal to the quantization axis. This corresponds to π and linear-σ transitions with $V\cos(\chi) = 0$ and $\cos(\xi) = 1/\sqrt{2}$. this configuration emphasizes the effect of the tensorial part.
- Config.3: The laser polarization is left handed and the propagation direction is collinear to the quantization axis. This corresponds to σ^- transitions with $V\cos(\chi) = 1$ and $\cos(\xi) = 0$. This configuration emphasizes the effect of the vectorial part.

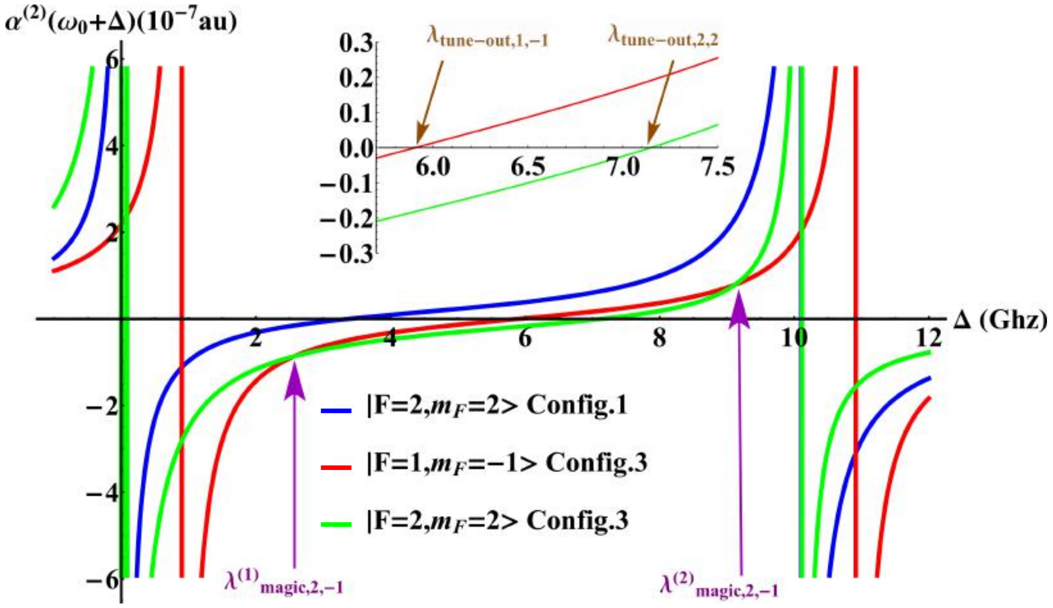

Figure 31: Lithium polarizability in atomic units as a function of the detuning Δ to the reference frequency ω_0 of the $|F = 2 > \longrightarrow |F' = 1 >$ transition. The laser is linearly polarized (Config. 1). The inset magnifies the region where the polarizability vanishes. Two 'tune-out' wavelengths are indicated which correspond to the $|F = 2, m_F = 2 >$ and $|F = 1, m_F = -1 >$ states. The frequency difference, 845.5 MHz, between the two 'tune-out' wavelengths corresponds approximately to the ground state hyperfine splitting $\delta_{HFS} = 803.5$ MHz.

The inset of Fig. 31 shows two "tune-out" wavelength of Config.3 which are labelled $\lambda_{tune-out,2,2}$ and $\lambda_{tune-out,1,-1}$. Additionally, two crossings between these two states dynamic polarizabilities exist and correspond to "magic" wavelengths which are labelled $\lambda^{(1)}_{magic,2,-1}$ and $\lambda^{(2)}_{magic,2,-1}$. Also the difference between Config.1 and Config.3 for a single state is clearly visible as the zero crossing is shifted by 5 GHz which indicates the large role played by the vector component $\alpha^{(v)}$. The calculated positions of these "tune-out" and "magic" wavelengths are listed in Tab. 5 and Tab. 6. Let us now discuss the effect of each polarizability components ($\alpha^{(s)}$, $\alpha^{(v)}$, $\alpha^{(t)}$) and of the laser polarization on these wavelengths.

^{7}Li *'tune-out' wavelength*

The tune-out wavelength values calculated by the simple approximation of eq. (76) gives:

$$\lambda_{tune-out,approx} = 670.971\,627\,3\,\mathrm{nm}$$

This value lies in between every set of wavelengths calculated for the hyperfine sublevels represented in Tab 5. At this wavelength, $10\,\mathrm{fm}$ corresponds to $7\,\mathrm{MHz}$. The tensor component $\alpha^{(t)}$ has a small ($30\,\mathrm{MHz}$ for $F = 2$ and $7\,\mathrm{MHz}$ for $F = 1$) effect on the 'tune-out' wavelength in each hyperfine manifold in Config.1. The difference between different F states is approximately equal, as expected, to the hyperfine structure. Config.2 confirms this effect of the tensor component as its pre-factor is maximum in this situation. However, it shows that a completely orthogonal polarization shifts the "tune-out" wavelength by a similar amount ($25\,\mathrm{MHz}$ for $m_F = 2$) which makes its value almost insensitive to small polarization residuals. However, the vector component $\alpha^{(v)}$ has a large effect inside each manifold ($3.7\,\mathrm{GHz}$ for $F = 2$ and $1.7\,\mathrm{GHz}$ for $F = 1$) as can be seen on Config. 3. This comes from the fact that the vector component derivative, close to the 'tune-out' wavelength, is much larger than the tensor and scalar components derivative (because of the $(-1)^K$ sign factor in eq. (72)) for $m_F \neq 0$ states. This large effect indicates that the quantization direction alignment orthogonal to the laser propagation direction has a large effect on the "tune-out" wavelength value.

Hyperfine sublevel	Config 1	Config 2	Config 3
$\|F = 2, m_F = 2 >$	670.9721146	670.9720793	670.9664622
$\|F = 2, m_F = 1 >$	670.9720793	670.9720968	670.9692737
$\|F = 2, m_F = 0 >$	670.9720677	670.9721027	670.9720677
$\|F = 2, m_F = -1 >$	670.9720793	670.9720968	670.9748373
$\|F = 2, m_F = -2 >$	670.9721146	670.9720793	$\emptyset$
$\|F = 1, m_F = 1 >$	670.9708450	670.9708507	670.9733984
$\|F = 1, m_F = 0 >$	670.9708565	670.9708450	670.9708565
$\|F = 1, m_F = -1 >$	670.9708450	670.9708507	670.968327

Table 5: Summary of the 'tune-out' wavelengths $\lambda_{tune-out}$ (nm) for the different hyperfine levels of ^{7}Li, between the two D lines. The different configuration corresponds to a combination of laser polarization and quantization axis described in the text. The empty value corresponds to a level which is only coupled to a single excited state which prevents the cancellation of the polarizability. These values are to be compared with the estimate $\lambda_{tune-out,approx} = 670.971\,627\,\mathrm{nm}$ of eq. (76). The calculated uncertainty on each of these values is $3.7\,\mathrm{fm}$.

^{7}Li *'magic' wavelength*

A set[8] of 'magic' wavelengths for Config. 3 between hypefine ground states of ^{7}Li are presented in Tab 6. They compare poorly with the approximate value of eq. (78):

$$\lambda_{magic,approx} = 670.971\,024\,\mathrm{nm}$$

which did not take into account the vector component. The value available in the litterature, 670.971 625 nm calculated by Safronova *et al.* [177] is also very different as it did not take into account the hyperfine structure. The first and second laser configuration do not have a 'magic' wavelength between the two D lines because the tensor component is too small, far from resonance, to compensate for the difference in scalar polarizability between different F sates. Interestingly, there is no 'magic' wavelength between the states $|F = 2, m_F = 1>$ and $|F = 1, m_F = \pm 1>$ because the vector part of the polarizability of the $|F = 2, m_F = 1>$ state is smaller than the one of $|F = 2, m_F = 2>$ which prevent the polarizabilities from being equal close to the D lines. Finally, the fact that there is only one 'magic' wavelength for the $|F = 2, m_F = -2>$ is due to the laser polarization choice which breaks the symmetry between different orientation states.

Hyperfine sublevels	Config. 3
$\vert F = 2, m_F = 2>$, $\vert F = 1, m_F = -1>$	$\left\{\begin{matrix} 670.9733291 \\ 670.9635046 \end{matrix}\right.$
$\vert F = 2, m_F = 1>$, $\vert F = 1, m_F = 0>$	$\left\{\begin{matrix} 670.9739934 \\ 670.9645429 \end{matrix}\right.$
$\vert F = 2, m_F = 0>$, $\vert F = 1, m_F = -1>$	$\left\{\begin{matrix} 670.9806735 \\ 670.9549675 \end{matrix}\right.$
$\vert F = 2, m_F = 0>$, $\vert F = 1, m_F = 1>$	$\left\{\begin{matrix} 670.9748475 \\ 670.9655926 \end{matrix}\right.$
$\vert F = 2, m_F = -1>$, $\vert F = 1, m_F = 0>$	$\left\{\begin{matrix} 670.9781470 \\ 670.9535853 \end{matrix}\right.$
$\vert F = 2, m_F = -2>$, $\vert F = 1, m_F = 1>$	670.9524365

Table 6: Summary of the 'magic' wavelengths λ_{magic} (nm) between different hyperfine levels of ^{7}Li and for different laser configurations. These values are to be compared with the simple estimate $\lambda_{magic,approx} = 670.971\,024\,\mathrm{nm}$ of eq. (78). The calculated uncertainty on each of these values is 5.4 fm.

4.1.5 Experimental measurements and applications

For alkali atoms, the exact position of the 'tune-out' wavelength is mainly linked to the ratio of the closest transition matrix elements. For example, the order of magnitude eq. (76) was derivated by assuming a ratio exactly equal to $\sqrt{2}$ and resulted in a 'tune-out' wavelength shifted from the D1 transition by $\frac{(\sqrt{2})^2-1}{(\sqrt{2})^2+1}\Delta_{FS}$. A recent de-

---

[8] I selected levels for which the 'magic' wavelength is far (> 1 GHz) from resonance. This is motivated by the approximation used to derive eq. (76) which is not valid close to resonance.

scription of 'tune-out' wavelengths link to transition ratio can be found in [181]. This method allows to measure accurately matrix elements of high excited states by measuring their ratios with lower lying states which are better known. The ratio itself is of interest because its deviation from $\sqrt{2}$ can be tested against relativistic corrections included in the modelling of many-body systems. Also, for smaller system, tune-out wavelength measurements compare with non-relativistic quantum electrodynamics calculations which might provide the opportunity to test different theoretical models.

Experimental protocols measuring or using these wavelengths are now going to be briefly reviewed.

Matrix elements evaluation

The most common method to determine atomic transition elements, and their ratio was excited states lifetime measurements with photoassociation spectroscopy [182]. The first 'tune-out' wavelength measurement providing an improved value matrix elements was done in Porto's group in 2012 [183]. They used a setup in which a dilute Bose Einstein Condensate of ^{87}Rb atoms pumped to the $|F = 1, m_F = -1 >$ was subject to a series of around ten pulses of standing light waves. Each pulse diffracted a small amount of the atoms into different $n \left(2\hbar\vec{k}_L\right)$ momentum states. This method enhanced the sensitivity to small light shift because, in the small depth limit, the population increases proportionally to $(n_p V_0)^2$, where n_p is the number of pulse and V_0 is the lattice depth, i.e the Stark shift. By changing the frequency of their lattice between the resonance frequencies with the 6P states and between the 6P and 5P states, for which transition matrix elements are accurately known by lifetime measurement, they measured two 'tune-out' wavelengths. These measurements lead to the transition matrix elements for the 6P states with an accuracy improvement of a factor 10. The same month, Holmgren *et al.*[184] published a measurement of the 'tune-out' wavelength for potassium at $\lambda_{tune-out,K} = 768.9712(15)\,\text{nm}$. They used a Mach Zehnder atom interferometer to measure the Stark shift induced on one arm. This resulted in a global differential phase shift which vanishes at the tune-out wavelength. Their experimental setup as well as fruitful discussions greatly inspired us for our own setup. More recently, ^{87}Rb transition ratio $R = 1.992\,21(3)$ was determined by Leonard *et al.*[185] with a similar technique increasing by two orders of magnitudes its accuracy. This value ruled out some less accurate theoretical calculations and remains the most accurate measurement made so far.

QED tests

In the context of QED tests, a 'tune-out' wavelength of a non-alkali atom state, a metastable helium state 2^3S_1, was recently calculated with high precision [186] and experimentally measured by Henson*et al.*[187]. They used a Bose Einstein condensate, magnetically trapped in their low field seeking $m_F = 1$ state, which were out-coupled from the trap with an RF sweep. Adding an optical potential, and the corresponding Stark shift, on the magnetic trap lead to a higher, or lower, confining trap depending on the positive (negative) sign of the shift. This resulted in an higher (resp. lower) outcoupling rate. By modulating the laser intensity they were able to detect the modulated outcoupling rate. The amplitude of the Fourier component at the modulation frequency provided an information on the depth of the Stark potential and allowed to measure the wavelength at which it vanishes: $\lambda_{tune-out,He^*} = 413.0938\,nm$. This measurement uncertainty lies two orders of magnitude lower than QED calculation.

Atom manipulation

These wavelengths can be used to simultaneously manipulate either different species [188] or different atomic states [189]. The different species manipulation protocol involves two optical lattices each tuned to one 'tune-out' wavelength of the two species. This choice allows to manipulate independently two co-located atomic clouds, each one interacting only with the lattice which is not 'tuned out' to it. This is useful to precisely control the environment seen by each species which allows either to cancel this contribution or to investigate the interaction difference of each species with the environment

The 'magic' wavelength choice for light shift insensitive atomic clocks has been abundantly discussed [190] and demonstrated (Cs [191],Sr[192],$^{40}Ca^+$[193]). They use 'magic' wavelength optical traps to increase the interrogation time of their atomic ensemble and achieve accuracy comparable to state-of-the-art clocks operating with atoms in free fall.

The use of state insensitive trapping have also been recently used by Li *et al.* [194]. By tuning the trapping frequency to a 'magic' wavelength, they prevented decoherence between two collective states corresponding to a ground and a single excited Rydberg state. This allows to increase the lifetime of their atomic memory which lead to deterministic atom-light entanglement.

Tune-out wavelength

The atomic light shift induced by an external oscillating electric field is given, to second order, by the dynamic polarizability (eq. (71)). For ^{7}Li $|F = 2, m_F = 2>$ state we expect it to vanish at the so-called "tune-out" wavelength:

$$\lambda_{tune-out,Config.1,F=2,m_F=2} = 670.9721146(37)nm$$

In frequency unit, it corresponds to $\Delta_{2,2,theo} = 3.3844\,GHz$ to the blue of the ^{7}Li $F = 2 \rightarrow F^{'} = 1$ transition. The exact value of this wavelength provides an information on the transition strengths and is useful to test ab-initio theories. For other atomic species, it was recently measured with $32\,fm$ accuracy for ^{87}Rb using atom interferometry.

4.2 EXPERIMENTAL SETUP

To measure the 'tune-out' wavelength of ^{7}Li which lies between the two D lines (see Tab. 5), we implemented a setup in which a laser beam is focused on one of the two paths in our interferometer (see Fig. 32).
The Stark shift experienced by the atom on this path can be expressed as :

$$\phi_{F,m_F} = -\int_{-\infty}^{\infty} \frac{\alpha^{(2)}_{F,m_F}}{4\hbar} E_0^2(t)\, dt$$

where the time dependent electric field amplitude is correlated to the atom classical trajectory. For an atom having a velocity $\bar{u}$ crossing a Gaussian intensity distribution it is:

$$E_0^2(t) = \frac{4\eta P_L}{\pi w_0^2} \exp^{-\frac{2(\bar{u}t)^2}{w_0^2}}$$

where $\eta = \mu_0 c \sim 377\,\Omega$ is the vacuum's impedance, w_0 is the laser beam waist and P_L is the laser power. This leads to the following phase shift:

$$\phi_{F,m_F}(\omega, P_L) = -\frac{\eta P_L}{\sqrt{2\pi} w_0 \hbar \bar{u}} \alpha^{(2)}_{F,m_F}(\omega) \tag{79}$$

The laser waist must be chosen smaller than the distance between the two arms and larger than the width of the atomic beam to produce an homogeneous phase shift on only one arm. For example, a laser power of $25\,mW$ focused on a $50\,\mu m$ waist and a polarizability which, close to the 'tune-out' wavelength depends on the detuning with a slope of approximately[9] 10^3 au/MHz we can estimate the phase shift of eq. (79) to 18 mrad/MHz. Therefore, the MHz sensitivity seems reachable since phase shifts of the order of the mrad have already been measured with our interferometer.

In the remainder of this section, we will focus on the technical implementation of this interaction region.

4.2.1 Optical setup

To be able to measure the 'tune-out' wavelength with a high accuracy, the laser setup has to meet several conditions:

- The laser frequency has to be known with an accuracy better than a few MHz.
- The laser frequency has to be stabilized down to 1 MHz during an interferometric sweep which lasts a few s.

---

[9] The conversion coefficient from atomic unit to SI units is $1/\left(4\pi\epsilon_0 a_0^3\right)$, where ϵ_0 is the vacuum's dielectric constant and a_0 is Bohr's radius.

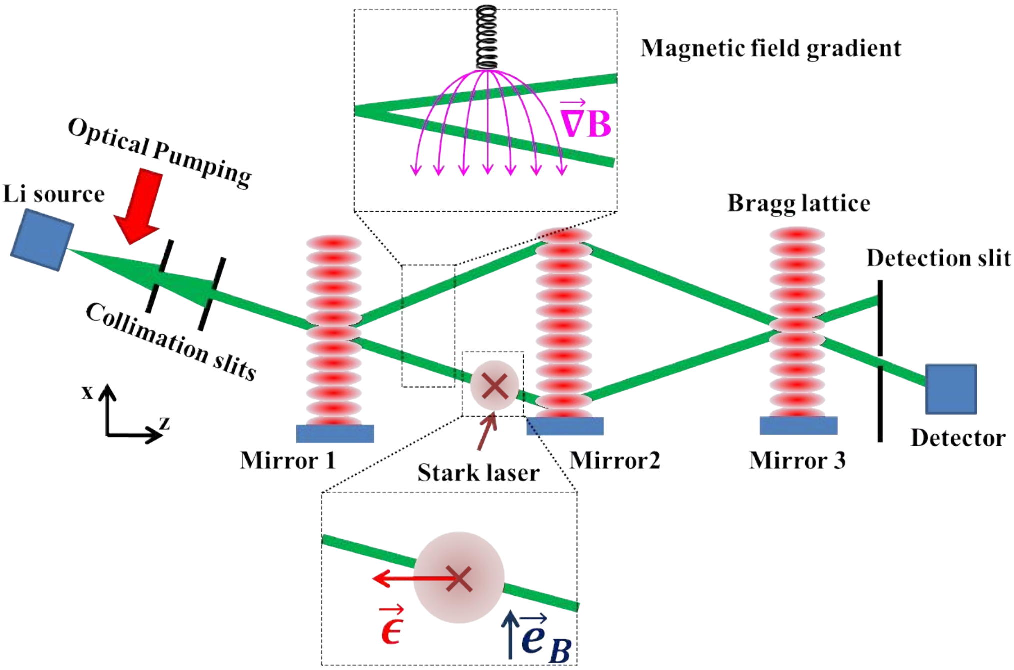

Figure 32: Schematic representation of the interferometer for the 'tune-out' wavelength measurement. In addition to the interferometer described on Fig. 4, an optical pumping stage, located between the skimmer and the collimation stage, and the corresponding magnetic gradient (see Sec.4.2.3) are represented. The interaction region with the Stark laser focused on the 'right' path is represented with the corresponding polarization and quantization axis.

- The laser frequency has to be swept around +3.4 GHz from the D1 frequency.
- The laser power available on the atoms has to be at least 10 mW.
- The polarization has to be purified and orthogonally aligned to the quantization axis to prevent the vector component of the polarizability to shift the 'tune-out' wavelength. It corresponds to Config. 1 defined previously.

The final optical setup used to produce the laser beam shone on the atomic beam is schematized in Fig.33. It consists in a master laser which serves as a stabilized frequency reference and a higher power laser, labelled 'Stark' laser. The master laser is an external cavity diode laser DL100 manufactured by Toptica®, which has a linewidth specified below 300 kHz. Its frequency is locked via biased[10] saturated absorption to the blue (218 MHz) of the D1 transition $F = 1 \rightarrow F' = 2$. From the amplitude of the error signal, and the width of the transition, we can infer that the reference laser stability is better than 1 MHz at 1 s.

The Stark laser is an amplified external cavity diode laser from Sacher®. It provides around 160 mW after optical isolation. A weak beam (2 mW) of the Stark laser is superposed with a fraction of the master laser, on the same polarization and the produced beat note is detected by a fast photodiode. The Full Width at Half Maximum of the beat note in a 1 ms time span was smaller than 1 MHz which ensured a relative frequency measurement accuracy better than 1 MHz. The beat note frequency

---

[10] An acousto-optic modulator shifts the laser frequency before the absorption cell by a constant value

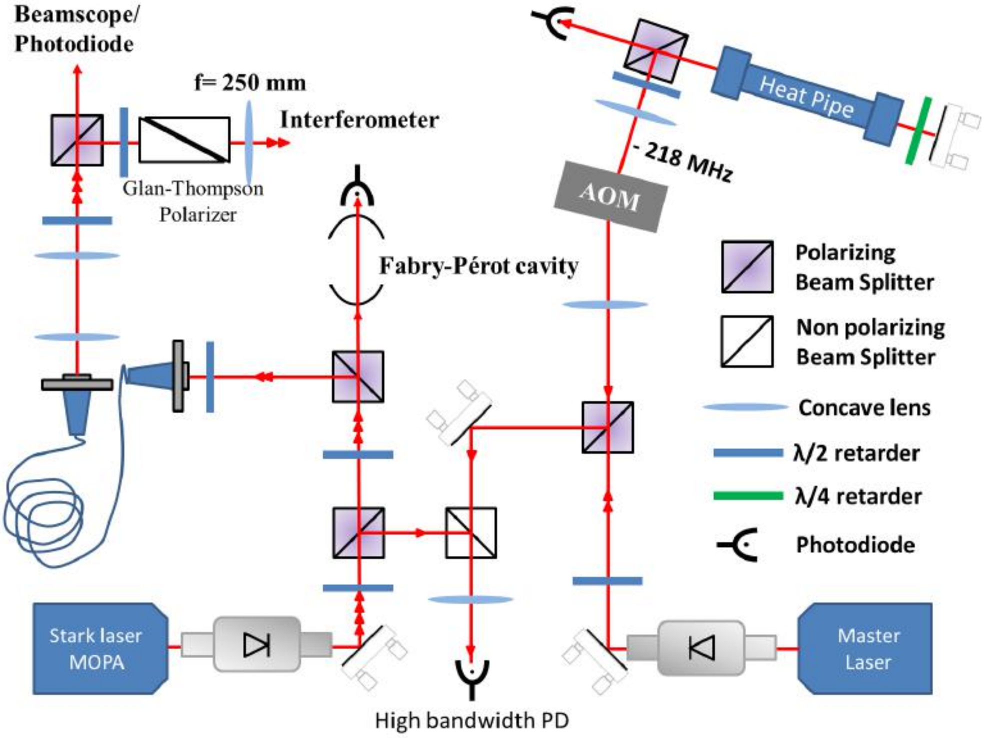

Figure 33: Schematic view of the laser system for phase shifting one arm of the interferometer. A master laser, locked to the blue (218 MHz) of the D1 line with saturated absorption is used as a frequency reference. The Stark laser is locked on a confocal Fabry-Pérot cavity $1-4$ GHz to the blue of the D1 line. A weak beam of the Stark laser is sent to a high bandwidth photodiode which records the beat note between the two lasers. The main beam is sent with a polarization maintaining fiber to the interferometer breadboard. On this breadboard, the laser beam is shaped, polarization purified with a Glan-Thompson polarizer and focused on one of the interferometric arms. A fraction of the power sent on the atomic beam is also monitored.

is limited below 3 GHz by our spectrum analyser[11]. Another weak beam of the Stark laser is sent to a confocal Fabry-Pérot cavity. The Stark laser frequency is locked on this cavity with a homodyne detection scheme. The cavity resonance frequency drifts on a time scale much larger than the time needed to record an interferometric signal which has little effect on the measured phase shift. We measured a typical drift of 8 MHz in 4 min and an averaged short time variance of 1 MHz at 1 s. We decided to monitor the frequency beat note to include this drift in our fitting procedure.

The remaining power of the Stark laser is injected into a polarization maintaining fiber, which keeps the power fluctuation below 3 % during a day. Finally, 90 % of the power is sent to a Glan-Thompson polarizer which filters the laser polarization just before the focussing lens and the viewport above the interferometer. A total power of around 40 mW was available at the entrance of the viewport which ensures a large enough phase shift.

---

[11] This justifies our 'biased' saturated absorption as well as the $F=2 \rightarrow F^{'}=2$ transition choice because we needed to have a frequency reference high enough to be able to monitor the beat note.

4.2.2 Laser's polarization and waist

Laser waist and divergence

Focusing a laser beam on only one arm of the two interferometers is a compromise between the field homogeneity across the interferometer arms, their spatial separation and the phase shift peak amplitude. Figure 34a represents the trapezoidal distributions of each arms atomic density along the Gaussian distribution of the laser intensity. To discuss this trade-off, I calculated the relative amplitude of the Stark phase induced by the velocity distribution in the interferometer and by the spatially dependent electric field amplitude. The result of this numerical calculation is represented on Fig. 34b, where the differential phase shift between the two arms is plotted as a function of the laser's center position X_0. We see that the larger the waist is, the higher is the phase shift. This results from the longer interaction zone (along the longitudinal direction) and the relatively small transverse overlap with the other interferometric arm. However, when we did the experiment, we were worried that a waist too large would reduce our sensitivity, which is why we aimed at a $60\,\mu m$ waist. In hindsight, we should have used a slightly larger waist.

We measured the size of the laser waist on the atomic beam by duplicating the focussing optics on the path to the monitoring photodiode. By using identical optical components separated by the same distances, we were able to estimate the waist to $w_0 = 61(2)\,\mu m$ and the Rayleigh length to $16\,mm$. We controlled the distance to the atomic beam better than a few mm. This was enough to ensure that the effective waist was known with a $10\,\%$ uncertainty which was necessary to keep the overlapping between the laser beam and the two atomic paths minimum. The maximum phase shift that can be experimentally induced between the two paths is $83\,\%$ of the theoretical value given by eq. (79).

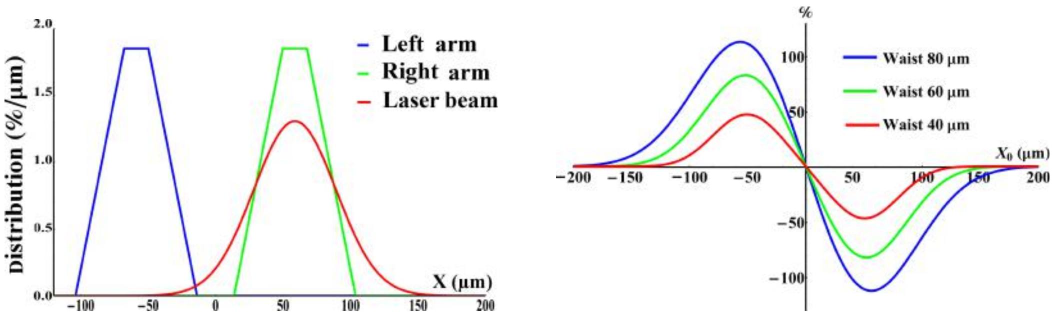

(a) Atomic and Intensity distribution

(b) Phase shift

Figure 34: **(a)**: Atomic distribution profiles and laser beam profile at the position of maximum path separation for the mean atomic velocity. The laser beam intensity has a small overlap with the left arm atomic beam which diminishes the differential phase shift.
(b) Percentage of differential phase shift plotted as a function of the laser beam center position for three different waists. The maximum ($100\,\%$) Phase shift corresponds to a monokinetic atomic beam interacting with a rectangular laser profile of $120\,\mu m$ width which does not overlap with the second arm.

Laser polarization axis

Using a Glan-Thompson polarizer, we aligned the laser polarization on the propagation direction (Z) of the atomic beam. This was done by aligning the reflected beam of the polarizer on the mechanical reference frame (MRF) of the optical table. This reference frame is aligned with the atomic reference frame (ARF) to approximately $17\,\mathrm{mrad}$.

The quantization axis was defined by a $1\,\mathrm{G}$ magnetic field produced along the (X) direction by 'Helmholtz' coils mechanically fixed on the MRF. This alignment was not as well controlled and is estimated at less than $90\,\mathrm{mrad}$. This is probably the main source of uncertainty on the angle between the laser polarization $\vec{\epsilon}$ and the quantization axis $\vec{e}_B$. However, it is not an issue because, as we will see in Sec.4.2.3, this can be quantified, and rejected, by performing differential measurement of the 'tune-out' wavelength for the two hyperfine levels $|F=2, m_F=2>$ and $|F=2, m_F=-2>$ for which the vector component changes sign.

4.2.3 Atom beam hyperfine sublevel

Because the atomic polarizability has a tensor component when the hyperfine structure is resolved (discussed in Sec. 4.1.4), we implemented an optical pumping scheme similar to the one described fully in [195] to be able to pump all the atoms in one or the other of the $F=2$ sublevels $|F=2, m_F=\pm 2\rangle$. This allowed us to cancel the systematic effect due to the residual vector component which is not zero when the laser polarization is not perfectly linear (as can be the case after transmission through a vacuum viewport with a small birefringence due to mechanical stress) or not perfectly orthogonal to the quantization axis (as discussed in Sec.4.2.2).

The principle of the optical setup is straightforward. A second extended cavity diode laser DL100 manufactured by Toptica® is frequency locked on the D2 transition $F=2 \rightarrow F^{'}=2$. A weak beam extracted from this laser is tuned to the repumping transition $F=1 \rightarrow F^{'}=2$ with an acousto-optic modulator in double pass configuration increasing the frequency by $803.5\,\mathrm{MHz}$ which corresponds to the groundstate hyperfine splitting. These two laser frequencies are superposed, circularly polarized, sent on the atomic beam (about $5\,mW$ of total power) and retro-reflected. Depending on the local magnetic field direction, which was controlled by three Helmholtz pairs under vacuum, the magnetic groundstates sublevels $|F=2, m_F=2>$ and $|F=2, m_F=-2>$ could be populated with a high efficiency. This stage was implemented before the collimation as photon absorption and emission broadens the atomic beam which is detrimental after the collimation stage.

To evaluate the residual population in the other sublevels, a small magnetic gradient was applied on the atomic path and is represented on Fig.32. When the different sublevels were significantly populated, the differential phases, proportional to $g_F m_F \mu_B \left|\vec{\nabla} B\right|$, accumulated by each sublevel washed out the interferometric signal.

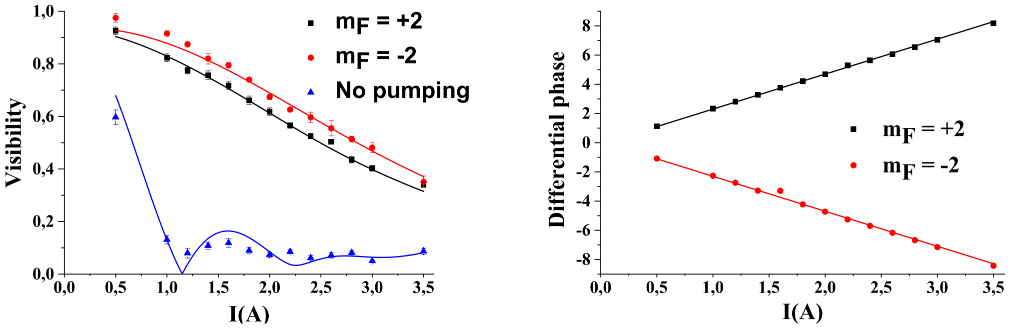

(a) Fringes visibility

(b) Fringes phase

Figure 35: Phase and visibility of the atomic fringes as a function of the coils' current. The lines correspond to a global fit leading to the populations presented in Tab.7 and the data points are much larger than their uncertainty. The visibility drops sharply when no pumping is implemented due to the difference (in amplitude and sign) between phases of every hyperfine sublevels. When optical pumping is implemented, this decrease is reduced and is now due to velocity spreading of the phase. The linearity of the mean phase and the absence of oscillations indicates a high pumping quality.

Comparing the visibility loss[12] as well as the mean interferometric phase when the optical pumping was ON and OFF allowed to extract the sublevels populations[13]. The measured visibility and phases are presented on Fig. 35 and the population estimates are summarized in Tab.7. Overall, the pumping efficiency is better than 95 %. As expected, the levels which have a residual population are the one closest to the pumped level ($|F = 2, m_F = -1 >$ in the case of the σ^- transitions) or polarized in the opposite direction ($|F = 2, m_F = 2 >$). This is due, respectively, to the dynamic of the pumping which empties last the neighbour state and to spin flips of the pumped atoms during their transit in the interferometer.

Hyperfine sublevel(s)	Population (%), σ^+	Population (%), σ^-
$\|F = 2, m_F = 2 >$	100^{+0}_{-4}	$0^{+2.2}_{-0}$
$\|F = 2, m_F = 1 >, \|F = 1, m_F = -1 >$	$0^{+1.5}_{-0}$	$0^{+1.4}_{-0}$
$\|F = 2, m_F = 0 >, \|F = 1, m_F = 0 >$	$0^{+0.7}_{-0}$	$0^{+0.7}_{-0}$
$\|F = 2, m_F = -1 >, \|F = 1, m_F = 1 >$	$0^{+0.5}_{-0}$	$0.7^{+2.4}_{-0}$
$\|F = 2, m_F = -2 >$	0^{+3}_{-0}	$99^{+1}_{-5.3}$

Table 7: Pumping efficiency in the different hyperfine sub-levels for two magnetic field directions corresponding to the pumping transitions usually denoted σ^+ and σ^-. The super (sub) scripts corresponds to upper (lower) error estimates (in %) of the fitting procedure which keeps the total population equals to 100 %.

---

[12] Due to the velocity distribution, the interferometer visibility still vanishes with a perfect optical pumping because of the Zeeman phase distribution, but oscillations around this perfect behaviour indicates remaining populations in the other sublevels.

[13] When the second order Zeeman shift is neglected, this method does not allow to decipher atoms in sublevels having identical $g_F m_F$ such as $|F = 2, m_F = 1 >$ and $|F = 1, m_F = -1 >$ for example.

4.2.4 Absolute frequency pointing

To calibrate our beat note frequency reading, we used the Stark laser to horizontally deviate atoms from the optically pumped atomic beam by resonant absorption. Because of the atomic beam high collimation, this resulted in a decrease in the detected atomic flux. Using the Bragg mirror M2, we were able to minimise the Doppler shift between the push laser and the atomic beam by taking advantage of the well controlled Bragg angle between the mirror's normal and the atomic beam. Our alignment ensured an angle between our push laser and the Bragg mirror smaller than $1\,\mathrm{mrad}$ which corresponds to a mean Doppler shift of $1.4\,\mathrm{MHz}$. We recorded the atomic signal as a function of the beat note frequency. A typical measurement is represented on Fig. 36 where the two D1 transitions ($F = 2 \rightarrow F' = 1$ and $F = 2 \rightarrow F' = 2$) are visible. Fitting the atomic signal with two Gaussian distributions (and a small slope due atomic flux drifts) we extracted the peaks positions, separation and Full Width at Half Maximum (FWHM).

The peaks separation of $91.1(2)\,\mathrm{MHz}$ was slightly smaller than the expected value of $92.1\,\mathrm{MHz}$. This is due to a Zeeman effect in the upper hyperfine levels which brings closer the polarized states $\left|F' = 2, m_{F'} = +2\right\rangle$ and $\left|F' = 1, m_{F'} = +1\right\rangle$. The corresponding magnetic field amplitude is 1.1 G which is consistent with the magnetic field used in the measurement region. The FWHM $10.3(2)\,\mathrm{MHz}$ is about twice the natural width of the transition. This broadening comes from the pushing laser intensity of about $7\,\mathrm{mW/cm^2}$ leading to a saturation parameter of three. Finally, the second peak mean position $-1110.2(5)\,\mathrm{MHz}$ is close to the expected value:

$$\Delta\omega_{\mathrm{beat}}/(2\pi) = \omega_{F=2,F'=1}/(2\pi) - \left(\omega_{F=1,F'=2}/(2\pi) + 218\,\mathrm{MHz}\right) = -1113.6\,\mathrm{MHz} \tag{80}$$

which assumes an exact reference frequency of the master laser. The difference of $3.4\,\mathrm{MHz}$ between the theoretical and the measured beat note can be explained by a frequency shift of our master laser's heat pipe due to a small Zeeman shift from the earth's magnetic field[14] and to the buffer gas in the heat pipe (Argon). The locking scheme could also induce a frequency shift in the master laser frequency because of the approximate centering of the error signal. Finally, the Zeeman shift in the main chamber (approximately $1.0\,\mathrm{MHz}$) also leads to a global frequency shift. For these reasons, we used our push measurement to calibrate absolutely our Stark's laser with the linear relation:

$$\omega_{\mathrm{Stark}}(\Delta\omega_{\mathrm{beat}})/(2\pi) = \omega_{F=2\rightarrow F'=1}/(2\pi) + (\Delta\omega_{\mathrm{beat}}/(2\pi) + 1110.2)\,10^6 \tag{81}$$

---

[14] The residual magnetic field due to heating elements of the heat pipe had been carefully minimized by the winding.

where, again, we use $\omega_{F=2 \to F'=1}$ as the reference frequency for our tune-out wavelength determination.

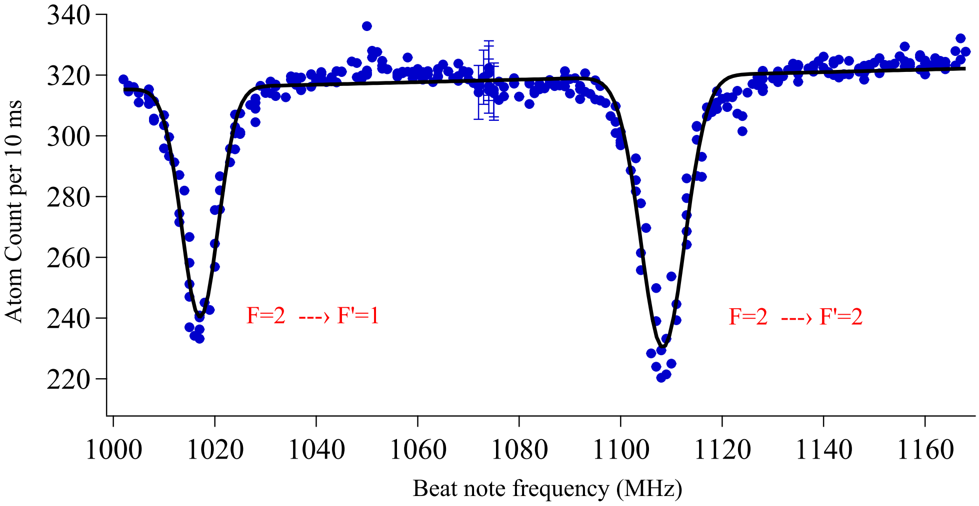

Figure 36: Detected atom number as a function of the beat frequency (notice the sign difference with eq. (80)!) between the push laser and the master laser. Resonant absorption deflects the atomic beam which reduces the atomic flux behind a detection slit. Two resonances are clearly visible and correspond to the $F = 2 \to F' = 2$ and $F = 2 \to F' = 1$ transitions. The position of the transitions allows to quantify the absolute frequency of the laser

4.2.5 Stark laser angle

The angle between the Stark laser and the atomic beam can induce both a residual vector component (previously discussed) of the polarizability and a Doppler shift of the laser frequency. To reduce this angle, we used a mirror placed on the optical board under vacuum which is almost parallel to the atomic beam. We superposed the reflected beam onto the incident beam and estimated our alignment to $\pm 4\,\mathrm{mrad}$. To quantify the induced Doppler effect, we performed an additional 'push atoms' measurement with the Stark laser in its final, vertical, position. A typical atomic signal is represented on Fig. 37. The relative depth of the $F' = 2$ (resp. $F' = 1$) peak is smaller (resp. larger) in Fig. 37 than in Fig. 36. This relatively small difference (around 20 %) of the total depth) is not well understood but might be due to the depumping time which is much faster in the vertical configuration as the laser intensity is much larger. The width of the peaks 14.8(5) MHz is due to power and Doppler[15] broadening and the peaks position 1098.8(3) MHz corresponds to a Doppler shift of 11.4(5) MHz. The corresponding Doppler angle of $7\,\mathrm{mrad}$[16] is slightly higher than expected but can be explained by the optimization of the phase shift amplitude which required a small adjustment in the beam's direction. The separation between the peaks 91.8(2) MHz is also consistent with the previous analysis.

---

[15] The atomic beam divergence in the vertical direction is of the order of $1\,\mathrm{mrad}$.

[16] This angle is counted positively when the laser beam is propagating towards the atoms.

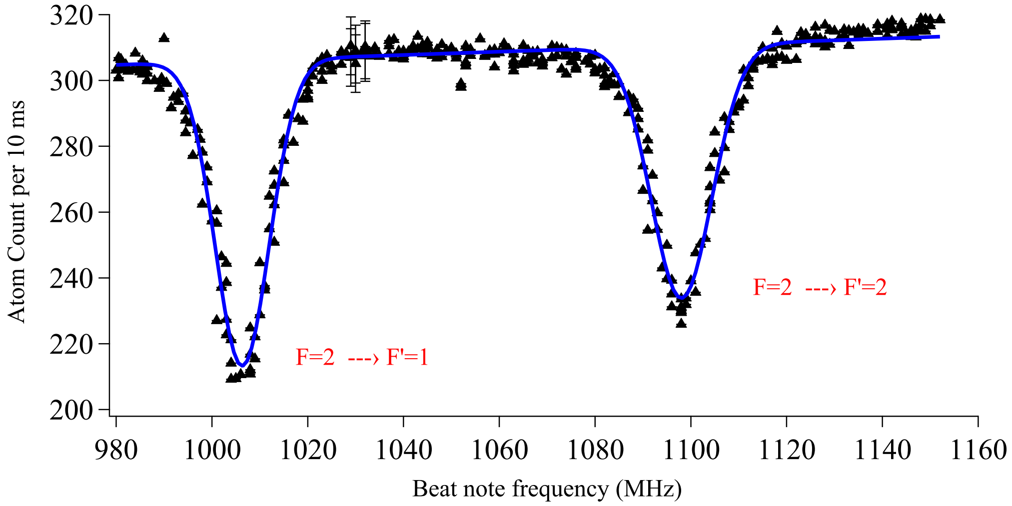

Figure 37: Detected atom number as a function of the beat frequency between the push laser and the master laser. The frequency shift allowed us to quantify the angle between the Stark laser and the atomic beam to 7 mrad.

System performances

In this section, we described the optical system implemented to phase shift our interferometer close to the tune-out wavelength. We have seen that the laser frequency is known with an accuracy limited by the Doppler angle between our push beam and the atomic beam and by the Zeeman shift whose sign has not been undetermined. The resulting frequency accuracy is estimated to 2 MHz.

The statistical uncertainty on the frequency is measured for each atomic fringes by monitoring the beat note. Typically, it [a] was of the order of 1 MHz and we rejected data for which it was larger than 5 MHz because of the large phase drift it implied.

Finally, we have seen that the laser frequency could be continuously controlled from the D1 frequency to a detuning of +4.11 GHz which is large compared to the expected detuning of 3.4 GHz. There is a few tens of mW available in a focused spot of approximately 60 µm waist which is enough for phase shifting by more than 10 mrad/MHz around the 'tune-out' wavelength.

In the interaction region, the laser's polarization is orthogonal to the atomic quantization axis to better than 90 mrad. This leads to a non-negligible polarizability vector component which will be rejected with differential measurement for two opposed angular momentum directions. The atomic beam is pumped in a single hyperfine state with at least 96 % efficiency.

---

[a] It corresponds to the square root of the sample's variance plus the square of the Half Width at Half Maximum (0.5 MHz) of the beat note. This assumes independent noise sources and corresponds to a worst case scenario.

4.3 EXPERIMENTAL RESULTS

We used the previously described apparatus to measure the 'tune-out' wavelength of lithium. The experimental protocol is similar to the one described in Chapter 2 and consists in repeated fringe recordings at fixed laser power and frequency. Each fringe was scanned with the third Bragg mirror M3 over almost two periods and consisted in a series of binary configurations:

1. No interaction: Stark laser OFF, the interferometric signal is recorded to be used as a phase reference
2. Interaction: Stark laser ON, the interferometric fringes are shifted.

A sinusoidal fitting procedure allowed to extract the relative visibility and phase of the interacting signal with respect to the non-interacting one. A typical interferometric signals is represented on Fig. 38 and exhibits almost identical visibility and a phase shift of $+213(2)\ \mathrm{mrad}$ is clearly visible between the signal with interaction and the signal without interaction. Simultaneously, the Stark laser beat note frequency is recorded. Its mean value and standard deviation during each fringe sweep is calculated and associated to the phase shift measured during the sweep.

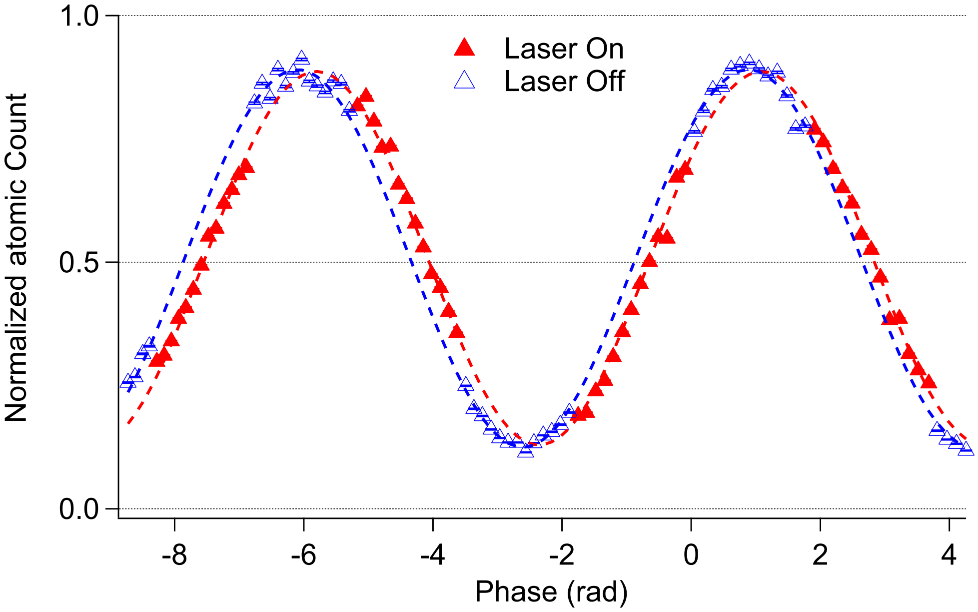

Figure 38: Typical interferometric fringe. The blue hollow triangles correspond to the the reference signal without interaction and its sinusoidal fit. The red triangles and its fit correspond to the interferometric signal with interaction and displays a visible phase shift with respect to the reference signal of $213(2)\ \mathrm{mrad}$.

By keeping the laser power constant and changing its frequency, we recorded the phase shift as a function of frequency in order to extract the position of the zero shift, corresponding to the 'tune-out' wavelength. One of the first measurement we performed consisted in comparing the phase shift behavior when the optical pumping was implemented or not. The result of such an experiment is represented on

Fig. 39. The frequency refered to as the "D1 line" corresponds to the frequency reference discussed in Sec. 4.2.4 which is $\omega_{F=2\rightarrow F'=1}$. As expected, close to the 'tune-out' wavelength calculated in Tab. 5, which corresponds, for the $|F=2, m_F=2\rangle$ level, to a detuning of $\Delta_{2,2,\mathrm{theo}} = 3384.4\,\mathrm{MHz}$, the phase shift of the optically pumped beam vanishes. The position of the unpumped 'tune-out' wavelength is a little bit more complicated to evaluate since it depends on the precise averaging of the 8 different ground state sublevels interferometric signals, for which diffraction efficiency and interferometric phases are different[17]. A simplistic approach consists in averaging the calculated 'tune-out' wavelengths of each hyperfine sublevel weighted by the hyperfine population. The idea consisting in distributing evenly the population in the two hyperfine sublevels is too crude because of the aforementioned hyperfine selectivity of our interferometer. But we can get a good estimate of the population imbalance from our optical pumping fitting procedure which leads to a detected population of each $F=1$ sublevel corresponding to approximately $8(2)\,\%$ of the total interferometric signal. Averaging the 'tune-out' wavelengths with this imbalance gives an expected detuning of $\Delta_{\mathrm{avg,theo}} = 3462(30)\,\mathrm{MHz}$. These theoretical values compares relatively well with the ones obtained by a linear fit of the data presented in Fig. 39: $\Delta_{2,2,\mathrm{exp}} = 3400(1)\,\mathrm{MHz}$ and $\Delta_{\mathrm{avg,exp}} = 3476(1)\,\mathrm{MHz}$. The difficulty to extract accurate information from the unpumped situation lead us to discard this option and, for the remaining of the chapter, we will focus on results obtained with an optically pumped atomic beam only.

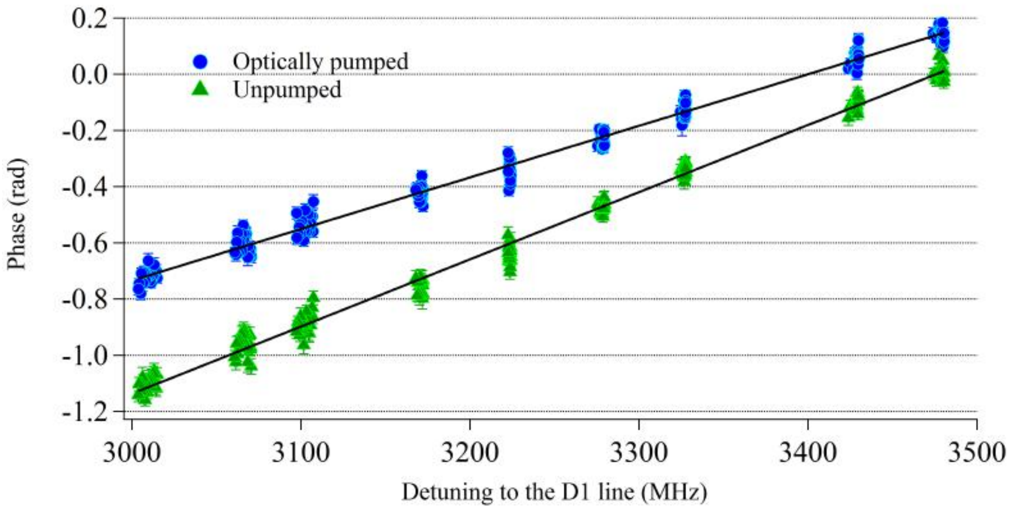

Figure 39: Phase shifts vs frequency with and without optical pumping. The Stark laser power is kept at $10\,\mathrm{mW}$ for both series. The lines correspond to linear fits and intersect the origin at $\Delta_{2,2,\mathrm{exp}} = 3400(1)\,\mathrm{MHz}$ (optically pumped) and $\Delta_{\mathrm{avg,exp}} = 3476(1)\,\mathrm{MHz}$ (unpumped).

But before discussing in more details the position of the 'tune-out' wavelength, I would first like to discuss the influence of the laser power on our measurements

---

[17] For a complete description of these effects, the reader can find a much more detailed discussion in the thesis of S. Lepoutre [98] and J. Gillot [130]. But mainly, the diffraction amplitude depends on the exact detunings in the Bragg interaction and the phases include residual magnetic gradients effects (or Stark shifts in our case).

which, in our first order Stark shift expansion, should only influence the slope of the phase as a function of frequency and not the position of the zero crossing.

4.3.1 Power dependence

To evaluate the exact value of the slope, we can use the phase shift of eq. (79). Close[18] to the tune-out wavelength, the dynamic polarizability is approximately linear:

$$\alpha^{(2)}_{2,\pm 2}(\omega) = -\kappa\left(\omega - \omega_{tune-out,2,\pm 2}\right)$$

with $\kappa \sim 10^3$ au/MHz. Taking into account the overlapping described previously (in Sec. 4.2.2) which reduces the experimental phase shift by 17 % compared to the theoretical expression, the resulting phase dependence is :

$$\phi_{f,m_F}(\omega, P_L) \simeq -KP_L\left(\omega - \omega_{tune-out,2,\pm 2}\right)$$

where $K = 0.22\,\mathrm{mrad/(MHz\,mW)}$. We tested the linearity of the phase by recording the phase as a function of frequency for different powers. The slope KP_L of of these recordings was fitted and is represented on Fig. 40 as a function of P_L. The linear behavior for low power is well represented by the previous model. Indeed, the linear fit gives an experimental value of $K_{exp} = 0.19(1)\,\mathrm{mrad/(MHz\,mW)}$. Its difference from the theoretical value can be attributed to a small displacement of the Stark laser focus position from the exact center of the interferometric arm and to a laser waist slightly smaller than expected.

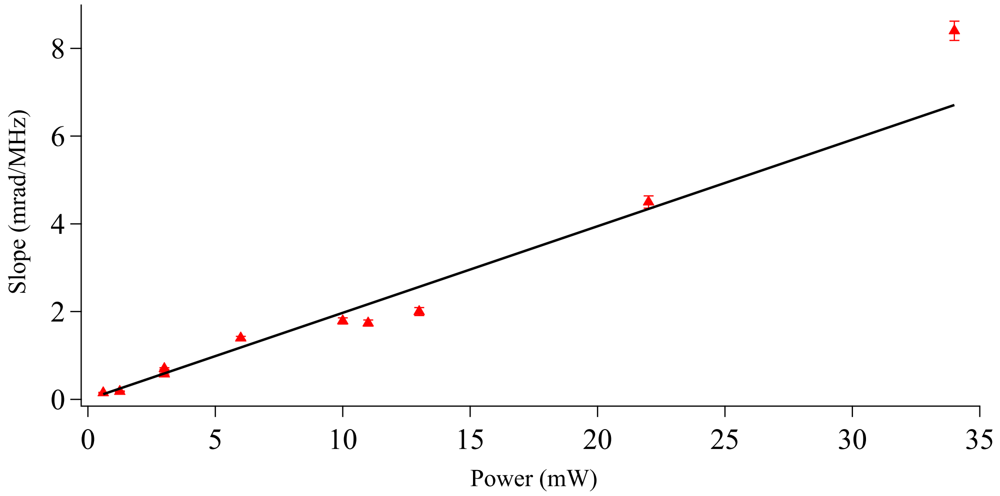

Figure 40: Phase shift slope as a function of the Stark laser power. The black line is a linear fit to the data points (red triangles) which takes into account the small power fluctuations during the recordings.

---

[18] As can be seen on Fig. 31, this assumption is valid in an interval at least 800 MHz long which is larger than the range over which we scanned the Stark phase.

Additionally, at high power, the slope seems to increase non linearly. This is not an artifact of the fitting procedure which takes into account the weight of each point corresponding to the power fluctuations during a sweep. Indeed, by plotting directly the phase shift at a fixed frequency (detuning of 3200 MHz compared to $\omega_{F=2\rightarrow F'=1}/(2\pi)$) on Fig.41, the quadratic dependence appears clearly. This is a signature of higher order terms in the polarizability development eq. (73) and in particular of the hyperpolarizability. To quantitatively estimate the validity of our experimental result we developed a theoretical model based on dressed states to evaluate the fourth derivative of the ground state energy with respect to the electric field amplitude. This work is still under development and will be discussed further in the perspectives.

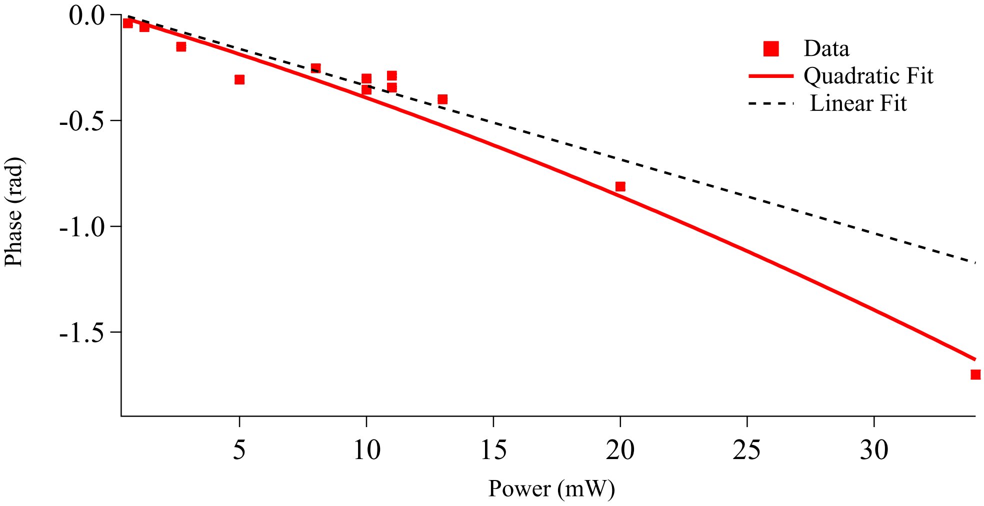

Figure 41: Phase shifts as a function of the laser power at a fixed detuning of 3200 MHz. The red squares are data points and the lines are fits with linear or quadratic power dependence. The deviation from a linear behavior is due to hyperpolarizability components in the Stark shift.

Order of magnitude

The hyperpolarizability order of magnitude can be evaluated using perturbation theory [196]. As already discussed in the introduction, the hyperpolarizability energy shift of an initial state $|g\rangle$ is calculated with the fourth order development of the dipolar coupling. It can be expressed as a sum over all the possible photon transitions which are:

$$\frac{\langle g|d|m\rangle\langle m|d|p\rangle\langle p|d|n\rangle\langle n|d|g\rangle}{(\omega_{mg}-\omega_L)(\omega_{pg})(\omega_{ng}-\omega_L)} \quad \text{or} \quad -\frac{\langle g|d|m\rangle\langle m|d|g\rangle\langle g|d|n\rangle\langle n|d|g\rangle}{(\omega_{mg}-\omega_L)(\omega_{ng}-\omega_L)^2} \tag{82}$$

where d is the dipole operator, $|m\rangle = \left|{}^2P_{1/2}\right\rangle$ or $\left|{}^2P_{3/2}\right\rangle$, $|p\rangle = \left|{}^2S_{1/2}, F=1 \text{ or } F=2\right\rangle$, $|n\rangle = \left|{}^2P_{1/2}\right\rangle$ or $\left|{}^2P_{3/2}\right\rangle$ are the intermediate states and the second term corresponds to the degenerate situation when the second intermediate state ($|p\rangle$) is identical to the initial state ($|g\rangle$).

The resonant coupling terms are shown on Fig. 42 where the virtual transitions are represented by arrows. The different paths (Ⓐ - Ⓗ) represent every possible two photon transitions. For example, Ⓐ corresponds to $\left|{}^2S_{1/2}, F=2\right\rangle \rightarrow \left|{}^2P_{1/2}\right\rangle \rightarrow \left|{}^2S_{1/2}, F=2\right\rangle$. For each physical four virtual photons trajectories, such as (Ⓐ+Ⓔ) or (Ⓓ+Ⓕ), an hyperpolarizability term (eq. (82)) arises.

With the transitions displayed on Fig. 42, eight different terms need to be taken into account. For this level of discussion, the transition strengths dependency on the laser polarization (i.e the exact Clebsch-Gordan coefficients) were not taken into account. This approximation gives an hyperpolarizability $\gamma \sim 10^{20}$ au at a wavelength close to the tune-out wavelength. Compared to the DC hyperpolarizability term (4350 au [196]), a resonant enhancement due to a much smaller energy denominators[19] of eq. (82) leads to a non-negligible contribution close to the tune-out wavelength. However, this calculation is an order of magnitude larger than the result we obtain when taking into account the exact transition strengths.

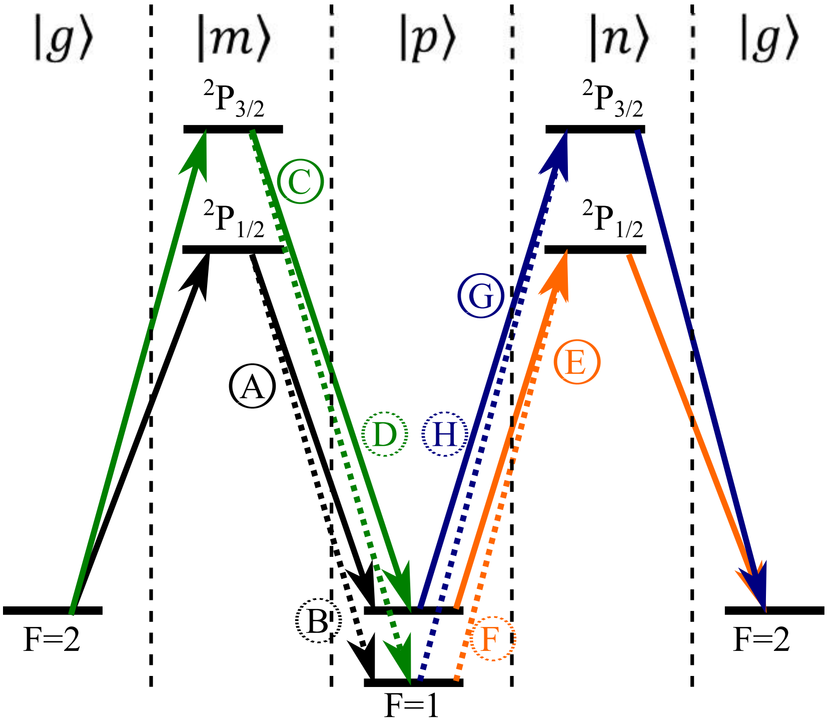

Figure 42: Virtual transitions considered for the evaluation of the hyperpolarizability amplitude. The intermediate states are labelled at the top of the figure. The degenerate terms are represented by solid arrows and non-degenerate terms by dashed arrows.

To keep this effect negligible, we chose a laser power low enough to remain in the linear regime (typically 10 mW), but estimated the shift induced by this effect to 1.5 MHz as, according to our preliminary results, the hyperpolarizability vanishes at a higher frequency than a 'tune-out' wavelength taking into account only the po-

---

[19] The hyperfine splitting and the detuning to resonance are of the order of 1 GHz which compared to the optical photon frequency $> 10^5$ GHz change the contributions of fourth order terms by more than 15 orders of magnitude.

larizability. The dispersion induced by the different laser powers was estimated to 1 MHz.

4.3.2 Residual vector component

Because the quantization axis and the polarization axis are difficult to precisely align, we measured the phase shift as a function of frequency for states of opposite projection on the quantization axis ($|F = 2, m_F = 2\rangle$ and $|F = 2, m_F = -2\rangle$ states). The residual polarizability vector component has opposite sign for the two states which allows to measure it independently of the static and tensorial parts. The result of this measure is represented on Fig. 43. The fact that the vector component lowers the 'tune-out' wavelength of the $m_F = +2$ state tells us that the sign of total vector component $-V \cos\chi \frac{m_F}{4} \alpha^{(\nu)}$ is opposite to the sign of the static part and that the tune-out measurements, which were performed with the $|F = 2, m_F = 2\rangle$ for which the pumping efficiency was slightly higher, will have to be shifted upward.

The frequency difference between the two 'tune-out' wavelength:

$$\Delta_{2,-2,exp} - \Delta_{2,2,exp} = 20.5(5)\,\mathrm{MHz}$$

tells us that the residual polarization coefficient $V \cos\chi$ is of the order of 0.25 %. This is obtained by calculating the 'tune-out' wavelength dependence on the residual polarization close to the ideal situation (Config. 1) and using this linear development to evaluate this effect. This value is a bit high compared to the expected combination of the Doppler angle (measured to 7 mrad) and the tilt between the quantization axis and the mechanical support (evaluated to 90 mrad) which, combined, lead to 0.12 % residual polarization. But the viewport birefringence due to mechanical constrains also increases this effect which was not quantified. In any cases, the order of magnitude seems reasonable and the shift of 10.3(5) MHz can be subtracted to the 'tune-out' frequencies of the $|F = 2, m_F = 2\rangle$ state.

4.3.3 Tune-out value

We performed a few measurements at different low laser powers (ranging between 5 mW and 13 mW) and fitted the phase shift as a linear function of the frequency to determine the 'tune-out' wavelength. The results are displayed on Fig. 44. There is a large discrepancy between the different values of the resulting 'tune-out' wavelength values. I think that it can be mainly attributed to the optical pumping efficiency which, as we have seen on the difference between pumped and unpumped beam, has a large effect on the 'tune-out' wavelength. Hence, different campaigns correspond to different pumping efficiency which shifts by 5 MHz $\%^{-1}$ the tune out position (making the hypothesis that the "unpumped" percent lies completely in the opposite $|F = 1, m_F = -1\rangle$ level). Additionally, it took us some time to simultaneously control all the different aspects of the experiment and some data points have been corrected by assuming a frequency locked on the next upper hyperfine transition which shifted the frequency by a total of 91.2 MHz which is disputable but did not change significantly the mean detuning value. Only three data points lie inside the 1σ error bars which indicates clearly a poor statistic. But we did not, at the time of the measurement campaigns, expected to reach this level of accuracy and did not perform additional measurements.

The result of this analysis is a detuning at which the phase shift vanishes of:

$$\Delta_{2,2} = 3398(8)\,\text{MHz}$$

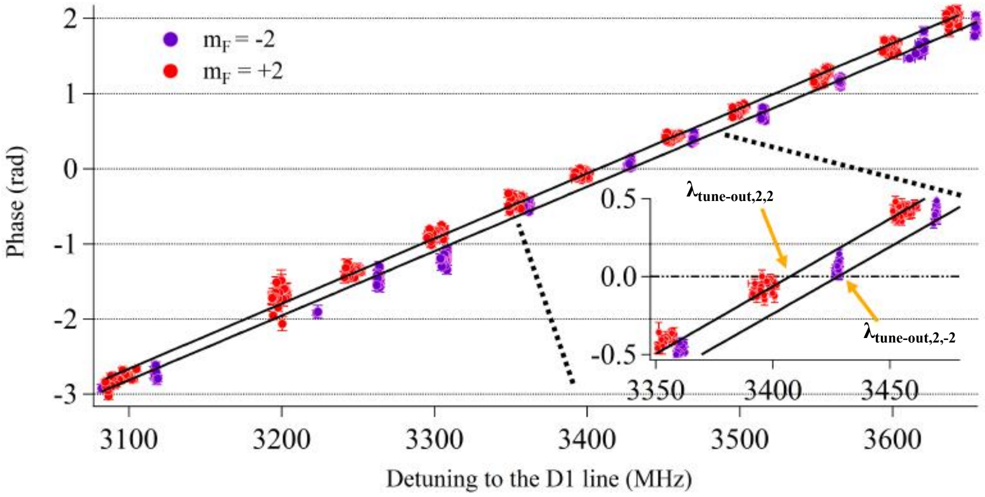

Figure 43: Phase shifts as a function of the laser detuning to the D1 line. The laser power is fixed at the highest power of 34 mW to increase the phase sensitivity. The shift between the two polarized states 'tune-out' wavelengths is visible and corresponds to 20.5(5) MHz.

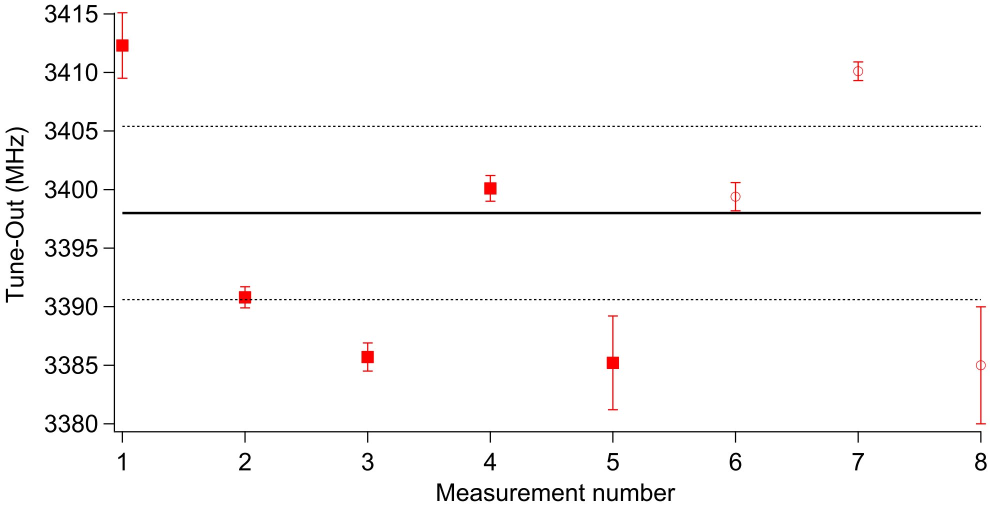

Figure 44: Detuning of zero crossings for eight different measurement campaigns. the values corrected by the hyperfine splitting are represented as hollow circles. The black solid line corresponds to a weighted average of the data and the dotted lines correspond to the associated statistical 1σ interval.

Parameter	Statistical	Systematic	Correction
Frequency reference $\omega_{F=2\rightarrow F'=1}$	0.5 MHz	±2.0 MHz	0 MHz
Optical pumping	6.6 MHz	0 MHz	0 MHz
Orthogonality with atomic beam	0.5 MHz	−11.5 MHz	−11.5 MHz
Residual vector component	0.5 MHz	10.3 MHz	10.3 MHz
Hyperpolarizability	1 MHz	1.5 MHz	1.5 MHz
8 campaigns	7.5 MHz	0 MHz	0 MHz

Table 8: Summary of main source of error in the tune-out wavelength measurement

4.3.4 Error Budget

Now that we have an experimental value of the zero Stark shift position, we can deduce from eq. (81) and after correction of systematic effects the exact 'tune-out' wavelength value of the $|F = 2, m_F = 2\rangle$ level. The main sources of systematics have been described in Sec. 4.2 and are summarized in Tab 8. After correction, the resulting 'tune-out' wavelength is:

$$\lambda_{2,2,tune-out} = 670.972097(15)[3]nm$$

There is a large difference (12 MHz) with the expected value:

$$\lambda_{tune-out,Config.1,F=2,m_F=2} = 670.9721146(37)nm$$

which could be explained by the matrix transition coefficient which we used in our theoretical description which relied on a ratio of 2. We can extract this parameter from the difference with our theoretical model which gives us a ratio $R_{Li} = 1.991(7)$. This result is to be treated cautiously as its statistical deviation from 2 is not well resolved. Especially when one estimates, from relativistic calculations [197], that R_{Li} deviation from 2 should be of the order of -3×10^{-5}. In addition, the deviation from 2 is expected to increase with the number of electron as can be seen on Tab. 9 which summarizes the ratio measurements for different alkali atoms. Therefore, the deviation from 2 for lithium atoms should be smaller than for sodium atoms which was measured in the range of 2 with a smaller (4×10^{-3}) uncertainty. To reach the 10^{-5} deviation level necessary for accurate comparison with theory, a 50 kHz 'tune out' wavelength uncertainty needs to be reached which is two order of magnitudes lower than our current control of statistical and systematic effects.

4.4 CONCLUSION

In this chapter, we have described a theoretical model which develops the atomic ground state energy in a power series expansion of the electric field amplitude in the

Atom	Ratio	Method	Reference
$_{11}$Na	1.9994(37)	Spectroscopy	[198]
$_{19}$K	1.9973(13)	Interferometry	cited in [175]
$_{37}$Rb	1.992 19(3)	Interferometry	[185]
$_{55}$Cs	1.9809(9)	Spectroscopy	[199]
$_{87}$Fr	1.9011(108)	Spectroscopy	[200]

Table 9: List of most accurate transition strength ratios measurements for Alkali atoms.

dipolar approximation. This allowed us to evaluate, for ^{7}Li, theoretically the wavelengths at which the second order term, called dynamic polarizability, vanishes (at 'tune-out' wavelengths) or is identical between specific levels (at 'magic' wavelengths). Then, we presented a few experimental techniques to measure these wavelengths as well as some of their applications. Inspired by the experiment done by Holmgren *et al.*[184], we decided to implement a similar setup on our lithium interferometer which was described in Sec. 4.2. The crucial points of absolute frequency pointing, atomic beam pumping and laser polarization were discussed and quantified. Finally, our experimental results were presented and compared to theory. The unexpected influence of the hyperpolarizability at higher powers constrained us to use lower power when measuring the 'tune-out' wavelength to minimize its systematic effect. By measuring the phase shift between states of opposite polarity ($m_F = \pm 2$) we were able to quantitatively reject the influence of the residual vector component. The hunting down of these systematic shifts allowed us to correct the mean 'tune-out' wavelength frequency. We were however limited by our optical pumping efficiency which induces a large statistical dispersion of our 'tune-out' wavelength measurement. Our experimental value of $\lambda_{2,2,tune-out} = 670.972097(15)[3]nm$ compares reasonably in terms of accuracy to state of the art 'tune-out' measurements.

PERSPECTIVES

The appearance of hyperpolarizability effects lead us to question further the validity of the theoretical model eq. (71) with which we evaluate the Stark energy shifts of the groundstate hyperfine levels. The dynamical propagation of the atomic populations coupled via the electric dipole Hamiltonian showed that hyperfine state mixing in presence of large electric field can not be neglected. Indeed, the transient superposition of $m_F = 2$ and $m_F = 0$ (resp. $m_F = -2$) states induced by two (resp. four) virtual photons processes leads to systematic phase shifts due to the polarizability (resp. hyperpolarizability) difference between these states as well as the Zeeman energy shift. Furthermore, population transfer to different hyperfine sublevels due to non-adiabatic transitions can leave the transmitted atomic population in a different hyperfine distribution which characteristically reduces the interferometric visibility.

In addition to these theoretical efforts allowing to quantify further systematics, experimental improvements of the optical pumping with a push beam removing unwanted hyperfine populations as well as complete removal of the vector component by minimizing the systematic shift between $\lambda_{tune-out,2,2}$ and $\lambda_{tune-out,2,-2}$ would enhance the reliability of this apparatus and reduce systematics effects. Coupled to more accurate frequency references and better stabilization of the confocal Fabry-Perot cavity sub MHz uncertainty seems reachable which would be a first step towards an accurate measurement of R_{Li}.

Part II

Design of a Bose Einstein Condensate setup

5 NEW BEC INTERFEROMETER: MOTIVATIONS AND DESIGN

Contents

An atom interferometer with a large spatial separation and a high repetition rate based on a dual isotopes atom chip is currently being developed in our group. In this chapter, we define the objectives of the new apparatus, some specific constraints have to be chosen in accordance with the scientific goals. These constraints and the scientific context will be discussed in the first section of this chapter.

The second part of this chapter will focus on the design of the new interferometer in regards of its objectives. I will first discuss the steps leading to a dual isotopes BEC with the description of the different magnetic fields sources needed to produce a magneto-optical trap, magnetic traps and Feshbach fields. Then, I will describe the dual isotopes evaporation strategies with a simple sympathetic theoretical model allowing us to dimension the critical parameters influencing the BEC production. Then, I will present a transport protocol based on an optical lattice which pulls the atoms from the chip's surface. Numerical simulations, realized in collaboration with the group of E. Rasel in Hanover (with N. Gaaloul in particular) were developed to characterize its feasibility. Finally, the different strategies to produce Large Momentum Transfer (LMT) interferometers will be discussed and the sensitivity function of a 7-pulse interferometric scheme will be derived.

5.1 A NOVEL ATOM INTERFEROMETER

5.1.1 Atom interferometry with Bose Einstein Condensates

In the prospect of developing a new experimental setup, it is important to define some specific characteristics which guide the conception and delimit the experimental field on which the project is intended to develop. In our case, we can summarize these characteristics in three axes. The novel interferometer will continue to be a separated arms atom interferometer, as was previously the lithium interferometer. Among the possible sources, the team chose to use a Bose condensed atomic cloud of rubidium to increase the spatial separation. These two aspects are motivated by the long term goals which are precision measurements of electromagnetic interactions and in particular of matter neutrality.

Let us now briefly review how these characteristics have been and will be implemented in the domain of experimental physics.

Large spatial separation

A spatial separation between coherent matter waves has been produced with various techniques such as material gratings [18], magneto-optical beams splitters [201], spatially separated traps [202] or optical beam splitters used either in a Raman [19], Bragg [22] or Bloch scheme [203]. The former were initially developed as proof of principle tools and produced spatial separations in the sub mm range. The latter techniques relied on the coherent transfer of $2n$ photon momenta to the atoms which were extensively used for inertial sensors as their sensitivity scales with the space-time area enclosed between the interferometer arms. One way to increase this area is to increase the momentum separation. This is the reason why particular effort was undertaken recently to produce interferometer with Large Momentum Transfer pulses using either single pulses ($\Delta p = 24\hbar k$ [204]) or multi pulses ($\Delta p = 4\hbar k$ [60], $\Delta p = 10\hbar k$ [205] $\Delta p = 80\hbar k$ [206],$\Delta p = 102\hbar k$ [61]) schemes[1]. Another way to increase the space-time area is to increase the interferometric time T to separate spatially the two interferometer arms. Apart from the interferometer based on Bloch oscillations, all the LMT interferometers previously citedwere spatially separated by less than[2] 1 cm (see Tab. 10).

The 10 m high apparatus operating at $12\hbar k$ developed in Kasevich's group very recently demonstrated a 8.2 cm spatial separation between their two interferometric arms [208]. The following year, they extended this performance to 54 cm separation with $90\hbar k$ LMT splitters [209]. These decisive advances in spatial separation opens the possibility to use macroscopic devices which interacts with each arms separately and pushes further fundamental questions on the decoherence between macroscopically separated wave-packets.

Publication (Year)	2n	T	Spatial separation
H. Müller *et al.*[204] (2008)	24	50 ms	3 mm
T. Lévèque *et al.*[60] (2009)	4	30 ms	400 µm
K. Y. Chung *et al.*[210] (2009)	2	400 ms	3 mm
R. Bouchendira *et al.*[203] (2011)	500	10 ms	2.9 cm
S.Y. Lan *et al.*[205] (2012)	10	250 ms	9 mm
G. D. McDonald *et al.*[206] (2013)	80	1.3 ms	600 µm
Sugarbaker thesis [208] (2014)	12	1.15 s	8.2 cm
T. Kovachy *et al.*[209] (2015)	90	1.04 s	54 cm

Table 10: Summary of the recent advances in large spatial separation atom interferometers. The combination of large momentum transfer 2n and large interferometric times T is necessary to a large spatial separation.

BEC interferometry

The use of BEC as atomic source for atom interferometry has been subject to recent theoretical [211]–[214] and experimental [23], [28], [215] efforts as it was shown that one of the limits of thermal cloud interferometry was the cloud tranverse motion in a distorted light beam wavefront [29], [203]. Louchet-Chauvet *et al.* showed that the phase shift spreading induced by beam aberrations due to a curvature radius R scales linearly with the cloud rms velocity Δv:

$$\Delta\Phi = \frac{k_{eff}}{R}\Delta v^2 T^2$$

---

[1] see Sec 5.5.1 for a description of LMT schemes

[2] Very long baseline interferometers [207] operating at $2\hbar k$ momentum separation have interferometric arms separated by about 5 mm and require meter long vacuum systems.

where $k_{eff} = 2nk_l$ is the effective wavevector separation between the two arms, k_B is Boltzmann constant and m is the atom mass. Let us take for example, a $\Delta v = 1\,\mathrm{cm\,s^{-1}}$ ^{87}Rb cloud diffracted by a perfect Gaussian laser beam focused right at the position of the first pulse on a $5\,\mathrm{mm}$ waist. Then, $1\,\mathrm{cm}$ away, at the position of the second pulse, the beam radius of curvature will be $R = 1000\,\mathrm{km}$. For a large $2n = 42$ momentum separation, the interferometric time is $T = 40\,\mathrm{ms}$ and the phase spread due to wavefronts curvature is $\Delta\Phi = 540\,\mu\mathrm{rad}$ which is larger than the Gouy phase ($100\,\mu\mathrm{rad}$ in this situation). However, State of the art vacuum windows induce locally much smaller curvatus radii which can create much larger phase spreading. It is the main systematic effect reported in [203]. Reducing the rms velocity is the easiest way to minimize this spreading without changing the interferometric time. A condensate opens the possibility to reduce this phase shift by a factor 100 with ultra cold BEC's with $\Delta v = 1\,\mathrm{mm\,s^{-1}}$ [216]. Drastically narrower velocity distributions have been demonstrated [217] and additional methods such as Delta kick cooling [202], [218], [219] can minimize this phase shift even more.

Another advantage related to the rms velocity is the possibility to use Large Momentum Transfer beam splitters. These atom optics tools are highly velocity selective and require a velocity spreading much smaller than the recoil velocity v_{rec} to be efficient. For example, the $102\hbar k$ beam splitting procedure demonstrated by Chiow *et al.*[61] used a cloud with $\Delta v = 0.6\,\mathrm{mm\,s^{-1}} < 15\,\%v_{rec}$ condensate and their multi pulses scheme still lead to a $90\,\%$ atom loss. This larger momentum separation allows to increase the interferometric time which, for inertial sensors, increases quadratically the interferometer sensitivity, motivating the use of these schemes.

These advantages have to be appreciated in the light of the often mentioned BEC's drawbacks:

- The production rate of these atomic clouds is usually much smaller than ultra cold atomic clouds which increases the time required to perform N_{exp} measurements. However, it was demonstrated [220] that atom chips are an adequate solution to reach production rate on the order of $1\,\mathrm{Hz}$.
- Atom-atom interactions in BEC's induce a density dependent inhomogeneous phase evolution. This effect leads to randomization of the phase between the two interferometer arms which is a severe limitation on the contrast in trapped interferometers [221], [222]. However, in the freely propagating case, it is possible to dilute the cloud with a preliminary expansion to reduce the cloud chemical potential[3] and to decrease the impact of phase diffusion between the two separated clouds. [224]

Therefore BEC interferometry shows promising features to increase atom interferometers sensitivity and accuracy in the future which is particularly interesting in the context of precision measurements.

---

[3] In a Castin Dum BEC propagation model [223], the atom-atom interaction energy scales with the inverse of the BEC volume which increases by a factor 10^5 in $200\,\mathrm{ms}$. This puts the chemical potential in the $10\,\mathrm{Hz}$ range during our interferometer, leading to de-phasing well below $1\,\mathrm{mrad}$.

Precision measurement

Atom interferometry has been an invaluable tool for precision measurements since the initial experiment of O. Carnal and J. Mylnek in 1991. Among the past and present field of applications, one can identify in particular:

- **Inertial forces measurements:** The intrinsic sensitivity of atoms to accelerations led to the measurement of the local gravity acceleration with an actual state of the art record sensitivity of $4 \times 10^{-9}\,\mathrm{m}/\mathrm{s}^2\sqrt{\mathrm{Hz}}$[31] and accuracy of $4 \times 10^{-8}\,\mathrm{m\,s^{-2}}$[29]. This sensitivity to inertial effects also led to the development of sensors for acceleration gradients [225], [226] and rotations [37], [227].

- **Fundamental constants measurements:** Atom interferometry has proven to be an accurate tool for precise determination of fundamental constants. Indeed, the phase in an atom interferometer is sensitive to the exact value of the differential potential energy between the two interferometer arms. This allowed the precise determination of the gravitational constant G [33], [228] by using large masses around the interferometric arms. Also, these potentials can be proportionnal to an integer multiple of the recoil velocity imparted to an atom during the diffraction process. This led to the accurate determination of the h/m ratio (h is the Planck constant and m the atomic mass) and the subsequent evaluation of the fine structure constant[203], [229].

- **Quantum tests:** An atom interferometer is also sensitive to the absolute value of the atomic energy on each of the two paths. This is particularly useful for the demonstration of quantum mechanics topological effects such as the geometrical phases discussed in 3.

The high sensitivity of these instruments makes them ideal candidate for fundamental physic tests. Very ambitious proposals, are spatial missions designed to test the Weak Equivalent Principle [80], to detect gravitational waves [230] or to probe the interface between quantum and gravitational physics [231]. Ground based experiments testing deviation from standard gravity and QED potentials with sub-$\mu\mathrm{m}$ range are currently being developed [82], [232].

In this fundamental domain of atom electromagnetic interactions another opened question is of great interest: is matter exactly neutral ?

5.1.2 Matter neutrality test

One of the first precision measurement planned on our setup is a test of matter neutrality which have been initially mentionned by Kasevich and Chu [233] and was afterward discussed by our group [234] and by the Standford's group [235].

The theoretical motivation for matter neutrality tests is related to the quantization charge issue in the Standard Model [236]. However, in the prospect of an extended Standard Model, charge quantization appears in different forms. Some models predict the de-quantization of charge only for neutrons and neutrinos which acquire finite opposite charges while the protons and the electrons keep the exact same opposite values. Inversely, complete charge quantization can be derived when additional couplings are included in the theory which concerns new physics such as right handed Majorana neutrinos. Additional theories such as CP violating mixing to the electromagnetic field or small photon masses can include non zero residual charges[235]. But this discussion is out the scope of this thesis.

The idea of a residual electric charge either due to the non zero neutron charge $q_n \neq 0$ or to the absolute charge difference between the proton and the electron charge $q_p + q_e = \delta q \neq 0$ finds its origin in a paper by Piccard and Kessler[4] (cited in the review by Unnikrishnan and Gillies [237]). In this paper, they claim a limit on $\delta q/q_e < 5 \times 10^{-21}$ with the gas efflux method using CO_2 molecules.

The principle of this method is to detect the potential change of a metal container which releases a compressed gaz. As the gaz flows out, the container potential is monitored. If the outgoing molecules, or atoms, have a residual charge, the container potential will be different after the release. This type of experiment was also carried out using Hydrogen, Helium [238] Argon, Nitrogen [239] and the final residual charge uncertainty reached a 10^{-21} electron charge level.

Other experimental techniques such as a levitated macroscopic object [240] or an acousitc cavity resonator [241] have been used to measure $\delta q/q_e$.

The levitator method [240] was initially motivated by the possible existence of fractionally charged particles or free quarks. Its principle relied on an experiment similar to the famous Millikan oil drops. A levitated object is subject to an electric field and its position is monitored as its charge is neutralized. For different field amplitudes, the trajectories cross exactly at the same position if there is no residual charge.

The acoustic resonator relied on the monitoring of the acoustic frequencies present in a cavity excited by an electric field at a given frequency. The amplitude of the acoustic spectrum at the field frequency depends on the residual charge amplitude.

Regarding the neutron residual charge, almost all experiment[5] performed up to date used another technique, the beam deflection [242]. This experimental setup relies on the deflection of a neutron beam by a strong electric field. The use of a collimated achromatic beam was necessary to reach a neutron charge upper bound $q_n/q_e = 10^{-21}$.

All these experiments reached the upper limit of $10^{-21} q_e$ on the residual charge and were mainly limited by the necessary cancellation of the residual charge induced by free charges. Table 11 summarizes some of the results obtained with these setups. A striking element is the lack of recent improvement on the 10^{-21} limit which emphasize the need for new approaches to go beyond this current limit.

In the absence of a specific theoretical model, experimental tests with an improved sensitivity are useful for more phenomenological theories which can transform an up-

---

[4] According to [237], Piccard & Kessler would have set up the experiment for testing Einstein's idea that residual charges might explain the Earth electromagnetic field with 'mass currents' circulating around the atmosphere.

[5] With the exception of the gas efflux performed by Hillas *et al.* [239] which used the differential upper bound of two atoms to evaluate the corresponding neutron upper residual charge.

Experiment type	year	residual charge	Reference
Gaz efflux	1959	$(\pm 1)10^{-21}$	[239]
Acoustic resonantor	1973	$(\pm 1.3)10^{-21}$	[241]
Levitated object	1987	$(0.8 \pm 0.8)10^{-21}$	[240]
Neutron Beam	1988	$(-0.4 \pm 1.1)10^{-21}$	[242]

Table 11: Comparison of the residual charge limit obtained with different experimental procedures. The residual charge denotes indifferently δq or q_n.

per limit on charge neutrality into specific constraints on the theory. This is why the development of an atom interferometer to test for matter neutrality was undertaken in our group.

Matter neutrality test using a Mach-Zehnder interferometer

The experiment principle (shown on Fig. 45) relies on the scalar Aharonov-Bohm effect. In the presence of an external electric potential V, the phase of an atomic wavefunction is shifted by an amount proportional to a potential atomic residual electric charge ϵe and the interaction time with the potential τ:

$$\Phi = \frac{\epsilon e V \tau}{\hbar}$$

To increase the sensitivity to a residual charge $\eta = \epsilon / A$, we can either increase A, which is the number of nucleons, the applied electrical potential V or the interaction time τ. Rubidium atoms allows to use the two bosonic isotopes ^{85}Rb and ^{87}Rb. This yields the additional possibility of a differential measurement allowing for a discrimination between neutron residual charge and proton-electron charge quantization.

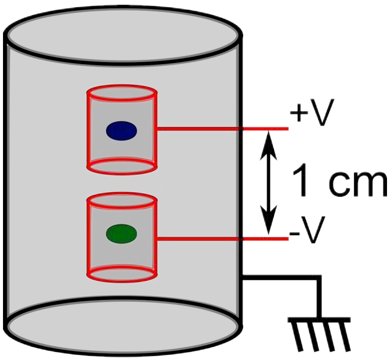

Figure 45
Scheme of the matter neutrality test using the scalar Aharonov Bohm effet.

To be able to produce large electric potential difference, separated arms interferometry is essential to have macroscopic potential sources creating up to $\Delta V = 10^5$ V potential difference between the two interferometer arms.

Finally, in order to have large interaction times, a fountain type interferometer has the advantage of the zero atomic velocity at the trajectory apogee where the interaction can be implemented. This allows interaction times τ with the electrodes of several ms. With this in mind, the electrical neutrality sensitivity can be expressed as:

$$\sigma_\eta = \frac{\hbar}{A e \Delta V \tau} \sigma_\Phi \tag{83}$$

where σ_ϕ is the interferometer phase sensitivity after averaging. For example, a phase sensitivity of $0.02\,\mathrm{mrad}$ directly leads to a residual charge sensitivity σ_η of the order of 3×10^{-25} which is four orders of magnitude better than current state of the art values.

However, reaching this phase sensitivity is challenging for long ($2T > 80\,\mathrm{ms}$) interferometers due to the phase noise induced, for example, by the accelerations associated with the reference mirror vibrations. We will see however that a first version of this interferometer, limited by vibrations, already improves a matter neutrality test by two orders of magnitudes. Also, with this method, a differential measurement of the interferometer phase makes it possible to get rid of systematic effects such as the diffraction beam wavefront previously discussed. A BEC source pushes further the possible rejection as its trajectory can be more accurately controlled compared to thermal clouds.

Using atom interferometry to test matter neutrality allows to measure the residual charge down to the single atom level which, compared to the previously described macroscopic experiments, reduces the number of possible experimental biases which makes the measurement analysis more robust.

5.1.3 Atom interferometer source

A schematic of the full interferometric sequence is represented on Fig. 46. A Bose Einstein Condensate will be produced in a combination of magnetic and optical trap and will be launched upwards. Large momentum transfer Bragg pulses will then separate the two interferometric arms during which the interaction with the electrodes will be pulsed. After reflection and recombination, the two interferometric outputs will be detected when they are spatially separated.

The remainder of this section will consist in examining successively the constraints on the atomic source and the diffraction process needed for this prospective experiment. A short discussion of the interaction region and detection scheme will be given for completeness.

Atomic source

As was described in Chap. 1, a continuous interferometer source can be described in terms of monochromaticity and brilliance. However, for a sequential experiment as is the case of pulsed beams or single cloud sources, it is more convenient to describe the source in terms of initial atom number, velocity width and repetition rate. The velocity distribution is relevant here because the interferometer contrast and the number of atoms contributing to the interferometer signal depend on the diffraction efficiency which, as we will see in Sec 5.5.1, depends on the velocity distribution.

The interferometer long term phase sensitivity σ_ϕ will be used to discuss its performance. It quantifies the ultimate sensitivity of the apparatus and can be related,

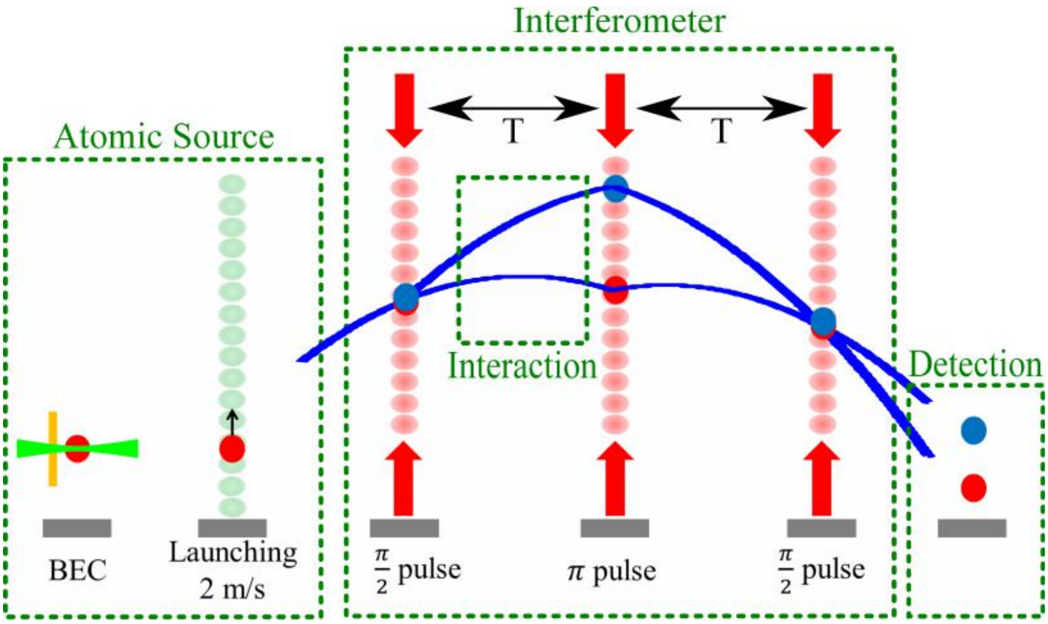

Figure 46: The four (dotted green) parts of our dual isotopes interferometer.

assuming the averaging[6] of a white noise source, to its shot to shot sensitivity σ_{shot}, to the cycle time τ_c and the integration time τ_{mes} by:

$$\sigma_\phi = \sigma_{shot}\sqrt{\frac{\tau_c}{\tau_{mes}}} \tag{84}$$

The lowest the phase sensitivity, the better the statistical phase uncertainty. In term of source characteristics, the ultimate[7] noise source in an atom interferometer is the quantum projection noise (QPN) which contributes to the shot to shot sensitivity by an amount:

$$\sigma_{QPN} = \frac{1}{\mathcal{C}\sqrt{N}}$$

where $\mathcal{C}$ is the interferometer contrast and N is the atom number contributing to the interferometer signal. To minimize this quantity, it is advantageous to use high atom numbers and to have the larger interferometer contrast, for example, 10^5 atoms and a contrast $\mathcal{C} = 0.5$ leads to a noise of $6\,\mathrm{mrad}$ per shot. To reach the $20\,\mathrm{\mu rad}$ phase sensitivity discussed previously, an integration time of six days with a duty cycle of $5\,\mathrm{s}$ (corresponding to $Nexp = 10^5$ measurements) are necessary.

However, additional statistical noise sources (such as vibrational noise) can lead to σ_{shot} higher than this fundamental limit and have to be kept in mind during the conception. In particular, the interferometer sensitivity function will be described in Sec. 5.5.2 which allows to evaluate the impact of different noise sources on the final interferometric phase noise.

---

[6] As long as phase drifts can be efficiently rejected by differential measurements.

[7] This does not take into account the possibility to use non classical atomic states which can reduce this limit down to the Heisenberg limit which scales as N^{-1}.

In regards of these limits, we opted for some specific technologies for our atom source.

Bose condensed atom source

Two main reasons motivate the choice of BEC as atom sources and they both come from the necessity of a very narrow initial velocity distribution.

- The first point is due to the ballistic expansion of the atomic cloud during its fountain trajectory. The velocity spread Δv of the initial atomic cloud equal to $\sqrt{k_B T_{emp}/m}$ (where an effective temperature T_{emp} is usually used to describe the velocity distribution, k_B is Boltzmann constant and m is the atomic mass). This distribution leads, when the role of interaction is negligible and the cloud expansion is purely ballistic, to a cloud size Δr at the fountain apogee (height $H \sim 0.3\,\mathrm{m}$) $\Delta r = \sqrt{2k_B T_{emp} H/(mg)}$ where g is the local gravitational acceleration. For state of the art atomic sensors, the temperature is on the order of a few µK leading to a cloud's radius $\Delta r \sim 2.5\,\mathrm{mm}$ which renders difficult an accurate control of systematics effects. Additionally, to reduce the impact of intensity fluctuations on the interferometer contrast, the Bragg lasers have to be large compared to the cloud size. Because they have to go through electrodes of centimetric size, their waists are limited to $w_0 \sim 5\,\mathrm{mm}$ which limits the cloud size to a few hundreds of µm. For example, to limit the thermal expansion to $500\,\mu\mathrm{m}$ at the fountain apogee, the initial cloud temperature has to be smaller than $30\,\mathrm{nK}$ in the transverse direction.

- The second point comes from atomic diffraction which relies on Bragg diffraction. As will be discussed in Sec. 5.5.1 high order Bragg diffraction pulses are highly selective in the atom velocity. Therefore, the velocity distribution width in the longitudinal direction has to be typically smaller than the recoil velocity $v_{rec} := \hbar k_L/m$ divided by the number of transferred photons n_B:

  $$\Delta v < \frac{v_{rec}}{n_B}$$

  This corresponds to cloud temperature of the order of $70\,\mathrm{nK}$ for $n_b = 5$.

Temperatures achievable with BEC of tens of nK are possible which corresponds perfectly to these constraints.

Atom chip

Equation (84) indicates that at constant measurement time, the phase uncertainty scales as $\sqrt{\tau_c}$, thus reducing the cycle time τ_c (or equivalently increasing the repetition rate), directly leads to an enhanced sensitivity. The production of large BEC at a high repetition rate requires initial high atomic densities. To combine a large atom number in a small volume, magnetic trapping produced by atom chips [243] are excellent candidates because of the proximity to the current sources leading to tight magnetic traps which reduces the duration of evaporative cooling. However, when it comes to fountain launching, the surface prohibitively diffracts the interacting beams when the chip's surface is vertical.

Dual isotopes condensation

The use of a dual isotopes interferometer allows to compare the measured phase shifts for two different neutron numbers, electron and proton numbers being equal. Therefore, the differential phase between this two isotopes directly leads to the test of the neutron charge. In our case, we planned to use the two isotopes of rubidium.

Because of its negative scattering length, it is not possible to Bose condense a large number of ^{85}Rb atoms[8]. In order to get similar phase sensitivity for both isotopes, it is mandatory to produce atomic clouds with comparable atom numbers. The use of a Feshbach resonance, allowing to tune ^{85}Rb scattering length to a positive value, is a simple choice for the production of dual isotopes condensate. In particular, the Feshbach resonance near a magnetic field of 155 G is broad (see Sec. 5.2.3) and has interesting collisional properties (see Sec. 5.3) for the rapid production of dual isotopes BECs. This is the reason why we opted for a hybrid atom chip which can transfer pre-cooled atomic clouds first into a magnetic trap and then into a pure dipole trap in which the final step towards condensation can be performed.

Fountain launch

The condensate will be launched by a moving lattice at $2\,\mathrm{m\,s^{-1}}$ in order to separate physically the atomic source production region from the interferometric region. This allows a precise control of the interferometric environment which is beneficial for systematic effect control and additional noise sources reduction. In particular, the UHV pumps or the magnetic fields necessary to the source production can generate residual magnetic fields which might produce detrimental phase shifts in the interferometers. Magnetic shielding combined with an homogeneous magnetic field in the interferometer region will reduce these effects.

Additionally, this fountain geometry allows to control the ^{85}Rb scattering length in the launching region to prevent the BEC collapse and to let the cloud expand to reduce the atom-atom interactions. Finally, long interaction times can be reached as the interferometer is performed at the fountain apogee where the atomic velocity vanishes.

5.1.4 Interferometric sequence

Separated arms can be realized with a Mach Zehnder type interferometer (similar to the one describe in Chap 1) which includes Large Momentum Beam Splitters (LMBS)

---

[8] The critical number of atoms that can be condensed in a harmonic trap (harmonic length a_{h0}) is proportional to $a_{h0}/|a|$ [244], where a is the s-wave scattering length.

(see Sec. 5.5.1). Increasing the spatial separation allows both to increase the interaction time with the electrodes and to apply higher potential difference.

Indeed, to amplify the differential Aharonov-Bohm effect, the two interferometer arms will interact with potentials of opposite signs. Hence, a very large electric field will be created in between the two electrodes charged at $\pm V$ which needs to be spatially separated to prevent cathodic arcing. According to the experimental tests presented in [245] (chap2, fig. 2.9), the sustainable applied potential difference increases linearly with the electrode separation at $10^{-9}\,\mathrm{mbar}$ with a slope of $25\,\mathrm{kV\,mm^{-1}}$. Therefore, a $8\,\mathrm{mm}$ spatial separation is enough for this potential difference.

Large spatial separation

A spatial separation of $1\,\mathrm{cm}$ is the minimum separation between the two atomic arms to be able to switch the electrodes only when the atomic trajectories are sufficiently far from the electrodes boundaries. Considering a single splitting pulse creating a coherent superposition of external states having momenta $mv_0 - N\hbar k_L$ and $mv_0 + N\hbar k_L$. The spatial separation between the two paths will be proportional to the interferometric time T: $\Delta H = 2N\hbar k_L T/m$. Therefore, increasing the interferometric time can be sufficient to have large spatial separation. However, phase noise of the Bragg beams due to the reference mirror acceleration vibrations scales as T^2 :

$$\sigma_{acc} = 2Nk_L T^2 \sigma_a$$

where σ_{acc} is the phase noise accumulated on the diffraction beams after $1\,\mathrm{s}$ and σ_a is the acceleration noise of the reference mirror at $1\,\mathrm{s}$. With a passive isolation platform, the typical acceleration noise is $\sigma_a = 4 \times 10^{-7}\,\mathrm{ms^{-2}}/\sqrt{\mathrm{Hz}}$ [246]. With our experimental parameters $2N = 42$, $T = 40\,\mathrm{ms}$, it leads to a phase noise of $200\,\mathrm{mrad}$ at $1\,\mathrm{s}$. From eq. (83), it means that the sensitivity to a potential residual charge reaches 10^{-21} when limited by this phase noise and integrates down to 5×10^{-24} with 10^5 measurements.

A first setup to go beyond this limit consists in the combination of an isolation platform and a seismometer which monitors the vibrations during each measurement. It is an efficient way to either correlate[9] the interferometric phase with the measured accelerations which can be used for post-correction or to actively stabilize the reference mirror. Both of these methods lead to a gain of approximately 5 on the short term phase noise[247]. This puts the shot to shot phase noise in the $50\,\mathrm{mrad}$ range, lowering the integrated residual charge sensitivity down to 10^{-24}.

Double interferometer

To overcome the vibrational noise limit, a double interferometer (represented on Fig. 47) is possible. It allows to reject the common vibrational noise between an upper interferometer (which can interact with the electrodes) and a lower similar interferom-

---

[9] This motivates the calculation of the interferometer sensitivity function presented in Sec. 5.5.2 which is needed for an efficient correction.

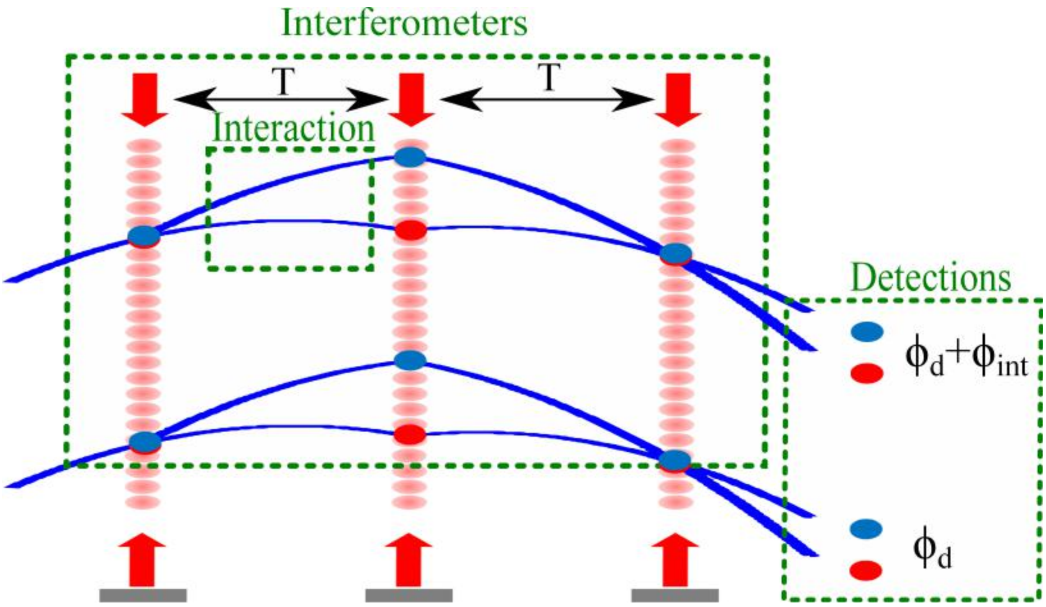

Figure 47: Principle of a dual interferometer: two spatially separated atomic cloud with identical velocities interact with the same laser pulses. Both interferometers acquire the laser phases ϕ_d but only the upper interferometer acquires the interaction phase with the electrodes. The common noise on ϕ_d can be efficiently rejected to keep only the information on the interaction phase ϕ_{int}

eter which solely contains the information on the phase noise due to the diffraction processes. A double atom interferometer setup was initially demonstrated by Snadden *et al.* [225] and applied recently [248], [249].The interferometer demonstrated by Chiow *et al.* [248] used Large Momentum Beam splitter and they obtained a 10 % interferometer contrast with $N = 20$ and $T = 50\,ms$. Comparing this result with their previous single interferometer, they were able to increase the interferometer time from $1\,ms$ to $50\,ms$ without loss in contrast showing clearly the efficiency of this method. The performance of this rejection scheme was discussed[10] by F. Pereira Dos Santos in [250] who has shown that phase sensitivities on the differential phase (ϕ_{int}) close to the QPN could be recovered even in the presence of large phase noise imperfectly correlated between the two interferometric outputs. This advanced setup motivated us to design a large condensate source to reduce further our interferometer ultimate sensitivity.

5.1.5 Interaction with electrodes

In order to reach a high sensitivity on matter neutrality, the interferometric environment has to be controlled in many different aspects. The position of the electrodes has to remain constant both on the short timescale (during the active interaction time τ) and on the long time scale (during the whole integration duration τ_{mes}). This requires a mechanical structure to maintain the electrodes rigidly fixed. Also, the

---

[10] Its application to Weak equivalent principle tests was also discussed in [45]

ramping of the electric potential will require large transient currents[11].Because the development of these experimental elements has yet to be done, we decided to produce the interferometer in an accessible region which necessarily is far away from the complex structure of the atomic source. This choice was also motivated by the good optical access which allows to image with high resolution the interferometer outputs. This means that the atomic initial velocity has to be large enough to enclose the interferometer in a separated vacuum cell. In practice the initial velocity has to be larger than $\sqrt{H_0 2g} \sim 2\,\mathrm{m\,s^{-1}}$, where $H_0 \sim 20\,\mathrm{cm}$ is the height above the atomic source of the first splitting pulse of the interferometric sequence.

5.1.6 Detection

In order to read out the interferometric phase, one finally has to be able to count either the total number of atoms on each external states or directly access the spatially dependent atomic distribution of each output atomic clouds. In both cases, optical access to the atomic clouds once they are sufficiently spatially separated after the final $\pi/2$ pulse has to be guaranteed. In practice, $3\,\mathrm{cm}$ below the electrode, large rectangular viewports provide an optical access with a numerical aperture of 0.2. The clouds are well separated by $1\,\mathrm{cm}$.

5.1.7 Conclusion

In this section, we have shown that a matter neutrality test with a 10^2 fold improvement of the current measures can be realized with an atom interferometer limited by vibration noise. Velocity dispersion, accurate control of the atomic trajectories and large spatial separation motivate the initial choice of a Bose condensed atomic source. In the prospect of a quantum projection noise limited measurement, particular effort needs to be undertaken to ensure the possibility of large atom numbers. To reach these performances with high repetition rates an hybrid trap on an atom chip will now be presented.

Interferometer version	Vibration limited	Rejection limited	QPN limited
σ_{shot}	$200\,\mathrm{mrad}$	$40\,\mathrm{mrad}$	$6\,\mathrm{mrad}$
σ_ϕ (10^5 measurements)	$700\,\mu\mathrm{rad}$	$150\,\mu\mathrm{rad}$	$20\,\mu\mathrm{rad}$
σ_η	5×10^{-24}	10^{-24}	3×10^{-25}

Table 12: Description of the two prospective limits on a matter neutrality test and the corresponding integrated sensitivities on the electron-proton charge.

---

[11] The produced magnetic fields might be quite large on the interferometric path which is why great care will have to be taken to symmetrize the setup to produce identical second order Zeeman phase shifts (atoms are usually prepared in a zero magnetic projection state) on the two interferometric arms.

Interferometer sequence

The atomic source will consist in a Bose-condensed cloud of 10^5 atoms with a momentum width in the LMT lattice direction of $0.2v_{rec}$. It corresponds to a longitudinal temperature of the order of $15\,nK$ which is challenging and might require additional cooling (or focusing) stages, such as Delta-Kick Cooling [251]. The cloud will be launched at $2.1\,m\,s^{-1}$ which corresponds to a fountain height of $23\,cm$. At its apogee, the condensate will have a radius of approximately $500\,\mu m$ and large momentum transfer beam splitter will create a superposition of momentum states separated by $42\hbar k_L$. With an interferometric time $T = 40\,ms$, interaction $\tau = 10\,ms$ with electrodes separated by $8\,mm$ at a potential of 10^5 V is possible. With a cycle time of 5 s, 10^5 measurements can be realized in 6 days. Depending on the limiting noise source, matter neutrality tests with increased sensitivity will be performed as is summarized in Tab. 12.

5.2 HYBRID ATOMIC SOURCE

The atomic source consists in a 3D-Mirror Magneto-Optic-Trap (3D MMOT) [252] of the two atomic isotopes. After a short cooling and compression stage, this cloud will be loaded into a pure magnetic trap (MT) [253] produced by a chip's wire. In this trap, a sympathetic cooling stage [254], induced by RF evaporation, will be performed and the resulting cloud will eventually be transferred into a purely optical trap produced by a pair of optical tweezers. A second evaporative step in presence of the Feshbach magnetic field will allow to reach condensation of both isotopes. The condensed cloud will be transported from the optical trap to the launching region with an optical lattice. After a final transfer into a vertical lattice, it will be launched by an accelerated lattice.

In this section, we are going to discuss the cloud production prior to the evaporation and transportation stages.

Among the required magnetic fields necessary for the planned cloud production, one can distinguish three distinct magnetic configurations that are going to be successively described:

- The MMOT quadrupole field, necessary to create magnetic gradients used in Magneto-Optical Trapping.
- The MT gradients generating a conservative magnetic trap minimum.
- The Feshbach magnetic field used to tune the collisional properties of ^{85}Rb.

5.2.1 3D-MOT configuration

Magneto optical traps are widely used to capture and cool atoms or even molecules [255]. Description of these traps can be found in [256],[257] and only their main characteristics will be presented here.

MOT principle

The magneto-optical force induced by a single laser field $\vec{E}$ on a two-level atom can be written:

$$\vec{\mathcal{F}} = \frac{\hbar \vec{k}_L \Gamma \Omega^2}{2} \frac{1}{\delta_{tot}^2 + (\Gamma'/2)^2}$$

where $\vec{k}_L$ is the laser light wavevector, Γ is the natural linewidth of the transition, $\Omega := \vec{d} \cdot \vec{E}/\hbar$ is the Rabi frequency, δ_{tot} is the total detuning experienced by the atom and $\Gamma' := \Gamma\sqrt{1+s}$ is the intensity broadened linewidth ($s := 2\Omega^2 / \left[\Gamma + (2\delta_{tot})^2 / \Gamma\right]$ is called the saturation parameter). Adding two excited states in a simple $F = 0 \longrightarrow F' = 1$ atomic transition leads to different energy levels which depend on the external magnetic field $\vec{B}$ via Zeeman interaction. In the first order perturbation expansion, this results in a magnetic dependent resonance transition $\omega_{0,B} = \omega_0 - g_F m_F \mu_B B$, where ω_0 is the resonance frequency in the absence of external field, g_F is the atomic level Landé factor, m_F is the atomic total angular momentum projection on the magnetic field direction and μ_B is Bohr magneton. Additionally, taking into account the atomic velocity, the total detuning can be expressed as:

$$\delta_{tot} = \delta - \vec{k_L} \cdot \vec{v} - g_F m_F \mu_B B$$

where $\delta := \omega_L - \omega_0$ is the unperturbed laser detuning. Hence, if the magnetic field amplitude B depends on the atomic position, it is possible to produce both a spatially and velocity dependent force on the atomic motion. In the weak intensity limit, this model extends directly to the interaction of an atom with two counter propagating (along the z quantization axis for example) laser beams by simply adding the two magneto-optical forces having opposite wavevectors. If the laser beam polarizations are chosen σ_+ and σ_- with respect to the quantization axis, each laser can only drive one atomic transition $m_F = 0 \longrightarrow m_{F'} = +1$ and $m_F = 0 \longrightarrow m_{F'} = -1$ which results in only one specific Zeeman detuning for each laser beam. If the external magnetic field is directed along the laser beams axis with a magnitude proportional to the distance from some $z = 0$ reference position, $B = \kappa z$ and changes direction at this point, it is possible to express the total force experienced by the atoms along the z direction as:

$$\mathcal{F}_{z,tot} = \frac{\hbar k_L \Gamma \Omega^2}{2} \left[\frac{1}{(\delta - k_L v - \beta z)^2 + (\Gamma'/2)^2} - \frac{1}{(\delta + k_L v + \beta z)^2 + (\Gamma'/2)^2} \right]$$

where $\beta = \mu_B \kappa$ is the Zeeman shift gradient and we have implicitly assumed identical amplitude of the two electric fields. Expanding this force around the magnetic field minimum and for small atomic velocities, one gets a total force:

$$\mathcal{F}_{z,tot} \simeq 2\hbar k_L \Gamma \Omega^2 \frac{\delta}{\left[\delta^2 + (\Gamma'/2)^2\right]^2} (k_L v + \beta z)$$

which acts as a cooling and trapping force when the laser is tuned to the red of the atomic resonance ($\delta < 0$). Combining three such pairs of counter-propagating laser beams with a quadrupole magnetic field (as produced by two coils in anti-Helmholtz configuration which have the same axis as one of the laser beams) and the correct laser polarizations allows to produce a three dimensional trapping and cooling force. This is represented on Fig. 48a where a six beams traditional MOT configuration is depicted.

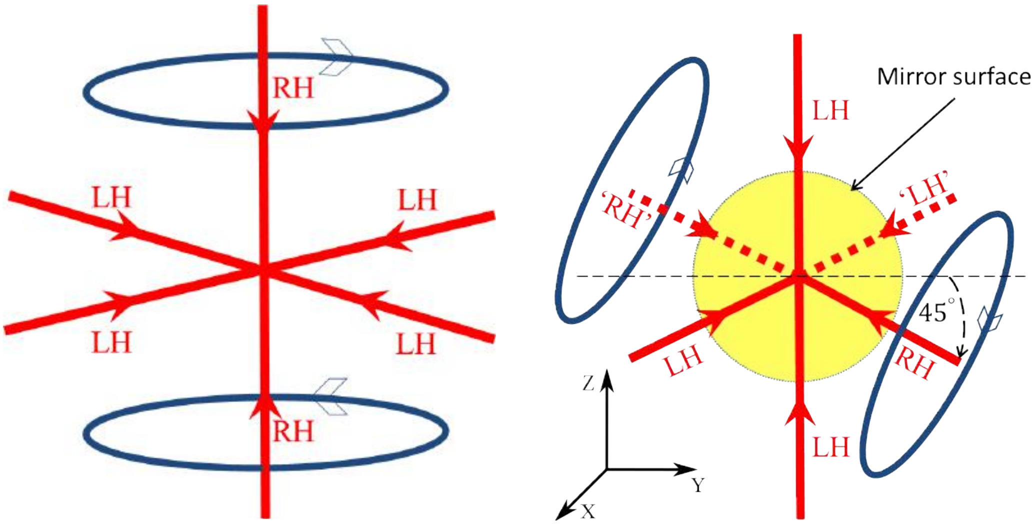

(a) Traditionnal MOT configuration

(b) Mirror MOT configuration

Figure 48: (a) Classical MOT configuration with a Quadrupole field produced by two Anti-Helmholtz coils (the arrow indicates the current direction). The laser polarization are denoted by LH (Left Handed) and RH (Right Handed) and are adapted to the magnetic field direction along the laser axis. In the overlapping region, atoms can be trapped and cooled.
(b) Mirror MOT configuration which produces the equivalent of the traditional MOT. The reflected beams on the mirror produce two additional beams with orthogonal polarizations that provide for the counter propagating laser beams for the incoming one.

Mirror MOT

We implemented a MOT closer to a surface with the so-called mirror MOT[252], [258]. This configuration uses a reflecting surface to produce two of the six beams of the traditional MOT configuration. By taking advantage of the polarization change upon reflection on a conductor with a 45° incident angle, it is possible to produce the polarization configuration required for magneto-optic trapping. This is represented on Fig. 48b where the dotted laser beams represent the equivalent laser beam corresponding to the reflections on the mirror surface. To match the quadrupole symmetry, which corresponds to the C_∞ symmetry group, one has to align the laser beam symmetry axis, which corresponds to the D_{4h} group, on the quadrupole axis. In the standard configuration, any of the three counter-propagating polarizations can be adjusted according to the field direction. In the mirror MOT configuration, only the reflected beam directions can be used as the reflection breaks the polarization symmetry for the unreflected beam. Some experiments [78], [259]–[261] used U-shaped wires positioned directly below the reflecting surface to produce, with an additional bias field, the necessary quadrupole magnetic field. We decided to keep an external anti-Helmholtz coils configuration.

5.2.2 Magnetic trapping

the next step is the transfer of the cloud into a pure magnetic trap. This type of trap [253] relies on the Zeeman potential energy $g_F m_F \mu_B B$ which presents a minimum for low magnetic field seeking states (for which the product $g_F m_F$ is positive) when the magnetic field amplitude itself has a local minimum. The principle of magnetic trapping can be understood with a simple configuration which consists in the combination of a single wire conducting a constant current and a homogeneous magnetic field orthogonal to the wire. This single wire trap will be presented first before discussing the actual magnetic trapping potentials designed for our experiment.

Single wire trap

The magnetic field produced by a single wire carrying a current I is:

$$\vec{B}_{SW} = \frac{\mu_0 I}{2\pi r} \vec{u}_\theta$$

where r is the distance from the wire and μ_0 is the vacuum permeability. Adding an external constant magnetic field of amplitude B_{bias} produces a magnetic field zero. This is illustrated on Fig. 49 were lines of constant magnetic field amplitude are represented in a plane orthogonal to the single wire. One sees that the total magnetic field vanishes at a given distance above the wire:

$$z_{min} = \frac{\mu_0 I}{2\pi B_{bias}} \tag{85}$$

At this position, the magnetic field can be approximated by a two dimensional quadrupole field in the transverse direction to the wire. At this stage, the magnetic potential experienced by the atoms is not confining in the wire direction and has a zero value at its center. A popular solution to both of these issues consist in adding two orthogonal wires to the initial single wire. If the currents in these wires are flowing in the same direction (a situation similar to a Helmholtz configuration) a magnetic field will be produced along the single wire which produces a magnetic potential with a non-zero minimum and a weaker confinement along the single wire direction. This situation can be realized in practice with a simple configuration called "Z" shaped traps which is described on Fig. 50a.

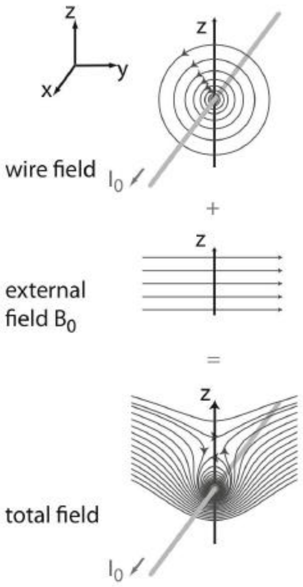

Figure 49
Magnetic trap produced by a single carrying wire and a transverse biais field. Adapted from [243]

Majorana losses

An important source of losses in this type of traps is the initial assumption that atoms remains in the low magnetic field seeking states. This hypothesis assumes that the magnetic moment of trapped atoms follow the magnetic field direction throughout their trajectories in the trap. This hypothesis remains valid as long as the Larmor frequency $\Omega_L := g_F m_F \mu_B B\left(\vec{r}\right)/\hbar$ is large compared to the typical frequency describing the atoms dynamic[12] Ω_{dyn}. When the magnetic field has a zero minimum, this condition can never be realised close to the minimum and the atomic magnetic moment changes direction compared to the magnetic field direction. This results in a "spin-flip" which transfers atoms in a non-trapped state, indcing atoms are lost. This is the reason why non zero magnetic field traps have been developed such as the TOP traps [262] and the Ioffe-Pritchard traps [263] which reduces this effect. Our "Z" shaped trap belongs to the second group of traps and we can estimate the loss rate $\gamma_{Majorana}$ induced by this effect.

Close to the trap minimum, the magnetic field amplitude can be expanded, in the simpler case of a symmetric trap, in a power series expansion:

$$B\left(r\right) = B_0 + \frac{b'' r^2}{2}$$

where B_0 is the magnetic field minimum and b'' is its spatial second derivative. To estimate the magnetic region in which atoms are lost due to spin flips let us evaluate the volume where the condition $\Omega_L \leqslant \Omega_{dyn}$ is not fulfilled. Close to the field minimum, the atomic dynamics is well represented by the frequency of the bottom harmonic potential, $\Omega_{dyn} = \sqrt{2 g_F m_F \mu_B b''/m}$. Therefore, the distance to the center at which the Larmor frequency becomes larger than the dynamic frequency is;

$$a_{Maj} = \sqrt{\frac{2\hbar}{m\Omega_{dyn}^2}\left(\Omega_{dyn} - \Omega_{L,0}\right)} \tag{86}$$

where $\Omega_{L,0} = g_F m_F \mu_B B_0/\hbar$ is the Larmor frequency at the center of the trap. As can be seen in this expression, this quantity makes sense if and only if $\Omega_{dyn} > \Omega_{L,0}$ which is automatically verified for zero minimum magnetic traps but which might not be the case for sufficiently large magnetic minima and as such can serve as a good experimental goal to prevent this type of losses.

Assuming that all atoms entering this volume are lost, we can find an analytic expression of the Majorana loss rate. The number of atoms entering a sphere of radius a_{Maj} during an infinitesimal time dt is $dN_{Maj} = n_0 \bar{v} dt \pi a_{Maj}^2$, where n_0 is the

---

[12] In other words, the characteristic time of the dynamical evolution $1/\Omega_{dyn}$ is much larger than the characteristic time of the atomic moment evolution $1/\Omega_L$ which ensures that the latter follows smoothly the magnetic field during the atomic motion.

atomic density[13] in the center of the trap and $\bar{v} = \sqrt{8k_BT/(\pi m)}$ is the mean velocity of an atomic cloud at temperature T. The resulting loss rate γ_{maj} is therefore:

$$\gamma_{maj} = \frac{1}{N}\frac{dN_{Maj}}{dt} = \frac{2\hbar\Omega_{dyn}}{\pi k_B T}\left(\Omega_{dyn} - \Omega_{L,0}\right)$$

One of the main issue of this type of losses is their polynomial divergence as the temperature tends to zero (for linear traps, the temperature dependence is even larger with a T^{-2} dependence [264]). For example, a typical harmonic trap has a frequency ranging from $\Omega_{dyn}/(2\pi) = 100\,\text{Hz}$ to 1 kHz. At a temperature of 5 µK, the Majorana loss rate ranges between 1 Hz and 120 Hz which prevents long trapping times. Hopefully, it is possible to prevent these losses either by preventing atoms from approaching the bottom of the magnetic trap (with an optical "plug [265] for example) or by having a minimum Larmor frequency $\Omega_{L,0}$ much larger than the trapping frequency. In practice, a field minimum $B_0 \sim 1$ G gives a minimum frequency $\Omega_{L,0} = 1.4\,\text{MHz}$ which is much larger than typical Ω_{dyn}.

The "Z" shaped traps described previously combines a non zero magnetic field and a versatile trapping geometry which allows to capture and compress an atomic cloud produced by a mirror MOT which we will now describe.

Mode matching capture

To transfer efficiently atoms from the mirror MOT to the magnetic trap, it is important to adapt the magnetic field geometry to the approximately spherical shape of the cold atoms in the mirror MOT. This design was carefully undertaken by J. Alibert who will present the procedure in more details. Figure 50b represents the magnetic field equipotentials designed to capture, almost 100 % of the MOT cloud. The capture relies on the sudden ramping up of the magnetic trap fields after the molasses. Assuming that the atoms did not have time to rethermalize during the transfer, we can apply the Virial theorem to estimate the temperature of the trapped atomic cloud.

In a linear trap, the total energy is three times the kinetic energy. Assuming[14] that the total energy of trapped atoms is the sum of the initial energy and the acquired potential energy due to the capture, one obtains the following equality:

$$T_f = \frac{T_i}{3} + \frac{2\int n_{MOT}(\vec{r})\, V_{MT}(\vec{r})\, d^3\vec{r}}{9Nk_B}$$

where T_i is the molasses initial temperature, T_f is the trapped atoms final temperature, n_{MOT} is the atomic density in the MOT and V_{MT} is the magnetic trap potential. Assuming a quadrupole potential $V_{MT}(x,y,z) = g_F m_F \mu_B b' \sqrt{\frac{x^2+y^2}{4} + z^2}$, where b'

---

[13] In a harmonic trap at thermal equilibrium, the peak density is given by:

$$n_0 = N\left(\hbar\Omega_{dyn}\right)^3 / \left[3\left(k_B T \Lambda(T)\right)^3\right]$$

with $\Lambda(T) = \sqrt{2\pi\hbar^2/(mk_BT)}$ the thermal de-Broglie wavelength.

[14] At this stage, the atom-atom interaction energy accounts for less than 1 ppm of the total internal energy.

is the magnetic field "gradient" and a spherically symmetric atomic distribution in the MOT $n_{MOT} = \frac{N}{(2\pi\sigma)^3} e^{-r^2/(2\sigma^2)}$, with σ the MOT typical width, we obtain the following expression for the final temperature:

$$T_f = \frac{T_i}{3} + \frac{2}{9\sqrt{6\pi}} \left[\ln\left(2+\sqrt{3}\right) + 2\sqrt{3} \right] \frac{g_F m_F \mu_B b' \sigma}{k_B} \tag{87}$$

where the numerical prefactor is of the order of 0.25. It is comparable to other prefactors found in the litterature (0.35 for an isotropic trap [266]).

This can lead to a large increase in the trapped cloud temperature if the second term exceeds the temperature reduction of the first term. For example, a $\sigma = 2\,\mathrm{mm}$, $T_i = 50\,\mu\mathrm{K}$ MOT, loaded in a $b = 20\,\mathrm{G/cm}$ quadrupole trap in a $g_F m_F = 1$ magnetic state will have a final temperature of $290\,\mu\mathrm{K}$ which is almost 6 times its initial temperature. To reduce this heating, it is advantageous to decrease the MOT size and to use smaller magnetic gradients at the beginning of the transfer. Typically[15], the MOT size scales, at constant atom number and large detuning, as $\left[\Omega^2/(\delta b')\right]^{1/3}$. Therefore, extinguishing the MOT light at higher magnetic gradient and larger detuning is an efficient way of reducing σ and the final temperature in the trap. This technique is usually denoted as a Compressed MOT (CMOT) [268]. In addition, eq. (87) corresponds to the worst case scenario with a sudden trap ramping. The more realistic trapped cloud temperature will be smaller due to a progressive transfer to the magnetic trap also inducing heating but at constant phase space density.

Our configuration

In addition to the efficient transfer, our magnetic trap is also designed to allow for a fast evaporation cooling stage which increases the atomic cloud phase space density by reducing its temperature through selective removal of atoms. This will be described in Sec. 5.3. In order to increase the evaporation cooling speed it is mandatory to have a large elastic collision rate Γ_{el} at the beginning of the evaporation. This collision rate depends on the atomic density, the mean velocity and the atomic elastic cross section (this will be discussed in more details in Sec. 5.3). One can show that Γ_{el} scales as the magnetic gradient b' to the power $4/3$ (and the temperature scales as $b'^{2/3}$). Therefore, it is interesting to initially compress the atomic cloud by increasing b' while keeping the phase space density constant. If the compression time is long compared to the thermalisation time, it is possible to realize an adiabatic compression at constant entropy.

Figure 51 presents the theoretical magnetic potentials at the end of a compression stage. Additional "I" wires (along the Z direction) were added to the "Z" shaped configuration to increase the magnetic trapping gradients in the Y direction. The current in the "Z" wire is 30 A, the current in the "I" wires is 20 A and the bias field is 50 G. An additional constant magnetic field along the Y direction of 7 G was added to push the MT position further from the wire.

---

[15] This expression assumes an homogeneous density in the MOT and takes into account the re-scattering force induced by light emitted in the MOT. This effect was initially discussed in [267]

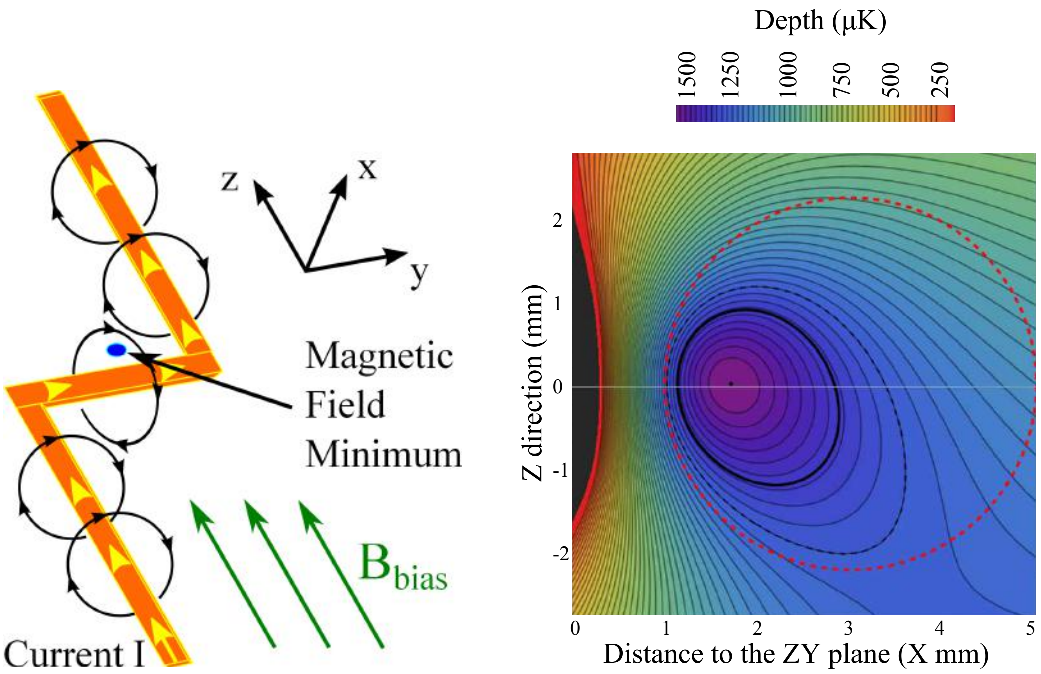

(a) Z wire trap

(b) Magnetic isopotentials

Figure 50: **(a)** Schematic representation of the "Z" shaped trap. A single current is driven through the wire (in orange) which produces a magnetic field represented by the black circles (lines of constant field in the case of an infinite wire). An additional bias magnetic field displaces the magnetic minimum (blue dot) from the (ZY) plane to a given height $X_0 \sim \frac{\mu_0 I}{2\pi B_{bias}}$ above the plane.
(b) The magnetic isopotentials produced by a "Z" shaped wires whose dimensions are adapted to match the cold atom cloud (dotted red circle). The black ellipsoïd represents the equipotential in the magnetic trap corresponding to the typical energy $k_b T$ of the loaded atomic cloud. On can see the magnetic potential "leak" due to the gravity field at position $(X = 3.5, Z = -2)$.

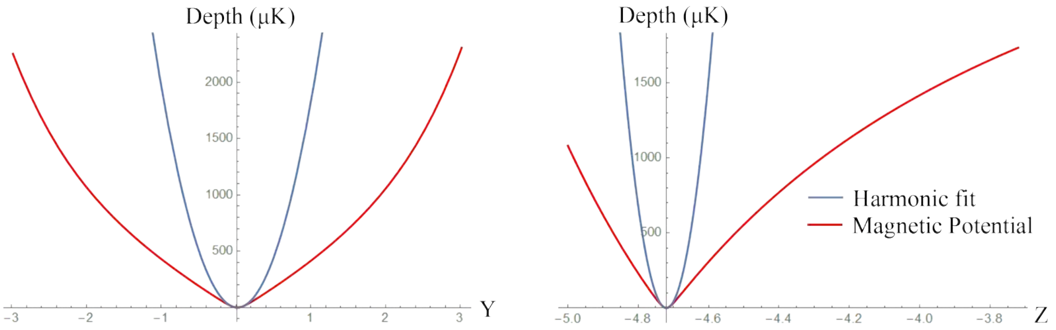

(a) Magnetic field potential in the wire's direction

(b) Magnetic field potential in the gravity direction

Figure 51: Magnetic potentials in the Y and Z directions of the "Z" shaped wire presented on Fig. 50a, two additional wires increasing the compression in the Y direction and a constant Bias field. The depth is given in temperature unit for a $g_F m_F = 1$ maximally trapping state.

In principle, a "Z" wire combined with a constant bias field is well described by the potential of a Ioffe-Pritchard (IP) trap which is the combination of a quadrupole field and a bias field. However, the two additional "I" wires and the constant Y magnetic field change the trap geometry. Therefore, an analytical description with a IP potential is not adapted for this geometry which is why I chose to describe it in terms of mean magnetic gradients and mean frequencies.

An important feature of these traps is their rather good linearity at large temperature (ranging from 100 μK to 1 mK) as is emphasized by the harmonic fit of the trap minimum and a reasonable trapping volume (1.5 mK height which is more than five times the cloud temperature T_f). With the previous parameters the mean magnetic field gradient $\sqrt[3]{b'_x b'_y b'_z}$ and the mean trapping frequency $\sqrt[3]{\omega_x \omega_y \omega_z}$ are respectively $50\,\mathrm{G\,cm^{-1}}$ and $(2\pi)\,370\,\mathrm{Hz}$ for Rubidium atoms in $g_F m_F = 1$ magnetic states. With these parameters, elastic collision rates of $10^3\,\mathrm{s^{-1}}$ can be achieved which is sufficient for the 1 s evaporation cooling scenarii described in Sec. 5.3.3.

5.2.3 Optical dipole trap

^{85}Rb negative scattering length at zero magnetic field prevents the Bose condensation of large atom number. Above a critical density, the ^{85}Rb BECs are unstable and collapse due to the formation of $^{85}\mathrm{Rb}_2$ molecules. Therefore, a constant and homogeneous magnetic field is necessary at the last stage to adjust ^{85}Rb scattering length via a Feshbach resonance. The magnetic field amplitude (160 G) is much larger than the trapping magnetic fields. Therefore an optical trap is used to confine the atoms. It is represented on Fig. reffig.chap6.hybridsetup where the mirror MOT and "Z" and "I" wires are represented on top of the reflecting surface. Crossed dipole beams produce the 3D tight confinement used to reach the BEC regime in an external homogeneous magnetic field.

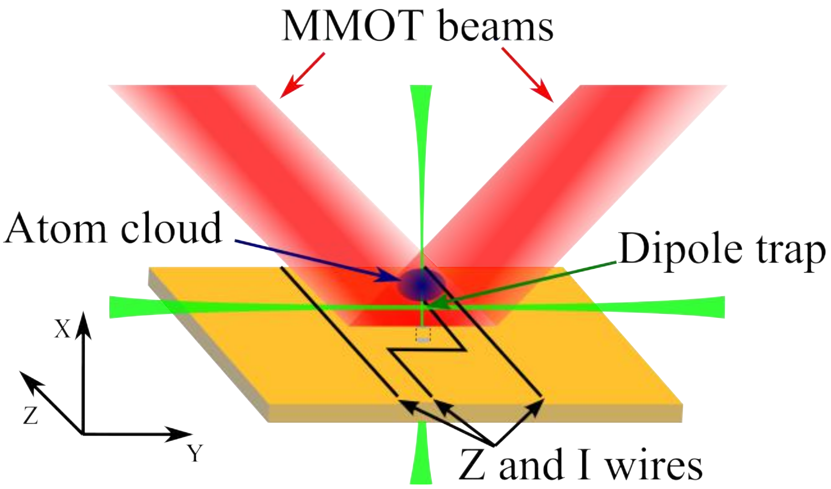

Figure 52: Schematic representation of the chip with the 3D MOT beams reflected on the surface, the atomic cloud, the "Z" and "I" wires as well as the crossed dipole trap.

Before describing the Feshbach magnetic fields characteristics in our experiment, I will briefly present the physical phenomenon of Feshbach resonances as well as the particular case of ^{85}Rb $|2,-2\rangle$ tunable scattering length.

Feshbach magnetic fields

Feshbach resonances are usually [269][270] described in the framework of scattering in a central potential. They consist in a resonant enhancement of the phase shift acquired during the collision which results in the divergence of the scattering length. In this framework, two atoms collides at low energy E_0 in the s-wave and the asymptotic energy of the collisional open channel corresponds to the hyperfine energies of the two atoms. This situation is represented on Fig. 53a where the asymptotic energy of the open channel corresponds to the zero energy point reference. Due to the hyperfine interaction with the nucleus spin, this collisional channel can be coupled to one or more closed channels which are not accessible at these low energies and correspond to different spin states. Only one of these channels is represented on Fig. 53a where one of its bound states E_{bound} is represented in the potential well. This coupling can be resonantly enhanced when the bound state energy is equal to the collisional energy $E_{bound} \longrightarrow E_0$ and results in a superposition with a molecular state during the collision which increases sharply the scattering length. To realize this enhancement, the Zeeman energy term can be used to control the relative position $\Delta E\left(B\right)$ between the two channels. In the basic situation of only one closed channel sufficiently coupled to the open channel, the total scattering cross section can be expressed as the product of the zero magnetic field term a_{bg} and a magnetic field dependent resonant part:

$$a\left(B\right) = a_{bg}\left(1 - \frac{\Delta B}{B - B_{res}}\right)$$

where ΔB is the width of the resonance and B_{res} is the resonance position.

^{85}Rb $|2,-2\rangle$ Feshbach resonance [271] is represented on Fig. 53b. This resonance is broad which means that it is possible to tune ^{85}Rb scattering length to a positive value without unrealistic conditions on the required magnetic field (control of a few $100\,\mathrm{mG}$). In addition, the resonance magnetic field has the advantage of being relatively small. To tune ^{85}Rb scattering length to a reasonable value for evaporative cooling (a few $100\,a_0$ as is the case for ^{87}Rb, see next section) it is necessary to produce a constant magnetic field region around $163\,\mathrm{G}$. At this field value, the scattering length slope is approximately $-50\,a_0/G$ which means that the field has to be homogeneous at the Gauss level to allow for an efficient evaporation.

To produce this homogeneous magnetic field over the evaporation and launching region, we have a pair of horizontal coils of radius R separated by R which is the distance of a Helmholtz configuration. The magnetic field produced at the center of the two coils is given by:

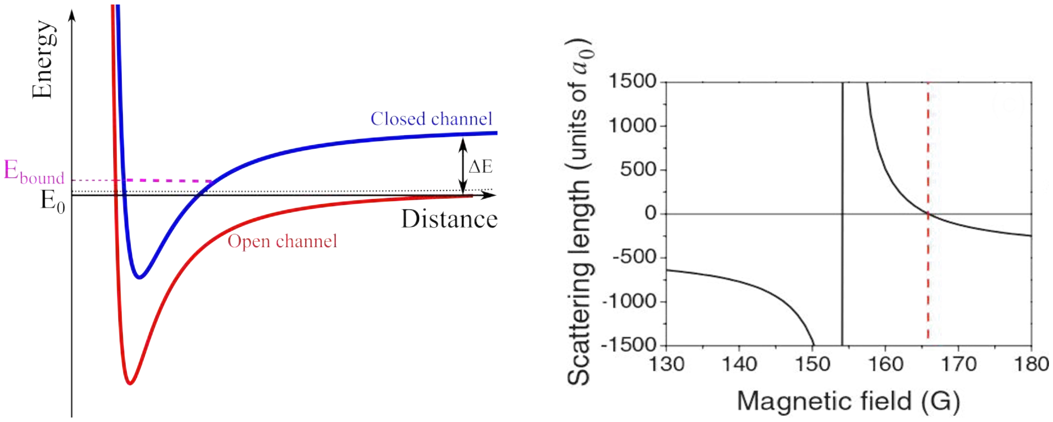

(a) Two channel model

(b) Feshbach resonance of ^{85}Rb $|2, -2\rangle$

Figure 53: **(a)** Open and closed collisional channels in energy unit as a function of the atomic separation. The long range distance ΔE between the closed and open channel can be tuned by adjusting the energy level of the contributing states.
(b) Graph from [271]. The scattering length in unit of Bohr radius around the Feshbach resonance at $B_0 =\sim 155$ G is represented in solid black line.

$$B_{Fesh}(I) = \left(\frac{4}{5}\right)^{\frac{3}{2}} \frac{\mu_0 n I}{R}$$

where $n = 56$ is the number of spires and $I = 32.4$ A is the current. Expanding the magnetic field around its maximal amplitude at the center gives us an idea of the magnetic field variation ΔB_{Fesh} over a distance δz orthogonal to the coils axis:

$$\Delta B_{Fesh} = \frac{3 B_{Fesh} (\delta z)^2}{2R^2} \tag{88}$$

Therefore, at 163 G, the distance over which the magnetic field amplitude remains higher than 162 G is $2/3\sqrt{1/163}R \sim 5\,\%R$ which, for our experimental apparatus, corresponds to 5 mm. This value is in fact overestimated as the real coils have a large (4 cm) thickness in the transverse and longitudinal directions. The real magnetic field will therefore be smoothed over these typical dimensions and the magnetic field variation will be smaller than eq. (88). In addition, its is also possible to sweep the current in the coils during the launching to ensure that the magnetic field is homogeneous over the cloud trajectory. The cloud expansion during and after the fountain launching will need to make sure that the ^{85}Rb cloud is dilute enough that the resonance crossing does not lead to a collapse.

Magnetic fields

High gradients magnetic fields for cooling and trapping as well as homogeneous magnetic fields necessary to tune ^{85}Rb scattering length are produced with a combination of macroscopic coils and wires. The final configuration combines an initially large trapping volume and reduced heating with a compressed trap leading to large collision rates ($1 \times 10^3\,\mathrm{s}^{-1}$). The Feshbach magnetic field of 163 G is produced by large Helmholtz coils ensuring a spatial homogeneity better than 1 G over a 1 cm radius region.

5.3 DUAL ISOTOPES EVAPORATION

In this section, I will present a theoretical model of sympathetic cooling used to estimate the optimal RF cooling trajectory. Different collisional channels, trap parameters (depth η, gradients and lifetime), and initial temperatures will be discussed. Also the two isotopes atom number ratio will show that depending on the final atom number goal, efficient strategies can be implemented.

Forced evaporation was historically first performed on a hydrogen cloud [272] and has been one of the major tools for the achievement of Bose Einstein Condensation. It relies on the cooling induced by thermalization of an atomic ensemble from which the high energy distribution tail is constantly removed. This can be realized with a RF field (frequency ν_{RF}) shone on a cold cloud trapped in a magnetic field potential. This is represented on Fig. 54 where the spatially dependent energy levels of the trapped ($g_F mF = 1$) and untrapped ($g_F mF = -1$) states are represented. By using the appropriate RF field, resonant transitions between these two states can be induced at a fixed energy level. This removes from the trap atoms which have an energy $\eta > 1$ times the mean energy in the cloud and reduces the cloud temperature T_0.

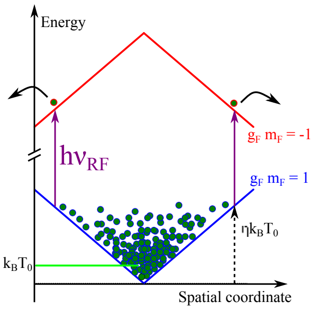

Figure 54
Magnetic potential energy represented for trapping and anti-trapping states.

To quantify the efficiency of this process on a dual isotopes mixture, we are first going to review a theoretical model developed to describe the main evaporation processes which directly affects the evaporation trajectory. Then, a direct extension of this model will allow us to discuss the optimal trajectories for our dual isotopes condensation.

5.3.1 Evaporation principles and power laws

The expression derived here follows directly the lecture notes of Cohen-Tannoudji 1996-1997 [273] given at Collège de France. They give the preliminary structure necessary for the sympathetic description used to simulate our evaporation scheme.

To describe the evaporation process, the atomic cloud is described by the statistical distribution of an ideal gas of identical and independent bosons. The thermodynamic quantities of the ensemble, such as the energy or the density of states, are expressed in terms of the cloud temperature T and atom number N. From this initial description, one can derive three equations which completely describe the evaporation.

1. The first equation is the expression of the total energy E of the gas trapped in a power law potential $U(r) = Cr^{3/\delta}$ having a finite effective depth $\eta = \epsilon_t/(k_B T)$, where ϵ_t is the potential energy at which atoms are no longer trapped. The total energy can be expressed as:

$$E = N\left(\frac{3}{2}+\delta\right)R\left(\frac{3}{2}+\delta,\eta\right)k_BT$$

where $R\left(\frac{3}{2}+\delta,\eta\right) = \Gamma\left(\frac{5}{2}+\delta,\eta\right)/\Gamma\left(\frac{3}{2}+\delta,\eta\right)$ is the ratio of two incomplete Gamma functions which describes the finite height effect of the potential on the energy distribution of the cloud. It is useful to introduce the parameter $\tilde{c} = \left(\frac{3}{2}+\delta\right)R\left(\frac{3}{2}+\delta,\eta\right)$ which collects this dependency and allows to express the energy in a more compact form $E = \tilde{c}Nk_BT$.

2. The second equation accounts for the atomic losses during the evaporation. Three different loss mechanisms dominate the analysis:

   - The atom losses induced by the evaporation (i.e collisions having an output channel of untrapped energy). The resulting atom losses rate is given by:

     $$\left(\frac{dN}{dt}\right)_{evap} = -\Gamma_{ev}N$$

     where $\Gamma_{ev} = \Gamma_{el}e^{-\eta}\left[\eta-\left(\frac{5}{2}+\delta\right)R\left(\frac{5}{2}+\delta,\eta\right)\right]$ is the evaporation rate which is proportional to the elastic collision rate $\Gamma_{el} = n\bar{v}\sigma_{el}$.

   - The atom losses induced by the inelastic collisions (which can be residual background or Oort cloud [274] collisions for example). They are given by:

     $$\left(\frac{dN}{dt}\right)_{inel} = -\Gamma_{inel}N$$

   - The atom losses due to the spilling. This loss mechanism comes from the trap depth lowering usually used to keep η constant[16]. By lowering the trap depth, some atoms are lost before colliding and as such do not contribute to the evaporation process. This term is given by:

     $$\left(\frac{dN}{dt}\right)_{spill} = -\Gamma_{spill}N$$

     where $\Gamma_{spill} = \tilde{\xi}\frac{1}{\tau_{ramp}}$ with $\tilde{\xi} = \left(\frac{3}{2}+\delta\right)\left[1-R\left(\frac{3}{2}+\delta,\eta\right)\right]$ and where τ_{ramp} is a characteristic time of the trapping depth lowering.

3. The third equation results from a detailed analysis of the energetic losses during the evaporation. They correspond to each atomic loss mechanism and can be described by:

---

[16] As the cloud cools, the trap depth becomes a larger fraction of the mean thermal energy k_BT, hence, to keep an effective evaporation process, the depth is adequately lowered.

- The energy loss due to the evaporation process which removes higher energy atoms from the cloud. This is given by:

  $$\left(\frac{dE}{dt}\right)_{ev} = -\Gamma_{ev}\left(\frac{\eta+\tilde{\kappa}}{\tilde{c}}\right)$$

  where $\tilde{\kappa} = 1 - \frac{P\left(\frac{7}{2}+\delta,\eta\right)}{P\left(\frac{3}{2}+\delta,\eta\right)} / \left[\eta - \left(\frac{5}{2}+\delta\right) R\left(\frac{3}{2}+\delta,\eta\right)\right]$ is the average height of evaporated atoms above the potential cut-off (in temperature unit)[17].

- The energy loss induced by inelastic collisions. This is simply:

  $$\left(\frac{dE}{dt}\right)_{inel} = -\Gamma_{inel}E$$

- The energy losses induced by the spilling process which removes atoms with energy ϵ_t:

  $$\left(\frac{dE}{dt}\right)_{inel} = -\frac{\eta\Gamma_{spill}}{\tilde{c}}E$$

From these three equations, one gets a differential system of two equations with two variables (the cloud temperature and number of atoms). This system can be rewritten as a set of two non linear first order differential equations[18]:

$$\begin{aligned} \frac{\dot{T}}{T} &= -\frac{\tilde{\alpha}}{1-\tilde{\alpha}\tilde{\xi}}\Gamma_{ev} \\ \frac{\dot{N}}{N} &= -\frac{1}{1-\tilde{\alpha}\tilde{\xi}}\Gamma_{ev} - \Gamma_{inel} \end{aligned} \tag{89}$$

where $\tilde{\alpha} = \left(\eta + \tilde{\kappa} - \tilde{c}\right) / \left(\tilde{c} + \tilde{\kappa}\tilde{\xi}\right)$. It is convenient to use a different pair of variables which are the peak atomic density and the average relative velocity. They are related to the previous variables by the expressions:

$$\begin{aligned} n &= \frac{N}{\Lambda^3(T)\,\xi(T)\,P\left(\frac{3}{2}+\delta,\eta\right)} \\ v &= \sqrt{\frac{8k_BT}{\pi m}} \end{aligned}$$

---

[17] In the limit of large depth, this parameter takes the simpler form $\frac{(\eta-7/2-\delta)(5/2+\delta)}{\eta-5/2-\delta}$ which is of the order of unity

[18] Indeed, both Γ_{ev} and Γ_{inel} depend on the atomic density and the mean atomic velocity which gives a power law non linear term $NT^{1/2-\delta}$ in both equations.

where $\xi(T) = A_{PL}\Gamma\left(\frac{3}{2}+\delta\right)(k_B T)^{3/2+\delta}$ is the partition function with A_{PL} depending only on the potential strength and the potential exponent[19] δ and the thermal de Broglie wavelength is $\Lambda(T) = \sqrt{2\pi\hbar^2/(mk_B T)}$. The resulting coupled differential equations are:

$$\begin{aligned}\frac{\dot{n}}{n} &= An\nu\sigma - \Gamma_{inel}\\ \frac{\dot{\nu}}{\nu} &= -Bn\nu\sigma\end{aligned}$$

where the coefficients A and B are constant:

$$\begin{aligned}A &= \frac{\delta\tilde{\alpha}-1}{1-\tilde{\alpha}\tilde{\xi}}e^{-\eta}\left[\eta-(\frac{5}{2}+\delta)R\left(\frac{3}{2}+\delta,\eta\right)\right]\\ B &= \frac{\tilde{\alpha}}{2\left(1-\tilde{\alpha}\tilde{\xi}\right)}e^{-\eta}\left[\eta-(\frac{5}{2}+\delta)R\left(\frac{3}{2}+\delta,\eta\right)\right]\end{aligned}$$

This reduced set of equations can be analytically solved when the inelastic collision rate is constant and gives power laws expressions which compare qualitatively with actual evaporation trajectories.

POWER LAW

It is experimentally easier to access the atom number and the cloud temperature than the cloud peak density. Therefore, to simplify the comparison to experiments, evaporation trajectory are usually represented in the (T, N) parameter space. Using eq. (89) one can show that, when the inelastic collisions are negligible, $\frac{T}{N^{\tilde{\alpha}}}$ is a conserved quantity. Hence, in a (T, N) logarithmic plot, the evaporation trajectory will be represented by a straight line with a slope $1/\tilde{\alpha}$.

RUNAWAY EVAPORATION

Another particular feature of the coupled set of equations is the so-called runaway evaporation. This phenomenon is an exponential increase of the evaporation efficiency. This can be directly seen on the elastic collision rate which diverges when two conditions are met:

- The inelastic loss rate is small compared to the initial elastic collision rate :

$$r = \frac{\Gamma_{inel}}{\Gamma_{el,0}} < 0.003$$

- The potential depth is such that the difference $A - B$ is positive and larger than r. This roughly translates to a parameter $\eta \sim 6$ at which $A - B$ is maximum.

---

[19] For example, in an isotropic harmonic trap, $A_{PL} = 1/\left[2(\hbar\omega)^3\right]$

Under these conditions, the phase space density diverges after a finite evaporation duration. Actually, additional inelastic losses increases r but, up to a point, this large increase can be used to reach the BEC regime.

5.3.2 Sympathetic cooling

In our experiment however, we are interested in dual isotopes evaporation and in particular in the initial sympathetic cooling process which allows to cool ^{85}Rb via thermalisation with ^{87}Rb. To simulate this process, I used the previously described theory and added an additional energy loss (or energy gain) term in each isotopes energetic analysis which takes into account the inter-isotopes elastic collisions. In practice, I considered two atomic clouds of temperatures T_{87} (resp. T_{85}) and atom number N_{87} (resp. N_{85}). The collision rate between these two atomic clouds is[20] be proportional to the inter-isotopes elastic cross section σ_{dual}, to the standard deviation between the two clouds velocity $\sqrt{v_{87}^2+v_{85}^2}$ and to the other isotopes density (n_{85} for the inter-isotopes collision rate of ^{87}Rb for example). Taking into account the simplest collisions which equally redistribute the energy between the two collisional partners, which is a good approximation in the case of two isotopes with very similar masses, we get the additional energy rate:

$$\left(\frac{dE_{87}}{dt}\right)_{dual} = \frac{T_{87}-T_{85}}{2T_{87}}\frac{1}{N_{87}}\sigma_{dual}\sqrt{v_{87}^2+v_{85}^2}\,n_{85}E_{87}$$

and a similar term for ^{85}Rb with inverted subscripts. Unraveling the exact same derivation, this sympathetic term resulted in a coupling term between the differential system of ^{87}Rb and the one of ^{85}Rb. This coupling can be expressed by:

$$\begin{aligned}
\dot{n}_{87} &= A_{87}n_{87}^2v_{87}\sigma - \Gamma_{inel,87} + C_{87}\sigma_{dual}\frac{v_{87}^2-v_{85}^2}{2v_{87}^2}\sqrt{v_{87}^2+v_{85}^2}\,n_{85}n_{87} \\
\dot{v}_{87} &= -B_{87}n_{87}v_{87}^2\sigma + D_{87}\sigma_{dual}\frac{v_{87}^2-v_{85}^2}{2v_{87}^2}\sqrt{v_{87}^2+v_{85}^2}\,n_{85}v_{87}
\end{aligned}$$

where the isotopes dependent constants A_{87}, B_{87}, C_{87} and D_{87} have been explicitly labelled with their corresponding isotope because the trapping potential height can depend on isotope specific parameters (such as the magnetic sublevel). The new constant coefficients are given by:

$$C_{87} = \frac{\tilde{\alpha}\tilde{\xi}}{1-\tilde{\alpha}\tilde{\xi}}\frac{\tilde{c}}{\tilde{c}-\eta-\tilde{\kappa}} \tag{90}$$

$$D_{87} = \frac{\tilde{\alpha}}{2\left(1-\tilde{\alpha}\tilde{\xi}\right)}\frac{\tilde{c}}{\tilde{c}-\eta-\tilde{\kappa}} \tag{91}$$

---

[20] See [275] for a description of molecular dynamics for example.

and a similar pair of differential equations holds for ^{85}Rb. Due to the temperature dependent elastic cross section of ^{85}Rb, I did not try to find an analytical solution of this coupled set of equations and used numerical integration.

Comparison with existing experiments

I tested this theoretical model with the experimental results published by Bloch *et al.* [254] and by Altin *et al.* [276]. In these two papers, sympathetic cooling in a magnetic trap between the two isotopes of Rubidium is described and the corresponding evaporation trajectories are represented on Fig. 55. These two experiments have collisional parameters relatively different because they do not use the same hyperfine sublevels for each isotopes.

1. In [254], ^{85}Rb is in the $|F = 3, m_F = 3\rangle$ state and ^{87}Rb is in the $|F = 2, m_F = 2\rangle$ state, this collisional channel will be labelled channel $(3, 2)$. The magnetic potential experienced by these two states are identical and only the isotope selective RF transitions induces differential losses between the two isotopes. In practice this led to isotope specific depths and the corresponding η_{87} and η_{85} truncation parameters.
2. In [276], ^{85}Rb is in the $|F = 2, m_F = -2\rangle$ state and ^{87}Rb is in the $|F = 1, m_F = -1\rangle$ state, this collisional channel will be labelled channel $(-2, -1)$. The magnetic potential experienced by ^{85}Rb is a factor $4/3$ larger than the one experienced by ^{87}Rb which contributes to the isotope selective RF transitions because ^{85}Rb density is reduced at the resonance position of the RF frequency. In this situation, both the potential strengths and the truncation parameters were isotopes specific.

To simulate these experiments, I used collisional properties available in the literature [276]–[279] summarized in Tab. 13, as well as the temperature dependent behavior of ^{85}Rb elastic cross section described by Burke *et al.* in [278]. The elastic cross section of ^{87}Rb does not significantly change (appart from a factor 2 increase around $400\,\mu$K) and was kept constant $\sigma = 8\pi a_{T,87}^2$ where $a_{T,87} = 106a_0$ [254]. So does the dual isotopes elastic cross section $\sigma_{dual} = 4\pi a_{T,87-85}^2$ where $a_{T,87-85} = 240a_0$(channel $(3, 2)$) $= 200a_0$ (channel $(-2, -1)$). The three body losses were not taken into account in the channel $(3, 2)$ due to the dominant two body loss rate. Inelastic losses induced by background collisions are also taken into account by adding to the inelastic collision rate a constant loss rate proportional to the inverse of the vacuum lifetime τ_{vac}.

The result of the numerical simulations are presented on Fig. 55c and Fig. 55d. Due to the large number of experimental parameters approximately known (such as the cloud lifetime and initial temperature in the case of Bloch's experiment or the truncation parameter during the evaporation process), these simulations can only serve as a qualitative test for our model. However, in both situations, the evaporation trajectories are well described by our numerical results and similar atom numbers are obtained (around 2×10^7 atoms of both isotopes at $20\,\mu$K for Fig. 55c and 2×10^6

Hyperfine sates	^{85}Rb $\vert F=3, m_F=3\rangle$ ^{87}Rb $\vert F=2, m_F=2\rangle$	^{85}Rb $\vert F=2, m_F=-2\rangle$ ^{87}Rb $\vert F=1, m_F=-1\rangle$
K_e	$1\times10^{-14}\,\mathrm{cm^3\,s^{-1}}$ $2\times10^{-16}\,\mathrm{cm^3\,s^{-1}}$	$3\times10^{-18}\,\mathrm{cm^3\,s^{-1}}$ $3\times10^{-18}\,\mathrm{cm^3\,s^{-1}}$
$K_{e,intra}$	$1\times10^{-15}\,\mathrm{cm^3\,s^{-1}}$	$3\times10^{-18}\,\mathrm{cm^3\,s^{-1}}$
K_3	Unavailable	$5\times10^{-29}\,\mathrm{cm^6/s}$ $4\times10^{-29}\,\mathrm{cm^6/s}$

Table 13: Collisional coefficients used in the numerical simulation.

^{87}Rb atoms and 10^6 ^{85}Rb atoms at 4 µK for Fig. 55d) . In particular, the decrease of the sympathetic cooling efficiency when the number of atoms in each isotopes becomes comparable is well represented on Fig. 55c where the losses of ^{85}Rb rapidly increases when the number of ^{87}Rb becomes smaller. In addition, the larger atom loss in the channel $(3,2)$ at higher temperature of ^{85}Rb in Fig. 55d coincides with the experimental losses. These losses are due to the much larger[21] two body inelastic coefficient K_e. One important feature not represented by this numerical simulation is the slope change in the number of ^{87}Rb when the two isotopes have similar atom numbers. This feature can be understood by the gravitational sag neglected in our model which displace the two atomic clouds by a small amount. When the cloud's size decreases due to larger atomic densities at lower temperature, which corresponds to the situation in 55b around 1 µK for example, the elastic collisions between the two isotopes happens only in the two distributions tails which reduces the efficiency of sympathetic cooling. Also Majorana losses were not included in this model because non-zero magnetic minima were used in both experiments. This loss channel becomes important at low temperature which might explain the higher loss rate of both ^{87}Rb trajectories.

5.3.3 Simulation of our setup

In order to dimension properly our magnetic traps, we used this model to have a general idea of the possible evaporation strategies. The first question we had to address was which atomic state were we going to use ? The choice of the ^{85}Rb $|F=2, m_F=-2\rangle$ and ^{87}Rb $|F=1, m_F=-1\rangle$ levels was advantageous for its low inelastic loss properties, its higher RF selectivity during the evaporation and corresponds to the magnetic states exhibiting the Feshbach resonance necessary to finish the evaporation in the optical trap. On the other hand, the ^{85}Rb $|F=3, m_F=3\rangle$ and ^{87}Rb $|F=2, m_F=2\rangle$ levels have a higher Landé factor $g_F m_F = 1$ and experience larger trapping potentials which allows to evaporate faster.

For typical magnetic fields such as the one presented on Fig. 50 with gradients of $b_0 = 200\,\mathrm{G/cm}$ and bottom frequencies of $\omega_0 = 200\,\mathrm{Hz}$ we simulated typical evaporation trajectories for both magnetic levels. The typical dynamic lengths in this

---

[21] As can be seen in Tab. 13 the loss rate is larger by two order of magnitudes compared to ^{87}Rb and almost four order of magnitudes compared to the $|F=2, m_F=-2\rangle$ magnetic state

situation (either harmonic oscillator length or first zero of the Airy function) are of the order of 1 µm. The theoretical model of coupled differential equations assumes that the dynamic remains in the collisionless regime. Indeed, in order to derive eq. (89), it was assumed that a collision producing an atom with an energy higher than $\eta k_B T$ necessarily lead to removal from the trap. This assumption translates into an atom mean free path much larger than the typical distance of a round trip in the trap which approximately corresponds to the "dynamical length". In our simulation, the atom mean free path will always be larger than 10 µm which ensures that our model remains valid throughout the evaporation. But before discussing the result, let us describe in more details the numerical simulation details.

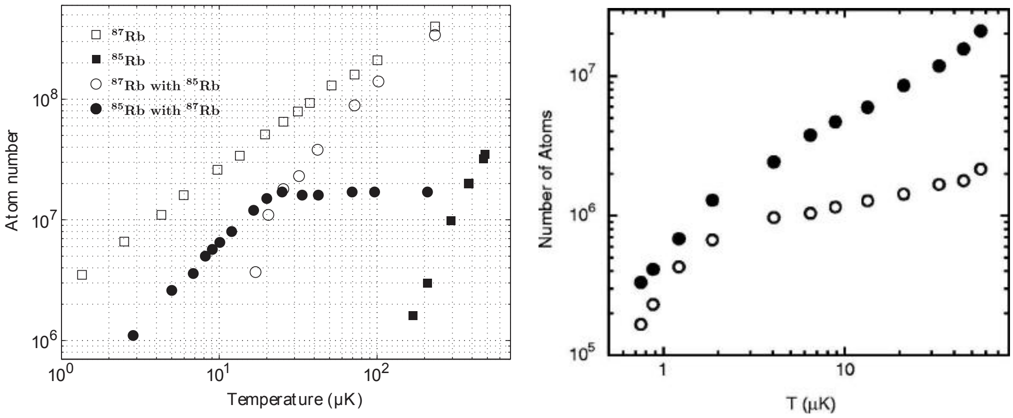

(a) Experimental trajectory from [276] **(b)** Experimental trajectory from [254]

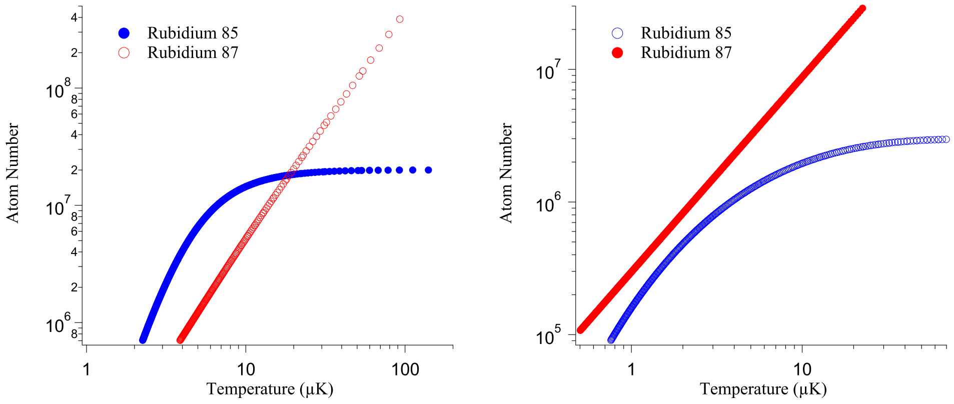

(c) Simulated cooling trajectory of [276] **(d)** Simulated cooling trajectory of [254]

Figure 55: **(a)** Figure from [276]. Approximately 10^9 ^{87}Rb atoms and 2×10^7 ^{85}Rb atoms are loaded into a cigar shaped trap having a mean frequency of 73 Hz. The vacuum lifetime is approximately 20 s and corresponds to the main source of inelatic losses.
(b) Figure from [254]. 8×10^8 ^{87}Rb atoms and 3×10^6 ^{85}Rb atoms are loaded into a cigar shaped trap having a mean frequency of 105 Hz. The number of atoms for two atomic isotopes (black dots, ^{87}Rb and white dots, ^{85}Rb) as a function of the cloud temperature.
(c) and **(d)**: Corresponding simulated evaporation trajectories.

Description of the numerical simulation

We use the coupled set of equations previously describedand start with an initial number of atoms $N_{87,\mathrm{ini}} = 5 \times 10^8$ and $N_{85,\mathrm{ini}} = 10^7$. Both cloud temperatures T_{87} and T_{85} are initially identical and corresponds to the temperature of the cloud in a compressed magnetic trap. A conservative value of 400 µK corresponds to the typical parameters b_0 and ω_0. The background collision rate is fixed at $0.02\,\mathrm{s}^{-1}$. From this initial cloud, we start the evaporation at constant $\eta_{\mathrm{lin}} = 6$ in a linear trap. As the temperature drops, the linear approximation begins to fail because the atoms lies at the bottom of the trap. To distinguish between the linear and the quadratic regime, we stop this first step when the phase space density in both traps are equal[22]. From this final state, a new evaporation simulation starts in a pure harmonic trap with an identical $\eta_{\mathrm{quad}} = 6$. The evaporation is continued until the cloud temperature drops to 5 µK which defines the final state. This double stage evaporation simulation could have benefited from an analytical expression of the density of states which provides a unified description in between the two limiting cases. This was done for the case of a bi-dimensional Ioffe Pritchard trap [280]. However, our trap geometry is not well approximated by simple analytical formulas as it results from the complex combination of three wires and two external fields (see Sec. 5.2.2). But the numerical results presented in [280] show that the transition between the two evaporation regime happens precisely when the cloud temperature is equal to U_0/k_B, where U_0 is the IP trap minimum. Analytically, I found that this temperature corresponds exactly to situation where the phase space density in the 2D linear trap is equal to the phase space density in the 2D harmonic trap. Therefore, our criteria seems reasonable.

Magnetic states comparison

Figure 56 presents different evaporation trajectories of the two possible collisional channels $(3,2)$ and$(-2,-1)$. On Fig. 56a, one sees the transition point between the linear and quadratic traps around 100 µK for the first channel and 50 µK for the second channel. This is due to the fact that less ^{87}Rb atoms are lost during the first evaporation in the linear trap (the phase space density is linear in the atom number) and because the trap is less confining in the second channel. In both cases, the evaporation is in the runaway regime and typically, about 90 % of the evaporation duration is in the linear trap. It appears that the second channel results in a much larger ^{85}Rb atom loss than the first channel. This is because the main atom loss mechanism in this channel are the background collisions[23]. Therefore, the atom losses scales linearly with the evaporation duration which is 6 times longer, resulting in much larger ^{85}Rb losses. Note the similar behavior at high temperature of ^{85}Rb atom number in the first channel with the beginning of an exponential decrease prevented by the accelerating evaporation efficiency.

---

[22] The phase space density in a quadratic trap behaves as T^{-3} while the phase space density in a linear trap evolves as $T^{-9/2}$. Hence, as the temperature drops, the linear phase space density increases faster than the quadratic phase space density which explains the existence of this transition point.

[23] Apart for ^{85}Rb in the first channel for which at typical initial density of $1 \times 10^{12}\,\mathrm{cm}^{-3}$ the inelastic loss rate is similar to the background loss rate $\sim 0.01\,\mathrm{s}^{-1}$

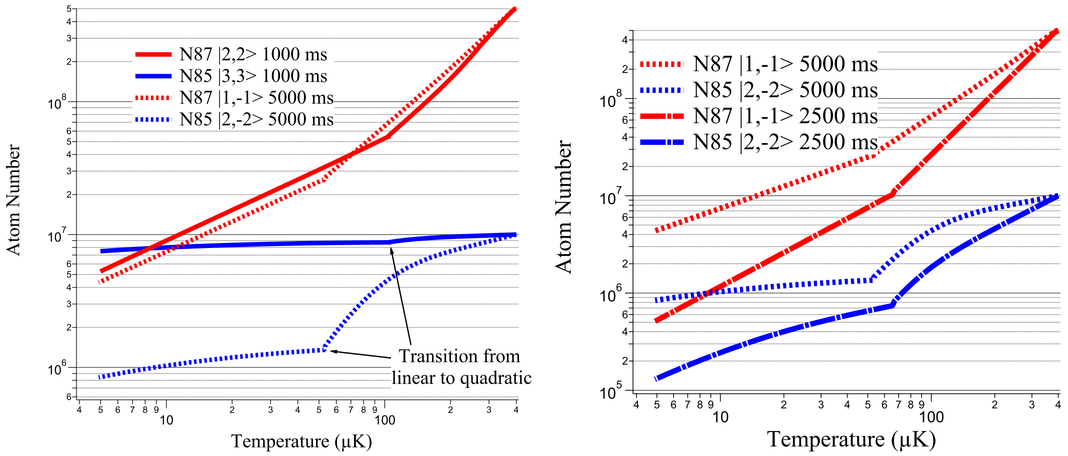

(a) Different collisional channels **(b)** Different η

Figure 56: (a) Comparison of the two possible collisional channels used during the evaporation. The atom number of each isotopes is represented as a function of the cloud temperature. The total duration of the evaporation is indicated in the legend for each channel.
(b) Comparison of two evaporation trajectories in the collisional channel 2. The dashed line correspond to an evaporation at $\eta = 6$ and the dot-dashed line correspond to an evaporation at $\eta = 4$.

On Fig. 56b a faster evaporation scheme was chosen in the second channel to try to bypass this initial large atom loss. An evaporation at $\eta = 4$ is represented which does not result in a runaway evaporation but was approximately half as long as the initial trajectory. As expected, this less efficient evaporation does not lead to less atom losses, but it can reduce the evaporation time which is critical to get a high repetition rate. This faster cold cloud production leads to approximately 90 % atom losses which is not realistic if the final atom number is critical.

Before concluding on this aspect, let us first discuss the issue of magnetic state preparation. Indeed, pumping atoms in the ^{85}Rb $|F = 3, m_F = 3\rangle$ magnetic state (and the corresponding one for ^{87}Rb atoms) is straightforward when starting from an optical molasses. It is also possible to pump atoms in the lower hyperfine level ^{85}Rb $|F = 2, m_F = -2\rangle$ but the polarization required to produce a dark state are different for the two pump frequencies. By adjusting the initial MOT loading, we can however reasonably expect to be able to control the initial atom number loaded in the magnetic trap in any of the chosen magnetic state. If we start the evaporation in the first channel, we will need to implement some coherent state transfer (such as STIRAP protocols which where demonstrated to be possible directly in magnetic traps [281]) but the transfer to an opposite magnetic orientation have additional difficulties (such as the transitional non trapped state $|F = 3, m_F = 0\rangle$) and can lead to large atom loss during the transfer. A possible solution would be to implement this magnetic transfer in the optical dipole trap but inelastic losses due to the large atomic density can lead to significant atom losses during the transfer.

Therefore, it is not clear whether we should use the first collisional channel or the second one in terms of final atom number. But in terms of evaporation duration of the order of, or smaller than, 1 s only the first evaporation channel seems reasonable with the current magnetic fields. However, as is represented on Fig. 57, quick evaporation in the second channel is possible with higher gradients of $b_1 = 350\,\mathrm{G/cm}$ and trapping frequencies of 300 Hz. These values simply compensate for the smaller Landé factor and the resulting evaporation trajectory is similar to the one in channel 1 with smaller magnetic fields which is represented on Fig. 56a.

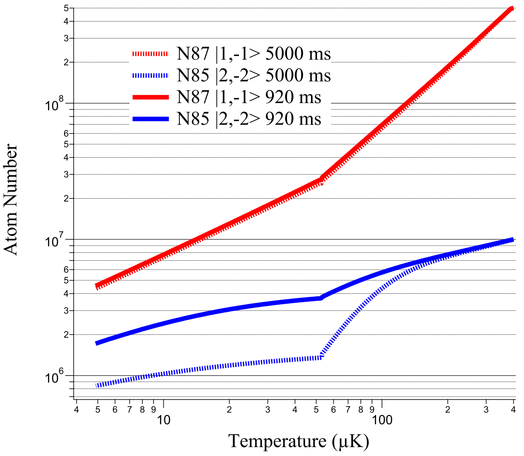

Figure 57: Different traps:
Dashed line:b_0=200 G/cm, $\omega_0/(2\pi)$=200 Hz
Solid line:b_1=350 G/cm, $\omega_1/(2\pi)$=300 Hz

Temperature, background collisions and atom ratio influence

With these evaporation trajectories, high final phase space densities are reachable in reasonable times. For example, the phase space density in the collisional channel 1 is 3×10^{-3} at the final temperature of 5 μK. With this density, we will see in the next section that Bose Einstein Condensation in the final optical trap is reachable. But let us first discuss the effects of the initial temperature, the background collision rate or the initial ^{85}Rb atom numbers.

To quantify these effects, I simulated the evaporation trajectory in the channel 1. The result of these simulations are represented on Fig. 58. and Fig. 59

What we learn from these trajectories is that the initial temperature is decisive. As can be seen on Fig. 58a, an initial cloud of 600 μK needs 6 times more time to cool down to 5 μK than a 400 μK one. It also leads to a final atom number 10 times smaller for ^{87}Rb and 5 times smaller for ^{85}Rb. This comes from the fact that a smaller initial number of ^{85}Rb was used in this situation. Indeed, keeping 10^7 ^{85}Rb in the initial cloud prevented to achieve a 5 μK temperature because the thermal load of ^{85}Rb on the ^{87}Rb cloud was too large and could not be efficiently cooled down below 100 μK, which corresponds to the temperature at which the elastic collision rate of ^{85}Rb starts to become comparable to the one of ^{87}Rb allowing ^{85}Rb to starts evaporating on its own. This is mainly due to the longer evaporation time in the linear trap which leads to large losses from background collisions. As expected, a lower initial temperature of 200 μK leads to a much faster evaporation and a higher ^{87}Rb final number.

Figure 58b presents the result of different background collision rates. We see that the evaporation trajectory is not too sensitive to the inelastic losses induced by the surrounding vacuum. However, when the lifetime approaches the evaporation duration, this parameters starts to reduce the evaporation efficiency as expected by the

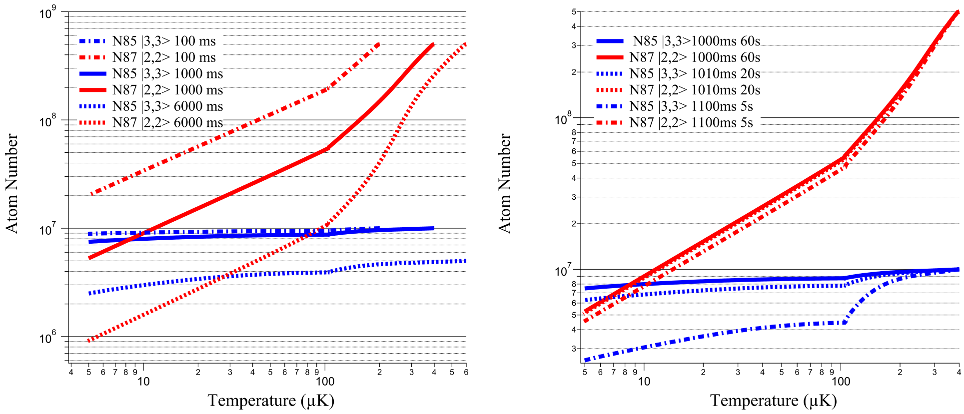

(a) Different initial temperature **(b)** Different background collision rates

Figure 58: **(a)** Evaporation trajectories for different initial temperatures (dash-dotted: 200 µK, solid line: 400 µK, dashed line: 600 µK).
(b) Evaporation trajectories for different background collision rate (the lifetime is indicated in the legend). As long as the evaporation time is much smaller than the background lifetime, it has little consequences on the final state and/or the evaporation time.

induced loss of low energy atoms, preventing the thermalisation to a lower temperature. The evaporation time slightly increases too but this effect is at most of the order of 10 %.

Finally, the effect of the initial ^{85}Rb atom number is represented on Fig. 59. I represent the final atom number ratio N_{85}/N_{87} as well as the evaporation time for some of these points. An important feature is that the initial ^{85}Rb atom number mainly influence the duration of the evaporation. Indeed, the final number of ^{87}Rb changes by 40 % when the number of ^{85}Rb atoms is multiplied by 10. But it does not change its efficiency as the evaporation remains in the runaway regime. Additionally, one can see that increasing the initial number of ^{85}Rb atoms tends to slow the evaporation process. Therefore, this initial atom number has to be carefully optimized to produce the desired condensate. On the other hand, controlling the final ratio of the two atomic isotopes atom number can be crucial for some experiments because the dual isotopes cloud shape and miscibility [282], [283] depends on this ratio. This theoretical model might allow to optimize the evaporation strategies according to the desired final ratio.

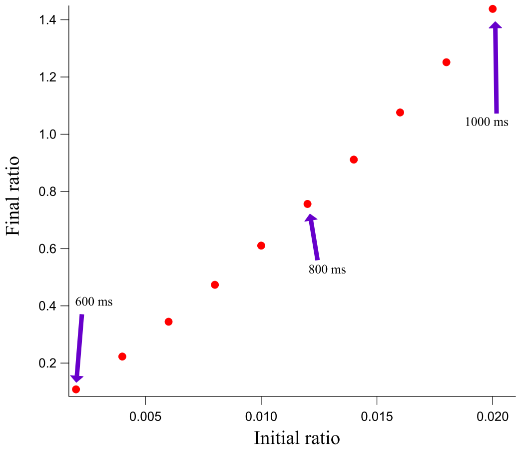

Figure 59
Final atom number ratio $N_{85,\mathrm{final}}/N_{87,\mathrm{final}}$ as a function of the initial atom number ratio $N_{85,\mathrm{ini}}/N_{87,\mathrm{ini}}$. The evaporation duration for initial ratios of 0.002, 0.012 and 0.02 are represented besides the points.

Transfer to the dipole trap

To reach the BEC regime with both isotopes, we need to finish the evaporation in a Feshbach magnetic field. The ultra-cold atomic cloud obtained at the end of this first evaporation will be transferred into a pure optical dipole trap (ODT)[24]. This trap will be produced by crossed laser beams described in Sec. 6.3.2. To transfer the majority of atoms into the ODT, its size must not be too small compared to the initial cloud[25]. An interesting feature of this transfer is the continuous evaporation of atoms trapped in the ODT. This leads to an optically trapped cloud with a temperature similar to the previous temperature in the magnetic trap[26]. Since the trapping frequencies in the dimple are usually higher than the one in the magnetic trap, this leads to a phase space density increase proportional to the ratio of the final frequency over the initial frequency to the cube.

Condensation in Feshbach magnetic field

To estimate the final evaporation trajectory, I use a conservative atom number of 2×10^6 at a temperature of $5\,\mu K$. It corresponds either to he final atom number presented on Fig 56b (channel 2) or to the final atom number presented on Fig 58b (channel 1) with an additional atom loss due to the transfer to the right magnetic state. The most common strategy for evaporation in an ODT consists in decreasing the potential depth to keep the evaporation threshold η constant. Scaling laws for this evaporation process lead to [286]:

$$\begin{aligned}\left(\frac{N_f}{N_i}\right) &= \left(\frac{U_f}{U_i}\right)^{3/\left[2\left(\eta'-3\right)\right]}\\ \left(\frac{D_f}{D_i}\right) &= \left(\frac{U_f}{U_i}\right)^{3\left(\eta'-4\right)/\left[2\left(\eta'-3\right)\right]}\end{aligned}$$

where i (resp. f) denotes the initial (resp. final) state, U is the optical potential depth and $\eta^{'} = \eta + (\eta - 5)\,/\,(\eta - 4)$. To reach quantum degeneracy, the phase space density has to attain the well known value of 2.612 which will be our final state criterion for this last step. The initial phase space density (PSD) in our optical trap is of the order of 2×10^{-2} at the beginning of the evaporation (with trapping frequencies of 500 Hz). Therefore, a factor 130 on the PSD is needed to reach degeneracy. With a trapping depth[27] $\eta = 7$, this means that the optical potential has to be lowered by a factor 65 which corresponds to a final depth of 550 nK. At this stage, the number of atoms remaining is 4×10^5 at a temperature of 50 nK. The duration of this stage is governed

---

[24] We note however that without ^{85}Rb atoms, our simulated final phase space densities of ^{87}Rb, which are close to the condensation threshold, allow to reach condensation without additional evaporation (as described in [284]) in the ODT.

[25] In [285], they found that almost all Cesium atoms were transferred into the dimple when its radius was larger than $150\,\mu m$ which is to be compared to the cloud initial radius of $325\,\mu m$ corresponding to a ratio of 1/2. In our situation, the initial cloud radius will be approximately $140\,\mu m$ which constrains the dimple radius to $70\,\mu m$

[26] It can even be smaller due to "evaporation" (or loss) of atoms in the tail of the magnetic trap.

[27] Which corresponds to a trade-off between speed and efficiency.

by the initial elastic collision rate[28] $\Gamma_{el} \sim 770\,s^{-1}$ and corresponds approximately[29] to 3 s.

5.3.4 Comparison with other BEC machines

The atomic cloud trajectory summarized in Tab. 14 can be compared, in terms of condensed atom production rate, with existing setups using either all optical setups [287], [288], atom chips [78], [220], [289]–[291] or hybrid setups for dual isotopes [67], [282]. Figure 60 summarizes the performances of these experiments and we can see that our estimation seems reasonable. It is similar to the fastest BEC machine for a single isotope configuration (not described) and is expected to perform as efficiently as the recent ^{85}Rb/^{87}Rb all optical BEC machine of [67].

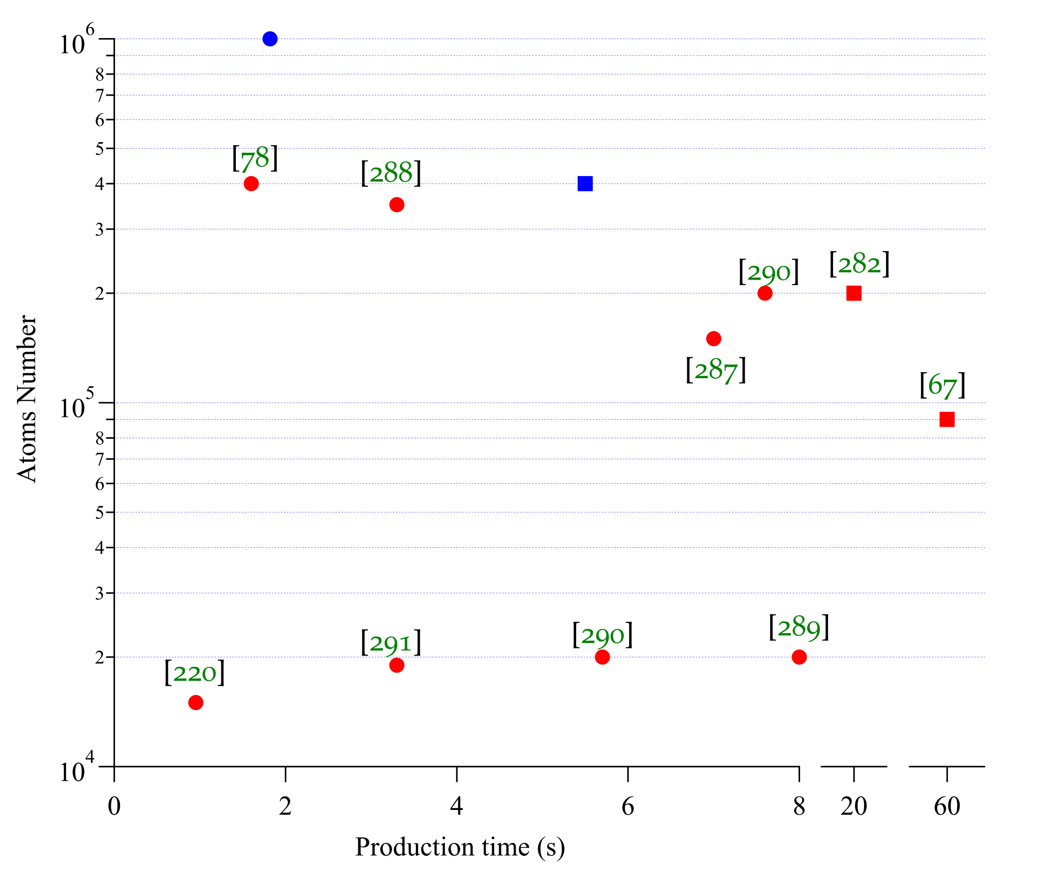

Figure 60: Demonstrated high production rates ($\leqslant$ 8 s,circles) of ^{87}Rb BEC sources, adapted from [78]. All dual isotopes sources ^{85}Rb/^{87}Rb are also represented (squares). The red points correspond to published experiments (notice the temporal axis break for dual experiments) and the blue points correspond to the characteristics infered from our simulations. Our dual evaporation is calculated to perform much faster than the two published experiments [67], [282] thanks to the fast loading rate and the tight initial magnetic trap.

---

[28] Weighted by $2e^{-\eta}(\eta - 4)\eta'/3$ and by a correction factor taking into account inelastic losses during the evaporation process.

[29] As we will see in the next section, our crossed dipole beams have a large waist difference which we could use to implement a runaway optical evaporation [287] by controlling the trap depth with the large beam while keeping the larger trapping frequencies with the smaller beam. The duration and efficiency of this stage could therefore benefit from further investigations.

Evaporation

We combine sympathetic RF evaporation in a tight ($b_0 = 200\,\mathrm{G/cm}$, $\omega_0/(2\pi) = 200\,\mathrm{Hz}$) magnetic trap and induced evaporation in a crossed dipole trap ($\bar{\omega}/(2\pi) = 500\,\mathrm{Hz}$) to produce a large $^{87}\mathrm{Rb}/^{85}\mathrm{Rb}$ BEC. To quantitatively estimate this setup performances, a sympathetic cooling numerical model was developed and simulated successful evaporation strategies over a wide range of initial parameters (Hyperfine state, atom number, temperature, trap depth). The different evaporation steps of a reasonable strategy are summarized in the following Table.

Production step	N $^{87}\mathrm{Rb}/^{85}\mathrm{Rb}$	T	PSD	Time
3D MOT	1×10^{9} / 2×10^{7}	50 μK	5×10^{-7}	1 s
MT	5×10^{8} / 1×10^{7}	200 μK	1×10^{-6}	1.05 s
CMT	5×10^{8} / 1×10^{7}	400 μK	1×10^{-6}	1.15 s
Evaporated CMT	5×10^{6} / 2×10^{6}	5 μK	3×10^{-3}	2.15 s
DT	2×10^{6} / 1×10^{6}	5 μK	2×10^{-2}	2.5 s
Evaporated DT	4×10^{5} / 2×10^{5}	0.05 μK	2.612	5.5 s

Table 14: Summary of the cloud characteristics during its different preparation stages.

5.4 CLOUD TRANSPORT IN AN OPTICAL LATTICE

Then, the transport from the optical trap to the launching position will be the subject to particular focus as numerical simulations were performed to ensure the feasibility of the planned strategy. Finally, some details about dual isotopes launching in accelerated lattices will be discussed.

One of the major advantages of an atom chip BEC source is the tight magnetic trapping potentials resulting from the proximity to the wires. In our case, this becomes an inconvenient because of the lattice and Bragg beams which are diffracted by the surface.

A transportation scheme using an optical guide coupled to a moving lattice was considered because a high degree of control of the final cloud position and velocity. It was necessary to prevent fluctuations in the fountain trajectories and in the diffraction efficiencies. Its principle relies on the possibility to load a BEC in an optical lattice, to accelerate and decelerate the latter, and to unload the condensate in its final position while keeping the phase coherence of the condensate. This type of manipulation can be viewed as optical Bloch oscillations [292], [293] which we are going to describe first (for a recent description see P. Cladé chapter in [16]). Then the transport procedure will be described and its main impediments will be emphasized. The numerical model used to simulate this transport and their results will conclude this section.

5.4.1 Bloch oscillations

Let us consider the simplest case of a single atom interacting with two counter-propagating laser beams in a 1D model. The total electric field is the sum of two sinusoidal terms:

$$\mathcal{E}_{tot} = \mathcal{E}_1 \cos\left(k_1 z - \omega_1 t + \phi_1\right) + \mathcal{E}_2 \cos\left(-k_2 z - \omega_2 t + \phi_2\right)$$

where $\mathcal{E}_i$ are the field amplitudes, ω_i their frequencies, k_i their wavevector amplitude and ϕ_i their reference phase. Assuming for simplicity an equal amplitude $\mathcal{E}_0$, we can factor this into:

$$\begin{aligned}\mathcal{E}_{tot} = 2\mathcal{E}_0 \cos&\left[\frac{\left(k_1 + k_2\right) z - \left(\omega_1 - \omega_2\right) t + \left(\phi_1 - \phi_2\right)}{2}\right] \\ &\times \cos\left[\frac{\left(k_1 - k_2\right) z - \left(\omega_1 + \omega_2\right) t + \left(\phi_1 + \phi_2\right)}{2}\right]\end{aligned}$$

If the frequency difference $\omega_2 - \omega_1 = \Delta\omega$ is small compared to the optical frequencies $\Delta\omega \ll \omega_i$ the total electric field oscillates at the optical mean frequency $\omega_1 + \Delta\omega/2$ with an effective phase $\left(\phi_1 + \phi_2\right)/2$ and a spatially dependent amplitude. As was described in Sec 1.2, if the frequencies are far detuned from the atomic resonance frequency $\omega_i - \omega_0 = \Delta \ll \Gamma$ the atom-light interaction can be expressed as:

$$\hat{V}_{eff} = \frac{\hbar\Omega_{eff}}{2}\left[1 - \cos\left(2k_{eff}\hat{z} + \Delta\omega t + \bar{\phi}\right)\right] \tag{92}$$

where $k_{eff} = \left(k_1 + k_2\right)/2$ and $\bar{\phi} = \left(\phi_1 - \phi_2\right)/2$. This corresponds to an optical lattice having a spatial periodicity π/k_{eff} moving in the $-z$ direction at a constant velocity $\Delta\omega/\left(2k_{eff}\right)$.

Assuming $\Delta\omega = 0$, we can describe the atomic wave-function using the Bloch theorem. The potential periodicity allows to describe the atomic wave-function, solution to the effective Hamiltonian $\hat{H}_{eff} = \hat{p}^2/\left(2m\right) + \hat{V}_{eff}\left(z, t\right)$, with the Bloch basis:

$$\Psi_q^n\left(z\right) = u_q^n\left(z\right) e^{iqz}$$

where q is the atomic quasi-momentum[30] defined by the atomic momentum modulo k_{eff} and $u_q^n\left(z\right)$ are periodic functions solutions to the eigenvalues equation:

---

[30] The physical interpretation of this quantity is not straightforward as the momentum is not a conserved quantity in presence of an external force. This is the reason why an "effective" momentum, q, is introduced which represents only partially the atomic motion but corresponds to a "good" quantum number when treating the effect of the potential on the atom. To recover the atomic momentum, one has to combine both n and q to retrieve $k = q + nk_{eff}$ which will represent an atomic eigenstate in free flight.

$$H_{eff}u_q^n(z) = E_q^n u_q^n(z)$$

The eigen-energies E_q^n are labelled with their band index n and are usually represented in the first Brillouin zone (corresponding to $q \in [-k_{eff}, k_{eff}]$) as can be seen on Fig. 61 where multiple Brillouin zones have been represented. When the lattice is at rest, the problem is time independent and an atom having an initial quasi-momentum q_0 will remain in a superposition of $u_{q_0}^n(z)$.

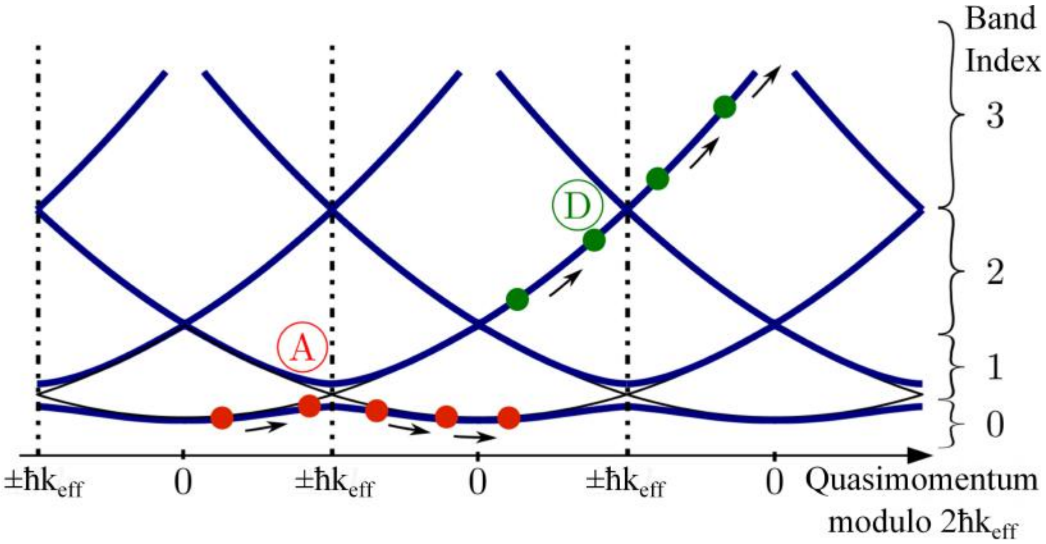

Figure 61: Figure adapted from [294]. The band structure of an accelerated lattice is represented as a function of q and the lattice wave-vector. Two different transfers at the Brillouin sides are represented corresponding to adiabatic (**A**) and diabatic (**D**) trajectories.

However, when one includes the lattice translation in the z direction with a frequency difference $\Delta\omega(t)$, one can show that an atom initially in the lowest energy band will follow the lattice. Its velocity, in a semi-classical picture, will be given by:

$$v(t) = v_0 + \frac{\Delta\omega(t) - \Delta\omega(t_0)}{k_{eff}} \tag{93}$$

where v_0 is the atomic initial energy at $t = t_0$. This acceleration is known as Bloch oscillations and originate from the adiabatic passage at the Brillouin borders of the atomic wavefunction. This transfer ensures that the atomic wave-function follows the lowest energy band, in the reference frame of the lattice. It is also possible to represent this velocity change as stimulated absorption and emission from one laser to the other. The subsequent recoil velocities imparted to the atom changes its motion by discrete amounts proportional to $2v_{rec} = 2\hbar k_{eff}/m$. Therefore, eq. (93) is only approximate as it does not take into account the discrete nature of photon transfer between the atom and the electric field. When the semi classical velocity is not congruent with the initial velocity modulo $2v_{rec}$, the final atomic state will be in a coherent superposition of two momentum states $k_0 + 2pk_{eff}$ and $k_0 + 2(p+1)k_{eff}$, where p is the integer part of $[\nu(t) - \nu_0] / (2\nu_{rec})$.

Additionally, this description does not take into account the number of non adiabatic transitions at each transfer. To evaluate the fraction of atoms lost during these transitions, one can use the Landau-Zener formula:

$$P_{Zener} = e^{-\frac{a_c}{a(t)}} \tag{94}$$

where $a_c = \frac{\pi\Omega_{eff}^2}{16k_{eff}}$ is a critical acceleration depending on the lattice depth and $a(t) = \frac{d\Delta\omega(t)}{dt}$ is the lattice instantaneous acceleration. The lattice depth Ω_{eff} appears explicitly in this condition because the adiabaticity depends on the distance between the first and second energetic bands which increases as the coupling to the field increases. Two different atomic trajectories are represented on Fig. 61 and corresponds to the two following cases. The atom remains in the lower band (adiabatic) and continues to being "trapped" in the lattice (and its velocity in the laboratory frame increases according to eq. (93)) or the atom changes band (non-adiabatic) and does not follow the lattice translation which results, in the moving frame of the lattice, in a periodic increase of its quasi-momentum.

In practice, eq. (94) is not too constraining because it is possible to have a very large critical acceleration a_c with deep lattices. For example, $a_c = 1000\,\mathrm{m/s^2}$ for ^{87}Rb in a lattice at $1560\,\mathrm{nm}$ with $\Omega_{eff} = (2\pi)\,23\,\mathrm{kHz} = 24\omega_{rec}$, where $\omega_{rec} = \frac{\hbar k_{eff}^2}{2m}$ is the recoil frequency. This allows for example to increase the atom's velocity by $2\,\mathrm{m\,s^{-1}}$ in $20\,\mathrm{ms}$ while keeping the atom losses below $2\,\%$. [31]

This technique will be used to transfer our atomic cloud to a launching region, where another Bloch acceleration will launch the BEC upwards.

5.4.2 Transport from the surface

The experimental scheme is represented on Fig. 62. From the initial crossed dipole trap, the atoms will be transferred into an horizontal lattice made of two counter-propagating laser beams with a controlled frequency difference $\Delta\omega(t) = \omega_2 - \omega_1$. An appropriate frequency ramp $\Delta\omega(t)$ described in the numerical section will transport the cloud farther from the surface.

Because the transport distance, $x_0 = 4.5\,\mathrm{mm}$, is approximately equal to the Rayleigh length of the guide used to produce the lattice, the optical potential amplitude will change during the acceleration. This is represented on Fig. 63 where the transverse frequencies $\omega_y(x)$, $\omega_z(x)$ and gravitational sag position $z_0(x)$ are shown as a function of the distance from the waist. This transportation scheme constrained the waist of the longitudinal dipole trap beam as it has to maintain the atoms against gravity even at the final cloud position (x_0).

---

[31] Indeed, the number of transition required to accelerate to $2\,\mathrm{m\,s^{-1}}$ is 340. The atom loss can be estimated as $1 - \left(1 - e^{-\frac{a_c}{a_{max}}}\right)^{340}$. Therefore, with a maximal acceleration of $100\,\mathrm{m/s^2}$, the losses remains below $2\,\%$.

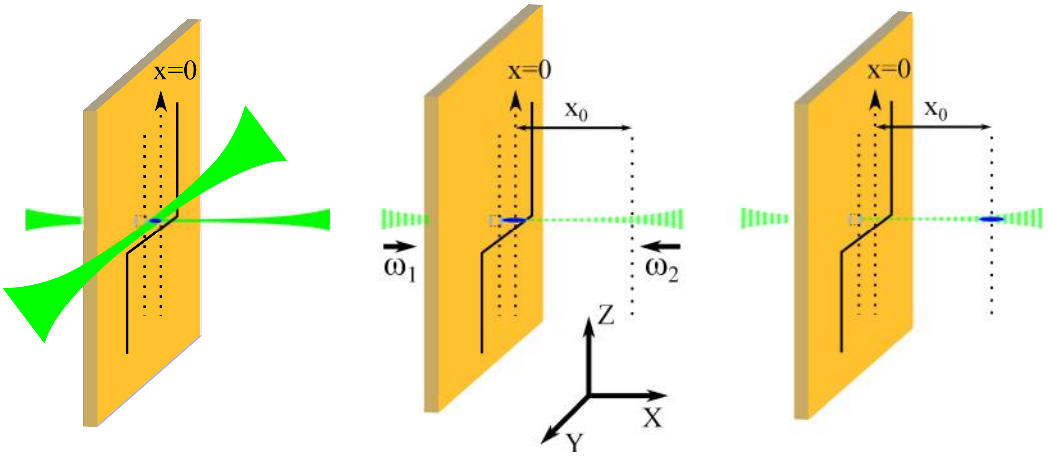

Figure 62: Description of the experimental scheme simulated for the BEC transport. The initial BEC will be loaded from the crossed dipole trap into a lattice. The optical equipotentials will then be translated by changing the frequency difference between the two beams until the cloud is displaced by a chosen distance x_0 from its initial location.

To fix ideas, using the theoretical expression of the laser intensity of a perfect TEMoo mode, this means that the potential created by a laser guide can be expressed as:

$$U_{tot}\left(x, y=0, z\right) = \rho \frac{I_0^2}{1+\frac{\lambda^2 x^2}{\pi^2 w_0^4}} e^{-\frac{2z^2}{w_0^2\left(1+\frac{\lambda^2 x^2}{\pi^2 w_0^4}\right)}} - mgz$$

where the $x = 0$ origin is taken at the laser waist w_0, I_0 is the laser beam peak intensity and ρ is coefficient which only depend on the laser beam wavelength and atomic polarizability (see **grimm_optical_1999** for a review):

$$\rho = \frac{3\pi c}{2\omega_{D1}^3 \epsilon_0} \left[\frac{\Gamma}{\omega_0 - \omega_L} + \frac{\Gamma}{\omega_0 + \omega_L}\right]$$

Γ is the transition linewidth and ω_0 is the barycentre of the D lines. For the 1560 nm wavelength, $\rho = 4.1 \times 10^{-37}\,\mathrm{m^2\,s}$ which corresponds to $\rho/k_B = 29\,\mathrm{mK}/\left(W\,\mu\mathrm{m}^{-2}\right)$ in more practical units. If the potential minimum $\partial U_{tot}/\partial z|_{z=z_0(x)} = 0$ is located at a position small compared to the local waist, $z_0\left(x\right) \ll w_0\sqrt{\left(1+\frac{\lambda^2 x^2}{\pi^2 w_0^4}\right)}$, one can get approximate analytical solutions. The gravitational sag is given by:

$$z_0\left(x\right) \sim \frac{mgw_0^2}{4\rho I_0^2}\left(1+\frac{\lambda^2 x^2}{\pi^2 w_0^4}\right)^2 \tag{95}$$

To minimize atom losses induced by this gravitational sag, it is interesting to find the optimal waist which minimizes $z_0\left(x_0\right)$ at the end of the transport. This can be done by differentiating eq. (95) with respect to w_0. One finds that $z_0\left(x_0\right)$ is minimum for an optimal waist $w_{0,\mathrm{opt}} = \sqrt[4]{\lambda^2 X_0^2/\pi^2} \sim 47\,\mu\mathrm{m}$ which corresponds to the waist chosen in all our simulations.

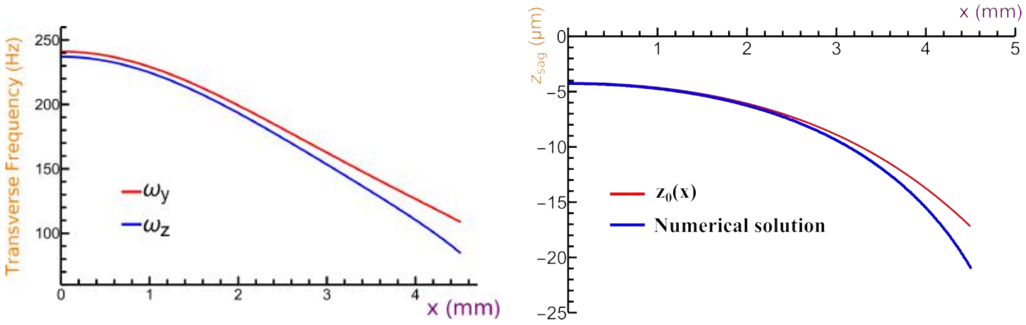

(a) Guide trapping frequencies

(b) Gravitational sag

Figure 63: **(a)** Evolution of the two transverse trapping frequencies as a function of the distance from the laser waist. In both directions, the trapping parameters change by more than a factor 2. The laser power is 1 *W* and waist $w_0 = 47\,\mu\mathrm{m}$.
(b) Position of the potential minimum (gravitational sag) as a function of the distance from the laser waist. The red curve corresponds to the approximate solution of eq. (95) showing good agreement with the blue one which is the exact numerical solution.

In collaboration with N. Gaaloul in Hanover and with two of his students, R. Corgier and S. Loriani, we developed a numerical simulation of this procedure in order to find the fastest transfer time and to take into account the possible effects of gravity on the transport efficiency (characterized with the number of transferred atoms as well as the velocity distribution broadening). It is also planned to use these simulations to discuss the effects of lattice depths fluctuations and lattice phase noise on the transport efficiency.

5.4.3 Numerical simulations

The principle of the simulation relies on the Gross-Pitaevskii equation which describes, in the mean field approximation, the N-particles wavefunction of the condensate. Its time dependent form is:

$$i\hbar \frac{\partial \phi(\vec{r},t)}{\partial t} = \mathcal{H}(\vec{r},t)\,\phi(\vec{r},t) = \left[-\frac{\hbar^2}{2m}\,\triangle + V_{\mathrm{ext}}(\vec{r};t) + Ng\,|\phi(\vec{r},t)|^2\right]\phi(\vec{r},t) \quad (96)$$

where $V_{\mathrm{ext}}(\vec{r};t)$ denotes the external potential and $g = \frac{4\pi\hbar^2 a_s}{m}$ describes the s-wave scattering between atoms in the condensate, where a_s is the scattering length ($a_s = 100a_0$ for ^{87}Rb). The wavefunction $\phi(\vec{r},t)$ is an approximation of the exact N particles wavefunction. This approximation is valid as long as the number of particles is large (which allows to neglect depletion of the condensate to excited modes and the resulting interaction terms) and the density is sufficiently small ($n \ll a_s^{-3}$) in order to neglect higher order atom-atom interactions to keep only the term $Ng\,|\phi(\vec{r},t)|^2$ which is the first order Hartree-Fock development.

The numerical propagation of eq. (96) discretizes the time evolution of a given initial wavefunction $\phi\left(\vec{r}, t_0\right)$ and performs, at each time step, the unitary transformation:

$$\phi\left(\vec{r}, t+\delta t\right) = e^{-\frac{i\mathcal{H}(\vec{r},t)\delta t}{\hbar}} \phi\left(\vec{r}, t\right)$$

where $\mathcal{H}\left(\vec{r}, t\right)$ is the Gross-Pitaevskii Hamiltonian (eq. (96)). The time step δt needs to be small compared to the smallest dynamical process. In our case, it corresponds to the high trapping frequencies at the bottom of each lattice wells $\omega_{lat}/\left(2\pi\right) \sim 10\,\mathrm{kHz}$. In practice, the time step is chosen such as $\delta t \omega_{lat} \ll 1$ and the convergence of numerical results with decreasing time steps is checked.

Due to the non-local (in $\vec{r}$ space) character of the Laplacian in the Hamiltonian it is advantageous to express the wavefunction in $\vec{k}$ space in which this operator is local. Fourier transforms are therefore necessary to propagate easily the wavefunction in each space where the corresponding propagator has the simplest form. However, these numerical operations are time consuming which is why a split step method is used [295], [296] to reduce the number of these transformations. Discussion on the numerical aspects of these simulations can be found in the theses [297], [298].

EFFECTIVE 1D MODEL

In the absence of gravity, the external potential is axially symmetric and an effective 1D Hamiltonian can be derived from eq. (96). This is numerically important as the computation time is reasonable even with the large number of grid points required by the large scale difference between the lattice period and the condensate size. However, including gravity in the simulation required some approximations in order to proceed further numerically.

Because of the large transverse frequencies compared to the initial longitudinal one, it is reasonable to neglect the initial transverse excitations which are much more energetic. Additionally, the loading and transport protocol should be slower than the typical transverse dynamic time ($2\pi/\omega_{y,z}$), the transverse dynamic can thus be adiabatically eliminated during the transport which assumes that it keeps its stationary shape. These two reasons motivated us to use an approximate solution for the ground state wavefunction which is propagated only in the x direction and fixed in the transverse directions:

$$\phi\left(x, y, z; 0\right) = \varphi\left(x; t\right) f_y\left(y, x; t\right) f_z\left(z, x; t\right)$$

where $\varphi\left(x; t\right)$ is an un-constrained wavefunction, solution of an the effective 1D Hamiltonian $\hat{H}^{1D}_{eff}$ (eq. (98) below), $f_z\left(z, x; t\right)$ and $f_y\left(y, x; t\right)$ are Gaussian Ansätze:

$$f_l\left(l, x; t\right) = \frac{1}{\sqrt{\pi^{1/2}\eta_l\left(x, t\right)}} e^{-ik_l(t)l} e^{-\frac{(l-l_c(t))^2}{2\eta_l^2(x,t)}} \tag{97}$$

where $l = y, z$ which have parametrized width $\eta_l(x,t)$, center $l_c(t)$ and phase $k_l(t)$. These solutions adequately describe the transverse wavefunction in harmonic traps for low atom numbers $< 10^3$ but deviate from the exact solution at higher atom numbers due to the non-linear interaction term. Nevertheless, this factorized form can still give us some insight into the loading and transport dynamic as it includes spatial terms which, as we discussed previously, evolves significantly during the transport. In addition, the transverse effect of gravity can be represented by both $z_c(t)$ and $k_z(t)$ which represent the mean center and the momentum of the cloud in the z direction. The effective Hamiltonian takes into account these additional terms:

$$\begin{aligned}
\hat{H}^{1D}_{eff} &= -\frac{\hbar^2}{2m}\nabla_x^2 + V_{eff}(x,t) + N\frac{g}{2\pi\eta_z\eta_y}|\varphi(x,t)|^2 \\
&\quad -\hbar\left(\dot{k}_y y_c + \dot{k}_z z_c\right) + \frac{\hbar^2}{2m}\left(k_y^2 + k_z^2 + \frac{1}{2\eta_y} + \frac{1}{2\eta_z}\right) \\
&\quad +\frac{1}{2}m\omega_y^2(x)\left(\frac{\eta_y^2}{2} + y_c^2\right) + \frac{1}{2}m\omega_z^2(x)\left[\frac{\eta_z^2}{2} + (z_0(x) - z_c)^2\right]
\end{aligned} \tag{98}$$

where we have omitted the explicit space and time dependence of the Gaussians parameters, $V_{eff}(x,t) = V_{ext}(x, y_c, z_c; t)$ is the 1D external potential and $\omega_y(x)$ (resp. $\omega_z(x)$) is the harmonic potential in the transverse y (resp. z) direction which takes into account a spatially dependent trapping frequency. In this effective Hamiltonian, one can group the different contributions in different categories. The first three terms (red) corresponds to the Gross Pitaevskii Hamiltonian in an effective 1D dimension. The terms (purple) which depend on $k_{y(z)}$ and $y_c(z)$ are energy terms which take into account the total energy change induced by the transverse velocities and position. The remaining terms (blue) which depend on $\eta_{y(z)}$ represent the competition in the transverse direction between reducing the potential energy (reducing $\eta_{y(z)}$) and reducing the kinetic energy (increasing $\eta_{y(z)}$ to reduce the velocity distribution). Also, the effect of gravity is included in the exact location of the potential minimum $z_0(x)$ and on the external potential.

Three scalar equations are coupled to this effective Hamiltonian for each transverse direction:

$$\begin{aligned}
\frac{1}{2}m\omega_y^2(x)\,\eta_y^4(x,t) &= \frac{\hbar^2}{2m} + N\frac{g}{4\pi\eta_z(x,t)}|\varphi(x,t)|^2\,\eta_y(x,t) \\
\dot{k}_y(x,t) &= -\frac{1}{\hbar}\frac{\partial V_{ext}(\vec{r},t)}{\partial y}\Big|_{x, y=y_c(t), z=z_c(t)} \\
\dot{y}_c(t) &= \frac{m k_y(t)}{\hbar}
\end{aligned}$$

with similar equations for z and we recall that $V_{ext}(\vec{r}; t)$ is the complete external potential prior to 1D transformation.

This model allows us to combine a fast numerical computation with some of the interesting features such as the displacement (and possible oscillations) in the transverse direction and the effect of large local densities in the lattice wells during the transport. But before, let us describe the dipole guide and lattice parameters during the transport.

5.4.4 Loading from the dipole trap

The condensate groundstate is numerically computed in the initial cigar shaped trap $(\omega_\perp/(2\pi) = 210\,\text{Hz}, \omega_\parallel = 1.5\,\text{Hz})$ for 10^4 ^{87}Rb atoms. It corresponds to the trap for which the crossed dipole beam has been adiabatically[32] turned off. The counter propagating beam intensity is then ramped up to load the atoms into the optical lattice. To ensure an adiabatic loading in the lowest Bloch band, one can use the sufficient condition $|d\Omega_{eff}(t)/dt| \ll 16\omega_{rec}^2$ adapted from Denschlag *et al.* [302]. We use a sinus ramping function characterized by the ramping time τ_{load}:

$$\Omega_{eff}(t) = s\omega_{rec}\sin^2\left(\frac{\pi t}{2\tau_{load}}\right) \tag{99}$$

where s is the lattice depth[33]. The adiabatic condition can therefore be expressed as $\tau_{load} \gg s\pi/(64\omega_{rec}) \sim s \times 8\,\mu\text{s}$. For a deep $(s = 50)$ lattice, we typically use $\tau_{load} = 4.5\,\text{ms}$ which corresponds to an order of magnitude between the two timescales. We checked that no diffracted momentum components were populated during this stage by immediately unloading the lattice which result in a single momentum distribution centered around the initial cloud mean momentum $p = 0$. The initial and loaded wavefunction are represented on Fig. 64a in position space and on Fig. 64b in momentum space. The inset emphasizes, on a logscale, that initially no other momentum components than the $p = 0$ are present. The loaded wavefunction displays clear peaks at multiples of $2k_L$. Also, the momentum width is initially very narrow (FWHM $10^{-2}\nu_{rec}$) both in the harmonic trap and in the lattice. The initially shallow trap is an important step of this transportation protocol as direct loading and transport from a tighter $(\omega_\perp/(2\pi) = 210\,\text{Hz}, \omega_\parallel = 15\,\text{Hz})$ trap lead to higher losses of the transported cloud.

5.4.5 Transport in the lattice

In order to keep the size of the numerical grid reasonable we use the reference frame of the moving lattice. This leads to unitary transformations of the effective Hamiltonian (98). This procedure is described in details in [303] and we will only mention that it simply results in a spatially dependent potential term $m\hat{x}a(t)$ added to eq. (98). We ramp up the lattice acceleration smoothly up to a constant value a_{lat}. After

---

[32] Faster processes relying on shortcut to adiabaticity could also be used [299]–[301] as the longitudinal frequency $1.5\,\text{Hz}$ requires a very long $\sim 1\,\text{s}$ adiabatic expansion.

[33] We are using the convention which is based on the recoil energy $E_R = \hbar^2 k_L^2/(2m)$ as unit of lattice depth. We note that the lattice energy $E_L = 4E_R$ is also used in the literature but did not choose this convention.

a constant acceleration stage, the lattice acceleration is ramped down to zero. A similar deceleration stage is then performed which brings back the lattice and the cloud at rest in the laboratory frame. The result of this transportation protocol is represented on Fig. 64.

The lattice depth and acceleration ramps are shown on Fig. 65a. For these simulations, the spatially dependent transverse frequencies and lattice depth were included in the numerical propagation using approximate analytical expressions such as eq. (95). The change in lattice depth is the reason why different "accelerations" are used for the acceleration stage and deceleration stages. In practice, using a deceleration amplitude half as large as the acceleration was sufficient to prevent non-adiabatic transitions.

The condensate mean position and velocity are represented resp. on Fig 65c and Fig. 65d. Clearly, the condensate follows perfectly the lattice dynamic as the position difference compared to the lattice position remains below $10^{-2}\,\mu m$. Also the relative velocity is less than $5 \times 10^{-3} v_{rec}$ which, compared to the $140 v_{rec}$ maximum velocity is completely negligible. Additionally, the momentum distribution width (in velocity unit) is represented as a function of time. The initial increase is a known effect [304] of progressive wavefunction dephasing between each lattice wells due to the inhomogeneous value of the chemical potential. Interestingly, the spatially dependent depth seems to lead to partial re phasing as the width tends to decrease slightly at the end of the transport. In a situation were the depth would have been kept constant, the final width in the X direction would have been almost a factor of two larger !

The final cloud prior to and after unloading is represented on Fig. 64c in position space and on Fig. 64d in momentum space. The final cloud shape is typical of a Thomas-Fermi inverted parabola distribution as is expected for an interacting condensate. The final momentum distribution has negligible (10^6 times smaller than the main $p = 0$ component) residual momentum components at multiples of $2\hbar k_L$. The momentum distribution is asymmetric which leads to a non-zero mean velocity of $10^{-2} v_{rec}$. This residual velocity is not well understood but might be due to the final potential asymmetry: the guide, and lattice, depth changes by approximately 10 % over the whole cloud. Nevertheless, compared to the cloud velocity distribution this is a very small value which will not significantly deflect the atoms of the perfect fountain trajectory.

Nevertheless, this transportation protocols is robust against condensate numbers and exact lattice depth. Indeed, keeping all dynamical parameters constant, increasing the number of atoms up to 10^6 or changing the lattice depth by 10 % did not change the shape of the transported cloud. Also, faster accelerations than the one presented here (up to $300\,m/s^2$) showed similar performances.

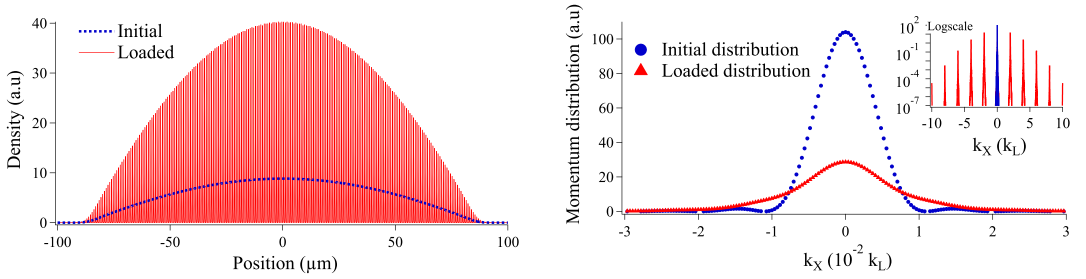

(a) Wavefunction in position space

(b) Wavefunction in momentum space

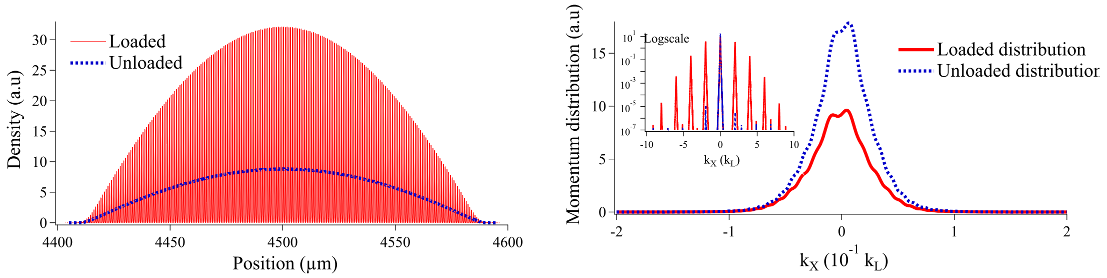

(c) Wavefunction in position space

(d) Wavefunction in momentum space

Figure 64
Simulation results of the transport protocol (see text).

(a): Wavefunction probability distribution, $\int\int |\phi(x,y,z;t)|^2 \, dy\,dz$, as a function of the position along the lattice direction at three initial stages. Initial wavefunction ($t = 0$ ms) and loaded wavefunction before transport ($t = 5$ ms).

(b): Fourier transform probability distribution, $\int\int \left|\tilde{\phi}(k_x,k_y,k_z;t)\right|^2 dk_y\,dk_z$, as a function of the momentum k_x along the lattice direction at three initial stages. Initial Fourier transform ($t = 0$ ms) and loaded wavefunction before transport ($t = 5$ ms). The inset shows the loaded momentum distribution on a much wider momentum grid and with a logarithmic scale for the Y axis. Distinct peaks at multiples of $2k_L$ are present in the loaded wavefunction. Notice the very small x-range.

(c): Same as **(a)** except for the stages. Transported stage ($t = 26.181$ ms) and unloaded stage ($t = 28.681$ ms)

(d): Same as **(b)** except for the stages. Transported stage ($t = 26.181$ ms) and unloaded stage ($t = 28.681$ ms). Notice the ten times larger x-range than **(b)**.

5.4.6 Amplitude and phase noise

Further simulation are currently under way to take into account the effect of phase fluctuations and lattice depth evolution during the transport. To do so, we include Gaussian noise both on the lattice depth s and on the reference phase $\bar{\phi}$ (see eq. (92)).

The efficiency of the transport is evaluated by computing the overlap between the unperturbed final wavefunction ϕ_0 (such as the one displayed on fig. 64c) and the transported wavefunction with noise ϕ_{noise}. The corresponding efficiency criterion η_{noise} is defined as:

$$\eta_{noise} = \left| \int_{-\infty}^{+\infty} \phi_{noise}(x,0,0;t_f)\, \phi_0(x,0,0;t_f)\, dx \right|$$

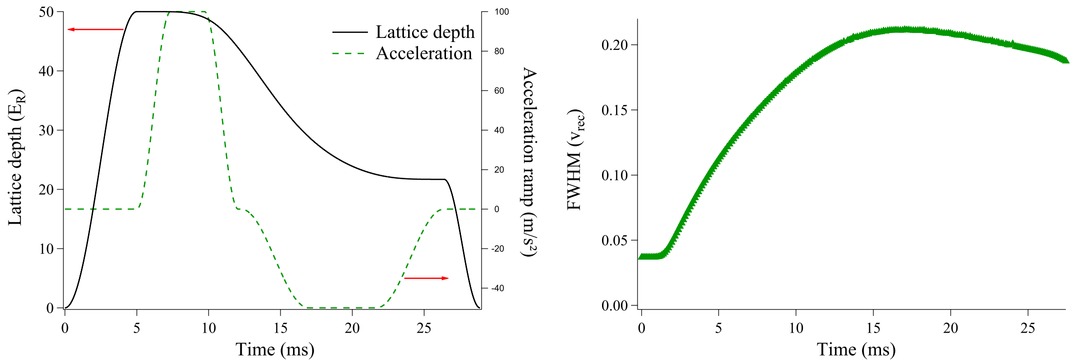

(a) Lattice parameters **(b)** Velocity distribution width

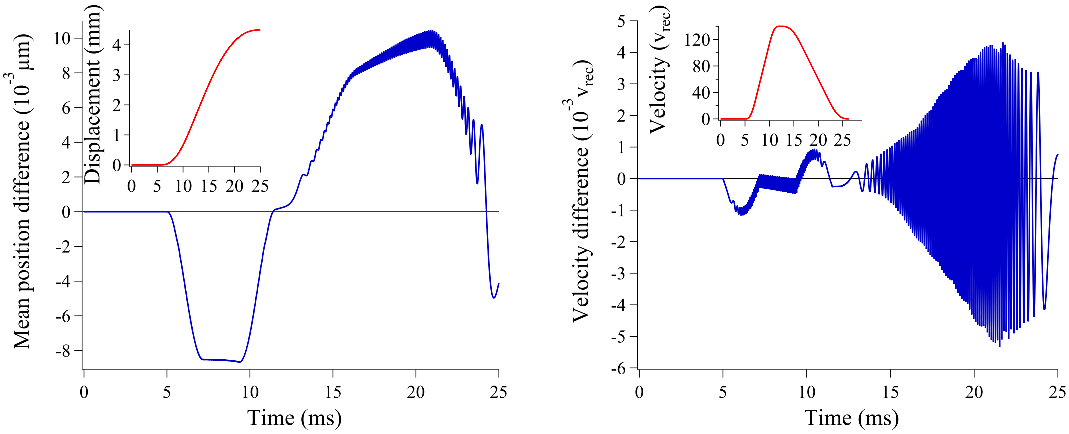

(c) Mean cloud postion **(d)** Mean cloud velocity

Figure 65: **(a)**: Lattice parameters as a function of time. Both the lattice depth (left, solid line) and the lattice acceleration (right, dashed line) are shown. Notice the spatially depend depth due to the laser intensity decrease and the smallest deceleration due to the smallest depth.
(b): Evolution of the condensate velocity width as a function of time. When loaded into the lattice, it corresponds to the weighted average of each velocity component ($2n\nu_{rec}$) Full Width at Half Maximum.
(c): Difference between the mean position of the wavefunction and the accelerated frame position. The inset displays the mean position with 4.5 mm displacement.
(d): Difference between the mean velocity of the wavefunction and the accelerated frame velocity in ν_{rec} units. The inset displays the mean velocity.

The width of the Gaussian distributions are parametrized such that[34] the standard deviation of the depth and phase for a single simulation is, on average, controlled.

For a given mean standard deviation (MSD) of phase (or amplitude), multiple simulations are performed with randomly distributed phase (or amplitude) fluctuations. The preliminary result indicate that a phase MSD of $10(2)$ mrad (resp. $30(10)$ mrad) during the whole transport leads to $\eta_{noise} \sim 99(1)\,\%$ (resp. $\eta_{noise} \sim 90(2)\,\%$). Therefore, the transport seems feasible with standard laboratory phase locking. The transportation is even more robust to amplitude noise as a 4 % amplitude MSD leads to

---

[34] The sum of k independent centered normally distributed random variables with width σ_1 is described by a centered normal distribution with width $\sigma\sqrt{k}$. Therefore, we choose σ so that $\sigma\sqrt{N_{numeric}}$ is equal to a particular mean standard deviation , where $N_{numeric}$ is the number of numerical steps at which a random variable was sampled.

less than 2 % losses. It ensures that local fluctuations of the counterpropagating fields should not reduce the transport efficiency.

Additional investigations of the transport efficiency are being developed. First a better statistic on our current values and a larger panel of phase and amplitude MSD will improve our test of a white noise spectrum. Then, it will be interesting to see if the noise spectrum at specific frequencies (such as the lattice trap typical frequencies $\omega_{\mathtt{trap}}/(2\pi)$ or the transverse guide frequencies) can resonantly disturb the transport.

Transport

To transport the condensate away from the mirror surface an optical lattice transport protocol is considered. To take into account the beam divergence and experimental imperfections, numerical simulations developed in collaboration with Hanover's group is currently under development. Preliminary results indicate that the transport is efficient as all the atoms are transported to their final location and there remain no diffracted momentum components at the end of the transport. This transportation protocol is reliable as fluctuations of the atom number or of the lattice amplitude do not significantly reduce its efficiency. However, phase fluctuations as large as 30 $\mathtt{mrad}$ can reduce the transport efficiency by as much as 10 % which indicates that an active relative phase stabilization can be beneficial.

5.5 INTERFEROMETER

With this BEC source, a large spatial separation Mach-Zehnder type interferometer will be performed. The scheme presented on Fig. 46 was only an approximate representation of the different strategies for Large Momentum Transfer Mach Zehnder Interferometer (LMTMZI). In this section, we are going to discuss in more details how a coherent superposition of momentum states $|p\rangle$ and $|p + 2N\hbar k\rangle$ can be experimentally produced.

5.5.1 Large Momentum Transfer

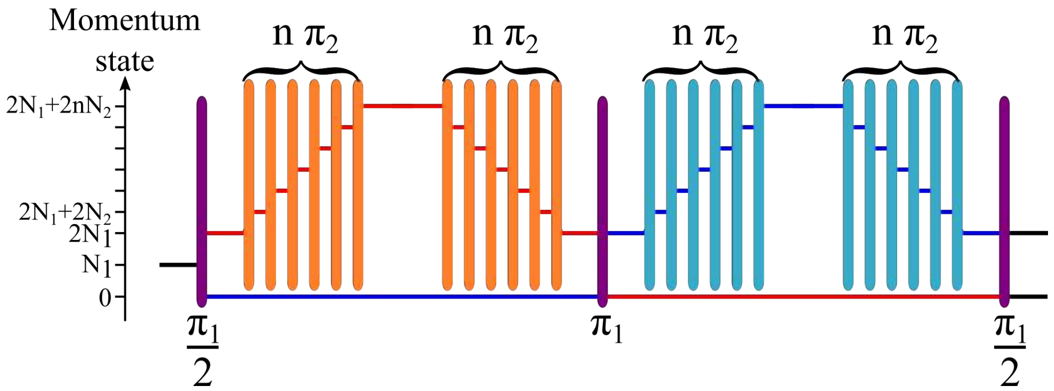

Figure 66: Momentum state of upper (red) and lower (blue) interferometric arms. The π_1 pulses diffract both arms while the π_2 pulses are resonant with only one arm.

High order Bragg pulses

One way to produce a LMTMZ consists in a combination of Bragg pulses as shwon on Fig. 66 and was recently applied to produce a $102\hbar k$ momentum separation[61]. To increase the momentum separation between the two interferometric arms, the cloud is initially split in two momentum states separated by $2N_1\hbar k_L$[35] (First $\pi_1/2$ pulse[36], duration τ). Then one of the two arms (let us choose the upper one for simplicity) is subject to a series of n π_2 pulses which are resonant only with the upper arm momentum states. Theoretically, each pulse transfers successively the upper arm in the momentum states $\{(N_1 + 2N_2)\,\hbar k_L, (N_1 + 4N_2)\,\hbar k_L, ...\}$. At the end of this sequence, the two interferometric arms are separated by a large momentum $2\,(N_1 + nN_2)\,\hbar k_L$. The cloud then propagate freely during the interferometric time T. An inverse sequence is performed on the upper arm, bringing it back to the momentum state $N_1\hbar k_L$ and the two arms are simultaneously transferred in the opposite state with a π_1 pulse. Finally, the symmetric manipulations are performed on the lower arm

---

[35] With this notation, we assume that the two counter propagating beams are perfectly aligned and we neglect the small wavevector difference due to the slight frequency difference, which is justified by the fact that the frequency difference is typically of the order of the Doppler frequency shift and the recoil frequencies which are $\sim$ 1 MHz for a $1\,\mathrm{m\,s^{-1}}$ atomic velocity and 3.77 kHz respectively. These values correspond to fractions 1×10^{-8} and 1×10^{-11} of the laser frequency which are completely negligible.

[36] This notation is inspired by Bragg diffraction. I wanted to emphasize the different roles played by the two types (π_1 and π_2) of Bragg pulses which interact with both arms or with a single one.

(serie of π_2 pulses, free propagation and transfer back to the initial state). The interferometer is then recombined with a final $\pi_1/2$ pulse mixing the two paths. Figure 67 represent the atomic trajectories and the corresponding Bragg pulses corresponding to this sequence with $N_1 = 1$, $N_2 = 5$ and $n = 4$.

Theoretical description of these High order Bragg diffraction pulses exist for different diffraction regimes (top hat pulses [305], perturbative expansion for Gaussian pulses [306], chirped laser frequencies[37] [308]) and often based on the effective Hamiltonian derived in Chap 1 eq. (6).

To model the LMT scheme, one often uses on the effective Rabi frequency [306]:

$$\Omega_{eff}(N) = \frac{\Omega_{eff}^N}{(8\omega_{rec})^{N-1}} \frac{1}{[(N-1)]^2}$$

where Ω_{eff} is the effective two photon coupling strength, N is the Bragg diffraction order and ω_{rec} the recoil frequency. This term gives an effective coupling rate in the sub-system formed by the two momentum states $(|p\rangle, |p + 2N\hbar k\rangle)$. This approximation is valid as long as the interaction time is long and the intermediate levels are negligibly populated $(4(N-1)\omega_{rec} \gg \Omega_{eff})$. Unfortunately, for large momentum transfers, this condition leads to prohibitively long Bragg pulses which leads to large losses induced by spontaneous emission[38] or requires a very large detuning from resonance Δ. The laser power required to keep the pulse duration small with respect to the atomic motion during the pulse increases to the power N with the detuning.

This is the reason why numerical integration of the system of equation formed by the two momentum states $(|p\rangle, |p + 2N\hbar k\rangle)$ as well as all the intermediate and some neighbouring states are necessary to evaluate the efficiency of these high order Bragg pulses. It was shown by Szigeti *et al.*[213] that high efficiency ($> 90\,\%$ per π pulse) could be realised for narrow velocity atomic cloud ($\Delta v < 0.1 v_{rec}$) which can be produced either by velocity selective Raman pulses [309] or ultra cold clouds such as BECs. For a $N = 5$ Bragg pulse, they calculated an optimal coupling $\Omega_{eff} \sim 50\omega_{rec}$ and a pulse duration $\tau_{opt} = \frac{0.35}{\omega_{rec}}$. This is consistent with the experimental parameters of Chiow *et al.*[61]: a $\frac{0.25}{\omega_{rec}}$ duration, and a $33\,\omega_{rec}$ two photon coupling were used to produce $N = 6$ Bragg diffraction of a $4\,nK \leftrightarrow 0.1 v_{rec}$ atomic cloud with a $94\,\%$ transfer efficiency.

Bloch oscillations

Another possible LMT uses a combination of an initial first order Bragg pulse followed by a coherent acceleration of one of the two momentum states. It was recently demonstrated [204], [206], [294] as an efficient tool for LMT beam splitter. It is important to note that, compared to the transport protocol which loaded all the atoms in the

---

[37] This method is a combination of the time dependent light intensity, constant frequency, used in Bragg scattering and the constant light intensity, time dependent frequency, used in the Bloch oscillation scheme. It was recently used [307] to produce a $30\hbar k$ momentum separation interferometer with $5\,\%$ visibility.

[38] Which, at constant interaction time $\tau_\pi = \pi/\Omega_{eff}(N)$, scales as $1/\Delta^2$, where Δ is the Bragg laser detuning from resonance.

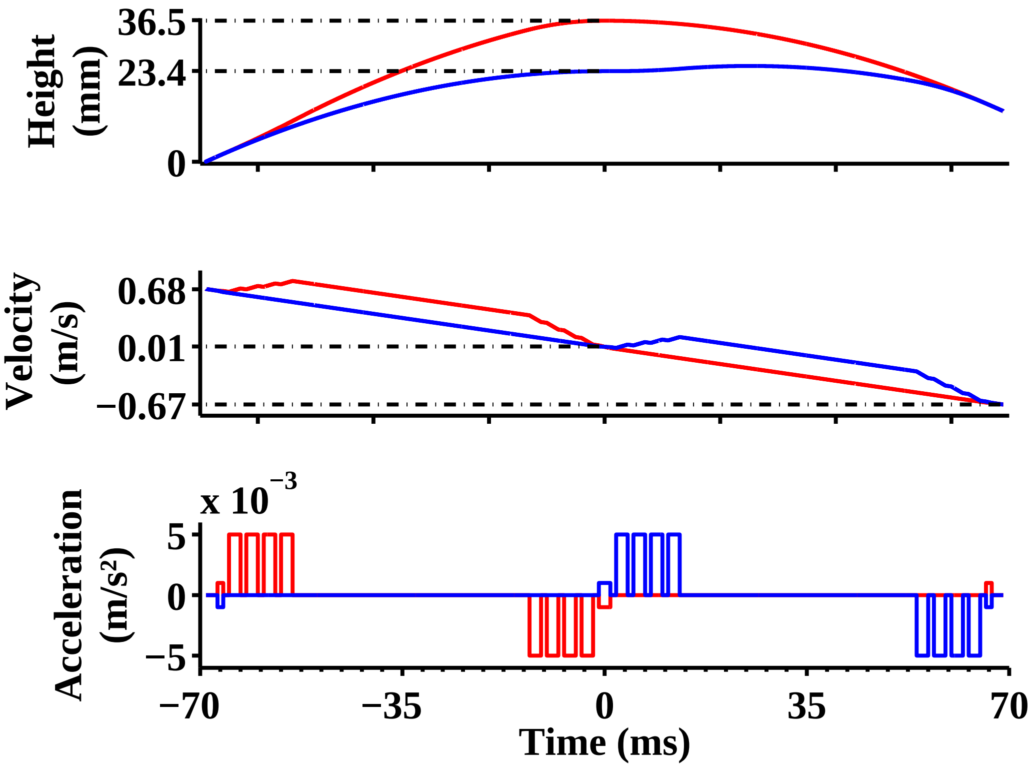

Figure 67: Interferometric sequence of the LMT Multi Bragg interferometer. The two interferometric paths positions, velocities and accelerations are represented as a function of time. The separation parameters were $T = 40\,\text{ms}$, $\tau = 1\,\text{ms}$ (exaggerated for the purpose of this figure), $N1 = 1$, $N2 = 5$ and $n = 4$.

same band, this protocol requires to load two initially separated momentum states $|p\rangle$ and $|p + 2\hbar k\rangle$ into two different Bloch bands. Only one of the two components will follow adiabatic transitions as its quasi-momentum q increases which requires the lattice depth to be between $0.5\hbar\omega_{rec}$ and $1.5\hbar\omega_{rec}$ [310]. This separation scheme has the advantage of an approximately constant efficiency ($\sim 95\,\%$ per pulse) over a $\sim 0.4 v_{rec}$ wide velocity range. However, the lattice acceleration is highly dependent on its intensity which produces spatially dependent phase shifts and renders this diffraction scheme sensitive to intensity noise.

Planned sequence

As a first sequence for LMTMZI, we opted for the high order Bragg schemes which were experimentally demonstrated in a few interferometers [61], [204]. Using four $N_2 = 5$ high order Bragg pulses, we plan to produce $42\hbar k$ momentum separation between our upper and lower interferometric arms which, for an interferometric time $T = 40\,\text{ms}$, will be sufficient to have a spatial separation of $1\,\text{cm}$ between the two atomic paths apogees and an interaction time with the electrodes larger than $10\,\text{ms}$ as discussed in Sec. 5.1.4. To produce these pulses, a $1\,W$ Bragg laser, $10\,\text{GHz}$ detuned from resonance is currently being developed. We expect to have approximately $300\,\text{m}W$ laser power available in two beams having a well defined frequency difference $\Delta\omega(t)$ which, used in a retro-reflected σ^+ configuration, will produce an optical lattice stationary in the reference frame of the atomic cloud[39]. With 2 mm waist Gaussian beams, this will result in a maximal two photon coupling $\Omega_{eff} = 100\omega_{rec}$ sufficient for optimal diffraction. Combining the expected losses of a 10 nK $\sim 0.10\nu_{rec}$ atomic cloud (10 % per pulse) as well as the losses induced by spontaneous emission (2 % per pulse), we can expect that 35 % of the initial atoms will contribute to the interferometric signal. With an initial condensate of 2×10^5 atoms (see Tab 14 in Sec. 5.3), this results in almost 7×10^4 atoms which leads to a minimum Quantum Projection Noise of 6 mrad as used in our phase sensitivity estimate (Tab. 12, Sec. 5.1.7).

To reach this noise limit, we need to reject efficiently the phase noise of our measurements which requires a precise knowledge of the interferometer sensitivity to noise sources. This is why, a preliminary work on the LMTMZI modelling will now be discussed.

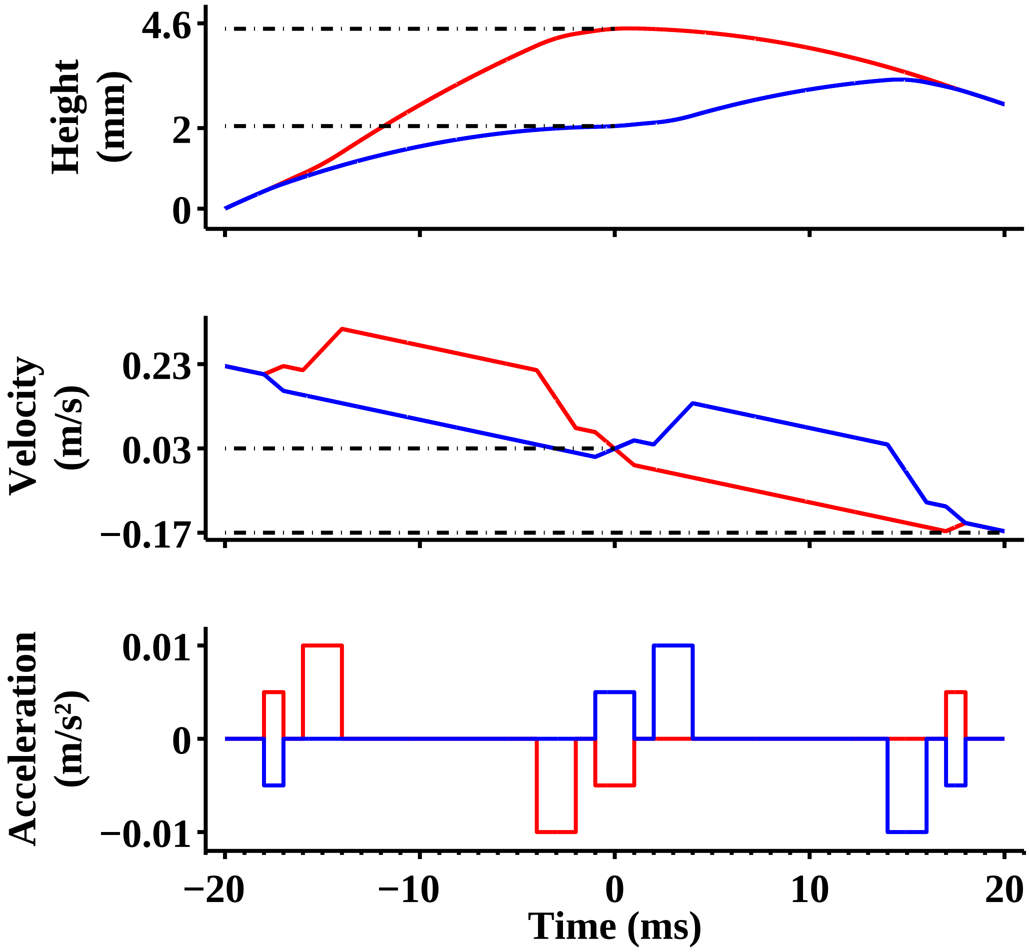

Figure 68: Interferometric sequence of the LMT Multi Bragg interferometer. The two interferometric paths positions, velocities and accelerations are represented as a function of time. The separation parameters were $T = 10$ ms, $\tau = 1$ ms. For clarity, the number of transferred momenta has been increased to $N1 = 5$, $N2 = 10$ and $n = 1$. The result of the calculation corresponds to the values given in the text.

---

[39] As well as an optical lattice moving at twice the atomic velocity in the opposite direction to which the atoms are insensitive

5.5.2 LMTMZ sensitivity

I calculated the sensitivity function $g_s(t)$ of a LMTMZ interferometer based on High order Bragg pulses using a method similar to the one developed by P. Cheinet described in details in his thesis [311]. This tool corresponds to the impulse response function of the interferometer and was initially developed in the context of atomic clocks.

The function $g_s(t)$ is defined as the effect on the interferometric phase of a phase jump $\delta\phi$ happening at a time t on the phase difference between the diffracting lasers. In the LMTMZI, the interferometric output is the atomic population in one of the two momentum states $\pm N_1 \hbar k_L$. If we denote by P_+ the normalized population in the momentum state $+N_1 \hbar k_L$, we can relate the atomic population to the interferometric phase:

$$P_+(\Phi) = \frac{1-\cos(\Phi)}{2}$$

This leads to the following expression of the sensitivity function :

$$g_s(t) = \lim_{\delta\phi\to 0} \frac{d\Phi(\delta\phi, t)}{d\delta\phi} = \frac{2}{\sin(\Phi)} \lim_{\delta\phi\to 0} \frac{dP_+(\Phi, \delta\phi, t)}{d\delta\phi} \tag{100}$$

where $\Phi(\delta\phi, t)$ ($P_+(\delta\phi, t)$) denotes the interferometric phase (population) if a phase jump $\delta\phi$ occurred at time t. This function is particularly useful to express the interferometric phase Φ as a function of the laser phase $\phi(t)$ during the interferometer:

$$\Phi = \int_{-\infty}^{+\infty} g_s(u) \frac{d\phi(u)}{du} du \tag{101}$$

which, as we will see in the next sections, is a useful formalism to discuss the effect of noise sources on the interferometer phase.

As an example, we can take the three pulses Mach-Zehnder interferometer with infinitely short pulses. In this situation, the function $g_s^{MZ}(t)$ can be estimated[40] by considering the following cases:

- The phase jump happens before the first Bragg pulses, $t < -T$. The interferometer will not be sensitive to this jump as no laser phase has been imprinted on the atomic wavefunction. In this case, $g_s^{MZ}(t) = 0$
- The phase jump happens in between the first $\pi/2$ and the π pulse. In this situation, the final interferometric phase will be $\phi_1 - 2(\phi_2 + \delta\phi) + (\phi_3 + \delta\phi)$. Therefore, its derivative with respect to $\delta\phi$ is $g_s^{MZ}(t) = -1$.

---

[40] It is convenient to use the center of the middle π pulse as a time reference because the sensitivity function is then an even function of time.

- Similarly, on finds that a jump between the π and the second $\pi/2$ pulse lead to a sensitivity function of $g_s^{MZ}(t) = +1$ and that a jump after the second $\pi/2$ jump has no influence on the interferometric phase $g_s^{MZ}(t) = 0$.

A more detailed analysis of this sensitivity function, including the finite duration of the Bragg pulses, gives a similar function with smoothed edges at the time of the Bragg pulses. The exact expression of g_s^{MZ}[311] is in this case:

$$g_s^{MZ}(t) = \begin{cases} \sin\left[(t)\,\Omega_{eff}\right] & t \in [0;\tau] \\ 1 & t \in [\tau; T+\tau] \\ \sin\left[(t-T)\,\Omega_{eff}\right] & t \in [T+\tau; T+2\tau] \end{cases} \tag{102}$$

where Ω_{eff} is the effective Rabi frequency of the Bragg pulse. As g_s^{MZ} is an odd function of time, the $t < 0$ part is completely defined by eq. (102).

Let us now describe the principle of the calculation used to obtain the sensitivity function of the LMTMZI. For the sake of simplicity, only the $N_1 = 1$, $N_2 = 1$ and $n = 1$ case has been treated yet.

Formalism

In this section, we are going to describe the expressions used to calculate the sensitivity function for the simplest LMTMZI presented on Fig. 68. The calculation relies on the matrix formalism used to express the atomic state after the interaction with a top hat light pulse. Let us denote by $|e\rangle$, $|f\rangle$ and $|g\rangle$ the momentum states $|\hbar k_0\rangle$, $|\hbar(k_0 + 2k_L)\rangle$ and $|\hbar(k_0 + 4k_L)\rangle$, where $\hbar k_0$ is the initial atomic momentum in the laboratory frame. We will assume that no other momentum states are populated during the Bragg pulses and we will write the atomic state as:

$$|\Psi(t)\rangle = C_e(t)\,|e\rangle + C_f(t)\,|f\rangle + C_g(t)\,|g\rangle := \begin{pmatrix} C_e(t) \\ C_f(t) \\ C_g(t) \end{pmatrix}$$

For the π_1 pulses we can express the transfer matrix $M_{e\leftrightarrow f}(t_0, \phi, \Omega_{eff}, \tau)$ between the transferred state $|\Psi(t_0+\tau)\rangle$ and the incoming state $|\Psi(t_0)\rangle$ as:

$$M_{e\leftrightarrow f}(t_0, \phi, \Omega_{eff}, \tau) =$$

$$\begin{pmatrix} \cos\left(\frac{\Omega_{eff}\tau}{2}\right) e^{-i\omega_e\tau} & -ie^{i[(\omega_1-\omega_2)t_0+\phi]}\sin\left(\frac{\Omega_{eff}\tau}{2}\right) e^{-i\omega_f\tau} & 0 \\ ie^{-i[(\omega_1-\omega_2)t_0+\phi]}\sin\left(\frac{\Omega_{eff}\tau}{2}\right) e^{-i\omega_e\tau} & \cos\left(\frac{\Omega_{eff}\tau}{2}\right) e^{-i\omega_f\tau} & 0 \\ 0 & 0 & e^{-i\omega_g\tau} \end{pmatrix}$$

where $\omega_{e,f,g}$ denotes the different atomic states frequencies and $\omega_{1,2}$ are the two laser frequencies (in the laboratory frame). This transfer matrix assumes that the momentum states $|\hbar(k_0+3k_L)\rangle$ and $|\hbar(k_0-3k_L)\rangle$ are two far detuned to be efficiently coupled to the lattice which is why the population in the $|g\rangle$ is unaffected[41]. Similarly, one can define the transfer matrix of the π_2 pulses as:

$$M_{f\leftrightarrow g}(t_0,\phi,\Omega_{eff},\tau) =$$

$$\begin{pmatrix} \exp^{-i\omega_e\tau} & 0 & 0 \\ 0 & \cos\left(\frac{\Omega_{eff}\tau}{2}\right)e^{-i\omega_f\tau} & -ie^{i[(\omega_3-\omega_4)t_0+\phi]}\sin\left(\frac{\Omega_{eff}\tau}{2}\right)e^{-i\omega_g\tau} \\ 0 & ie^{-i[(\omega_3-\omega_4)t_0+\phi]}\sin\left(\frac{\Omega_{eff}\tau}{2}\right)e^{-i\omega_f\tau} & \cos\left(\frac{\Omega_{eff}\tau}{2}\right)e^{-i\omega_g\tau} \end{pmatrix}$$

where $\omega_{3,4}$ are the two laser frequencies (in the laboratory frame) producing the co-moving lattice. The freely propagating transfer matrix $MF(u)$ corresponds to the $\Omega_{eff}=0$ case applied to the previous matrices and can be written:

$$MF(u) = \begin{pmatrix} e^{-i\omega_e u} & 0 & 0 \\ 0 & e^{-i\omega_f u} & 0 \\ 0 & 0 & e^{-i\omega_g u} \end{pmatrix}$$

With this formalism, one can chain the transfer matrix corresponding to the different Bragg pulses of the LMTMZI to calculate the atomic population and phase, during the interferometer. For example, the matrix $M_{e\leftrightarrow f}\left(t_{\pi_1/2},\phi,\Omega_{eff},\pi/(2\Omega_{eff})\right)$ represents the first $\pi_1/2$ pulse and $M_{f\leftrightarrow g}\left(t_{\pi_2},\phi,\Omega_{eff},\pi/(\Omega_{eff})\right)$ represents the subsequent π_2 pulse. By choosing the time reference in the middle of the central π_1 pulse, the total interferometric matrix can be expressed as the product:

$$\begin{aligned} & M_{e\leftrightarrow f}(T+5\tau+2t_c,\phi_3,\Omega_{eff},\tau).MF(t_c) \\ & .M_{f\leftrightarrow g}(T+3\tau+t_c,\phi_3,\Omega_{eff},2\tau).MF(T).M_{f\leftrightarrow g}(\tau+t_c,\phi_2,\Omega_{eff},2\tau) \\ & .MF(t_c).M_{e\leftrightarrow f}(-\tau,\phi_2,\Omega_{eff},2\tau).MF(t_c) \\ & .M_{f\leftrightarrow g}(-3\tau-t_c,\phi_2,\Omega_{eff},2\tau).MF(T).M_{f\leftrightarrow g}(-T-5\tau-t_c,\phi_1,\Omega_{eff},2\tau) \\ & .MF(t_c).M_{e\leftrightarrow f}(-T-6\tau-2t_c,\phi_1,\Omega_{eff},\tau) \end{aligned} \tag{103}$$

where t_c is the cycle time between Bragg pulses and we have emphasized the interferometer arm on which the pulses are acting by using the same color code as Fig. 68. Applying this interferometer sequence to an initial state $(1,0,0)$ gives a population in the $|f\rangle$ state at the end of the interferometer sequence:

$$|C_f(T+5\tau+2t_c)|^2 = \frac{1-\cos[2(\phi_1+\phi_3-2\phi_2)]}{2}$$

---

[41] This explains the $e\leftrightarrow f$ subscript as only these two momentum states are coupled during the interaction.

as is to be expected for this interferometer.

Sensitivity function derivation

To obtain the sensitivity function from this formalism, one splits the transfer matrices applied at the time t into a product of two matrices having a phase difference $\delta\phi$. For example, if the phase jump happens at a time $t \in [-3\tau - t_c, -\tau - t_c]$, the fifth matrix:

$$M_{f\leftrightarrow g}\left(-3\tau - t_c, \phi_2, \Omega_{eff}, 2\tau\right)$$

becomes:

$$M_{f\leftrightarrow g}\left(t, \phi_2 + \delta\phi, \Omega_{eff}, -\tau - t_c - t\right) M_{f\leftrightarrow g}\left(-3\tau - t_c, \phi_2, \Omega_{eff}, 3\tau + t_c - t\right)$$

And the phase in the following matrices will also be incremented by an amount $\delta\phi$ to take into account the phase jump on the following pulses. Computing the resulting population in the final state $|C_f\left(T + 5\tau + 2t_c, \delta\phi\right)|^2$ and using eq (100) one obtains the Large Mach-Zehnder sensitivity function:

$$g_s^{LMZ}(t) = \begin{cases} \sin\left(t\Omega_{eff}\right) \quad t \in [0,\tau] \\ 1 \quad t \in [\tau, \tau + t_c] \\ \left.\begin{array}{l} \frac{1}{4}\sin\left[2\Delta\omega\left(t - t_c - \tau\right)\right]\sin^2\left[\left(t - t_c - \tau\right)\Omega_{eff}\right] \\ +\cos\left[2\Delta\omega\left(t - t_c - \tau\right)\right]\cos\left[\left(t - t_c - \tau\right)\frac{\Omega_{eff}}{2}\right] \\ +2\sin^2\left[\left(t - t_c - \tau\right)\frac{\Omega_{eff}}{2}\right] \end{array}\right\} \quad t \in [\tau + t_c, 3\tau + t_c] \\ 2 \quad t \in [3\tau + t_c, T + 3\tau + t_c] \\ \left.\begin{array}{l} \frac{1}{4}\sin\left[2\Delta\omega\left(t - T - t_c - 5\tau\right)\right]\sin^2\left[\left(t - T - t_c - 5\tau\right)\Omega_{eff}\right] \\ +\cos\left[2\Delta\omega\left(t - T - t_c - 5\tau\right)\right]\cos\left[\left(t - T - t_c - 5\tau\right)\frac{\Omega_{eff}}{2}\right] \\ +2\sin^2\left[\left(t - T - t_c - 5\tau\right)\frac{\Omega_{eff}}{2}\right] \end{array}\right\} \quad \begin{array}{l} t \in [T + 3\tau + t_c, \\ \quad T + 5\tau + t_c] \end{array} \\ 1 \quad t \in [T + 5\tau + t_c, T + 5\tau + 2t_c] \\ \sin\left((T + 6\tau + 2t_c - t)\Omega_{eff}\right) \quad t \in [T + 5\tau + 2t_c, T + 6\tau + 2t_c] \end{cases} \tag{104}$$

where for each pulse, we have assumed the resonance condition to be fulfilled : $\omega_1 - \omega_2 = \omega_e - \omega_f$, $\omega_3 - \omega_4 = \omega_f - \omega_g$ and we have chosen the highest sensitivity point $\Phi = \pi/2$. The quantity $\Delta\omega = \omega_g - \omega_e = 4\omega_D + 16\omega_{rec}$. The $t < 0$ part of g_s is obtained by using the time reversal symmetry of the interferometer which results in an odd function. Fig. 69 represents g_s for $T = 1\,\mathrm{ms}$, $\tau = 100\,\mu\mathrm{s}$ and $\omega_D = 0$. The sensitivity function of the three pulse interferometer is included as a comparison. An interesting feature of this sensitivity function is its dependence on the energy difference between the $|e\rangle$ and the $|g\rangle$ state. It can be understood as a energy shift induced by the interaction with three different momentum states. Indeed, the three sates cannot be simultaneously degenerate in any reference frame. Therefore, it is not possible to continuously describe the two interferometric arms in a single frame (accelerated due to gravity) were both interferometer arms have the same energy. The inset of Fig. 69 presents an enlarged view of the sensitivity function during one of the π_2 pulse which depends on $\Delta\omega\tau$.

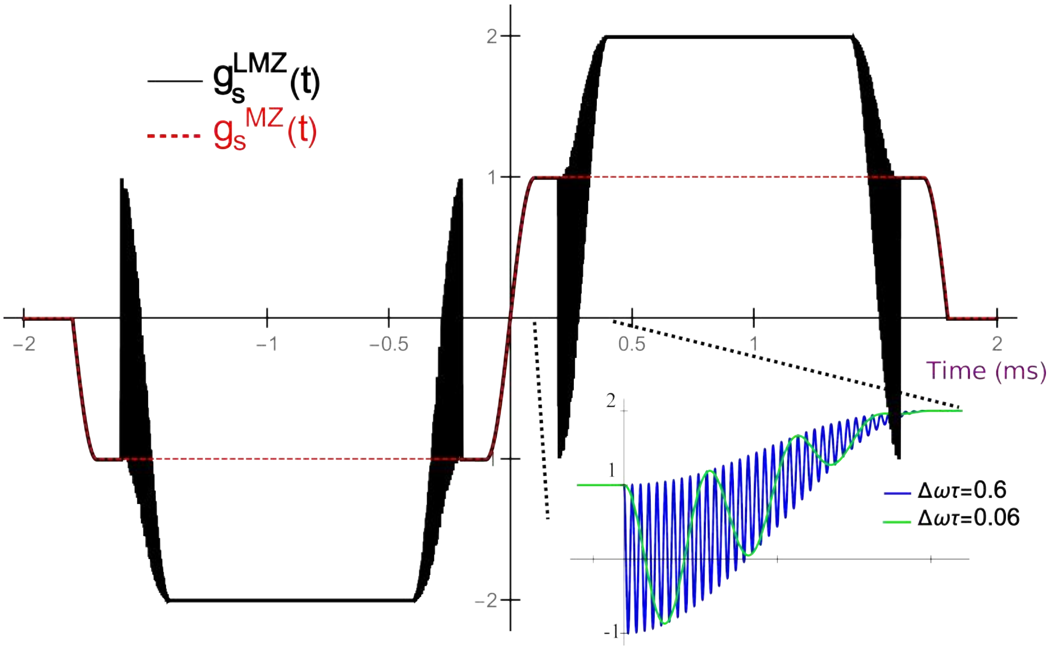

Figure 69: Complete sensitivity function (black) of eq. (104) compared to the three pulse sensitivity function (red, dashed). The interferometer parameters are $T = 1\,\mathrm{ms}$, $\tau = 100\,\mu\mathrm{s}$ and $\omega_D = 0$. A comparison of the energy dependent part for two smaller impulsion times $\tau = 10\,\mu\mathrm{s}$ (blue) and $\tau = 1\,\mu\mathrm{s}$ (green) is shown on the bottom right.

Phase noise sensitivity

From eq. (101) one sees that in addition to providing a simple expression of the interferometric phase when the laser phase is changed from pulse to pulse, the sensitivity function also allows to quantify the interferometer phase noise. For example, in the presence of a sinusoïdal phase fluctuation, $\phi(t) = S_0 \cos(\omega_0 t)$ eq. (101) gives us the amplitude of the corresponding interferometric phase $\delta\Phi$:

$$\delta\Phi = S_0\omega_0 \int_{-\infty}^{\infty} -g_s(t) \sin(\omega_0 t)\, dt$$

which is proportional to the Fourier transform G of g_s:

$$G(\omega) := \int_{-\infty}^{\infty} g_s(t)\, e^{-i\omega t} dt$$

evaluated at the noise frequency ω_0:

$$\delta\Phi = iS_0 \omega_0 G(\omega_0)$$

When the phase noise is described by a spectral density $S_\phi(\omega)$, the interferometer phase standard deviation σ_Φ is given by [312]:

$$\sigma_\Phi^2 = \int_0^\infty |\omega G(\omega)|^2 S_\phi(\omega) \frac{d\omega}{2\pi}$$

To extract information from this expression, one needs to know the transfer function $H(\omega) := |\omega G(\omega)|$. In the limit of short diffraction pulses (neglecting the energy dependent part $\Delta\omega \ll 1/\tau$) and zero cycle time $t_c = 0$, a simple analytical expression of the transfer function for the Large Mach-Zehnder can be obtained:

$$\begin{aligned} H^{LMZ}(\omega) = \sin\left(\frac{T+6\tau}{2}\omega\right) \quad \frac{16\omega\Omega_{eff}}{|\omega^2 - \Omega_{eff}^2|} \Bigg\{ &\cos\left(\frac{T+6\tau}{2}\omega\right) \\ &+ \frac{\Omega_{eff}}{2\omega}\left[\sin\left(\frac{T}{2}\omega\right) + 3\sin\left(\frac{T+4\tau}{2}\omega\right)\right]\Bigg\} \end{aligned} \quad (105)$$

which presents similar feature compared to the Mach Zehnder sensitivity function calculated and described in [311]. The sinusoidal first factor periodically cancels the transfer function at frequencies multiple of $1/(T+6\tau)$ which conveys the physical fact that the interferometer is insensitive to fluctuation that are identical at each diffracting pulses. At frequencies higher than the pulse duration $1/\tau$, fluctuations tend to average during each pulses which can be seen on the low-pass filter factor $\frac{16\omega\Omega_{eff}}{|\omega^2 - \Omega_{eff}^2|}$. Finally, another set of frequencies cancels the last factor in brackets. One can note the $1/(T+4\tau)$ and $1/T$ particular frequencies which correspond to the shorter time scale between π_2 pulses (either on the same arms or on opposite arms) which can also lead to a partial compensation of phase noise at these frequencies.

This transfer function is represented on Fig. 70 for the parameters $T = 50\,\text{ms}$ and[42] $\tau = 20\,\mu\text{s}$. Due to the large oscillatory behaviour, the high frequency part has been averaged on one frequency period $1/(T+6\tau)$ to emphasize the low-pass filter and the secondary zeros.

The precise knowledge of this transfer function is important either to define the interferometer sequence to reject particular frequencies that might have large spectral components or to implement active noise rejection with an external vibration sensor. However, the result presented here are only the first step as both higher number of

---

[42] It corresponds to the limit of the $\Delta\omega \ll 1/\tau$ assumption.

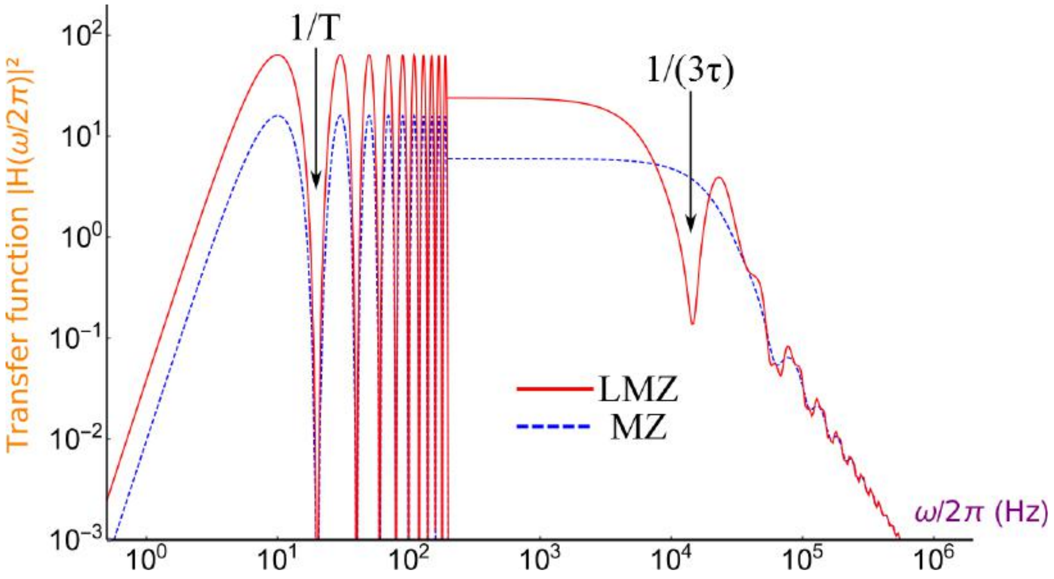

Figure 70: Transfer function of the Mach-Zehnder sensitivity function (102) (blue, dashed) and the Large Mach Zehnder sensitivity function (104) (red, full). The amplitude at low frequency are different due to the scale factor between the two interferometers. A large dip in the second function at 15 kHz reflects how the different frequencies $1/(T+6\tau)$, $1/(T+4\tau)$ and $1/T$ can cancel the transfer function around the $1/(3\tau)$ frequency.

pulses are used to create Large Momentum Mach Zehnder Interferometer and they often consist in more complicated pulse shape with additional transient atomic states.

LMT Interferometer

Our expected interferometric sequence will consist in a LMT multi-Bragg interferometer with $42\hbar k_L$ momentum separation. With moderate power (300 mW) and detuning ($\delta = 10$ GHz) we expect to get 7×10^4 atoms contributing to the interferometric signal. To reach the QPN, vibrational noise rejection is mandatory and motivated us to develop the initial tools required to evaluate the exact sensitivity function and the corresponding transfer function of this LMT interferometer. As an example, a 7 pulse interferometer sequence was described. In particular, its transfer function was calculated and displayed a new particular frequency $1/(3\tau)$ at which its sensitivity decreases.

5.6 CONCLUSION

To perform an improved measurement of matter neutrality, a new apparatus was conceived and is currently under development in our group. This chapter shows how this new experiment should improve the current knowledge on the residual charge by a factor of 200 when its shot to shot sensitivity is limited by Quantum Projection Noise. This measurement relies on the large spatial separation ($> 1\,\mathrm{cm}$) of a Bose-condensed atom interferometer operated at a cycle time of $6\,\mathrm{s}$. To reach these performances, specific development of a dual isotopes atomic chip source was undertaken. The resulting magnetic field configurations combined with numerical simulation of a dual isotopes evaporation showed how dual condensation could be achieved in a final optical trap. A transport protocol of a single isotope BEC, based on a guided optical lattice, was then described and the first numerical results obtained with an effective 1D Hamiltonian were shown.

In most of these steps, the additional isotope, ^{85}Rb, required special care which emphasizes the inherent difficulty to produce and manipulate such a cloud. I dare-say that the precautions implemented to circumvent these difficulties form a solid guideline for the future developments.

Finally a brief description of the two main scenarii used for Large Momentum Mach Zehnder interferometers allowed us to describe the requirements in terms of laser power and detuning necessary for $42\hbar k$ multiple Bragg beam splitters. Also, the sensitivity function of a 7-pulses Mach Zehnder interferometer was derived theoretically which is a first step towards a complete description of multi-pulses atom interferometers.

6 EXPERIMENTAL SETUP

Contents

The global objectives and specificities of this new experiments are established. In this chapter, I describe the experimental setup. This description is purposefully very detailed in order to provide a usable source of information for the next generation of P.h.D. students on this setup and potentially for the development of similar setups. At the end of each section, the main points are summarized for the reader eager to avoid these detailed descriptions.

I will describe the main parts of the experiment: the vacuum system, the laser system and the magnetic sources. The vacuum chamber was designed to incorporate a 2D MOT source to a main chamber were the 3D MOT and the subsequent atom traps. Ultra high vacuum pressure are required for these steps and will be characterized accordingly. The laser system necessary for the trapping, cooling, imaging and state preparation of the dual isotope source will then be described with particular focus on the frequency control and the long term stability of the setup. The optical system developed for the superposition and fiber injection of all the required laser beams will then be specified. Finally, the large magnetic coils and the mesoscopic chip structure and fabrication will be explained as well as some of the practical issues (wire temperature and optical access of the dipole beams) raised by this macroscopic structure.

Finally, a short presentation of the imaging system used to characterize the MOT will be given.

A general overview of the complete experimental structure is presented on Fig. 71 which displays front and rear views of the apparatus and its mechanical support.

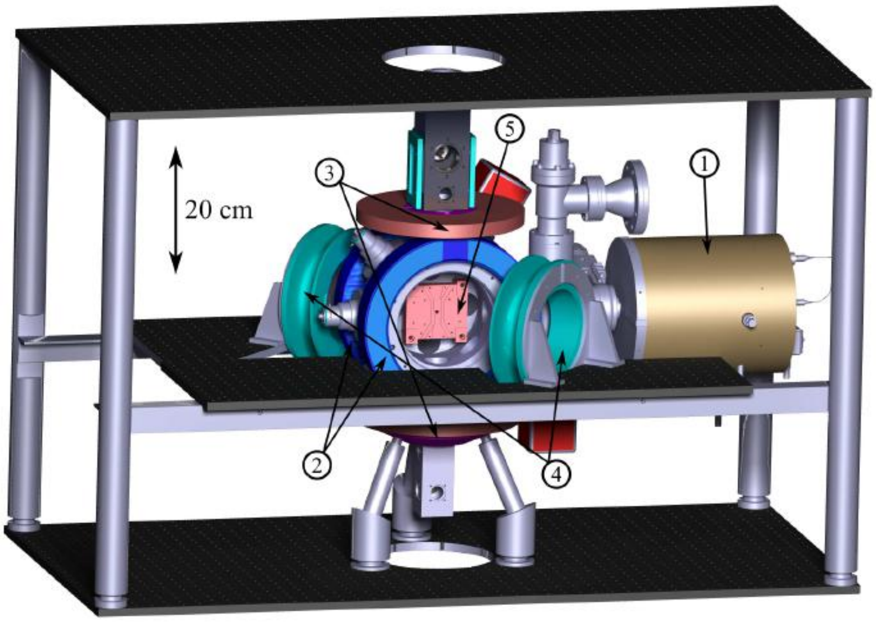

(a) Front view

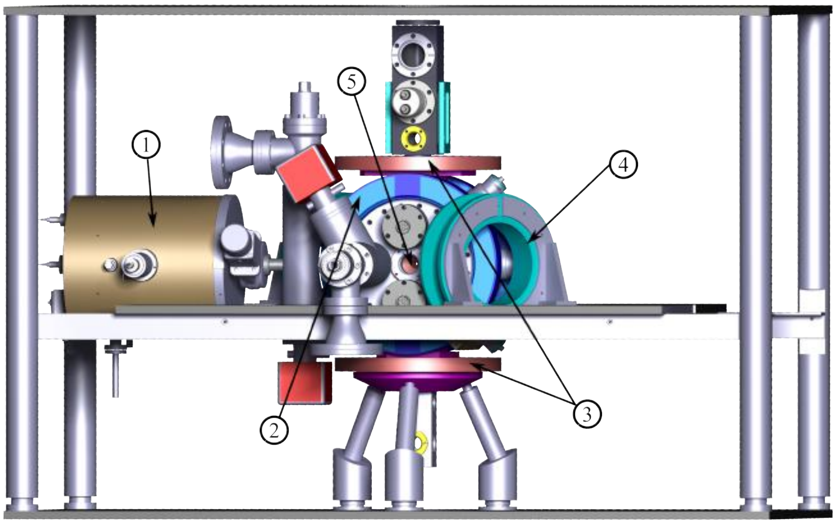

(b) Rear view

Figure 71: Schematic representation of the complete experimental setup. The 2D MOT with its magnetic shield ① (Golden rod cylinder), the magnetic coils for the Feshbach magnetic field ② (blue disc), bias field ③ (pink disc), quadrupole fields ④ (turquoise supports) and the chip support ⑤ (pink block at the center of the apparatus) are clearly visible. The vacuum chambers will be presented on Fig. 73 and on Fig.72 with clearer details. The mechanical support includes aluminum optical breadboards. All the surrounding metallic parts have been carefully separated (by a mechanical cut and with Kapton insulated screws) to prevent any eddy currents in the structure. The total dimensions of the structure is $120\,\mathrm{cm} \times 79\,\mathrm{cm} \times 60\,\mathrm{cm}$.

6.1 VACUUM SYSTEM

In order to create an appropriate environment for our cold atomic beam source and atomic clouds in the different traps, we mainly have to take into account the background collisions which principally lead to losses. The typical decay time τ_{back} of an atomic ensemble in a trap depends on the background pressure[1]: $\tau_{back} = \left(10^{-8}/P(mbar)\right)$ s. Typically, a pressure below 10^{-10} mbar is necessary to have trap lifetimes longer than the evaporation duration. For atom chips, the evaporation can be much faster than for macroscopic magnetic traps which relaxes the requirement on the background pressure[2]. On the other hand, atom chips usually increase the pressure as they can include additional degassing parts compared to other vacuum systems. Which is why we designed a vacuum system with a low pressure in the BEC production region, i.e the main chamber, even in the presence of the atom chip. In this section, we are going to describe this system and show that the vacuum performances reached are acceptable.

6.1.1 Principal vacuum chambers

The vacuum system consists in 4 principal chambers:

- The vacuum chamber of the 2D-MOT source is represented on Fig. 73d. It was made by the SYRTE and consists in a rectangular parallelepiped chamber connected via a Lesker® VAT-54124-GE02 valve to a Rubidium dispenser. Rectangular viewports (25 mm × 90 mm) provide access to the transverse sides and a 1 ″ diameter viewport provides optical access along the chamber. The atomic flux emitted is collimated by an exit hole 0.75 mm diameter and 16 mm long.
- The main vacuum chamber for the source contains the atom chip. It is an octagonal titanium chamber represented on Fig. 73c. The incircle has a 200 mm diameter and the chamber is 100 mm thick. Among its eight sides, three are CF 35 flanges for the connection to the other chambers and five are sealed with 2 ″ diameter viewports. The chamber front is sealed with a $\phi = 170$ mm, 20 mm thick window. The chamber back is a CF 100 flange which incorporates four CF 35 pods. At the center of this flange, a 1.5 ″ diameter viewport provides optical access through the chip (It can be seen clearly on Fig. 71b).
- The lower interferometer chamber, represented on Fig. 73b, is located 84 mm below the main chamber. It is a 50 mm × 50 mm × 130 mm rectangular parallelepiped titanium chamber with two CF16 viewports on its upper sides and four 1 ″ diameter viewports on its lower sides. A final 1 ″ diameter viewport seals the lower 50 mm × 50 mm face.

---

[1] In principle, this depends on the other colliding particle mass, temperature, cross section and partial pressure [313], but this practical rule of thumbs is useful for order of magnitudes considerations.

[2] For example, in Sec. 5.3 we have seen that $\tau_{back} \sim 20$ s is sufficient for dual isotopes evaporation which corresponds to a background pressure of the order of 5×10^{-10} mbar

- The upper interferometer chamber, represented on Fig. 73a, is located 66 mm above the main chamber. It is a 70 mm × 70 mm × 200 mm rectangular parallelepiped titanium chamber with three CF25 flanges, two 1″ diameter viewports on its lower sides and two 90 mm × 40 mm × 15 mm rectangular viewports. A final 2″ diameter viewport seals the upper 70 mm × 70 mm face.

6.1.2 Assemblies

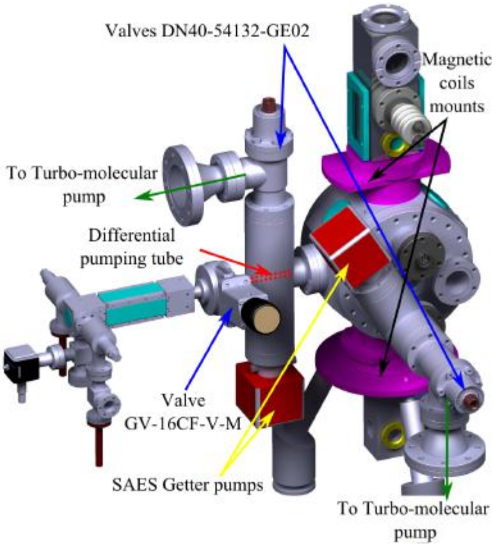

Figure 72
Assembled vacuum system showing the connecting cross to the 2D MOT and the T connected on one of the rear pods. The empty pod was later used to add a CapaciTorr® D50 NEG pump to the main chamber. The pink elements between the main chamber and the upper and lower chambers correspond to the magnetic coils supports

The assembled vacuum system is presented on Fig. 72. The main chamber is connected to a pumping section made of a 70 mm diameter titanium cross. A non magnetic valve (DN40-54132-GE02 VAT) on one of the orthogonal arms leads to the turbo molecular pump . The other orthogonal arm is connected to a D100-5 SAES® Getter pump. The last "arm" consist in a 90 mm long, 3 mm diameter differential pumping tube connection to the 2D MOT source. A copper valve GV-16CF-V-M from Lewvac® was inserted between the 2D MOT and this tube to isolate, if necessary, the source from the main experiment. Indeed, the 2D MOT can be connected to a smaller turbo pump which is sufficient to replace a dispenser relatively rapidly.
The lower and upper chambers are directly mounted on the main chamber via CF 35 flanges connected with tubes 34 mm diameter and 40 mm diameter respectively.
One of the four rear pods of the main chamber is connected to a 70 mm diameter T titanium connector. The bent part leads to a D200-5 SAES® Getter pump. The straight part is connected to a DN40 54132-GE02 VAT valve which itself can be connected to the turbo molecular pump.

6.1.3 Viewports and indium seals

Apart from the two CF16 viewports of the lower chamber, all viewports were fixed on the chamber using an indium sealing technique. They were all made of BK7 glass coated to have a low reflectivity at 780 nm; 1064 nm and 1560 nm. This was chosen in accordance with the wavelength required for atomic cooling, imaging and with the available high power lasers potentially usable for atomic manipulation. The seal-

(a) Upper

(b) Lower

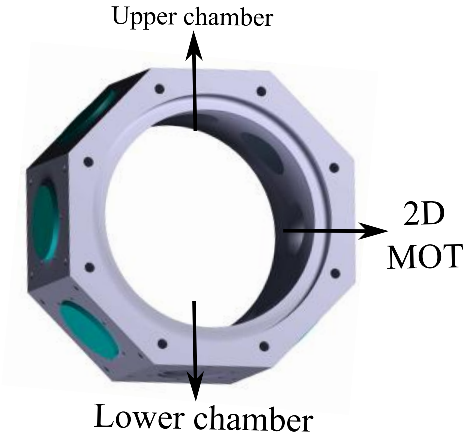

(c) Main

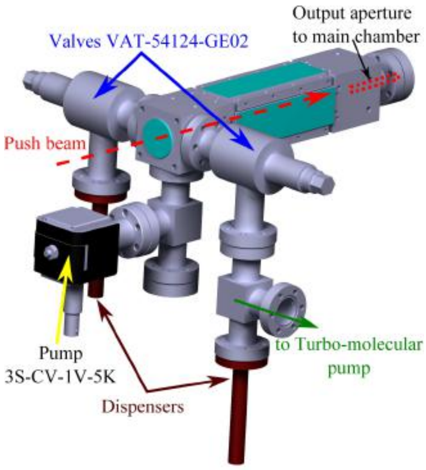

(d) 2D MOT

Figure 73: Schematic representation of the four main vacuum chambers. The final assembly is represented on Fig. 72

ing technique relies on the molecular adhesion between a pure indium gasket and the surfaces of the BK7 glass on one side and the metal flange on the other side. This technique was initially developed for cryogenic vacuum experiments as the sealing does not rely on mechanical constraints (as is the case for copper gasket for example) but on a chemical bound which is far more robust to deformations. However, one of the main drawbacks of this technique is the relatively low bake-out temperature (indium melting point at $1\,\mathrm{atm}$ is $157\,°\mathrm{C}$) which prevents to bake the assembled chamber to temperature higher than $110\,°\mathrm{C}$, increasing exponentially the bake-out duration. However indium magnetic properties are interesting as its diamagnetic susceptibility is much smaller than the one of alloys used in non-magnetic seals of commercial viewports (which have a residual magnetic field of a few $10\,\mathrm{mG}$). Additionally, the smaller mechanical constrains on the viewports reduces optical wave-front distortions.

The viewport of the 2D MOT were sealed with indium. The procedure consists in four main steps.

First, one has to remove the oxide layer which covers the indium wire. To do so, precision wipes (lint free) from Kimtech Science and a few drops of acetone were used to remove the thicker part of the oxide layer. Multiple cleaning were necessary to obtain a shiny surface. Then, the wire was put in a hydrochloric acid bath at $10\,\%$ equivalent mass. After $60\,\mathrm{s}$, using ceramic tweezers, the wire was directly transferred to a first distilled water bath. After 10 minutes, the wire was dried on a clean wipe and put in a different distilled water bath. After another 10 minutes, the dried wire was ready to be modeled to its gasket shape.

Using a Teflon cylinder, the indium gasket with the right diameter was created. To do so, an initial approximate circle was shaped and the wire was cut with approximately $2\,\mathrm{mm}$ extra length. This additional wire length was knotted around the other wire end as represented on Fig 74. The knot was "tightened" using clean tweezers to obtain a knot height similar to the wire diameter to have a gasket as flat as possible.

Then, using the same Teflon cylinder, the gasket was carefully positioned on the win-

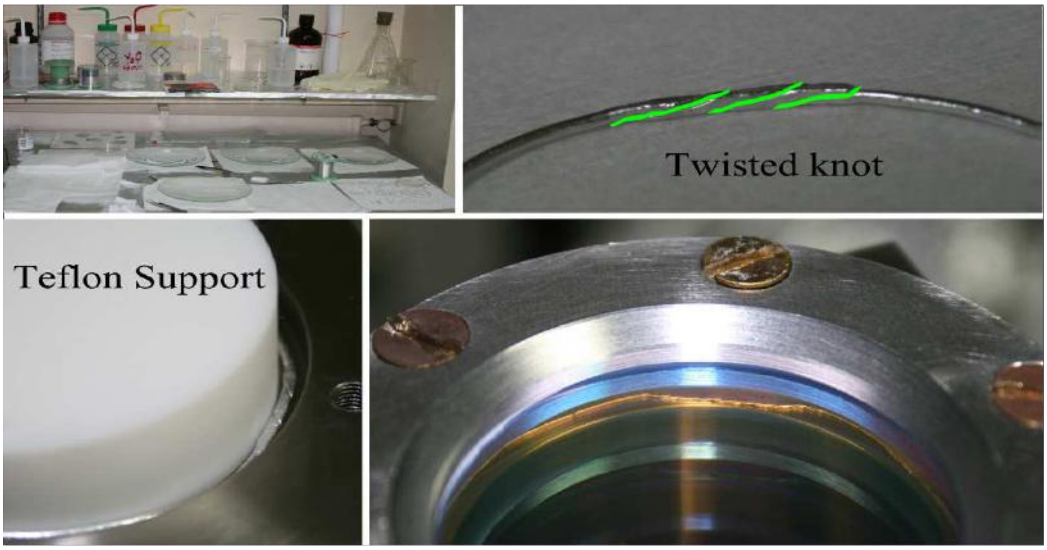

Figure 74: The four steps of the indium sealing technique. Left top: All the elements of the cleaning procedure described in the text are visible. Right top, knot of an indium gasket with the twined laces indicated in green. Left bottom, indium gasket positioned on the viewport flange with a Teflon tool. Right bottom, sealed viewport and its back flange, the pressed seal is visible with its larger width at the knot location.

dow flange. With care being taken to ensure appropriate centering.

Finally, the window was placed on the gasket, and a back flange was used to press the seal with an even compression all along the seal's length. This procedure was similar to the sealing of copper gasket apart from the maximum torque applied on the screws. By steps of $0.2\,\mathrm{N\,m}$, a maximum torque of $1\,\mathrm{N\,m}$ was applied on a $2''$ diameter $15\,\mathrm{mm}$ thick window, on each of the 6 screws. In principle, the back flanges can be removed once the vacuum is established and the seal is complete, but we did not chose to do it as they do not reduce much the optical access.

6.1.4 Assembly and bake-out

To test the airtightness of the vacuum chambers, the whole vacuum system was put together without the chip mount. Particular care was taken on the screws and other assembly elements to reduce the amount of stray magnetic fields around the interferometer regions. Titanium (resp. nickel free brass) screws were used for the assembly of the titanium chambers and the large flanges (resp. of the viewports back-flanges). As can be seen on Fig. 72, the magnetic coils supports are fitted to the vacuum system and had to be mounted at the same time. I will come back to these elements in Sec. 6.3.

The pressure, at room temperature, decreased to approximately $2 \times 10^{-8}\,\mathrm{mbar}$ in a week. To reach the $10^{-10}\,\mathrm{mbar}$ range quickly, we baked-out the whole apparatus. For ten days, the vacuum chambers were heated to approximately $100\,^{\circ}\mathrm{C}$. The differential temperature across the different parts was kept below than $10\,^{\circ}\mathrm{C}$ to prevent thermal dilatation from creating additional mechanical stress. After bake-out, the pressure rapidly decreased and at $5 \times 10^{-9}\,\mathrm{mbar}$ the ion pumps were turned on and the NEG were activated. Pressure of the order of the ion pumps sensitivity limit 1×10^{-11} mbar was then reached in three days.

Repeating this procedure after adding the mesoscopic chip (see Sec. 6.3.1 for its description) resulted in a slightly higher final pressure 10^{-10} mbar read on the ion pumps. During this operation, an additional NEG pump (CapaciTorr® D50) was installed on one of the four rear pods right at the center of the main chamber.

6.1.5 Pressure during operation

Reaching UHV pressure when the system is baked-out is only the first step towards good vacuum. One also needs to have the appropriate pressure during the apparatus operation. This is the reason why differential pumping stages are present between the 2D MOT source and the main chamber. The 2D MOT aperture already has a conductance $C_{2D} = 12.1 d^3/l = 3 \times 10^{-3}\,\mathrm{L\,s^{-1}}$, where d and l are the cylindrical aperture diameter and length in cm, which reduces the gas charge at its output. The pressure in the 2D MOT during operation is typically smaller than 5×10^{-7} mbar therefore, the gas charge at the aperture output is 2×10^{-9} mbars/L. The 100 L/s D100 getter pump situated at the 2D MOT output should be able to pump this charge down to a pressure of 5×10^{-11} mbar. But the distance between the 2D MOT output and the chip's mirror (400 mm) and the capture radius of the 3D MOT (5 mm) reduces the usable beam solid angle to 0.17 sr (corresponding to a beam angular aperture of 15 mrad). Therefore, an additional differential pumping stage (represented on Fig. 72), reduces the gas charge by half[3] and should not change the 3D MOT loading rate (the geometrical 2D MOT aperture with this additional tube is 15 mrad). Reducing the gas load tends to extend the ion pumps lifetime which motivates this additional differential stage.

In practice, we have seen that the pressure indicated by the ion pumps increases slowly during the day (from 2×10^{-10} mbar in the morning to 6×10^{-10} mbar at the end of the day) which indicates that vacuum conditions in the main chamber are probably changing due to residual rubidium gas. However, quantitative measurement of the trap lifetime needs to be undertaken as soon as the atoms are magnetically trapped[4] in order to be sure of our vacuum quality.

Vacuum system

The complete vacuum system consists in four Titanium chambers. Differential pumping stages, ion pumps and NEG lead to a pressure in the main chamber around 5×10^{-10} mbar. Indium sealing techniques were used for most of the viewports to limit the stray magnetic fields and the wavefront distortions on the diffracting beams.

---

[3] The conductance of the second tube is similar to C_{2D}: $3.6 \times 10^{-3}\,\mathrm{L\,s^{-1}}$

[4] MOT lifetimes have already been estimated and seems to be in the 15 s range. Even though additional loss mechanisms can prevail during this type of measurements it still indicates that the background lifetime is at least 15 s, corresponding to a background pressure below 7×10^{-10} mbar.

6.2 LASER SYSTEM

The dual isotope objective of our atom source guided most of our choices on the design of the laser system for cooling and imaging light as it required four laser frequencies. Besides, in the perspective of long measurement campaigns, the optical system had to be robust and reliable. This section will consist in a complete description of the laser system realized during my thesis and will show how it fulfills the aforementioned objectives while generating the necessary intensities and combined frequencies for the atom sources different production steps.

6.2.1 Overview

Laser cooling of alkali atoms requires simultaneously at least two frequencies per atomic isotope. For Rubidium, the $P_{\frac{3}{2}}$ hyperfine structure is larger than the states linewidth Γ. Therefore, the superposition of only two frequencies is sufficient to perform Doppler and sub-Doppler cooling as well as optical pumping and imaging. These frequencies are generally denoted cooling and repump frequencies as they correspond, in the steady state MOT operation, to the cycling frequency which reduces the atomic motion and to the frequency which prevents atom losses to dark states. The exact frequencies required for ^{85}Rb and ^{87}Rb are summarized on Fig. 75. One can see that the repump frequency remains constant and that the "cooling" frequency needs to be tuned a few Γ below the cycling transition during the 3D MOT stage. Additionally, to efficiently pump the atoms in a low field seeking dark state (^{87}Rb $|F=2, m_F=2\rangle$ for example), the "cooling" frequency is tuned to the lower transition, 44Γ below the MOT cooling transition. This means that only the cooling laser frequencies need to be dynamically changed over a typical range of 20Γ as the optical pumping light can be produced with an additional constant shift. Also, for sub-Doppler cooling, optical pumping and imaging, the light intensity needs to be controlled independently between cooling and repump frequencies which requires independent control of the laser power.

6.2.2 ^{85}Rb Laser setup

The laser system used for ^{85}Rb is a commercial system developed by Muquans®. It relies on two Distributed FeedBack (DFB) laser diodes with a master and slave architecture (cf. Fig. 76). The master laser is amplified by a commercial Erbium-doped fiber amplifier (EDFA) from Keopsys (CEFA-C-PB-HP-PM-40-NL1-OM1-B301-FAFA). A third amplified output is frequency doubled in Periodically-Poled Lithium Niobate (PPLN) crystal and provides around $280\,mW$ of Repump light. A weak beam is used in a saturated absorption cell which locks the master frequency on the $|F=2\rangle \longrightarrow |F'=1\rangle$ transition. The slave laser is phase-locked on the master laser and similarly amplified and doubled. It has two high power outputs ($160\,mW$) and a third lower power one ($30\,mW$). The frequency difference $\Delta_{f,85}$ between the master

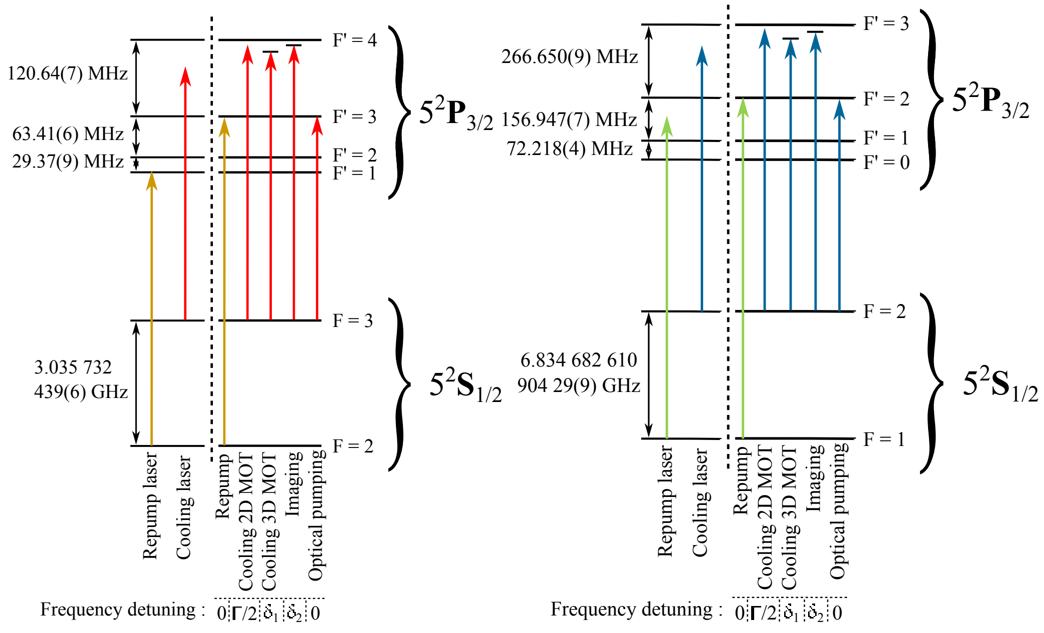

(a) ^{85}Rb (b) ^{87}Rb

Figure 75: Energy levels of the electronic transitions used for laser cooling, pumping and imaging of ^{85}Rb and ^{87}Rb. The left hand side transitions represent the frequencies at which the Repump and Cooling lasers are locked. The right hand side summarizes the different frequencies required in each experimental steps and gives the corresponding typical detuning of each beam.

and slave laser is controlled by a direct Digital Synthesizer (DDS) clocked by an external frequency. The frequency difference between the outputs of this laser system is given by the relation $\Delta_{f,85} = 2 * 32 * f_{DDS}$ which takes into account a division factor of the beat note frequency between the master and slave and the frequency doubling. This allows to control the slave output's frequency ("Cooling") hundreds of MHz around the $|F = 3\rangle \longrightarrow |F' = 4\rangle$ transition frequency.

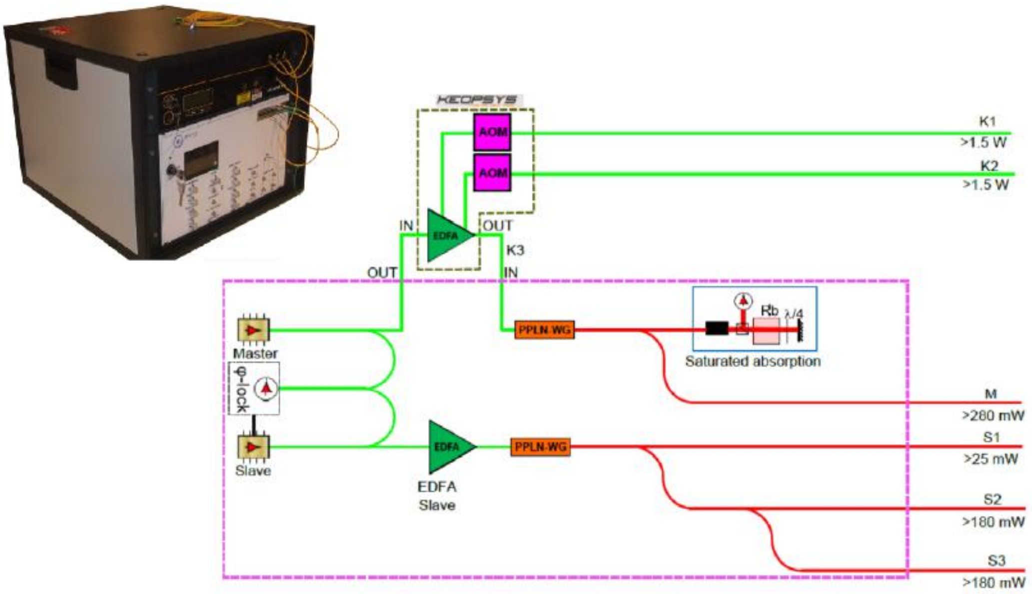

Figure 76: Scheme of the Muquans laser.

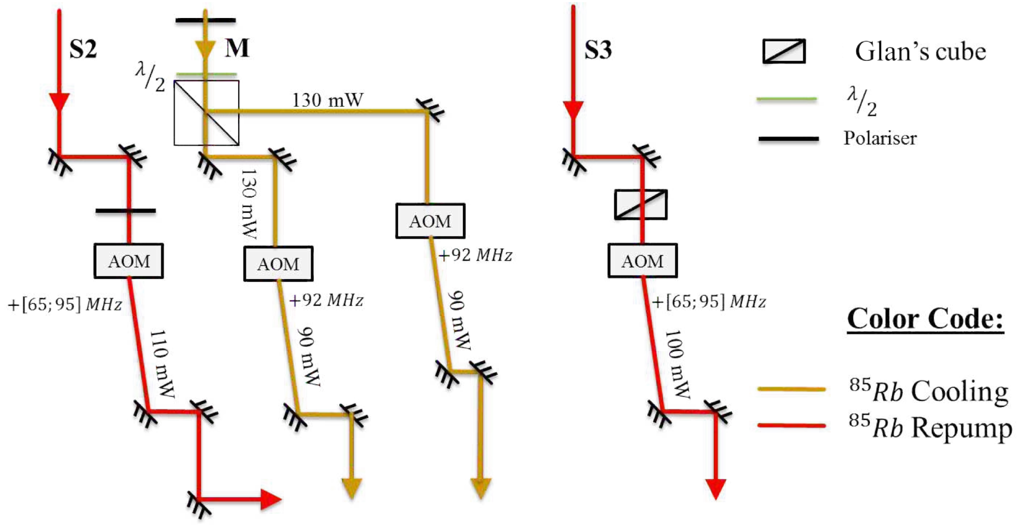

Figure 77: Schematic representation of the ^{85}Rb optical bench.

6.2.3 Frequency adjustment and stability characterization

The laser frequency provided by this system does not correspond to the repump transition $|F=2\rangle \longrightarrow |F'=3\rangle$ represented on Fig. 75a. This is the reason why additional frequency shifts provided by Acousto-Optic-Modulators (AOM) from Crystal Electronics® (ref: 3080-122) were implemented. They are also used as fast shutters. The optical drawing is represented on Fig. 77 were the repump (**M**) and cooling (**S2**,**S3**) outputs are injected in AOM's and, for the repump light, split into two different beams which will be described further in Sec. 6.2.6. The AOM's are driven by an RF source at 92.8 MHz (Repump) and 80 MHz (Cooling) which shifts the repump laser to the required $|F=2\rangle \longrightarrow |F'=3\rangle$ transition frequency and offsets the cooling laser by a constant amount[5]. The RF source is made of a Voltage Controlled Oscillator (VCO, model ZX95-100-S+), a switch (ZX73-2500-S+) to control the amplitude and a 25 dB high power amplifier (ZHL-3A-S+) produces the required 10 dBm for the AOM's. The diffraction efficiencies in the +1 order are higher than 70 % which is close to the specified maximum (85 %).

Additional polarizing elements were included before the AOM's. This choice is motivated by the large fluctuation of the polarization direction that we observed at the fiber outputs. Indeed, these long term fluctuations reach the 10 % level which degrades our power stability as subsequent polarizing elements are used on the optical path. To minimize this effect, polarizers used at their maximal transmission are included which reduces the subsequent power fluctuations as they depend on the square of the polarization direction. The small polarization fluctuation is illustrated on Fig. 78 were we show the Allan variance of the polarization filtered laser outputs. The long term relative stability remains below 10^{-4} at 5 h $\sim 2 \times 10^4$ s which is sufficiently low for laser cooling experiments. A particular feature around 100 s showing a transitory increase in fluctuations is probably linked to the air conditioner which has a typical period of a few minutes.

---

[5] It corresponds to the central frequency band of the AOM's which is the most efficient region

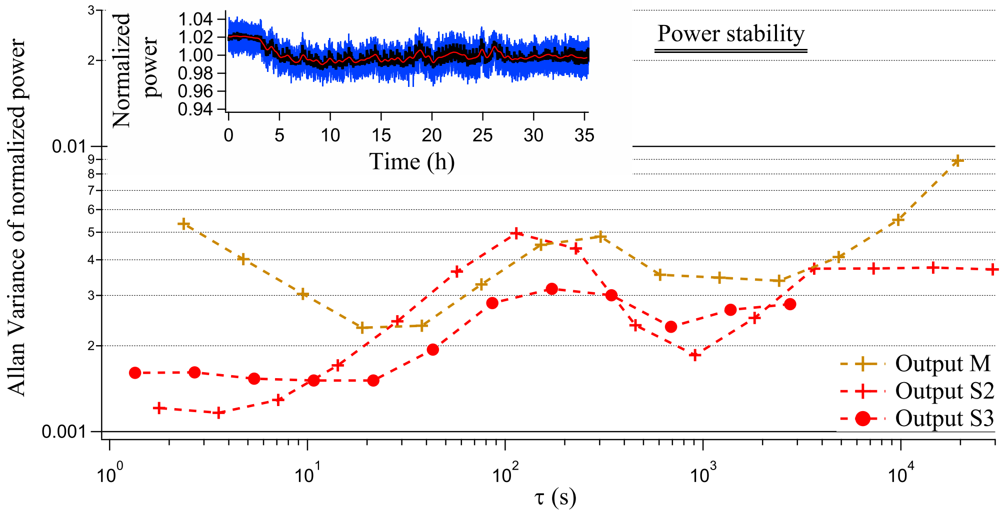

Figure 78: Allan variance of laser power for this setup. The inset shows a typical recording of the normalized power at output S2. The blue background corresponds to a sampling rate of $\tau = 1$ s, the black lines corresponds to a sampling rate of $\tau = 10^2$ s and the red line to smoothed mean value.

Regarding the frequency stability of this laser system, we will see in Sec 6.2.4 that the long term frequency drift is below 200 kHz. This ensures a reliable cooling sequence as the frequency needs to be adjusted to better than a fraction of the transition linewidth.

6.2.4 ^{87}Rb Laser setup

The ^{87}Rb laser setup is designed on the same principle as the ^{85}Rb one (cf. Fig. 79). A repump laser is locked close to the repumping transition with a saturated absorption setup and a cooling laser is locked at a given frequency difference $\Delta_{f,87}$ with respect to the repump laser. However, two main differences distinguish this setup from the ^{85}Rb one. The first one is the lasers which, for ^{87}Rb, are an extended cavity laser diode from Toptica® (DL Pro 100 780-11355) as repump laser and an amplified and doubled Telecom laser system manufactured by Quantel ® (EYLSA 780 MSA) as cooling laser. The available laser powers are better distributed for laser cooling experiments as the repump laser total power is around 60 mW and the cooling laser total power is slightly less than 1 W which corresponds to the ratio of 1:20 for repumping light versus cooling light. The second difference is the frequency locking instead of the phase locking.

The repump laser locking scheme relies on a FM-spectroscopy technique applied to a saturated absorption setup. The Electro-Optical Modulator (EOM), from Qubig® (ref: EO-F6-25L3), produces the phase modulation. Detecting the saturated absorption with a fast photodiode and demodulating the signal directly provides an error signal usable in a PID loop. The correction is implemented with the digital laser locking module from Toptica®. The laser is locked on the $|F = 1\rangle \longrightarrow |F' = 1/F' = 2\rangle$ crossover peak of ^{87}Rb. To increase the absorption amplitude, we used a heating element to get the cell to 50 °C which provided a ten fold improvement of the Signal/Noise ratio. After optimization of the PID parameters, the laser remains locked for days.

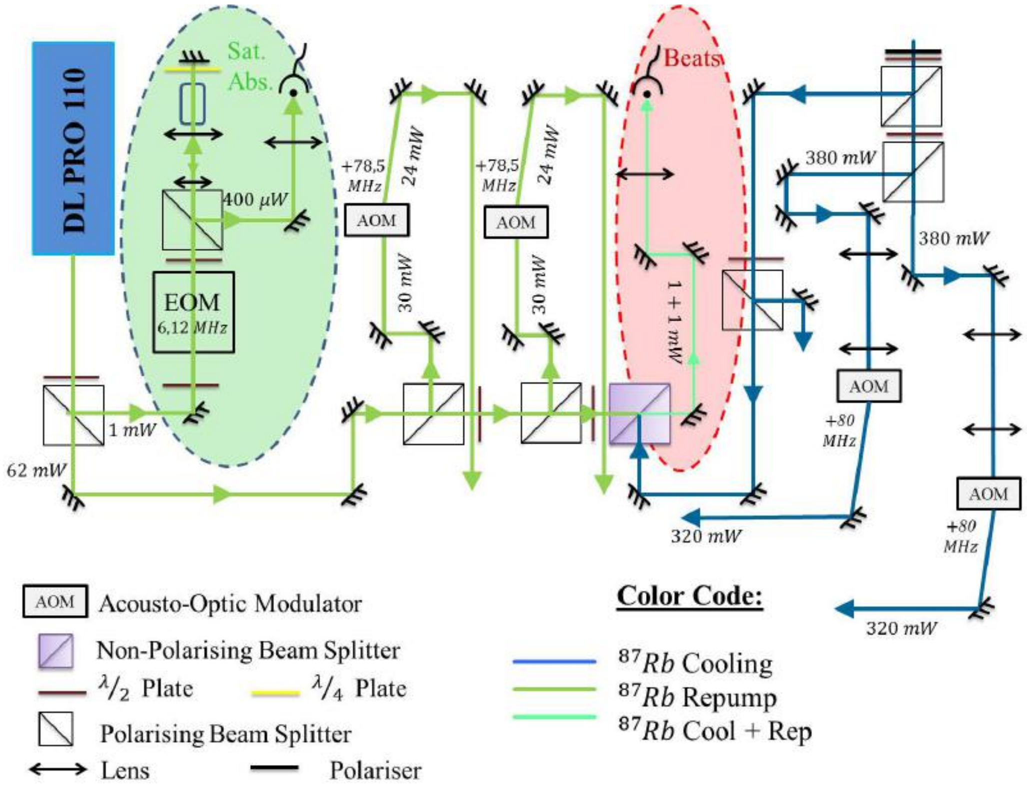

Figure 79: Schematic representation of the ^{87}Rb optical bench. The two frequency control parts are emphasized in green and pink colors.

Frequency stability

By monitoring the beat note between this repump laser and the ^{85}Rb repump laser, we estimated the long term frequency drifts of our two locking systems as well as the laser linewidths. The result of this measurement is presented on Fig. 80. The Allan deviation of the frequency beat note is represented for times up to 10^4 s. We see that the long term frequency fluctuations, which we can assume to a good extend uncorrelated, are around 200 kHz. It shows that both laser frequencies are controlled, relatively to their mean value, down to a fraction ($\Gamma/40$, assuming identical independent noise sources) of the transition linewidth. It guarantees that the laser source is stable enough for laser cooling. On the short time scale the frequency fluctuations are well integrated by a white noise model (black line). The short term jitter is about 500 kHz at 100 ms. Also, the beat note linewidth at 1 ms was of the order of 500 kHz which tells us that the ^{85}Rb repump laser linewidth is at least[6] 400 kHz. This is coherent with typical DFB linewidths which are of the order of 1 MHz.

---

[6] Extended cavity laser diode have much narrower linewidth, specified at 100 kHz by Toptica® for example, than DFB diode lasers. This is the reason why beat note linewidth is probably dominated by the ^{85}Rb repump laser.

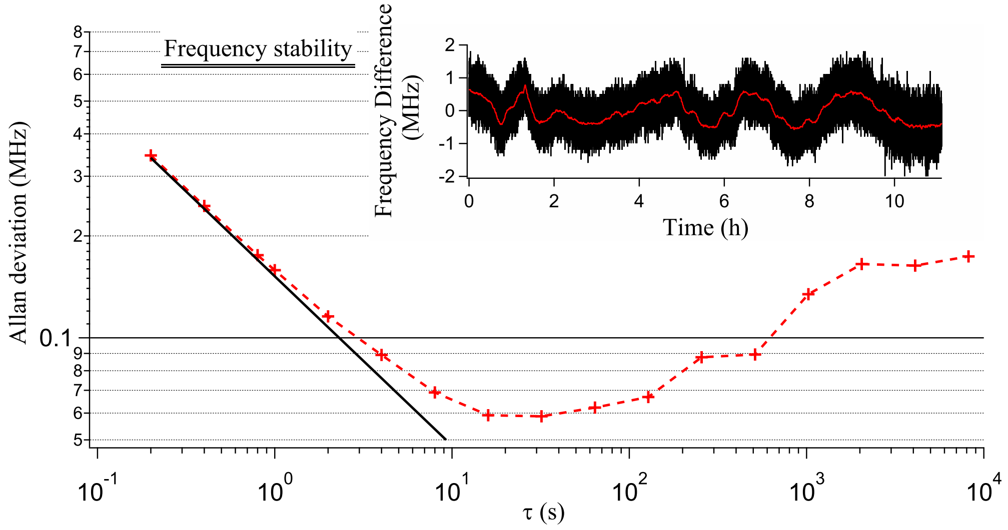

Figure 80: Allan deviation of the frequency beat note between the two ^{85}Rb and ^{87}Rb repump lasers (red cross, the dashed line is a guide to the eye). The black line represents white noise integrated from 0.2 s to 10 s. The inset shows the temporal frequency difference evolution subtracted by its mean value. In black is represented the full data set and in red its averaged value over 100 s.

Slave locking scheme

The beat note produced by interferences on a fast photodiode (Hamamatsu® G4176-03 with a 25 GHz frequency cut-off) of two laser beams from both laser allows to lock the cooling laser frequency with respect to the repump laser (see Fig. 79 red shaded area). The beat note frequency corresponds to the frequency difference between two hyperfine levels: 6.568 GHz. We used a combination of frequency mixers to divide the measured frequency into the frequency range $(0-500\,\text{MHz})$ of a frequency-to-voltage converter. This is represented on Fig. 81 where two frequency mixing are performed. The first mixing produces a signal at the frequency difference $\Delta_{f,87} - f_{VCO,1}$, where $f_{VCO,1} = 4.1925\,\text{GHz}$ is a fixed value. This signal is amplified and mixed with a second frequency $f_{VCO,2}(V_{tune}) \in [1.4; 2]\,\text{GHz}$ which can be dynamically controlled by an external tuning voltage. The high frequencies are filtered out and only the low frequency component $f_{VCO,2} - (\Delta_{f,87} - f_{VCO,1})$ lies in the conversion range of the frequency converter.

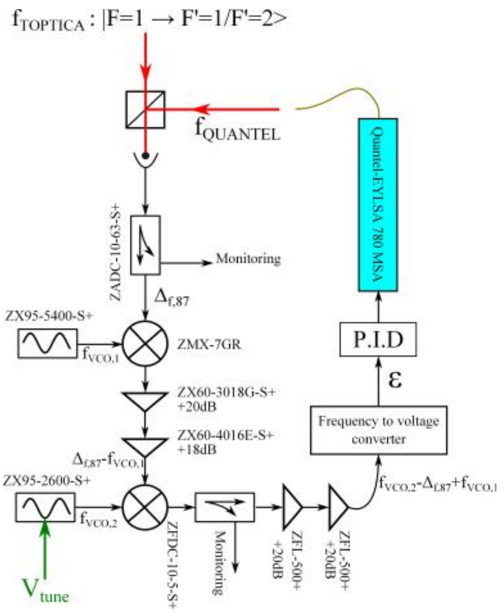

Figure 81
Schematic representation of the frequency chain, frequency converter and servo-loop system used to lock the ^{87}Rb cooling laser on the ^{87}Rb repump laser.

In a 300 MHz wide band around 500 MHz, this converter produces an error proportional to the beat note frequency:

$$\epsilon\left(\Delta_{f,87}, V_{tune}\right) = A + B\left[f_{VCO,2}\left(V_{tune}\right) + f_{VCO,1} - \Delta_{f,87}\right]$$

where A is a fixed offset and $B = 20\,mV/MHz$ is the converter gain almost constant within the frequency range. This signal is used as an error input for PID controller which provides the feedback signal applied on the cooling diode laser current. The long term frequency stability of this system is stable below the 100 kHz level at 10^4 s which indicates that the cooling frequency stability is mainly limited by the repump laser locking system. On the shorter time scale, the beat note spectrum is rather large (FWHM of 5 MHz for a 1 ms acquisition) which tends to indicate a large frequency jitter. A possible solution to reduce this broad spectrum would be to use another laser diode source such as a RIO® Planex laser diode.

We opted for this locking system to have dynamical control on the locking frequency via $f_{VCO,2}\left(V_{tune}\right)$. An agile system allows to sweep the detuning of the cooling laser over 70 MHz between the MOT and the molasses in less than 1 ms. The frequency change of our system is presented on Fig. 82 were a sudden change in the VCO frequency of up to 13 linewidths is monitored on the error signal provided by the frequency converter. It shows that the laser frequency is brought to its final value in approximately 300 µs regardless of the frequency change amplitude and that the overshoot is equal to 2 % of the frequency kick amplitude. These performances are sufficient for our optical molasses which uses a detuning sweep of -10Γ in a few 100 µs.

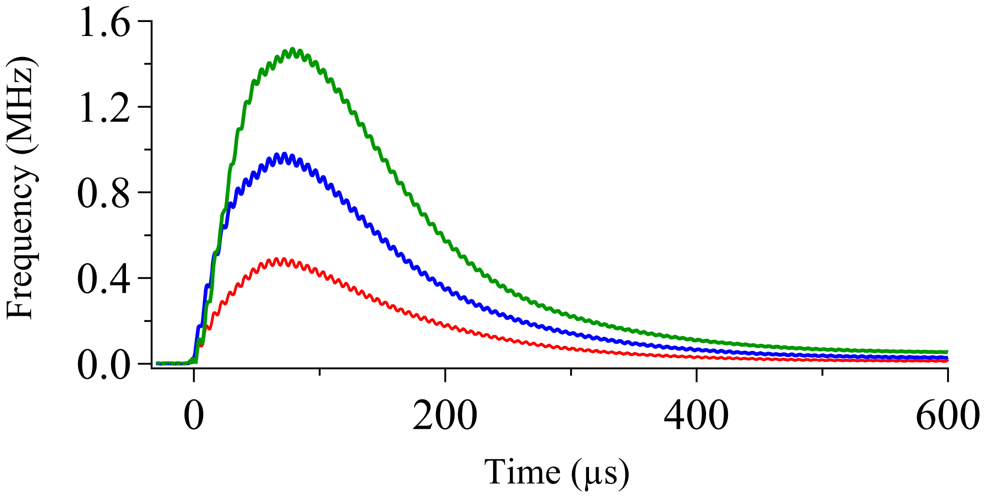

Figure 82: Temporal evolution of the error signal after a sudden change of the VCO tuning potential. Different detunings (4Γ red, 9Γ blue and 13Γ green) are represented and show that without any shaping of the tuning command, the laser frequency follows the command in less than 300 µs.

Frequency shift and intensity control

Additional AOMs frequency shifts, dynamically shuts the light from both lasers and produce two sets of Cooling and Repump beams. They are represented on Fig. 79 along the two locking systems. The repump light is shifted 78.5 MHz up to produce the $|F=1\rangle \longrightarrow |F'=3\rangle$ resonant frequency and the cooling laser is up-shifted by 80 MHz.

The two sets of Cooling and Repump beams are then combined with the ^{85}Rb frequencies.

6.2.5 Fiber distribution

In order to optimize the stability of the cold atoms production, we chose an optical setup which provides different frequency combinations directly from optical fibers. In this section, I am going to show how light for the 3D MOT, the imaging beam, the 2D MOT and the optical pumping beams are generated from the two laser sources.

3D MOT beams

Four laser beams (indicated by △) are combined to produce the 3D MOT light. They include one ^{85}Rb Cooling beam, one ^{85}Rb Repump beam, one ^{87}Rb Cooling beam and one ^{87}Rb Repump beam. The optical setup is represented on fig. 83. They are first recombined isotope by isotope on a 50/50 non polarizing beam splitter (orange and turquoise). Then, each of these (Cooling+Repump) beams are recombined with the other isotope beams on a second 50/50 non polarizing beam splitter. Four beams (pink) are produced with all four frequencies aligned on the same polarization. They are all injected in four polarization maintaining fibers. As we cannot optimize perfectly the spatial mode for each frequencies independently, the injection efficiency is not always optimal. I still managed to obtain at least 50 % of the available power (up to 80 %) at the fiber outputs. This is summarized for all four frequencies in Tab. 15.

2D MOT beams and optical pumping light

The four remaining laser beams (indicated by ★) were recombined by type (i.e ^{85}Rb and ^{87}Rb cooling frequencies together). This choice was made as it is useful for optical pumping stages or blow-away beams to control separately the cooling or repumping frequencies for each isotopes. Also, for the optical pumping stage, the "Cooling" frequency has to be tuned to the lower transition, $|F=2\rangle \longrightarrow |F'=2\rangle$ for ^{87}Rb, while the Repump frequency does not need to be shifted. Therefore, we used an additional AOM for the Cooling beams only.

Besides, we needed to increase our ^{85}Rb cooling power and ^{87}Rb repump power for our 2D MOT which is done with a tapered amplifier. This scheme allowed to keep the amplifier in steady state while shutting the laser intensities for the other beams.

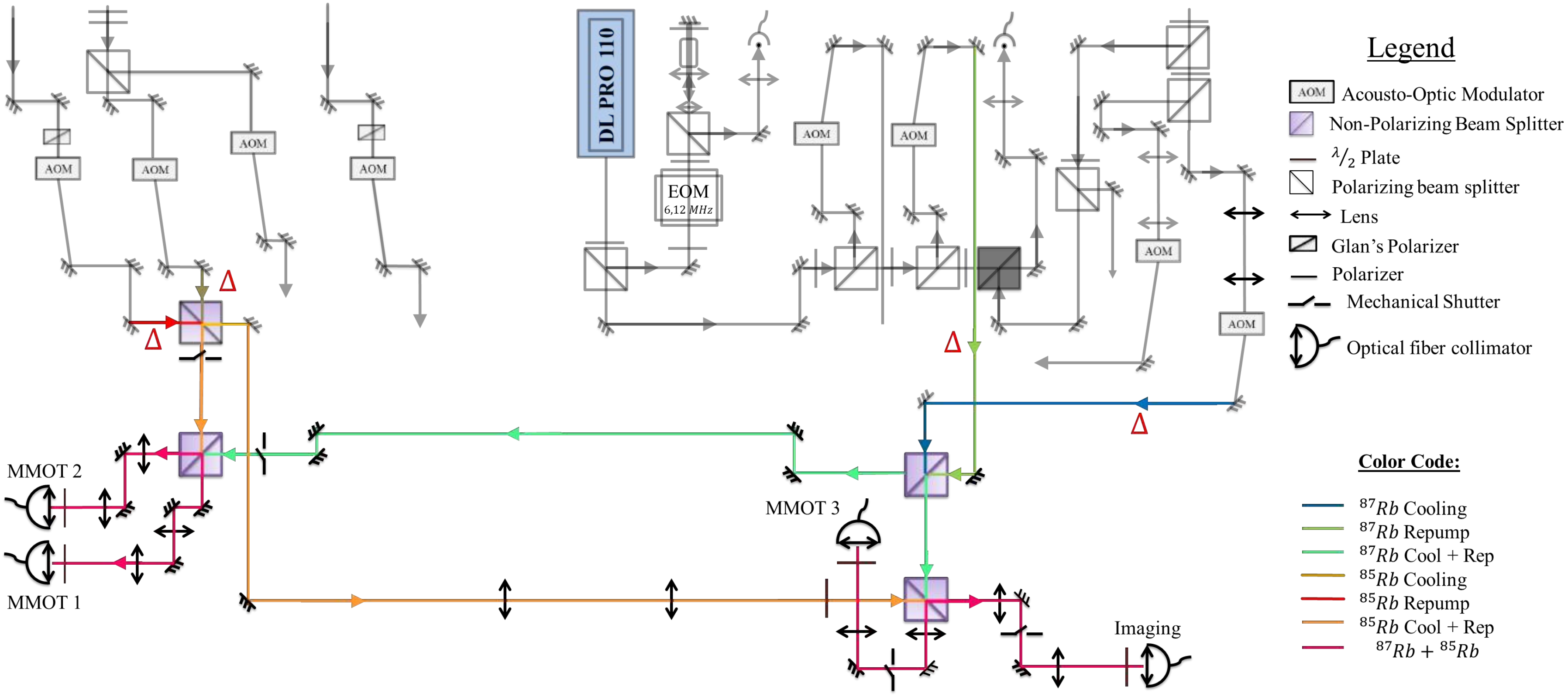

Figure 83: Description of the optical setup used to inject the four different frequencies on the same polarization in each fiber for the MMOT operation.

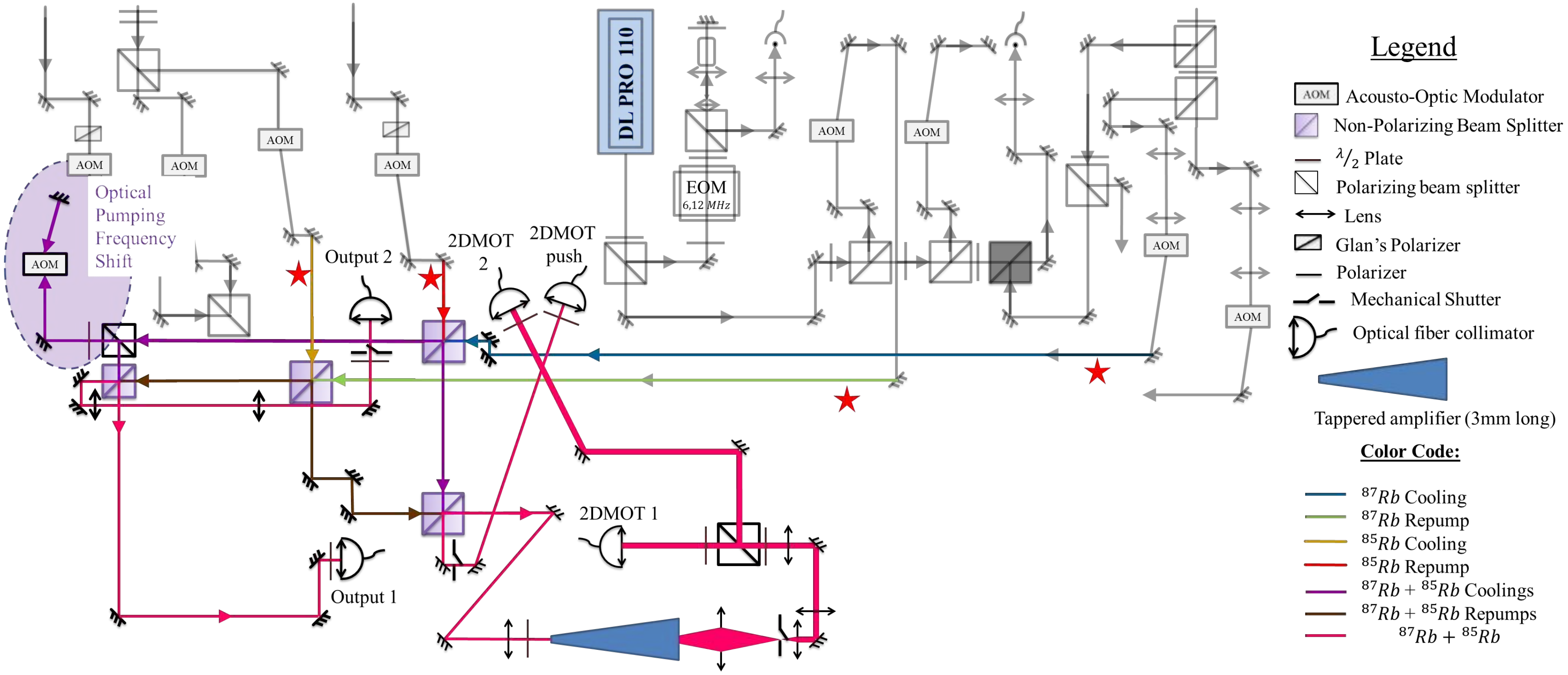

Figure 84: Description of the optical setup used to inject the four different frequencies on the same polarization in each fiber for the 2D MOT operation and for additional probing beams.

This superposition scheme is represented on Fig. 84. It produces two outputs (1 and 2) containing the frequency shifted cooling beams and the repump beams. The other two beams are dedicated to the 2D MOT. One beam corresponds to the push beam schematized on Fig. 73d which increases the flux of the 2D MOT source. The other beam is injected in a tapered amplifier semiconductor (EYP-TPA-0780-01000-3006-CMT03). Temperature control of the semiconductor is ensured with a temperature module from wavelength electronics® (PTC5K-CH-5 A) and results in a temperature stability of 0.05 °C. The maximum current of the amplifier is 1.5 A and is provided by an standard low noise power supply (PLD5K-CH-5-A). With 20 mW input power, we have 400 mW output at 1 A with a single beam. Combining four different frequencies in the amplifier leads, at low intensity (below 500 mA), to an output power equal to the linear sum of the output powers obtained for each separated frequencies. This indicates that the amplification regime remains linear in this configuration. However, increasing the amplifier gain leads to wave mixing which generates additional frequencies. This is represented of Fig. 85 where the beat note spectrum between the frequencies present in the tapered amplifier output is shown for two different crystal currents. I have labelled f_{1-4} the frequencies present at the amplifier input, they correspond respectively to ^{85}Rb Repump (1 mW), ^{85}Rb Cooling (10 mW), ^{87}Rb Repump (1 mW) and ^{87}Rb Cooling (10 mW) frequencies, where the powers in bracket correspond to the input powers. This spectrum shows that the ratio of cooling powers over repump powers remains around 10 for both currents as the peaks corresponding to $f_{1,3} - f_{2,4}$ remain at the same levels compared to the $f_2 - f_4$ peak. Also, on the 1000 mA spectrum the higher frequency components such as $2f_2$, $2f_4$ and $f_2 + f_4$ increase. These components are below 1 % of the total power as can be seen by the relative amplitude of the $2f_2 - 2f_4$ peak compared to the $f_2 - f_4$ one. But compared to the 500 mA spectrum they are at the level of repump powers at higher current (the $2f_2 - 2f_4$ peak is comparable to the $f_1 - f_3$ peak). These frequencies are not an issue as they are far from excited state transitions. Even if they tend to reduce the amount of effective power in the cooling beams. See for example, how the $f_2 - f_4$ peak diminishes at higher current indicating a loss of power in these frequencies.

In any cases, injecting $50\,mW = (2+23+2+23)mW$ of total power in the amplifier operated at 1 A produces 450 mW of total power which is collimated and shaped in an approximately circular laser mode (3 mm radius). A polarizing cube splits it into two balanced beams 220 mW each which are injected with 50 % efficiency into two polarization maintaining fibers. Typical powers available for the 2D MOT are thus 50 mW per cooling frequency and 5 mW per repump frequency which, as we will see in Sec. 7.1 is enough for optimal operation.

Fiber performances

The stability the powers at the fiber output was characterized and a long term stability below 1 % during a day is ensured on all fiber outputs. The result of a typical measurement is presented on Fig. 86 were the Allan variances of a week-end long measurement is presented for three of the four frequencies present in one fiber. The

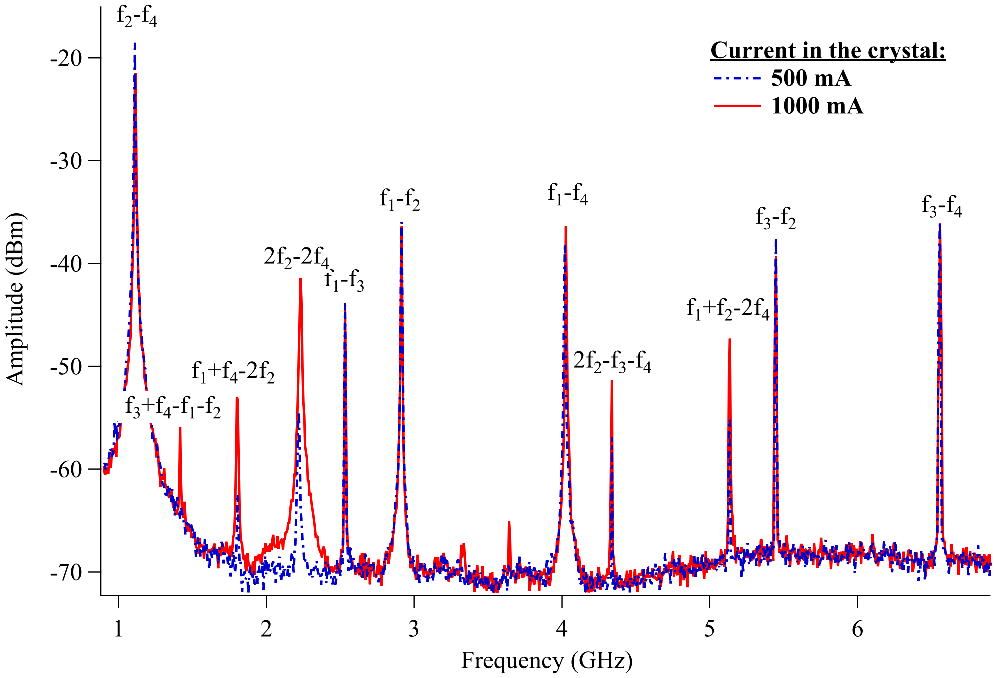

Figure 85: Comparison of the self beat spectrum of the amplifier output light. The same amount of output power (1 mW) is focused on a photodiode whose output is send to a spectrum analyser. The beat frequencies between each frequency components are labelled accordingly. The beat amplitudes indicate the relative amount of each field amplitude. In particular, the repump frequencies amplitude remain constant compared to the cooling frequencies amplitude which corresponds to a 1/10 ratio.

power stability before the fiber collimator of output S2, corresponding to one ^{85}Rb cooling beam, was already presented on Fig. 78 and can be used as a comparison. The short term stability is around 10^{-4} of the total power[7]. A transitional feature around 1 h probably indicates thermal effects.

The polarization direction at the fiber output is also essential to have a good control of the laser beam polarization state in the experiment. A polarization extinction ratio measurement, evaluating the amount of polarization in the orthogonal state, was performed for each fiber and on each frequencies. This measurement relies on the rapid dephasing between the two principal polarization axis in the fiber induced by a local temperature change. We measure the polarization direction at the fiber output by measuring the transmitted and reflected intensities of a polarizing beam splitter. We observe a precession of the polarization state around one of the two principal polarization axis. A half wave plate placed before the fiber collimator allows to align the injected polarization on one of these two principle axes[8] which minimizes the precession amplitude. For all our fibers, Polarization Extinction Ratio (PER) better

---

[7] It does not represent the stability during operation as time constants in AOM's are more of the order of 100 ms which will dominate the power fluctuation at the short time scale, additional investigation of the cycle stability, once the experiment is running will be performed to quantify the exact short term stability

[8] Usually, one axis showed better performances than the other.

than[9] 1 : 100 for all frequencies were obtained, ensuring at most 1 % of residual polarization in the orthogonal state at the fiber output.

These four frequencies beam are then shaped and properly polarized directly on the separated apparatus.

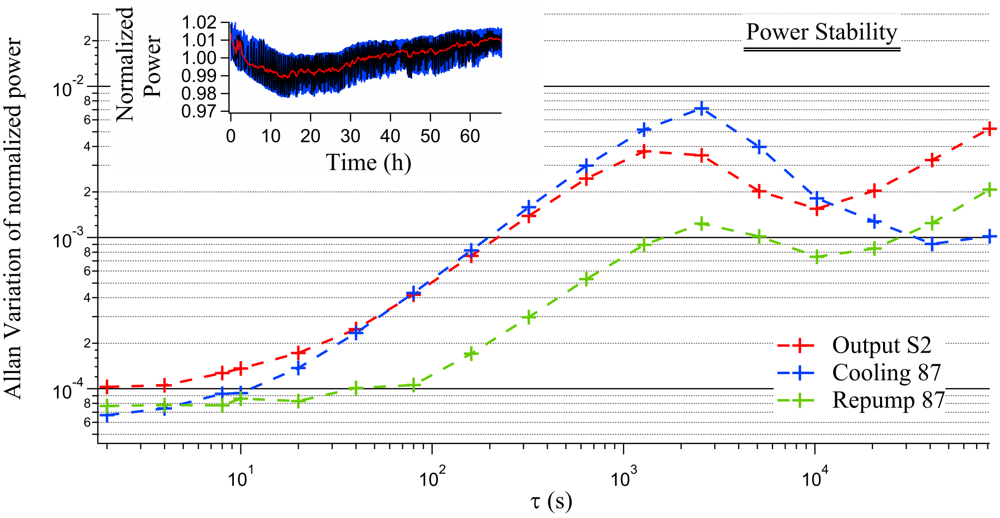

Figure 86: Allan variance of laser power at the fiber's output. The inset shows ^{87}Rb cooling power time evolution at a $\tau = 10\,s$ sample rate (blue background) at a $\tau = 10^4\,s$ sample rate (black line) as well as the smoothed mean value (Red line).

	Cooling ^{85}Rb	Repump ^{85}Rb	Cooling ^{87}Rb	Repump ^{87}Rb
Typical input	20	1.8	82	4
Output MMOT 1	14	1.6	50	2.5
Output MMOT 2	10	1.1	40	2.1
Output MMOT 3	14	1.4	76	2.6
Output Imaging	13	1.3	50	1.8

Table 15: Summary of the available powers (in mW) at each fiber outputs. The input power is only given as a reference as input powers varied between each fibers and between each frequency by more than 20 %

6.2.6 Collimation to the vacuum chamber

2D MOT beams

The optical setup was included in the 2D MOT system (see Fig. 87). It consists in a pair (horizontal and vertical) of light sheets produced by two polarizing beam splitters in series which distribute evenly the power into three beams. As the elliptical ratio of the distributed beam is large (7 mm width for a 3 mm height), it results in an almost continuous sheet of light for transverse cooling. Rectangular quadrupole coils operated at different currents (this will be described in more details in Sec. 7.1) produce the magnetic field configuration for the transverse collimation. A final

---

[9] In practice, it is possible to have better PER for two frequencies among the four present (probably due to non-polarizing splitters imperfections), ^{87}Rb cooling frequency was chosen as reference and PER better than 1 : 1000 were obtained for every fiber.

pushing beam 0.7 mm waist is directed along the 2D MOT chamber to increase the atomic flux towards the 3D MOT.

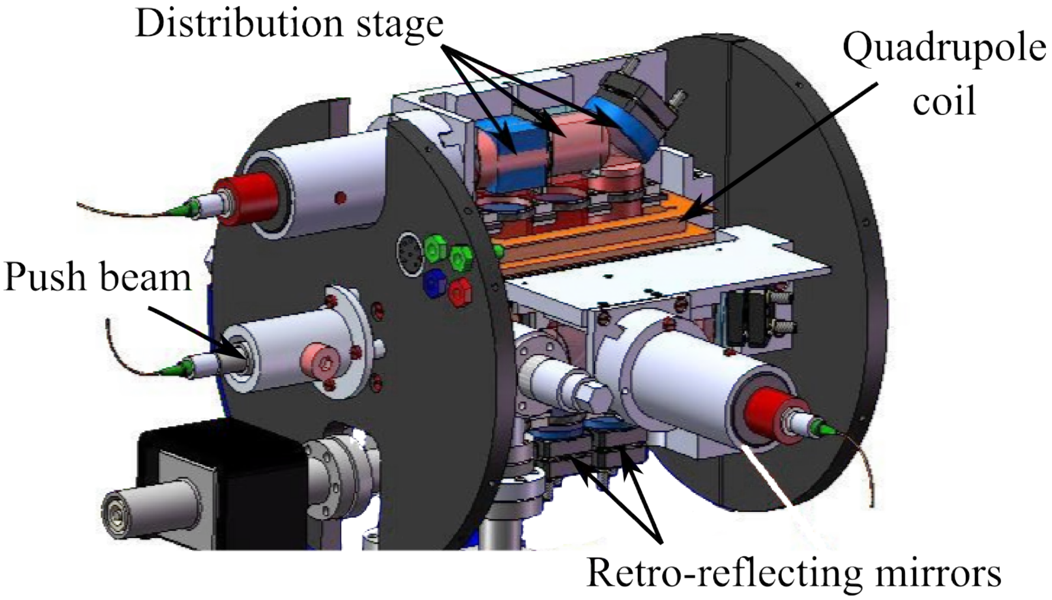

Figure 87: Collimation to the 2D MOT.

Mirror MOT beams

There are three 3D MOT beams used in a retro reflected mirror MOT configuration. Two horizontal beams are aligned at 45° with respect to the chip surface[10] and a third vertical beam is retro-reflected. All beams are collimated to 7 mm waists and their divergence over 5 m was measured below 0.2 mrad (a factor of 5 above the minimum divergence of a Gaussian TEM00 beam). The polarization is set by a QWP directly integrated in the collimator (Schäfter-Kirchhoff, 60FC-Q-4-M75-13) for the horizontal beams and by a 2 ″ diameter QWP for the vertical beam. This choice was motivated by the necessity of additional vertical beams (such as the Bragg beams) which will be superposed to the MOT beam with a polarizing beam splitter cube.

Complete view of the optical setup

The global setup is shown on Fig. 88. It fits on a 1.5 m × 1.5 m optical table and provides all fibered outputs to the main experiment. The control electronics and laser sources (apart from the ^{87}Rb repump laser, clearly visible in blue) are located on two separated racks not shown in the picture. A surrounding box allows good thermal equilibrium and acoustic isolations necessary for the stability of the repump laser (ECDL) and helpful for the long term stability of the optical alignments.

---

[10] The large 6.6 mm beam displacement induced by the front viewport constrained the size of the beams in our configuration.

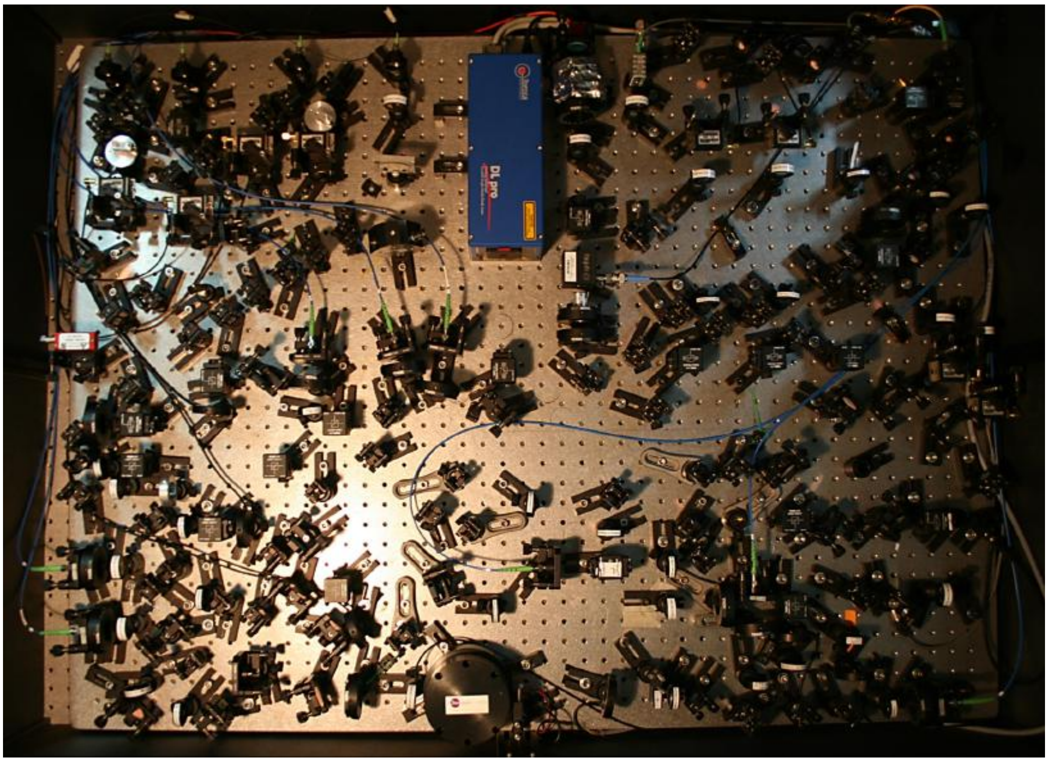

Figure 88: View of the compact optical setup.

Laser system

Laser light required for a dual isotope 2D MOT and 3D MOT is produced by two independent laser systems based on frequency doubled Telecom lasers (1560 nm). The frequencies are controlled via saturated absorption and master-slave architectures which remain locked for weeks. The long term frequency stability of both systems are suitable for continuous experiments with sub MHz drifts. The frequency tunability and agility of both cooling lasers are good enough for the characterization and optimization of cold atom clouds with more than 100 MHz accordability in at most 500 µs. Superposition of all the required laser frequencies is performed on a compact breadboard which includes a 4 frequencies tapered amplifier and provides fibered outputs to the experiment with good power and polarization stability. The dual isotope mixture implied a trade-off in the available laser power due to the difficulty to inject simultaneously four frequencies in the many fibers.

6.3 MAGNETIC SOURCE

The required magnetic fields have already been discussed in Sec. 5.2.2 and will be described in more details in Julien Alibert's thesis. Here, we only give the global geometry of the experimental setup.

6.3.1 Overview

Three pairs of magnetic coils are designed to carry high currents and as such are made of hollow rectangular copper wires watercooled during operation. An example of such magnetic coils is represented on Fig. 89b. These magnetic coils were made with the technical assistance of Laboratoire des Champs Magnétiques Intenses (LNCMI) which possess both the know-how and apparatus to realize robust and compact coils. The black coating that recovers the coil winding is a thermal insulating polymer (STYCAST U 2535 PT B) which also insures good thermal conductivity between the layers. The magnetic coils requiring high currents are the 3D MOT quadrupole coils (up to 200 A), the Feshbach coils (operating around 40 A) and the Bias coils (up to 80 A). The Feshbach coils were designed large enough to ensure good field homogeneity in the whole cloud production region. The Bias coils produce the bias field for the magnetic trapping on the chip (along the Z direction). The choice of external coils is easier in a laboratory leads to a high power consumption. However smaller, under vacuum, coils could be considered which drastically reduces the requirements in terms of electrical currents.

Auxiliary coils such as the displacement coils, optical pumping coils and compensation coils are operating at lower current and made of plain copper wires. The displacement coils are used to change the distance between the chip and the trapping minimum. The optical pumping coils produce a magnetic field directed along the (Y+Z) diagonal. The compensation coils are directed along the three spatial directions and surround the whole apparatus, they can be seen on Fig. 95. The quadrupole coils are dedicated to the 3D MOT operation. Most of the other coils will be operating simultaneously together with the wires on the mesoscopic chip.

Description of the mesoscopic chip

This chip was initially designed to be a thin Silicon Carbide crystal (transparent at 1560 nm). Gold wires can be directly deposited on its surface and they provide the reflecting layer for the MMOT. They were designed to be relatively thick (10 µm × 300 µm) in order to sustain high currents (10 A) resulting in large magnetic gradients. This design was developed in collaboration with the SYRTE and the CNES but technical difficulties delayed its fabrication. This is the reason why we made a mesoscopic chip which, apart from the wire dimensions, has a geometry very similar to the planned microscopic chip. This is not negligible as it increases the minimal distance between the wires and the atomic cloud from 200 µm (or less) to 800 µm.

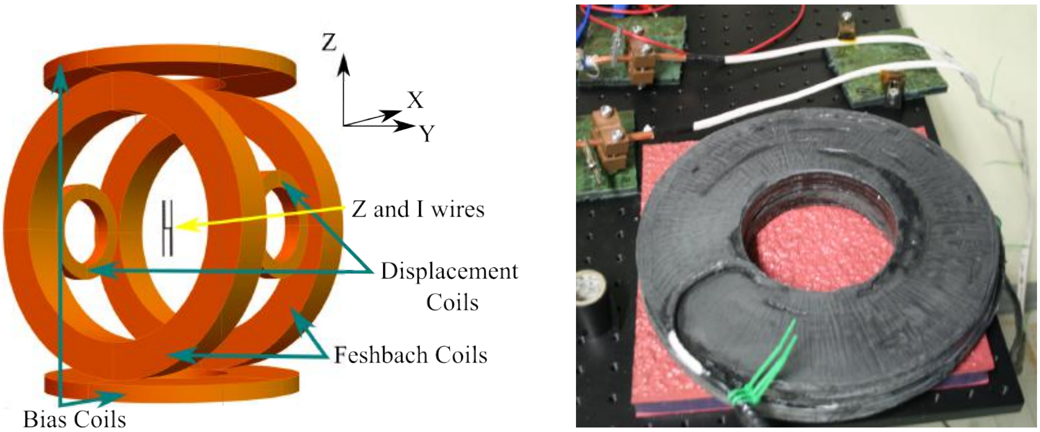

(a) Magnetic coils configuration **(b)** Experimental realization

Figure 89: **(a)**: Combination of the main magnetic field sources around the Z shaped trap. The perspective point of view corresponds to the rear of the main chamber.
(b): Water cooled magnetic coil with its connectors at the background (combination of standard swagelock® fittings and home made copper connectors).

Our trap consists in a "Z" wire and an external bias field plus two "I" wires for increasing confinement in the Y direction (see Sec. 5.2.2). The larger distance implies that higher currents are necessary to produce the same magnetic gradients. Especially in the capture stage from the molasse a large capture volume far from wires requires a large current. With 1 mm diameter wires 40 A are necessary to produce the magnetic fields presented on Fig. 51. The final design is represented on Fig. 90. It consists in a 50 mm × 50 mm × 20 mm oxygen free copper support which is extruded to receive the "Z" wire (blue), "I" wires (green) and an additional loop for the RF knife used during the forced evaporation. The wires were glued with EPO-TEK 301 which is UHV compatible, electrically insulating and a good thermal conductor. Curing at 60 °C for two hours was performed before adding a 100 μm thick indium sheet on top of the copper surface to reduce asperities between the surface and the MOT mirror.

This mirror is a 140 mm diameter, 200 μm thick glass substrate. It is transparent at 1560 nm and one face has a dichroic coating designed to transmit 1560 nm and optimized to have a high reflection coefficient for both incident linear polarizations at 780 nm and for an incidence angle of 45°. We measured a reflectivity better than 98 % and a transmission higher than 97 % (limited by the uncoated substrate face). We checked that a right handed polarization ($S_3 = 0.999$) was transformed into a left handed polarization ($S_3 = -0.990$) after reflection at 45°.

In addition to the adhesion of the indium sheet, four titanium screws with hand made indium washer maintain the mirror at the center of the support. The electrical connections with the feedthroughs is ensured by larger (2 mm diameter) copper wires (refered to as the conducting wires). These wires cannot transfer heat to a surrounding bulk which is why three wires in parallel have been used for the main "Z" wire supporting the highest current. In this configuration the conducting wires produce 27 times less heat than the "Z" wire and distribute the heat to multiple feedthroughs. The electrical contact between the chip's wire and these wires is ensured by Beryllium connectors. At the other end, the conducting wires are connected to beryllium push-on connectors fixed on 8 feedthrough copper pins 5 mm diameter. Each pin is specified for a maximum current of 12 A.

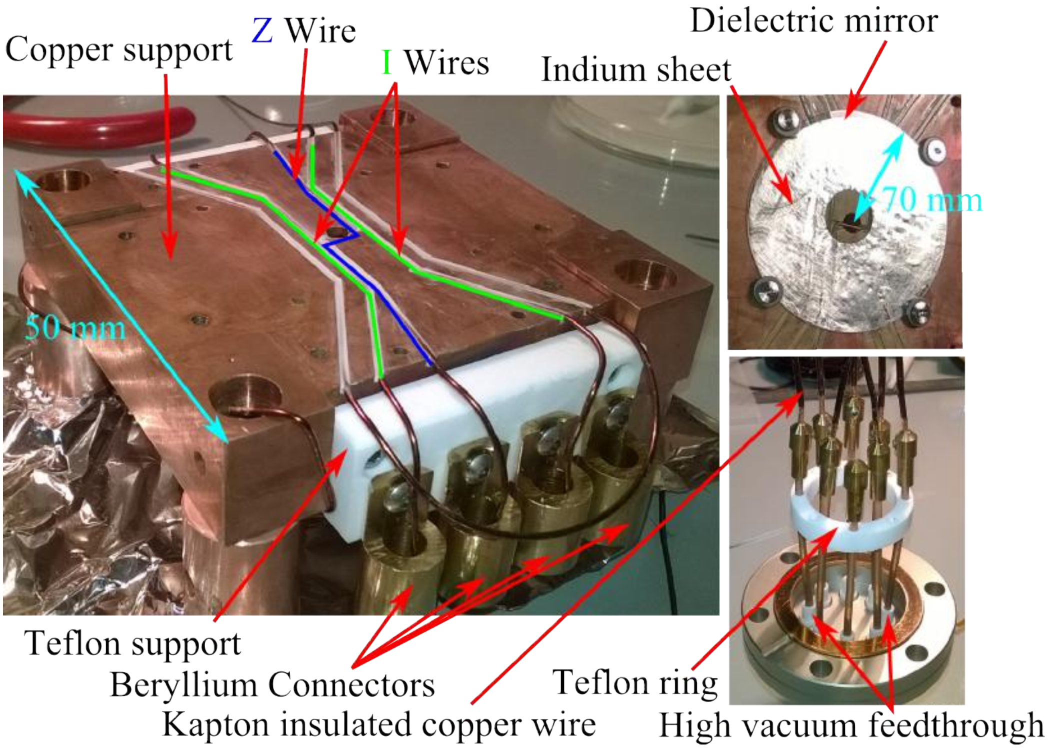

Figure 90: Technical realization of the mesoscopic chip with the corresponding wires, electrical connections and mirror. A Teflon ring was added between the electrical feedthrough wires to prevent contact between the connectors heads.

To ensure proper electrical isolation, the wires sheath is made of Kapton which is a poor thermal conductor. Therefore, we simulated the thermal conduction of the generated Joules heating to the surrounding copper support to ensure that high currents were reasonable for this structure.

Thermal problematic

Joules generated heat is already an issue for microscopic chips [314], but in our situation, even higher currents were necessary due to the large distance to the cloud. This is the reason why numerical simulations were implemented to ensure that the heating induced by these 40 A strategies were kept below reasonable values.

Heat transfer simulation

A finite element simulation of the wire heating was done using the Comsol Multiphysic® software. It solved both the time dependent heat equation in the different materials and boundaries and Ohm's equation in the wire. This allowed to take into account some specific feature such as the temperature dependent copper resistivity and the current density gradient around the wire edges. The chip model used in this simulation is represented on Fig. 91. It shows how the material bulk (copper) incorporates a wire (green) which has an insulating sheath. The contact between the sheath and the copper block is ensured by a filling material with properties adapted from the glue specifications.

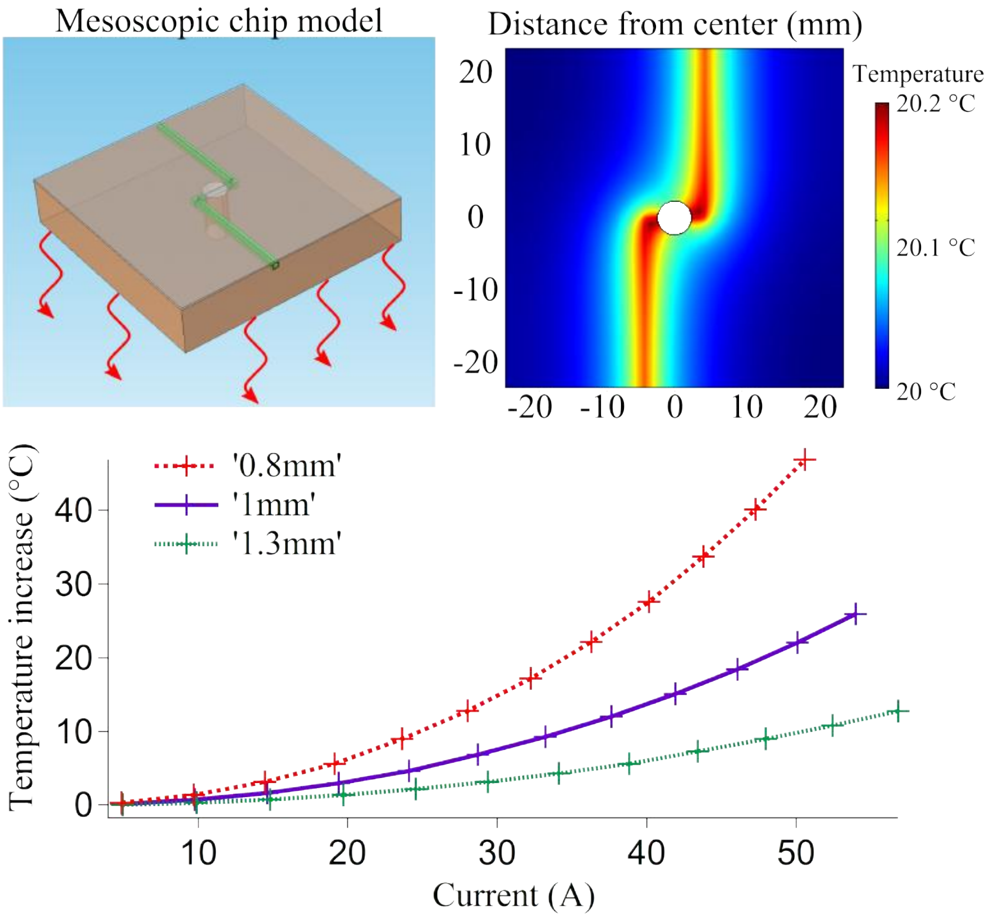

Figure 91: (Left Top): Simulated chip and heat transfer direction through the bottom face.
(Right Top): Steady state temperature profile below the wire.
(Bottom) Asymptotic temperature of three different wire diameters as a function of the current.

The simulation sets a total current $\pm I$ through the wire surface edges as well as an initial temperature of 20 °C. Thermal boundary conditions were chosen as to prevent any heat flux to the top and sides faces[11]. Heat can only be dissipated through the bottom copper face which was kept at constant temperature (infinite thermal bath). The stationary thermal state is represented by two plots on Fig. 91. The 2D-plot shows the temperature distribution in the plane just below the wire. One sees that the heat flow spreads in the transverse directions with negligible heating of the copper. The second graph shows the peak temperature in the wire as a function of the current for different wire radii. As expected, the Joules heating increases quadratically with the current, but an over quadratic behavior can be seen for the smallest diameter as the temperature rise increases the wire resistance. Some parameters such as the dimension of the central hole or the thickness of the insulating sheath were investigated to find the optimal parameters for our design. In the presented results, the Kapton thickness is 100 µm and the central hole has a 5 mm diameter. For a 1 mm wire radius,

---

[11] Conduction under vacuum is not possible and thermal radiation is negligible at these low temperatures.

one sees that the maximum temperature rise is smaller than 14 °C for 40 A which is small enough to prevent damages to the mirror substrate.

Electrical and thermal tests

We checked experimentaly that the chip wires could support higher and higher currents without damages nor runaway heatings as it can happen if the supply current remains constant as the temperature rises. This was ensured by monitoring the wire resistance as well as the ion pumps pressure which could indicate a change in the copper bloc degassing rate. No visible pressure change was seen which does not give a definitive test as the ion pump is not located in the main chamber. However, making simple assumptions, we can obtain a temperature estimate of the wire from the resistance rise recording.

We measured the total resistance R_{tot} of the circuit which was made of the conducting wires, the contact resistances and the "Z" wire resistance R_Z. With independent measurements, we were able to evaluate R_Z and obtained a value $5.8\,\mathrm{m\Omega}$ which is in good agreement with the predicted $5.5\,\mathrm{m\Omega}$ value calculated from the wire dimensions and copper resistivity. Then, monitoring the total resistivity as a constant current was driven through the wire, we extracted an estimation of the wire temperature increase. In this model we neglected the temperature rise of the conducting wires as they have a much smaller linear resistivity due to a larger diameter. The resistance rise was entirely attributed to the chip's wire and we obtained the following relation between maximum temperature rise ΔT and resistance rise ΔR_{tot}:

$$\Delta T = \kappa \frac{\Delta R_{tot}}{\alpha} \tag{106}$$

where $\alpha = 4 \times 10^{-3}\,\mathrm{K}^{-1}$ is copper thermal conductivity coefficient and $\kappa < 1$ is a numerical coefficient which can be expressed as an integral depending on the temperature distribution in the chip's wire. This coefficient drastically changes the temperature range over which the rise takes place. This is the reason why a conservative value of 11/12 was used. This value corresponds to the case of a wire exchanging heat only at its extremities with a bath kept at a constant temperature. In this case, the temperature profile is a parabolic function with maximum at the wire's center.

The result of this measurement is presented on Fig. 92 were the temperature rise is plotted as a function of time. We see that an initial 10 s rapid increase can be well described by an exponential phase with a rising time of 4.4 s and an asymptote at 18 °C. Then the long term increase tends to a linear behavior with a slope of $0.5\,^{\circ}\mathrm{C\,s^{-1}}$. When compared to the finite element simulations, we can see that the predicted temperature increase (14 °C) is lower than the measured asymptote. The amount of approximations used to obtain the temperature rise can certainly be incriminated for this difference (both the κ factor and the constant resistance of the conducting elements). In practice, the constant rise at long duration might be an issue for very long measurement campaigns which, even at a cycle time of 1/5, corresponding to the projected duration of the magnetic trap, might lead to a constant heating of the chip's

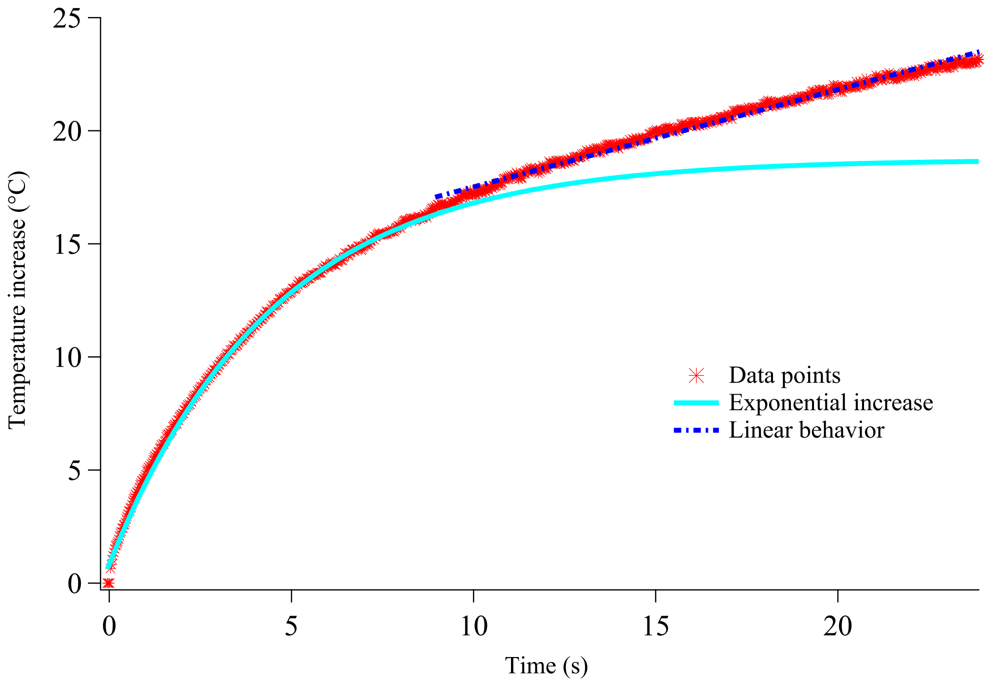

Figure 92: Extrapolated temperature increase of the "Z" wire during a continuous 40 A current supply. Two fits are shown and correspond to two different heat transfer mechanisms. First the rapid temperature increase establishes a temperature gradient between the wire and the surrounding support. Then thermal conduction through the Kapton sheath transfers heat to the copper support which leads to a second dynamical regime.

wire of about 0.1 °C per experiment cycle. Additional investigations of this heating and a full characterization of a potential active or passive cooling will be necessary to ensure the long term stability of this setup. It is not an issue at the moment as the cycling rate is much lower.

Magnetic sources

High magnetic fields for the MOT and magnetic traps are produced by water cooled magnetic coils operating at high currents ($\sim$ 100 A). We developed a preliminary mesoscopic magnetic chip which includes a dichroïc mirror that might be, in the future, replaced by an additional microscopic chip. High currents (up to 40 A) are used in 1 mm diameter copper wires. Thermal tests show qualitative agreement with our simulations and indicate that heating is negligible at short trapping times.

6.3.2 Constraints on the optical dipole trap

In addition to the trapping magnetic fields, the chip was designed with an optical aperture ($\phi = 5$ mm diameter) for a crossed dipole trap centered on the magnetic trap. Two power amplified outputs (1 W at 1560 nm) of the ^{85}Rb laser system are available. The dipole trap beams are constrained by the surrounding viewports and by the chip itself. It guided our choice of the central hole to have both an efficient heat transfer from the Z wire to the support as discussed in Sec. 6.3.1 and a focused transverse beam with a margin of alignment. This is represented on Fig. 93 were the chip and the viewports dimensions are summarized. For example, the transverse beam along the x direction can be focused to a $w_{1,0} = 50\,\mu\mathrm{m}$ waist and remain small compared to the mechanical apertures. For this example, the beam waist is $190\,\mu\mathrm{m}$ at the hole countersunk, which is a twentieth of the hole diameter. At the viewport position, the waist is $3.3\,\mathrm{mm}$ which is also $1/20$ of the aperture. This situation corresponds to the optimized laser waist discussed in the transportation protocol (Sec. 5.4).

for the second dipole trap along the y direction, the situation is somewhat more constrained by the chip's edges. If we denote by $X_0 \sim 500\,\mu\mathrm{m}$ the distance of the crossed trap center from the chips's surface, and $L_c \sim 48\,\mathrm{mm}$ the distance of the chip edge from the trap center, we can estimate the waist range which satisfy the following condition :

$$w\left(L_c\right) < \kappa X_0 \tag{107}$$

where $\kappa \sim 1/2$ is a numerical factor which imposes that the laser waist at the chip edges is smaller than the distance from the chip surface. Using the gaussian beam divergence formula $w_2\left(y\right) = w_{2,0}\sqrt{1+\left(y/z_R\right)^2}$ and solving the resulting second order inequation, one can show that the waist range satisfying eq. (107) is:

$$\frac{\kappa X_0}{\sqrt{2}}\sqrt{1-\sqrt{1-\frac{4L_c^2\lambda^2}{\pi^2\kappa^4X_0^4}}} \leqslant w_{2,0} \leqslant \frac{\kappa X_0}{\sqrt{2}}\sqrt{1+\sqrt{1-\frac{4L_c^2\lambda^2}{\pi^2\kappa^4X_0^4}}}$$

which is valid only for $\kappa > \kappa_{\mathrm{lim}} = \sqrt[4]{4L_c^2\lambda^2/\left(\pi^2X_0^4\right)}$ which corresponds to ~ 0.43 in our case. The optimal choice for $w_{2,0}$ in terms of diffraction by the edges corresponds to $\kappa = \kappa_{\mathrm{lim}}$ and gives[12] $w_{2,0,\mathrm{lim}} = 154\,\mu\mathrm{m}$. However, when taking into consideration the resulting depth of the optical trap, one can relax the condition on κ to create a tighter trap[13]. For example, $\kappa = 0.5$ gives a minimum waist $w_{2,0} = 105\,\mu\mathrm{m}$. In both of these cases, the beam waist at the viewport position is less than a fifth of the viewport radius.

---

[12] Note that this limiting value does not depend on X_0 !

[13] This of course leads to a certain amount of wriggles in the trap potential as the diffraction from the edges can modulate the intensity distribution of the beam but the distance from the diffracting edge is a hundred times larger than the wavelength which means that this effect is probably negligible.

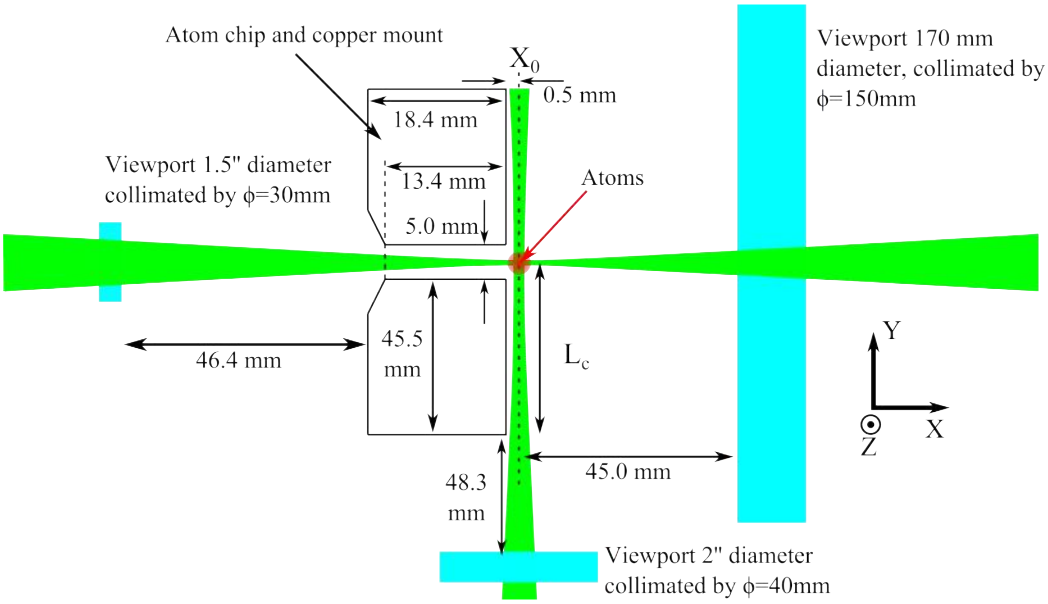

Figure 93: Sectional view of the copper support with detailed dimensions. The dipole trap beams parallel and through the chip are represented to emphasize the geometrical constraints induced by the support's geometry. The waists are not represented to scale to show the difference between the parallel 100 µm and the crossed 47 µm waists.

Dipole trap

The chip's support impedes the optical traps and optimal parameters for our geometry consist in a 100 µm waist for the grazing laser beam and 47 µm waist for the crossing beam (see Sec. 5.4.2). With the available laser power (1 W), it corresponds to an optical dimple 8.5 µK deep with frequencies $(53, 244, 241)$ Hz in the (X, Y, Z) directions.

6.4 IMAGING SYSTEM

We use three fluorescence detection schemes ss atom imaging systems. Two of them are CCD cameras (GS3-U3-14S5M-C) from Pointgrey® with a magnification system. The third one is a high gain photodiode (ϕ4 mm diameter, PDA36A from Thorlabs®) with a single collecting lens. They are represented on Fig. 94.

- The photodiode is used during the MOT optimization and gives an idea of the atom number collected in the cloud. It typically underestimate the number of atoms by 50 %. The detection system collects the fluorescence photons emitted by the trapped atoms. Neglecting the very small number of photons that can be reflected on the chip's mirror, one gets the following expression for the photodiode electric potential V_{ph}:

$$V_{ph} = G\alpha_{780}\hbar\omega_0 \frac{\Omega_1}{4\pi} \frac{s}{1+s+\left(\frac{2\delta_1}{\Gamma}\right)^2} \frac{\Gamma}{2} N_{at} \tag{108}$$

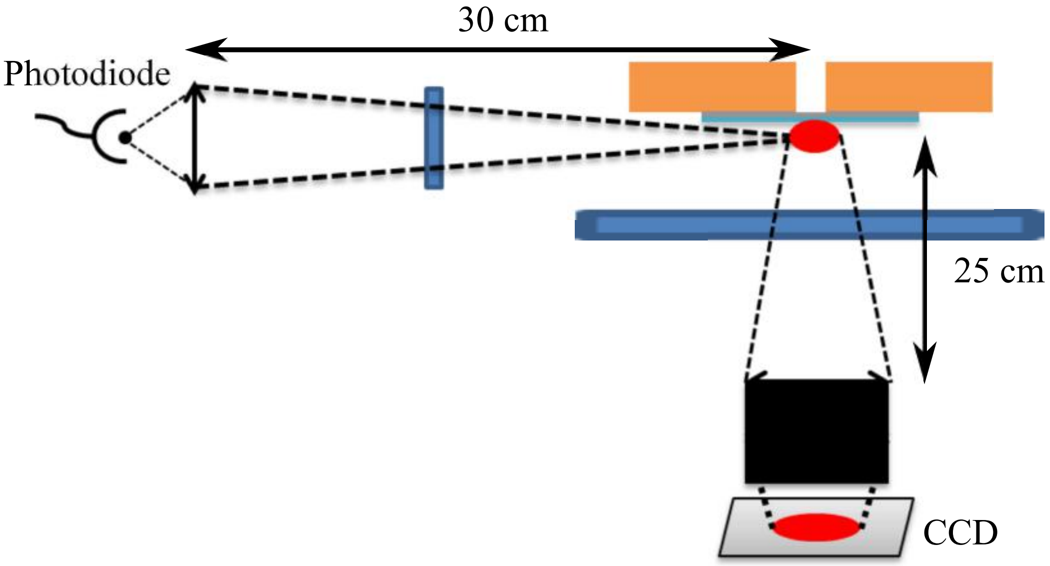

Figure 94: Schematic representation of the detection systems. Another CCD imaging setup identical to the one represented here is directed parallel to the chip surface.

where $G = 2.4(1) \times 10^6\,\mathrm{V\,A^{-1}}$ is the amplifier gain, $\alpha_{780} = 0.48(1)\,\mathrm{A\,W^{-1}}$ its spectral responsitivity, ω_0 is the photon frequency, $\Omega_1 = 4(1) \times 10^{-3}\,\mathrm{sr}$ the collection angle, $s\,(\sim 60)$ the light saturation[14] parameter, δ_1 is the MOT light detuning and Γ the transition linewidth. With these values, the number of atoms is easily calibrated by:

$$N_{at} \simeq \frac{V_{ph}\,(V)}{1.35} 10^9 \tag{109}$$

where V_{ph} is given in volts. This estimation provides only an approximate value of the atom number as the solid angle Ω_1 is not well known. Absorption and re-scattering effects can also lead to lower fluorescence signal for dense atom cloud as is the case at the end of the MOT loading and during the compression stage. We probably to under-evaluate the atom number with this fluorescence collection. However, it provides a practical tool as the signal can be easily and continuously monitored.

- The CCD setup is used to have both a finer control on the atom number estimation and a better synchronicity for the atomic cloud imaging. It also provides spatial information on the atom distribution. After calibration of the CCD efficiency (with a calibrated reference beam, for different camera gain, pixel number and integration time) we obtained, for our system, a proportionality coefficient between the number N_{e^-} of electron detected and the number of incident photons N_γ:

$$N_\gamma = 10^{-(Gain-20)/19} 340 N_{e^-}$$

---

[14] The saturation intensity used is $2.5\,\mathrm{mW/cm^2}$ as discussed in Sec. 7.2.2.

where Gain is the CCD amplifier gain. Using again a similar formula for the number of detected atoms, one gets, with $\Omega_2/(4\pi) = 1.6(1) \times 10^{-3}$ sr:

$$N_{at,i} = \frac{1 + s + \left(\frac{2\delta_1}{\Gamma}\right)^2}{s} \frac{2}{\Gamma\tau} 1.4(1) \times 10^5 N_{e^-,i} \tag{110}$$

where τ is the detection time and i labels the CCD i^{th} pixel. Compared to the photodiode detection scheme, this can be precisely calibrated by changing the saturation parameter, the laser detuning and the detection integration time, providing a much more accurate knowledge of the atom number.

Detection system

The MOT cloud analysis is performed both with a photodiode collection system and CCD sensors. Combined, they provide rapid and precise tools for the atom number evaluation and the spatial shape of the cloud.

6.5 CONCLUSION

In this chapter, the experimental setup was described and characterized. The vacuum system we built reached 10^{-10} mbar pressure range. Additional tests of lifetime in the magnetic traps are necessary to characterize further the vacuum quality in the vicinity of the chip. The dual isotope laser system was then described. It provides all the necessary frequencies for the MOT, the optical pumping and the imaging beams and we tested its capacity for long term measurements and the reliability of the locking system stable below 200 kHz. Both locking system are agile and allows for rapid change of the cooling laser frequencies as required by the cold cloud experimental sequence described in the next chapter. Finally, laser powers available at the fibers outputs are sufficient for dual isotope laser cooling and stable to better than 1 % for more than 2 days. The macroscopic magnetic sources as well as the mesoscopic chip were described. Most of them have already been implemented on the experiment and will be characterized fully in J. Alibert's thesis. Finally, the constraints on the transverse optical trap and the characteristics of the imaging system were discussed, giving a complete picture of the experiment, which is shown on Fig. 95.

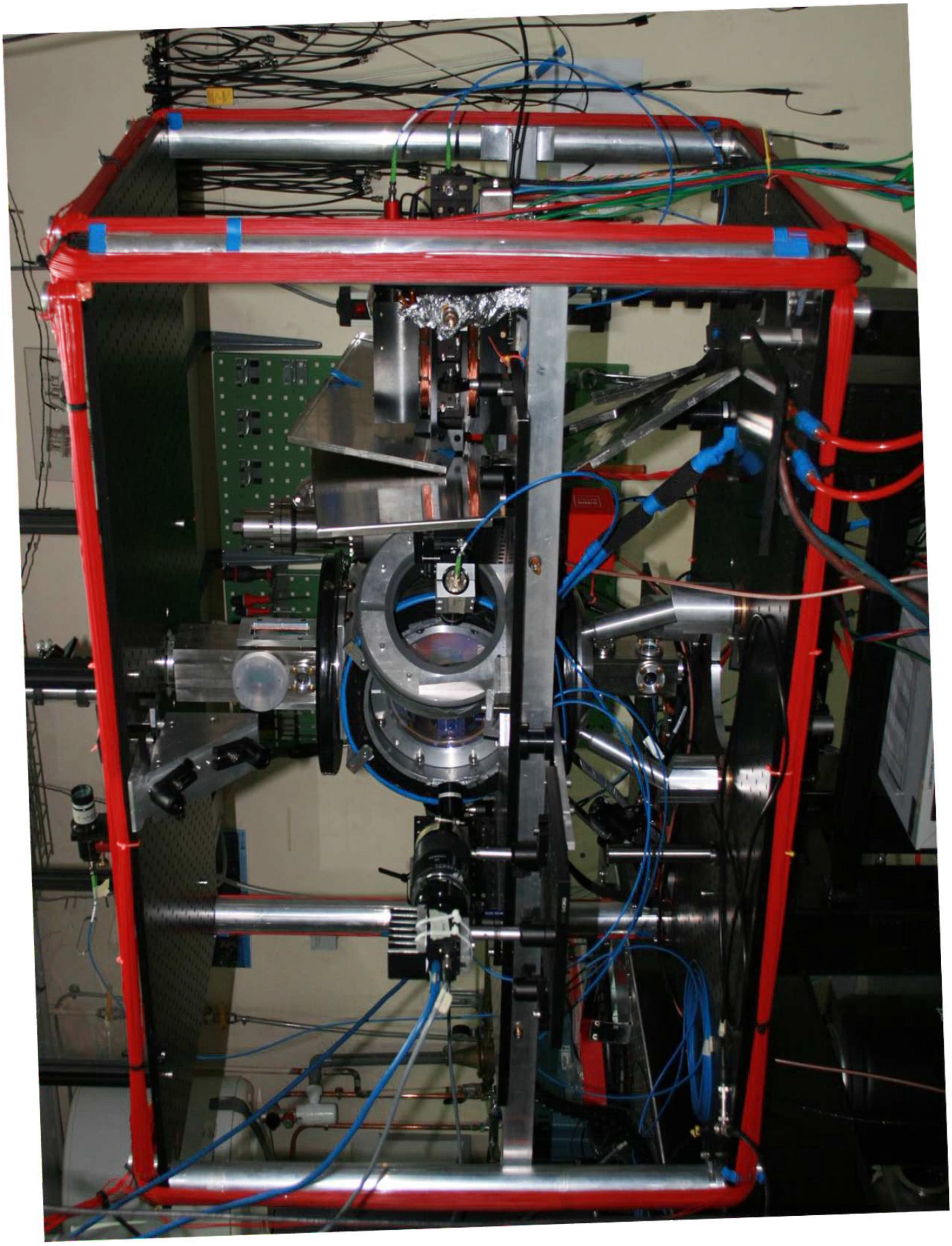

Figure 95: Global view of the experiment.

7 ATOM SOURCE

Contents

This chapter describes the performances of the atomic source at different stages. From the initial 2D MOT source to the magnetic trap loading, we will describe the main steps (MMOT loading, compression and molasses) which shape the cold atomic cloud. I will show how the cloud atom number, dimensions and temperature are measured with high saturation fluorescence imaging and discuss the limits of this method. I will conclude by presenting the initial result of the magnetic trapping which has not been optimized yet.

7.1 2D MOT SOURCE

The 2D MOT source was designed to produce a high atomic flux $\sim 10^{10}\,\mathrm{atoms/s}$ with a compact setup. It relies on a rubidium dispenser heated to 50 °C with two thermocoax®[1]. The rubidium enters a vacuum chamber were three transverse cooling and trapping regions collimate the rubidium towards the exit hole. rubidium atoms can be seen as three bright cigar shaped regions shown on Fig. 97. Balancing the laser power over the three transversal cooling stages slightly changed the relative height of each cigar but only an even distribution aligns them. However, in this configuration, their axis is slightly displaced compared to the center of the chamber (exit hole height) due to the gravitational potential. To compensate this offset, we slightly unbalanced the two vertical coil currents. This resulted in a good alignment between the three cigars and the 2D MOT output axis as can be seen on the inset of Fig. 97.

Loading the 3D MOT from this rubidium source, was initially not possible as its quadrupole field perturbed the magnetic field in the 2D MOT chamber. This is shown on Fig. 97 were the three cigar spots are represented with and without the quadrupole field of the 3D MOT. To isolate the 2D chamber from this field gradient, we added µ-metal shielding plates in between the 2D MOT chamber and the quadrupole coils. This can be seen on Fig. 95 where three metal plates are positioned as best as possible around the 2D MOT exit hole. To compensate for the residual horizontal magnetic gradient that persisted, we unbalanced the two horizontal 2D MOT coils current. This

---

[1] Both the dispenser and the valve leading to the chamber are heated to prevent any cold-finger condensation effect which reduces the rubidium gas flux to the 2D chamber.

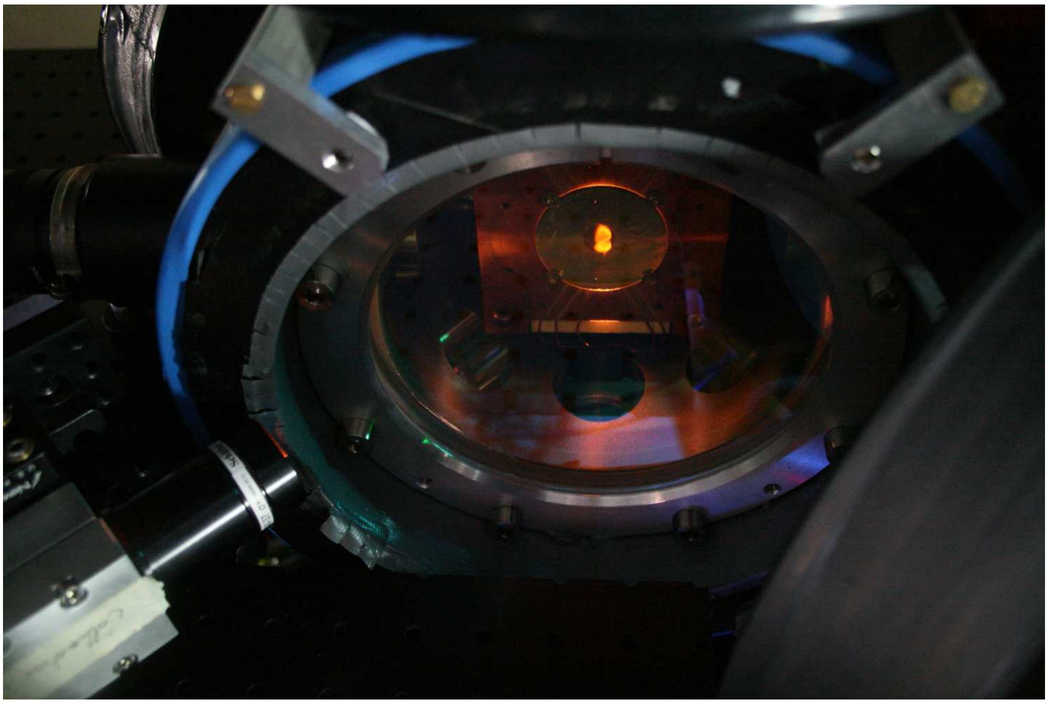

Figure 96: Picture of the experimental setup during the MOT phase. The atomic cloud, as well as its reflection on the chip's mirror, appear as a small orange (false color) spot, the size of a red currant. One MOT collimator as well as an out-of-focus quadrupole coil are visible at the foreground.

was enough to approximately align the three cigars on the chamber axis. In practice, it requires to increase by 5 % the current of one coil. This adjustment is very sensitive as a 1 % current change reduces by a factor 3 the 2D MOT loading rate.

In the remainder of this chapter, we are going to discuss the main parameters which influenced the 3D MOT characteristics (in terms of loading rate, atom number, temperature and size). Before, I would first like to emphasize that all this optimization was performed on ^{87}Rb as the requirement on the initial atom number are more stringent on this isotope than on ^{85}Rb. Still, we loaded both atomic species in this 3D MOT with high atom numbers (10^9 ^{85}Rb atoms were loaded simultaneously with 3×10^9 ^{87}Rb atoms[2]). It ensures that a dual species atomic cloud can be prepared with the required atom numbers for the sympathetic evaporation stage (50 times less ^{85}Rb atoms are necessary than ^{87}Rb atoms which corresponds to the initial state in Tab. 14, Sec.5.3).

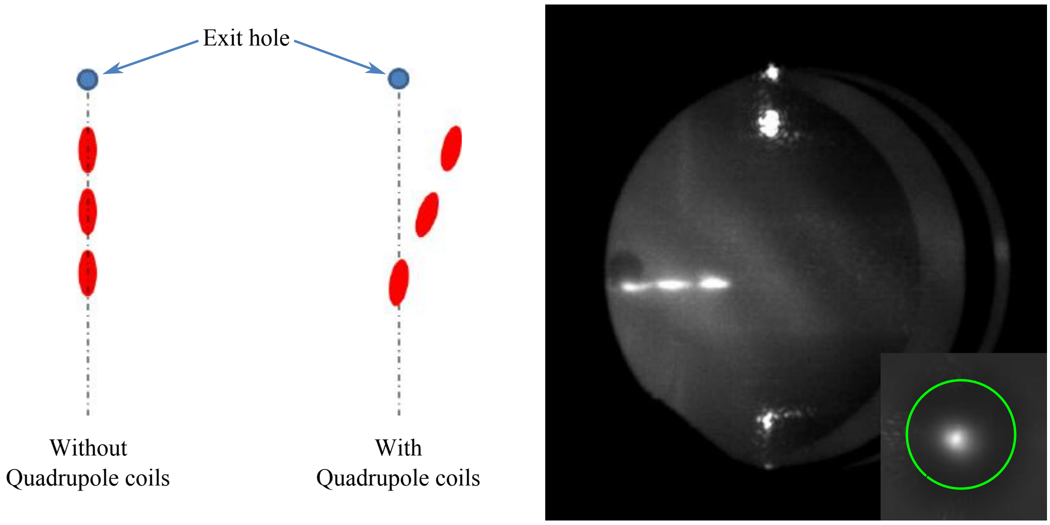

Figure 97: Right hand side: Picture of the 2D MOT clouds taken from the push beam viewport. The camera is slightly out of alignment to show the three cigar shaped regions. The exit hole is the black circle in the background. The vertical bright spots correspond to light scattered by edges inside the chamber. The bottom right inset corresponds to the in-axis view once the three clouds were aligned on the exit hole (emphasized by the green circle).
Left hand side: Effect of the quadrupole magnetic field on the 2D MOT prior to magnetic shielding and current imbalance between the 2D MOT coils.

7.1.1 Push beam optimum

A typical loading curve is shown on Fig. 98 where the number[3] of atoms captured in the 3D MOT is represented as a function of the loading time. After an initial exponential increase lasting ~ 1 s, the number of collected atoms saturates. We interprete the

---

[2] This value was obtained prior to the 3D MOT optimization which is why it seems relatively small compared to the values given afterwards.

[3] The photodiode signal has been corrected with the measured asymptotic atom number of the CCD cameras. Indeed, the atom number indicated by this system is about 2/3 smaller than the one measured by the CCD camera probably due to the calibration (solid angle, amplifier gain,...) uncertainty. The accuracy of our fluorescence imaging technique is discussed in Sec. 7.2.2.

saturation as due to the proximity of the surface which prevents the cloud from getting larger. The transversal and the pushing beams detuning δ_2 are identical but can be changed independently of the 3D MOT. We found that a laser detuning $\delta_2 = -\Gamma$ was the optimum choice for the 3D MOT loading rate, which is slightly smaller than the optimal detuning ($\delta_1 = -2\Gamma$) for the 3D MOT discussed in Sec. 7.2.4. This value is a trade-off between the transverse collimation which is expected to reach its lowest divergence for $\delta_2 = -\Gamma/2$ and the almost resonant frequencies ($\delta_2 < 0$) of counter-propagating atoms that are being accelerated back toward the 2D MOT exit.
The geometrical alignment of the pushing beam on the 2D MOT axis and its polarization direction were also critical which is the reason why an additional optical setup was installed and replaces the one initially planned (see Fig. 87).

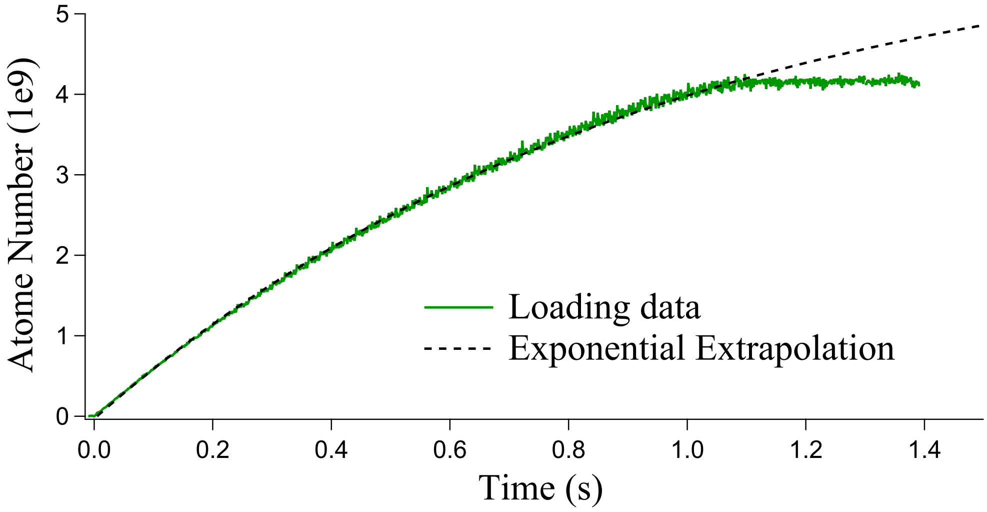

Figure 98: Atom number captured in the 3D MOT inferred from the photodiode signal eq. (109). The exponential fit gives a loading time of $950(10)\,\mu s$ and an asymptotic atom number of 6×10^9 $atoms$. However, the loading saturates to a lower atom number due probably to the proximity of the mirror surface.

Push beam intensity

In addition to the value of the 2D MOT detuning, the loading rate depends on the power in the pushing beam. This is represented on Fig. 99 where I show the loading rate for different powers in the push beam. An optimum at $300\,\mu W$, corresponding to an intensity of $20\,mW/cm^2 \simeq 6I_s$, leads to a loading rate of $11(2) \times 10^9$ $atoms/s$. This is comparable to other performances (10^{10} $atoms/s$ [311]) obtained with a similar setup.

7.2 OPTICAL TRAPPING AND COOLING

To go further into the description of our atomic source, I am first going to discuss the general experimental sequence as well as the detection system used. Then, the three main steps that are the mirror MOT (MMOT), the compressed MOT (CMOT) and the optical molasses will we characterized.

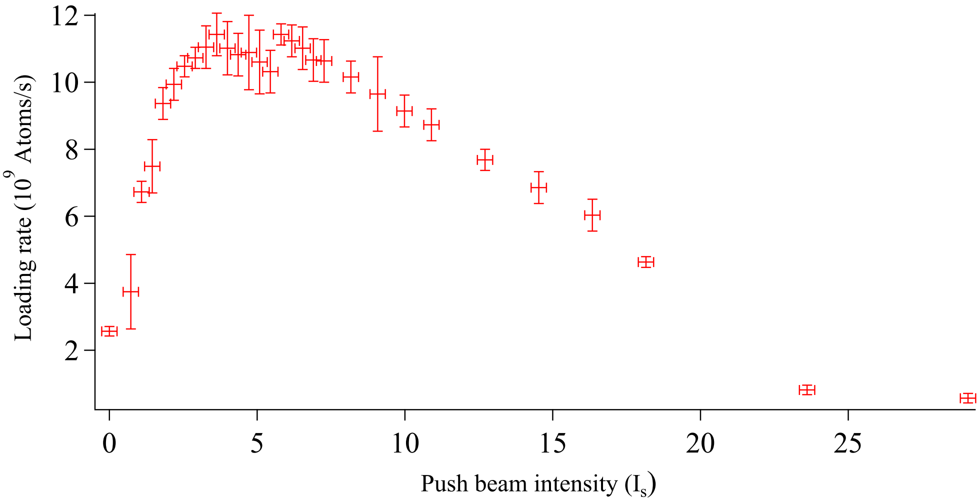

Figure 99: 3D MOT loading rate as a function of the push beam intensity. A clear optimum at 8 I_s leads to loading rates of 10^{10} atoms/s.

7.2.1 Experimental sequence

The complete experimental sequence is shown on Fig. 100 where the laser parameters and the quadrupole filed gradient are summarized. After an initial loading stage of 1 s, the magnetic gradient is ramped up and the cooling laser detuning is simultaneously increased (CMOT stage). This leads to an increased atomic density and a reduced cloud temperature (discussed in Sec. 7.2.5). In addition, a constant field along the Y direction is progressively ramped up during the CMOT to transport the magnetic field minimum closer to the surface. Then all magnetic fields are turned off and a molasses stage is performed by increasing further the laser detuning (see Sec.7.2.6). Finally, the laser intensities are ramped down by the AOMs with a small delay on the repumping light to keep all the atoms in the same hyperfine level $|F = 2\rangle$. This cloud is the final released atomic cloud. It can either be characterized with time of flight measurements (see Sec. 7.2.3) or transferred in the magnetic trap.

7.2.2 Atom number

In this subsection I discuss the imaging technique used to characterize the atomic cloud spatial distribution and total atom number. As discussed in Sec. 6.4 we use a set of two CCD sensors which collect fluorescence photons. A light pulse produced by all 3D MOT beams excites the atoms with controlled peak intensity I and detuning δ_1 with respect to the cooling transition. A second pulse provides the reference background without atom which, after substraction, gives an image of the atom cloud. Equation (110) gives the number of atoms as a function of the electron counts (related to the pixel depth) of this image.

To test the validity of this formula, identical clouds were produced and the imaging light parameters (intensity and detuning) were scanned. The results of this procedure are shown on Fig. 101 and on Fig. 102. Both the saturation profile $s/(1+s)$ and

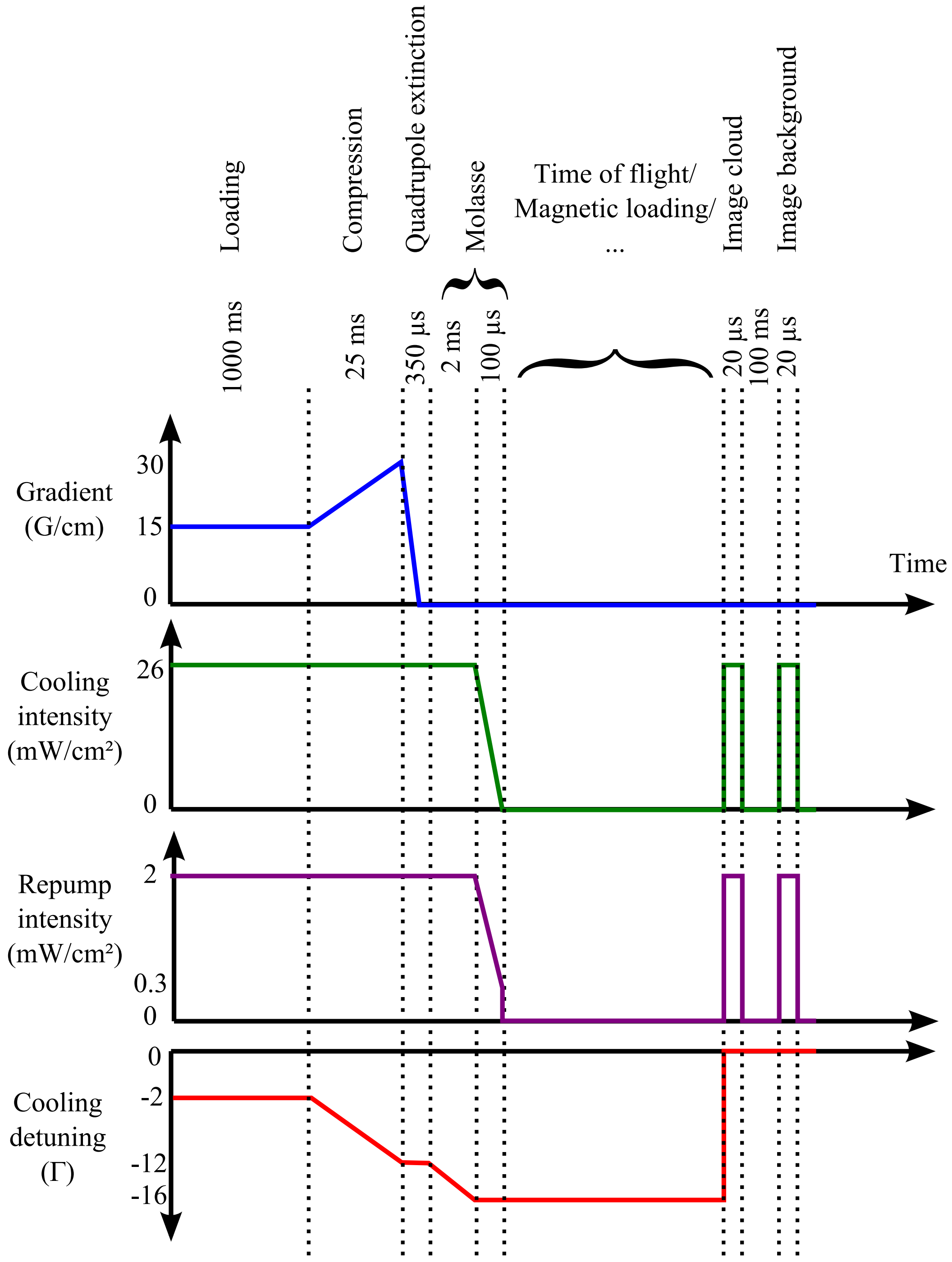

Figure 100: Temporal sequence of the laser and trapping parameters: quadrupole field gradient, intensity per laser beam and cooling detuning δ_1. The horizontal axis is not at scale but each step duration is indicated above the graphs.

Lorentzian shape $s/\left[1+s+(2\delta_1/\Gamma)^2\right]$ accurately describe the experimental data. In our case, the saturation parameter s does not correspond to an ideal two-level system saturation. Due to the number of different transitions that can be excited, s is defined by $s = I/I_s^*$, where I_s^* is an effective saturation intensity:

$$I_s^* = \alpha I_s$$

where $I_s = 3.58\,mW/cm^2$ is the saturation intensity of $F = 2 \to F' = 3$ for an isotropic light polarization and α is a numerical parameter.

Fitting with a saturation function $s/(1+s)$ the profile of Fig. 101, one can access I_s^* knowing the probe laser waist (0.7 cm). With this measure, I obtain an effective saturation intensity of $I_s^* = 3\,\mathrm{mW/cm^2}$. This value is smaller than I_s because most of the $F = 1,2 \rightarrow F' = 0,1,2$ transitions have smaller transition strengths than the $F = 2 \rightarrow F' = 3$ transitions.

Fitting with a Lorentzian distribution the profiles of Fig 102, one can see that the zero detuning agrees with an independent frequency calibration using a saturated absorption setup within its error bar (1 MHz). Also, from the Lorentzian widths, one recovers the saturated transition width $\Gamma(1+s)$ for two different saturation parameters $s = 4$ and $s = 14.5$. It corresponds to the two experimental parameters of $I_{peak,1} = 8\,\mathrm{mW/cm^2}$ and $I_{peak,2} = 32\,\mathrm{mW/cm^2}$ if the effective saturation intensity is $I_s^* = 2\,\mathrm{mW/cm^2}$.

The discrepancy between the two experimental effective saturation intensities emphasizes the difficulty to define this parameter when one deals with multi-level transitions coupled with the re-absorption of photons having a variety of polarization. For the purpose of this thesis, I used the intermediate value of $2.5\,\mathrm{mW/cm^2}$ to evaluate the saturation parameter. This is not an important issue for high saturation imaging as the exact saturation parameters does not need to be accurately known.

Indeed, we can see on Fig. 102 that probing the cloud with a saturated probe renders the number of electrons independent of the exact saturation parameter and we will see that it represents accurately the number of atoms in the cloud.

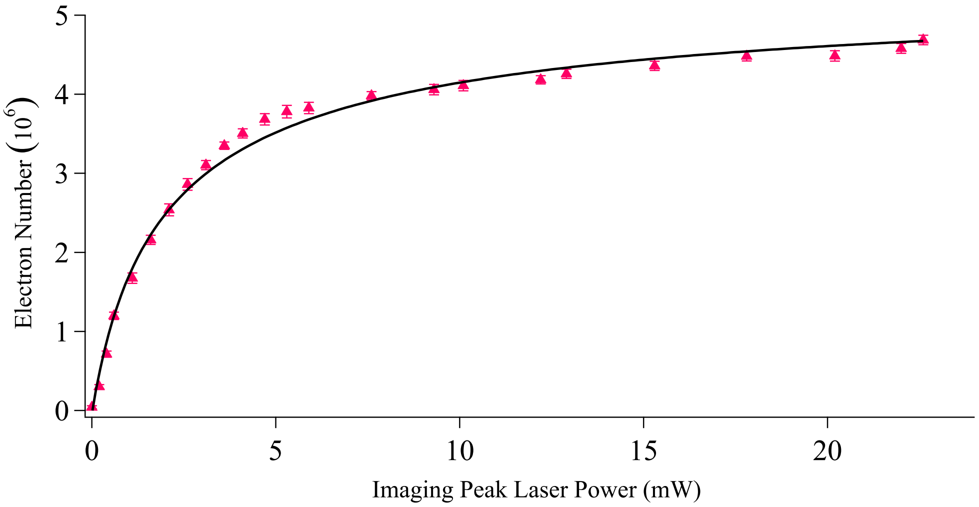

Figure 101: Electron count $\sum_i N_{e,i}$ as a function of the probe peak laser power. The fit corresponds to eq. (110) with fixed pulse duration, $\tau = 20\,\mu s$, detuning, $\delta_1 = 0$ and atom number N_{at}.

Highly saturated fluorescence imaging

Highly saturating beams allows to prevent the large absorption of dense clouds which usually reduces the saturation of the probe at the center of the cloud. It can lead to experimental bias in the atom number calibration as all the atoms do not

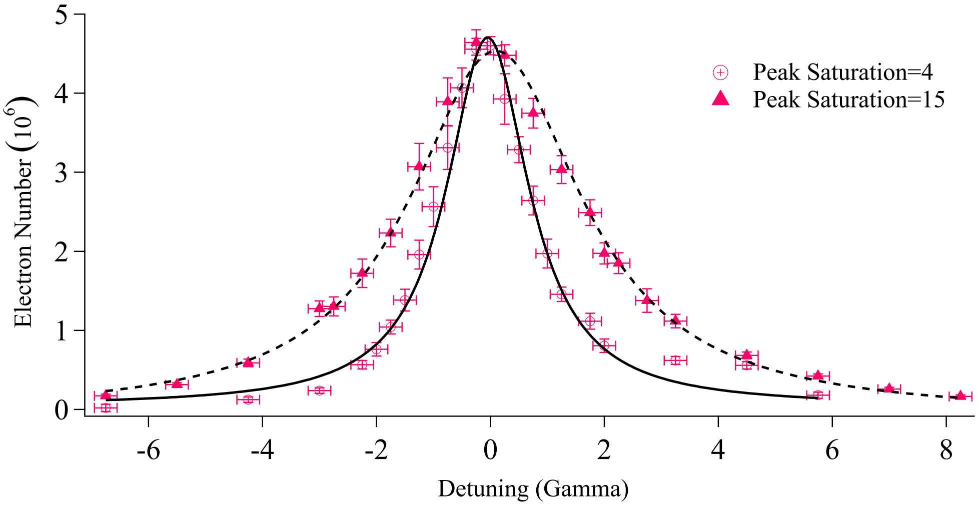

Figure 102: Electron count as a function of the probe detuning δ_1 for two different peak saturations infered from the Loretzian widths : $s = 4$ and $s = 15$. The number of electron has been corrected by the peak saturation factor $s/(1+s)$ to compare the peak amplitudes. The fits corresponds to the Lorentzian shape of eq. (110). The optical thickness for this calibration was approximately 5.

scatter photons at the same rate and the central scattered photons are re-absorbed by atoms from the external "layers".

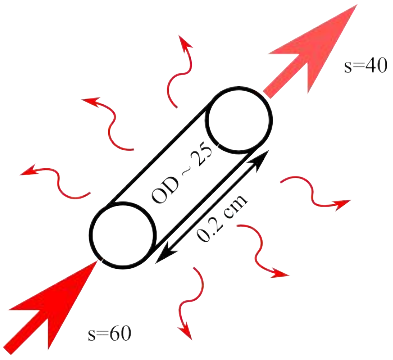

Figure 103
Absorption in a dense cloud.

To understand the situation, let us consider a cylinder of atoms, $100\,\mu m$ radius, $0.2\,cm$ long at the center of a dense $5 \times 10^{10}\,Atoms/cm^3$. This slab of atoms cloud can absorb at most (i.e at complete saturation) $6 \times 10^{13}\,photons/s$. A highly saturated laser beam ($s = 60$) conveys $1.9 \times 10^{14}\,photons/s$ through this cylinder. Therefore, assuming that all the excited atoms spontaneously emit outside of the laser beam, about 66 % of the photon flux remains after the cylinder. This shows that the initial assumption that all atoms are saturated by the laser intensity is valid as the intensity is still large ($s = 40$) after absorption.

Clouds are usually described by their peak optical thickness $\sigma n_0 l$ where $\sigma \sim 2.5 \times 10^{-9}\,cm^2$ is the resonant absorption cross section of a single atom. This parameter describes the atom absorption in the linear and individual regime with an intensity attenuation factor given by $e^{-\sigma n_0 l}$. The previous cylinder optical thickness is approximately 25. In the strongly non-linear regime, the excited state finite lifetime reduces the amount of photons absorption.

As a consequence, the fluorescence rate is accurately known, $\Gamma/2$ for all atoms, as long as the optical thickness is much smaller than the saturation parameter. Also, the attenuation due to absorption is well represented by the effective optical thickness $\sigma n_0 l/s$. If we consider the previous example, $\exp(-\sigma n_0 l/s) = 66\,\%$ which is exactly the proportion of transmitted laser light. Therefore, the re-absorption by the external "layers" of the fluorescence photons emitted by the center of the cloud is considerably reduced.

Only for high saturation fluorescence detection, both the number of detected photons and their spatial distribution accurately represent the atom number and its distribution. This is supported by a discussion in [315] where DePue *et al.* showed how saturated fluorescence is an accurate tool for atom number evaluation as long as the saturation parameter is four times larger than the cloud optical thickness.

Using all three MOT beams to image the MOT cloud allowed to reach a combined saturation intensity of $s_{max} sim78$. This saturation intensity is sufficient for the MMOT characterization, which has an optical thickness of the order of 20. Our atom number detection accuracy assumes that the scattered light emitted during the light pulse reaches the detector. With a conservative assumption that only a fraction $\exp\left(-\sigma n_0 l / s_{max}\right)$ of the scattered light is not re-absorbed and is not detected, we estimate the accuracy[4] of our MMOT atom number determination to better than 20 %. This is probably overestimated but since the statistical noise is of the same order of magnitude, it does not limit the discussion on the atom cloud characteristics. The condition of large saturation compared to the optical depth limit the efficiency of this detection scheme to clouds with optical depth below 25.

7.2.3 Temperature measurements

Time of flight method in cold atom experiments is routinely employed and was initially developed by Lett. *et al.* [316]. It is based on the release of the trapped cloud and the subsequent free space expansion of the atomic distribution which is well described by a Maxwell-Boltzmann distribution. The cloud has a time dependent width [317] in every direction:

$$\sigma^2_{x,y,z}\left(t\right) = \sigma^2_{0;x,y,z} + \frac{k_B T}{M} t^2 \tag{111}$$

where $\sigma_{0;i}$ is the initial Gaussian width in the $i = x, y, z$ direction, t is the expansion (TOF) time, M is the mass of the atom and T is the cloud temperature.

Imaging the cloud after different expansion times (typically starting at 1 ms and up to 50 ms) and fitting the transverse profile with a single Gaussian function (see next section for a discussion on the cloud profiles) provides information on the cloud width and position. A typical measurement is represented on Fig. 104. One can see that the quadratic behavior is unclear in the horizontal direction as a double peak distribution (see fig. 107) progressively merges into a single peak. On the other hand, in the vertical direction, the width clearly follows eq. (111) for TOF larger than 20 ms. This transition between two linear regimes occurs when the cloud density is similar to the uncompressed cloud. Indeed, for this measurement, the cloud initial density was 10^{11} Atoms/cm^3 and a 20 ms TOF decreased its density by a factor 2. At this point,

---

[4] Other parameters such as the amplifier gain and the collecting solid angle are known much more accurately.

the cloud optical depth is about a third of the saturation intensity which means that the fluorescence distribution begins to be realistic.

Note that this time of flight measurement corresponds to a denser atom cloud (CMOT) for which the transition was clearer. The y-axis intercept of the vertical direction linear fit gives an estimation of the initial cloud size ($2.6(1)\,\mathrm{mm}$). The slope gives a cloud temperature of $70\,\mu\mathrm{K}$.

Additionally, the cloud center evolution during the time-of flight measurement can provide some useful information on the cloud initial velocity and eventual accelerations induced by the magnetic field switch-off. The fitted center are shown on Fig. 105. A quadratic fit of the vertical center corresponds to the gravitational acceleration with a fitted value of $9.8(1)\,\mathrm{m/s^2}$. It indicates that our pixel calibration, performed independently, is accurate. Only the position for TOF larger than $20\,\mathrm{ms}$ were used as the cloud center prior to dilution is also not well measured.

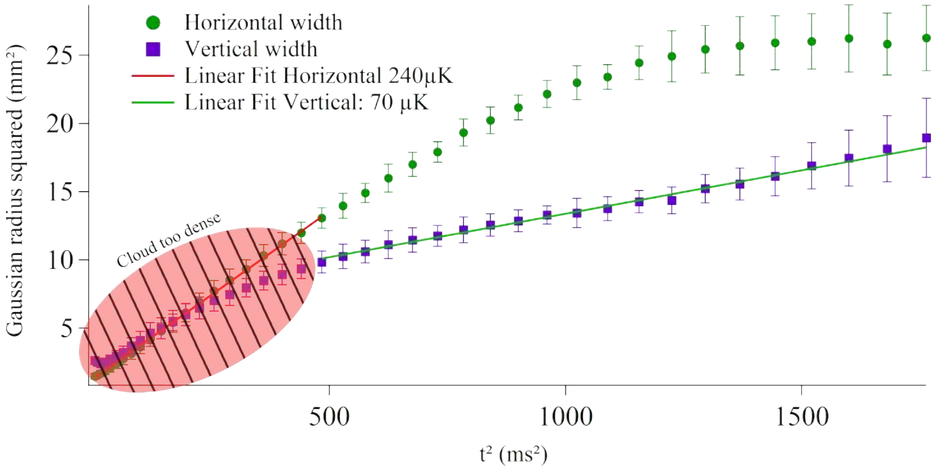

Figure 104: The parameters of the fitted integrated profiles are shown as a function of the free flight time. Widths squared as a function of time squared. Before $400\,\mathrm{ms}^2$, the vertical and horizontal widths do not reflect the actual cloud size as the density is too large to have a good fluorescence picture. However, after $20\,\mathrm{ms}$, the cloud is diluted enough to allow for the extraction of the widths which leads to cloud temperature of $70\,\mu\mathrm{K}$. Due to the chip surface, the horizontal width is hard to evaluate as it truncates the atomic profile at large TOF.

High saturation fluorescence imaging

To measure the ^{87}Rb cloud characteristics, we use a highly saturated light pulse coupled to a CCD sensor which collects fluorescence photons. This technique is accurate ($\sim 20\,\%$) when the cloud peak optical thickness is much smaller (at least a factor 3) than the probe saturation. If the initial optical thickness is too large, a preliminary expansion is necessary to obtain a fair representation of the atom distribution. This feature appears clearly in time of flight measurements which provide information on the cloud temperature and its initial size.

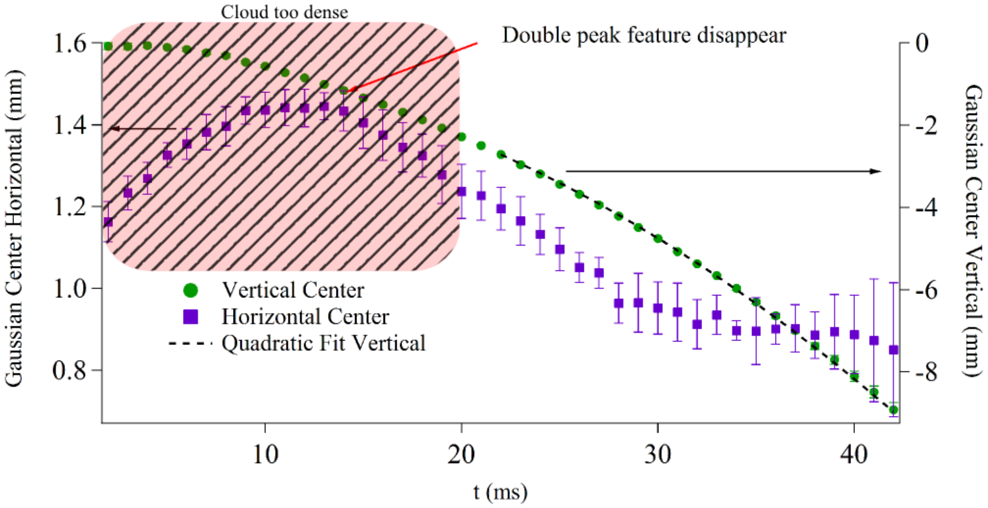

Figure 105: The parameters of the fitted integrated profiles are shown as a function of the free flight time. Center of the fitted Gaussian as a function of time. The Vertical position is a parabola as should be a fall in free flight. The horizontal position gets nearer to the surface at long times.

7.2.4 Loading the MMOT

With this tool, we are now capable to discuss the optimization of the cold atom cloud at its different stages. The first step consisted in improving the atom number of trapped atoms in the MMOT at a position close to the magnetic trap by adjusting the quadrupole fiels and the MMOT beams. The method we used consisted in adjusting the horizontality and verticality of the MMOT beams with an orthogonal reflection on the chip's mirror and by centering the vertical beam on the top and bottom viewports. Then, the MMOT coils' height and position was adjusted, keeping the beams alignment fixed, in order to have the largest, highest symmetry and optimal position (at the center of the chip's "Z" wire) cloud.

Afterwards, the laser beams parameters (relative power of the cooling over the repumping beam, total cooling power, different powers in the vertical beam with respect to the horizontal beams, magnetic gradient...) were systematically scanned but did not improve the MMOT performances. We found that $1/10$ of relative repumping power, highest cooling power available, balanced powers in all three directions and a magnetic field gradient of $15\,\mathrm{G/cm}$ were the optimal parameters.

The cooling laser detuning, on the other hand shows a clear optimum for loading high atom numbers. This is represented on Fig. 106 were the asymptotic number of loaded atoms is shown as a function of the cooling laser detuning δ_1. There is a clear maximum around -2Γ for the MMOT.

The measured profiles of the loaded cloud are represented on Fig. 107 where the fluorescence signal of the side camera is shown with its integrated profiles. This cloud corresponds to the initial density of $5(1) \times 10^{10}\,\mathrm{Atoms/cm^3}$. From this picture, one can extract the initial cloud's widths (at $1/e^2$) in the Z ($2.4\,\mathrm{mm}$) direction. In the vertical direction, an initial double peak structure requires a double Gaussian fit which gives two different widths. One (blue curve) is similar to the Z direction

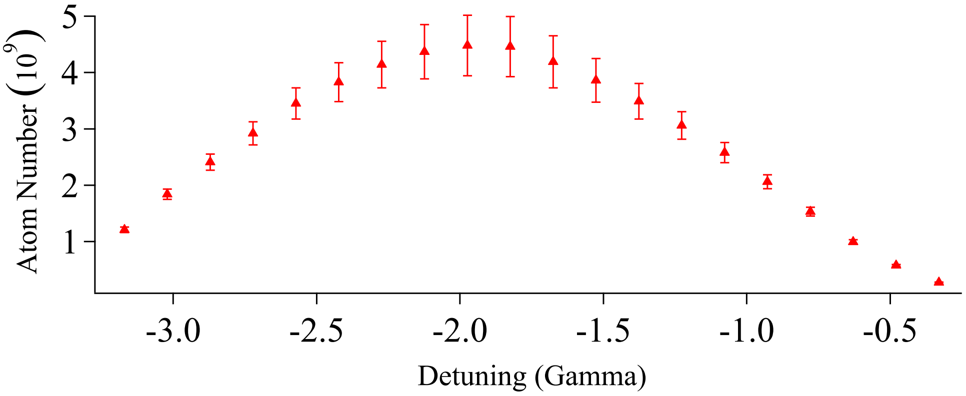

Figure 106: Asymptotic number of loaded atoms as a function of the cooling laser detuning δ_1. The maximum around -2Γ corresponds to a competition between the radiation pressure and the trapping force.

(2.5 mm) while the other (green curve) is much smaller (1.4 mm). The origin of this shape is not well understood but might result from different effects:

- A shadow effect due to the imbalance between the laser intensities of the counter propagating beams. It increases the trap spring constant on the side of the mirror as the beams are less attenuated by reflection than by transmission through the cloud.
- A radiative force induced by photons emitted by the MMOT and reflected by the mirror surface. It pushes the closest atoms away from the surface.

The optimized cloud at the end of the loading stage typically contains $5(1) \times 10^9$ atoms trapped 5 mm away from the chip's surface at a temperature of 150(20) µK. At this stage, the density is low enough to have an accurate picture of the cloud without any time of flight. Indeed, we measure[5] widths of ($\sigma_{0,x} = 2.9(2)$ mm, $\sigma_{0,y} = 3.5(2)$ mm and $\sigma_{0,z} = 2.4(1)$ mm). These values agree well with the y-axis intercept of time of flight measurements which is accurate when the density is much smaller than the saturation. The corresponding peak density $N_{at}/\left(4/3\pi\sigma_{0,x}\sigma_{0,y}\sigma_{0,z}\right)$ is $5(1) \times 10^{10}$ atoms/cm³ as previously claimed. This is the limit of our high saturation fluorescence detection. Therefore, for the following steps, the cloud will be initially too dense to be directly imaged and its widths will be evaluated from time of flight measurements after 20 ms free space expansion.

Lowering the cloud temperature and increasing its density are necessary to have an efficient transfer to the magnetic trap. This is the reason why compression stages and optical molasses were included at the end of our MMOT sequence.

7.2.5 Compressed MOT

During the compression stage, the magnetic gradient and the laser detuning δ_1 are increased in approximately 25 ms. The increased gradients leads to a tighter con-

---

[5] Due to the double peak feature, $\sigma_{0,x}$ is approximatively measured and the given value corresponds to the width of the convolution between the two fitted Gaussians.

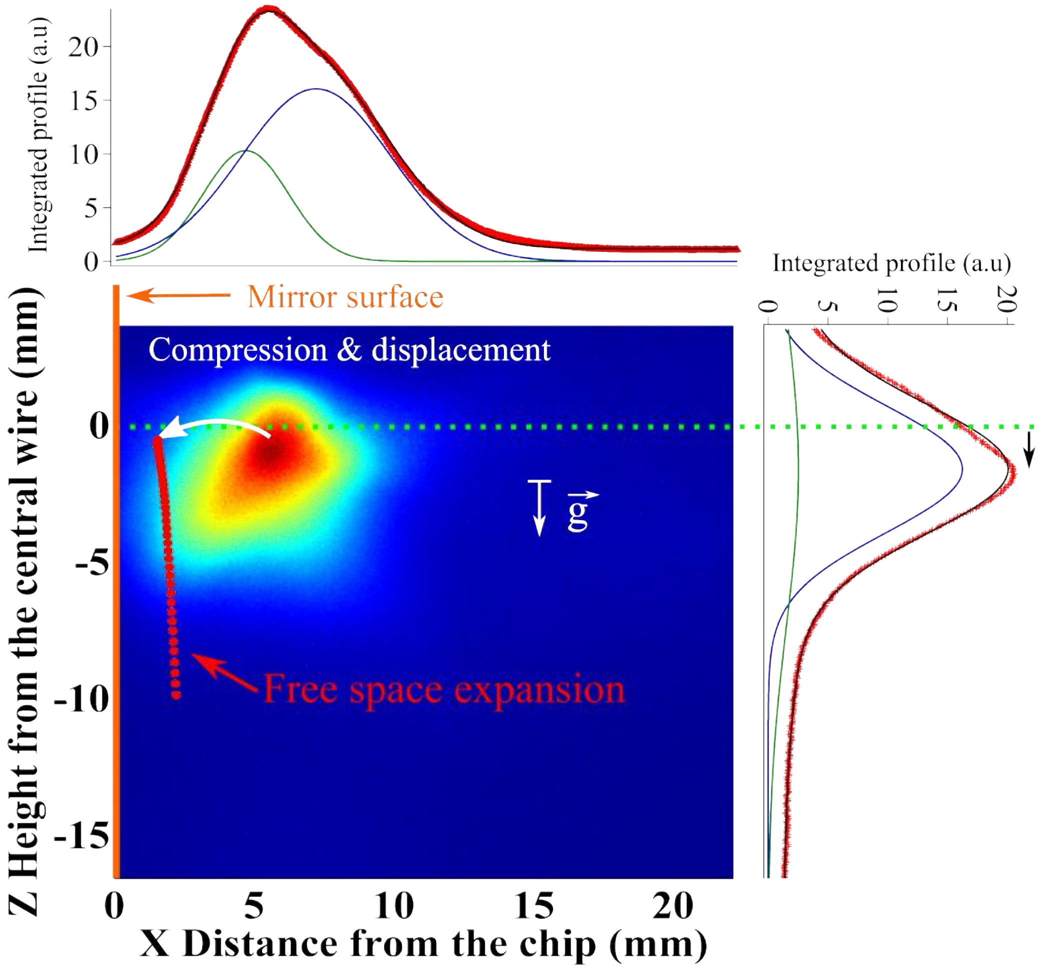

Figure 107: Fluorescence snapshot of the cloud at the end of the 3D MOT loading. The integrated profiles are shown along each sides and exhibit a double Gaussian shape shown by the green and blue curves whose sum (black line) fits the experimental data points (red dots). This is particularly striking in the (X direction) orthogonal to the chip surface were the two gaussian centers are separated by 2 mm. After ~ 15 ms, this double peak structure merges in a single shape which simplifies the width measurement in this direction. In the vertical (Z) direction, this is less problematic as the flat background does not influence the main peak width evaluation. Additionally, one can see that the cloud center is initially below (1 mm) the magnetic wire height. This is not voluntary as we are still in the process of optimizing the molasses overlap with the magnetic trap. The subsequent compression and displacement stage as well as the cloud center typical trajectory during a time of flight measurement are represented along the cloud distribution.

finement. But due to the radiation pressure, the cloud size cannot decrease if the scattering rate remains constant. This is the reason why the detuning is increased. During this stage, a constant bias field directed along the Y direction is linearly increased from[6] 0 to 3 G. We found no clear optimum in the compression duration as long as it was large compared to the magnetic field ramping time. However, the final detuning has a large effect on the cloud final temperature as is shown on Fig. 108. Keeping the other parameters constant (a final magnetic gradient of 30 G/cm, a con-

---

[6] The bias field depends on the magnetic gradient as we do not want the atomic cloud closer to the chip than its horizontal width, to prevent atom losses.

stant light intensity and a bias field amplitude of 4 G) the final detuning was scanned and the compressed cloud temperature measured with the previously described time of flight technique. An example of such measurement is shown on Fig. 109. From an initial temperature around 150 µK, the final temperature linearly decreases with the detuning down to approximately 50 µK. Even the "horizontal temperature", which is not a as well measured initially as the vertical temperature, displays a similar behavior. Increasing the detuning further than[7] -16Γ did not improved the final cloud temperature and, on the contrary, tended to increase the cloud temperature. During this stage, about 20 % of atoms are lost. It results in $4(1) \times 10^9$ atoms trapped in the CMOT. As expected, the density increases to 10^{11} $\mathrm{atoms/cm^3}$ ($\sigma_{0,x} = 1.7(2)$ mm, $\sigma_{0,y} = 2.5(2)$ mm $\sigma_{0,z} = 2.3(2)$ mm). Compared to the density in the initial magnetic trap (3×10^{11} $\mathrm{atoms/cm^3}$), we see that the obtained density is reasonable to assume an efficient transfer.

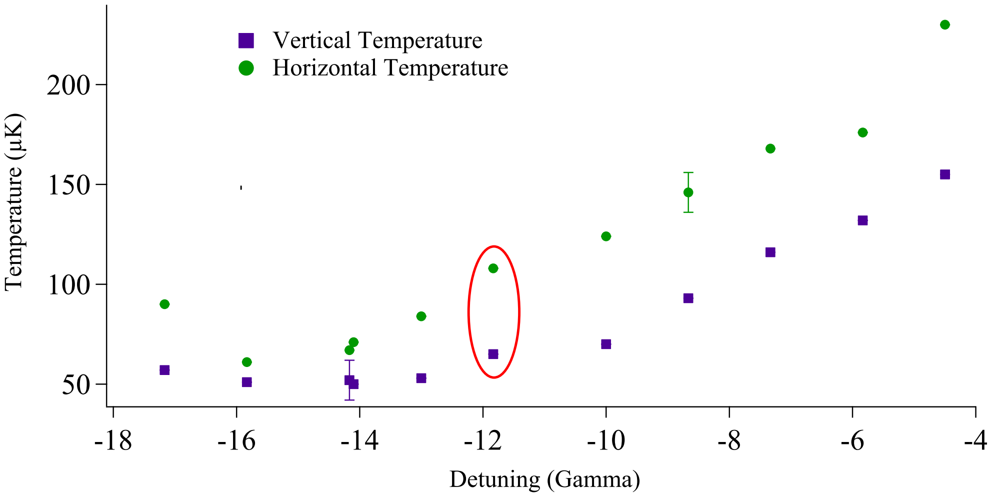

Figure 108: Evolution of the CMOT temperature as a function of the cooling detuning δ_1 during the compression stage. The temperature measured along the X and Z direction decrease linearly as a function of the detuning down to 50 µK at $\delta_1 = -15\Gamma$. The circled points correspond to the time of flight measurement displayed on Fig. 109.

7.2.6 Molasses

At the end of the compression stage, the laser parameters are kept constant for 350 µs which corresponds to the commutation time required to ramp the quadrupole coils current down to zero. The molasses detuning is then linearly swept during this last step from $\delta_1 = -10\Gamma$ to $\delta_1 = -14\Gamma$. The exact final detuning did not have a large influence on the final temperature. The molasses duration is on the contrary an important paramaters for the final cloud temperature. Its effect is represented on Fig. 110 where the molasse duration was scanned between 0.1 ms and 5 ms. During ms, the

---

[7] This large detuning is required by the highly saturated transition. Usually, smaller intensities are used during this stage as well as smaller detunings. We did not try this sequence as the cloud characteristics were already satisfying.

temperature fluctuates strongly which might indicate the presence of residual eddy currents producing uncontrolled magnetic fields. Indeed, sub-Doppler cooling mechanisms are hindered by non-zero magnetic fields [318], [319]. Nevertheless, after this initial stage, the temperature drops rapidly. From the compressed cloud temperature around 50 µK, the final cloud temperature gets down to 12 µK after 2 ms. Increasing further the molasses duration tends to increase the cloud temperature and to atom losses. Indeed, the atoms are not magnetically trapped anymore and starts to fall out of the laser beams.

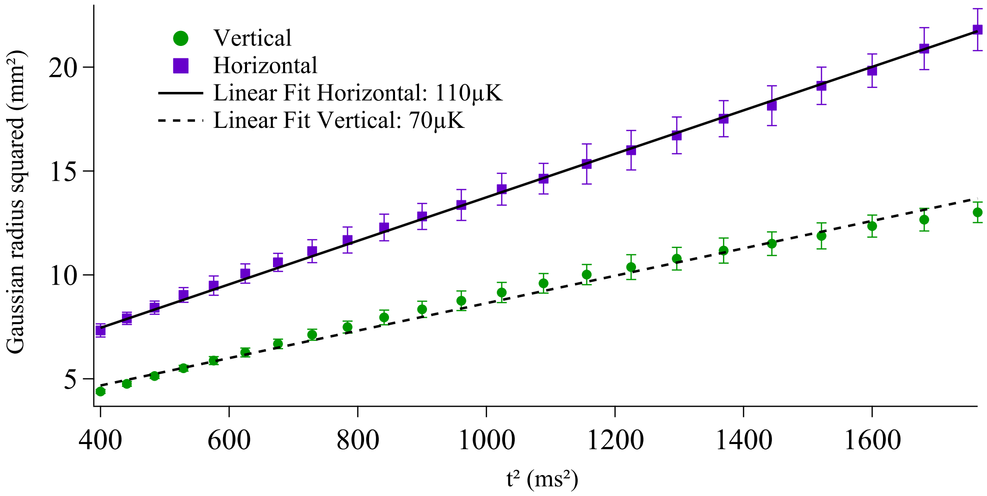

Figure 109: Typical time of flight measurement used for Fig. 108. TOF larger than 20 ms are represented as the density is initially two large for our imaging system. The bimodal distributions are merged which improves the Gaussian width extraction as can be seen by the more regular behavior of the two orthogonal directions. A discrepancy between the two temperature remains but almost vanishes when the cloud is completely compressed (see Fig. 108 at $\delta_1 = -16\Gamma$).

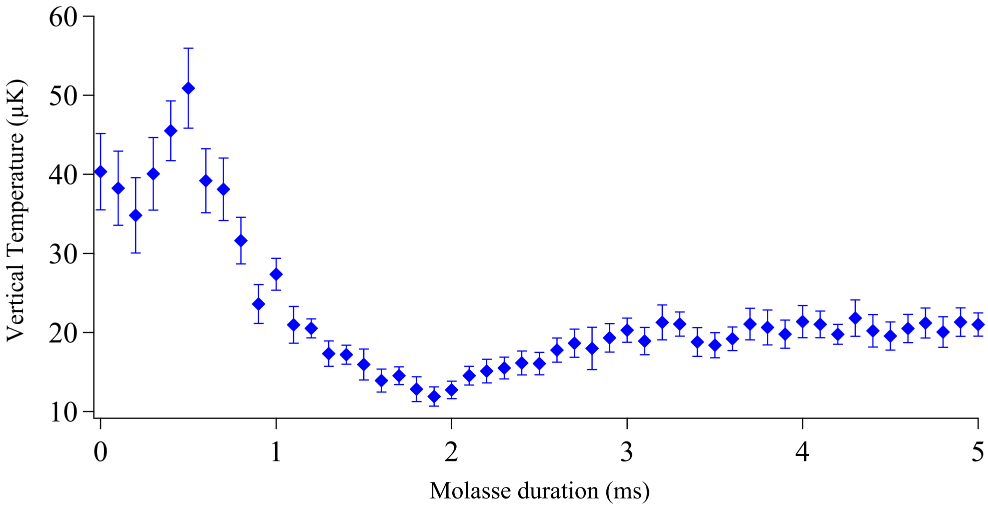

Figure 110: Vertical temperature as a function of the molasses duration at fixed final detuning $\delta_1 = -14\Gamma$. The temperature for short molasses time fluctuates a lot which might be due to residual magnetic fields induced by eddy currents. However, the final molasses temperature is stable below 12 µK at 2 ms.

At the end of this stage, the atom cloud contains approximately 2×10^9 atoms at a temperature of 12 µK. Its gaussian widths ($1/e^2$) in all three directions are $\sigma_{0,x} = 1.6(1)\,\mathrm{mm}$, $\sigma_{0,y} = 2.3(2)\,\mathrm{mm}$ and $\sigma_{0,z} = 2.6(2)\,\mathrm{mm}$ corresponding to a density of $5(1) \times 10^{10}\,\mathrm{Atoms/cm^3}$.

Atom cloud preparation

The production of a cold dense ^{87}Rb cloud is performed in three steps. An initial 1 s loading from the 2D MOT produces the MMOT cloud located 5 mm from the mirror surface. A compression and displacement stage of 25 ms increases the cloud density and moves it closer (2 mm) to the surface. Finally, a molasse stage of 2 ms cools the atoms down to 12(10) µK. The cloud characteristics are summarized in Tab. 16 where the Phase Space Density (PSD) has been included to show the gain at each step.

Production step	N	T (µK)	n_0 (atoms/cm^3)	PSD
MMOT	$5(1) \times 10^9$	150(20)	$5(1) \times 10^{10}$	2×10^{-7}
CMOT	$4(1) \times 10^9$	50(10)	10^{11}	2×10^{-6}
Molasses	$2.0(5) \times 10^9$	12(2)	$5(1) \times 10^{10}$	8×10^{-6}

Table 16: Atom cloud characteristics at end of the different stages.

7.3 CONCLUSION

From a completely empty lab room in the early 2014, we designed and developed an apparatus that is starting to produce cold atom clouds and which offers the possibility to create dual species atomic clouds. In this chapter, we discussed how the setup described in Chap 6 was initially optimized to have a large number of atoms 2×10^9 in a cold 12 µK compressed cloud located close (2 mm) to the mirror chip surface. We also presented the detailed experimental sequence as well as the highly saturated fluorescence technique we used to characterize the cloud. This imaging technique enables us to extract reliable quantities (atom number, size, temperature) of the cold atomic cloud as long as the optical thickness is much smaller than the saturation. The next step, transferring the cloud to the chip's magnetic trap, is already under development and the forced evaporation should soon follow !

Magnetic trapping

We have just started to load atoms in the magnetic trap produced by the chip. For the time being, we suddenly ramp up the current in the "Z" wire up to 40 A and found an optimal bias field along the Z direction of 50 G which corresponds to a magnetic field minimum 1 mm away from the chip's surface. We detect approximately 10^8 atoms remaining in the trap after 60 ms holding time, during which the untrapped cloud falls out of the trapping region. Optical pumping and adjusted overlap of the molasses with the magnetic trap is under way. The magnetic cloud temperature at this stage is around 160 µK. This temperature is promising as it is about half of the temperature (300 µK) that was used in our evaporating cooling model, which might lead to highest atom number, and shortest evaporation duration, than initially planned.

CONCLUSION

This thesis reviewed most of the work undertaken during my three years in the Atom Interferometry group in Toulouse in collaboration with Alexandre Gauguet, Matthias Büchner and Jacques Vigué. It was split into two main parts.

The majority of the first and a half year, I worked on the realisation of some experiments on the Lithium beam interferometer.

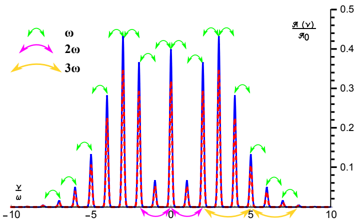

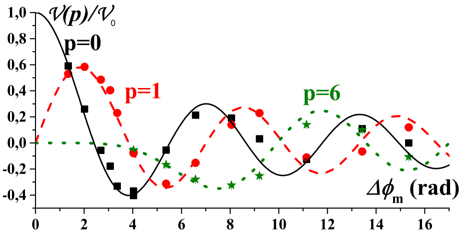

It started with the Kerr modulator experiment which produced diffraction in time of both interferometric arms, leading to an heterodyne and homodyne detection of the frequency side-bands generated in the atomic spectrum. The experimental setup was previously built by Jonathan Gillot and my work mostly consisted in implementing the different experiments that allowed us to test a theoretical model we developed . The agreement of the modulation amplitudes and phases motivated us to try a pedagogical experiment which resulted in the first atomic fax and radio. This was presented in Chap. 2 and published in [320].

Then, in the process of developing additional laser beams required for the Tune-Out wavelength measurement, we implemented the atom optics tool presented as the Pancharatnam dephasor. To understand the non-linear behaviour of our phase shifter, a detailed analysis of the experimental imperfections was developed. It allowed us to investigate the smallest deviations from the ideal Pancharatnam phase. Additional treatment of the experimental fringes, both optical and atomic, supported this investigation. The application of such a tool for precision atom interferometry benefited from this detailed description to pre-empt the limits of such an apparatus. This was presented in Chap. 3.

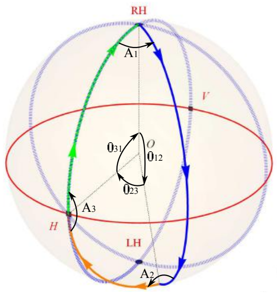

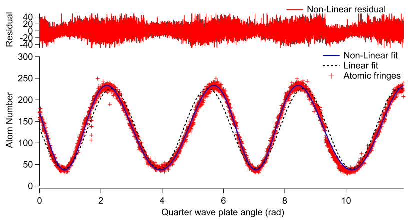

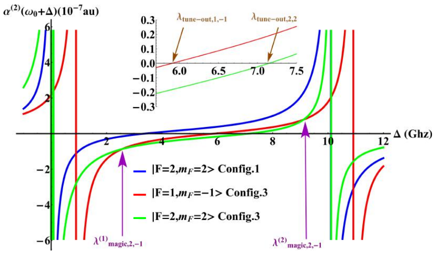

Next the theoretical modelling of ^{7}Li dynamical polarizability coupled with a sophisticated experimental setup allowed us to perform the first measurement of ^{7}Li $|F=2, m_F=2\rangle$ Tune-out wavelength:

$$\lambda_{2,2,tune-out} = 670.972097(15)[3]nm$$

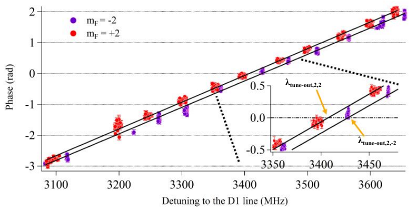

which updates the list of accurately measured Tune-Out wavelength for Alkali atoms with an uncertainty at the level of other state of the art measurements. This experiment also leads us to question the validity of our theoretical model which did not include hyperpolarizability effects that can shift the exact position of Tune-Out wavelengths.

The remaining year and a half, I worked with Julien Alibert and Alexandre Gauguet on the design and development of a new interferometer.

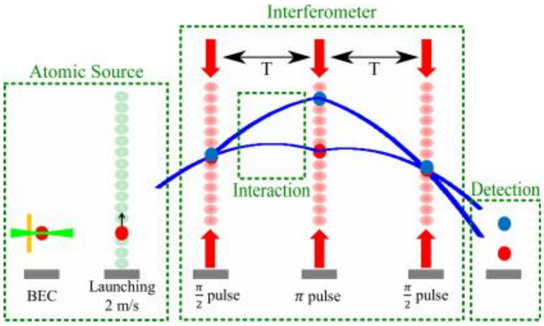

This new interferometer relies on a Bose-Einstein Condensate produced at a high repetition rate by combining an intense 2D MOT source, a Mirror MOT and an atom chip. This forms the source of a large spatial separation ($> 1\,\text{cm}$) fountain type interferometer produced by Large Momentum Transfer light pulses. In addition to investigating the use of condensates in atom interferometry, this setup is build to perform a matter neutrality test via an Aharonov-Bohm scalar phase. This is one of the reason why a dual isotopes (^{85}Rb/^{87}Rb) source was designed in order to test for both charge equality and neutron neutrality. These specific constraints required to be combined which needed both modelling (of the dual isotopes evaporation, of the transport from the chip,...) and theoretical development of the LMT interferometric schemes. This description of the future interferometer was presented in Chap 5.

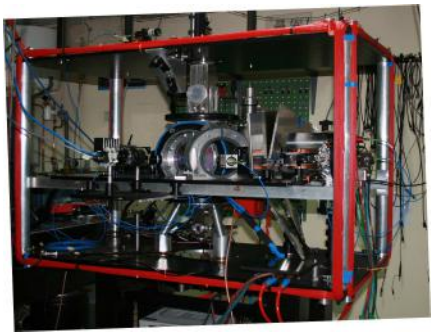

In parallel, the development of the laser setup, the magnetic field sources and the vacuum system was undertaken in our new experimental room. The journey from empty breadboards, separate vacuum pieces, raw copper wires, brand new lasers system and new electronics to the functional apparatus we have now was not particularly emphasized but was one of the most interesting part of my thesis. Nevertheless, the technical choices as well as the apparatus performances were presented in great details in Chap 6 and gave a good overview of each of these tasks.

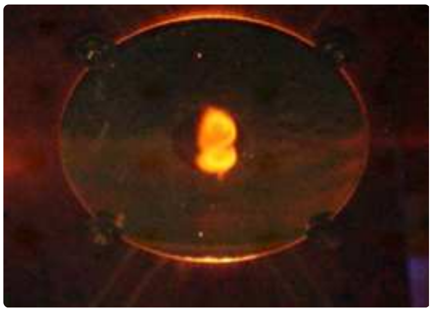

In the last chapter, some of the recent performances achieved with this apparatus were presented. As expected, we obtain a few billions atoms in our initial Mirror MOT in approximately 1 s. Compression, displacement and molasses stages lead to 2×10^9 Atoms close to the mirror surface at an ultra cold (12 μK) temperature. Magnetic trapping of this cloud is under way and we hope to proceed further down to BEC very shortly !

BIBLIOGRAPHY

[1] C. Davisson and L. H. Germer, "Diffraction of electrons by a crystal of nickel", *Physical Review*, vol. 30, no. 6, pp. 705–740, Dec. 1, 1927 (cit. on pp. 16, 288).

[2] I. Estermann and O. Stern, "Beugung von molekularstrahlen", *Zeitschrift für Physik*, vol. 61, no. 1, pp. 95–125, Dec. 14, 1929 (cit. on pp. 16, 288).

[3] L. Marton, "Electron interferometer", *Physical Review*, vol. 85, no. 6, pp. 1057–1058, Mar. 15, 1952 (cit. on pp. 17, 289).

[4] G. Möllenstedt and H. Düker, "Fresnelscher interferenzversuch mit einem biprisma für elektronenwellen", *Naturwissenschaften*, vol. 42, no. 2, pp. 41–41, 1955 (cit. on pp. 17, 289).

[5] R. G. Chambers, "Shift of an electron interference pattern by enclosed magnetic flux", *Physical Review Letters*, vol. 5, no. 1, pp. 3–5, Jul. 1, 1960 (cit. on pp. 17, 289).

[6] G. Möllenstedt and W. Bayh, "Messung der kontinuierlichen phasenschiebung von elektronenwellen im kraftfeldfreien raum durch das magnetische vektorpotential einer luftspule", *Naturwissenschaften*, vol. 49, no. 4, pp. 81–82, 1962 (cit. on pp. 17, 289).

[7] F. Hasselbach, "Progress in electron- and ion-interferometry", *Reports on Progress in Physics*, vol. 73, no. 1, p. 016 101, 2010 (cit. on pp. 17, 76, 289).

[8] H. Rauch, W. Treimer, and U. Bonse, "Test of a single crystal neutron interferometer", *Physics Letters A*, vol. 47, no. 5, pp. 369–371, Apr. 22, 1974 (cit. on pp. 17, 289).

[9] H. Rauch and S. A. Werner, *Neutron interferometry: Lessons in experimental quantum mechanics, wave-particle duality, and entanglement*. 2015, OCLC: 897442984 (cit. on pp. 17, 289).

[10] C. J. Bordé, "Atomic interferometry with internal state labelling", *Physics Letters A*, vol. 140, no. 1, pp. 10–12, Sep. 4, 1989 (cit. on pp. 18, 291).

[11] C. S. Adams, M. Sigel, and J. Mlynek, "Atom optics", *Physics Reports*, vol. 240, no. 3, pp. 143–210, May 1, 1994 (cit. on pp. 18, 291).

[12] J. Baudon, R. Mathevet, and J. Robert, "Atomic interferometry", *Journal of Physics B: Atomic, Molecular and Optical Physics*, vol. 32, no. 15, R173, 1999 (cit. on pp. 18, 291).

[13] A. Miffre, M. Jacquey, M. Büchner, G. Trénec, and J. Vigué, "Atom interferometry", *Physica Scripta*, vol. 74, no. 2, p. C15, 2006 (cit. on pp. 18, 291).

[14] A. D. Cronin, J. Schmiedmayer, and D. E. Pritchard, "Optics and interferometry with atoms and molecules", *Reviews of Modern Physics*, vol. 81, no. 3, pp. 1051–1129, Jul. 28, 2009 (cit. on pp. 18, 291).

[15] P. R. Berman, Ed., *Atom interferometry*. Academic Press Inc, 1997 (cit. on pp. 18, 291).

[16] G. M. Tino and M. A. Kasevich, Eds., *Atom interferometry*. IOS Press, 2014 (cit. on pp. 18, 180, 266, 291).

[17] O. Carnal and J. Mlynek, "Young's double-slit experiment with atoms: A simple atom interferometer", *Physical Review Letters*, vol. 66, no. 21, pp. 2689–2692, May 27, 1991 (cit. on pp. 18, 21, 291, 294).

[18] D. W. Keith, C. R. Ekstrom, Q. A. Turchette, and D. E. Pritchard, "An interferometer for atoms", *Physical Review Letters*, vol. 66, no. 21, pp. 2693–2696, May 27, 1991 (cit. on pp. 19, 21, 30, 140, 291, 292, 294).

[19] M. Kasevich and S. Chu, "Atomic interferometry using stimulated raman transitions", *Physical Review Letters*, vol. 67, no. 2, pp. 181–184, Jul. 8, 1991 (cit. on pp. 19, 21, 23, 140, 291, 292, 294, 296).

[20] F. Riehle, T. Kisters, A. Witte, J. Helmcke, and C. J. Bordé, "Optical ramsey spectroscopy in a rotating frame: Sagnac effect in a matter-wave interferometer", *Physical Review Letters*, vol. 67, no. 2, pp. 177–180, Jul. 8, 1991 (cit. on pp. 19, 21, 291, 292, 294).

[21] E. M. Rasel, M. K. Oberthaler, H. Batelaan, J. Schmiedmayer, and A. Zeilinger, "Atom wave interferometry with diffraction gratings of light", *Physical Review Letters*, vol. 75, no. 14, pp. 2633–2637, Oct. 2, 1995 (cit. on pp. 19, 21, 292, 294).

[22] D. M. Giltner, R. W. McGowan, and S. A. Lee, "Atom interferometer based on bragg scattering from standing light waves", *Physical Review Letters*, vol. 75, no. 14, pp. 2638–2641, Oct. 2, 1995 (cit. on pp. 19, 21, 140, 292, 294).

[23] Y. Torii, Y. Suzuki, M. Kozuma, T. Sugiura, T. Kuga, L. Deng, and E. W. Hagley, "Mach-zehnder bragg interferometer for a bose-einstein condensate", *Physical Review A*, vol. 61, no. 4, p. 041 602, Feb. 28, 2000 (cit. on pp. 19, 21, 141, 292, 294).

[24] C. C. R. Delhuille, "High-contrast mach–zehnder lithium-atom interferometer in the bragg regime", *Applied Physics B*, vol. 74, no. 6, pp. 489–493, 2002 (cit. on pp. 19, 21, 292, 294).

[25] J. D. Perreault and A. D. Cronin, "Observation of atom wave phase shifts induced by van der waals atom-surface interactions", *Physical Review Letters*, vol. 95, no. 13, p. 133 201, Sep. 19, 2005 (cit. on pp. 19, 21, 292, 294).

[26] Y.-J. Wang, D. Z. Anderson, V. M. Bright, E. A. Cornell, Q. Diot, T. Kishimoto, M. Prentiss, R. A. Saravanan, S. R. Segal, and S. Wu, "Atom michelson interferometer on a chip using a bose-einstein condensate", *Physical Review Letters*, vol. 94, no. 9, p. 090 405, Mar. 11, 2005 (cit. on pp. 19, 21, 292, 294).

[27] R. A. Nyman, G. Varoquaux, F. Lienhart, *et al.*, "I.c.e.: A transportable atomic inertial sensor for test in microgravity", *Applied Physics B*, vol. 84, no. 4, pp. 673–681, Aug. 16, 2006 (cit. on pp. 19, 23, 292, 294, 296).

[28] J. E. Debs, P. A. Altin, T. H. Barter, D. Döring, G. R. Dennis, G. McDonald, R. P. Anderson, J. D. Close, and N. P. Robins, "Cold-atom gravimetry with a bose-einstein condensate", *Physical Review A*, vol. 84, no. 3, p. 033 610, Sep. 9, 2011 (cit. on pp. 19, 21, 141, 292, 294).

[29] A. Louchet-Chauvet, T. Farah, Q. Bodart, A. Clairon, A. Landragin, Sébastien Merlet, and F. P. D. Santos, "The influence of transverse motion within an atomic gravimeter", *New Journal of Physics*, vol. 13, no. 6, p. 065 025, 2011 (cit. on pp. 19, 141, 143, 292, 294).

[30] Y. Bidel, O. Carraz, R. Charrière, M. Cadoret, N. Zahzam, and A. Bresson, "Compact cold atom gravimeter for field applications", *Applied Physics Letters*, vol. 102, no. 14, p. 144 107, Apr. 8, 2013 (cit. on pp. 19, 21, 292, 294).

[31] Z.-K. Hu, B.-L. Sun, X.-C. Duan, M.-K. Zhou, L.-L. Chen, S. Zhan, Q.-Z. Zhang, and J. Luo, "Demonstration of an ultrahigh-sensitivity atom-interferometry absolute gravimeter", *Physical Review A*, vol. 88, no. 4, p. 043 610, Oct. 8, 2013 (cit. on pp. 19, 21, 23, 143, 292, 294, 296).

[32] M. Hauth, C. Freier, V. Schkolnik, A. Senger, M. Schmidt, and A. Peters, "First gravity measurements using the mobile atom interferometer GAIN", *Applied Physics B*, vol. 113, no. 1, pp. 49–55, Apr. 16, 2013 (cit. on pp. 19, 21, 292, 294).

[33] G. Rosi, F. Sorrentino, L. Cacciapuoti, M. Prevedelli, and G. M. Tino, "Precision measurement of the newtonian gravitational constant using cold atoms", *Nature*, vol. 510, no. 7506, pp. 518–521, Jun. 26, 2014 (cit. on pp. 19, 21, 23, 143, 292, 294, 297).

[34] U. Sterr, K. Sengstock, J. H. Müller, D. Bettermann, and W. Ertmer, "The magnesium ramsey interferometer: Applications and prospects", *Applied Physics B*, vol. 54, no. 5, pp. 341–346, 1992 (cit. on pp. 19, 21, 292, 294).

[35] A. Morinaga, T. Tako, and N. Ito, "Sensitive measurement of phase shifts due to the ac stark effect in a ca optical ramsey interferometer", *Physical Review A*, vol. 48, no. 2, pp. 1364–1368, Aug. 1, 1993 (cit. on pp. 19, 21, 292, 294).

[36] A. Görlitz, B. Schuh, and A. Weis, "Measurement of the aharonov-casher phase of aligned rb atoms", *Physical Review A*, vol. 51, no. 6, R4305–R4308, Jun. 1, 1995 (cit. on pp. 19, 21, 292, 294).

[37] T. L. Gustavson, P. Bouyer, and M. A. Kasevich, "Precision rotation measurements with an atom interferometer gyroscope", *Physical Review Letters*, vol. 78, no. 11, pp. 2046–2049, Mar. 17, 1997 (cit. on pp. 19, 21, 23, 143, 292, 294, 296).

[38] A. Peters, K. Y. Chung, and S. Chu, "Measurement of gravitational acceleration by dropping atoms", *Nature*, vol. 400, no. 6747, pp. 849–852, Aug. 26, 1999 (cit. on pp. 19, 21, 292, 294).

[39] T. Heupel, M. Mei, M. Niering, B. Gross, M. Weitz, T. W. Hänsch, and C. J. Bordé, "Hydrogen atom interferometer with short light pulses", *Europhysics Letters (EPL)*, vol. 57, no. 2, pp. 158–163, Jan. 2002 (cit. on pp. 19, 21, 292, 294).

[40] T. Müller, T. Wendrich, M. Gilowski, C. Jentsch, E. M. Rasel, and W. Ertmer, "Versatile compact atomic source for high-resolution dual atom interferometry", *Physical Review A*, vol. 76, no. 6, p. 063 611, Dec. 13, 2007 (cit. on pp. 19, 21, 292, 294).

[41] A. Gauguet, B. Canuel, T. Lévèque, W. Chaibi, and A. Landragin, "Characterization and limits of a cold-atom sagnac interferometer", *Physical Review A*, vol. 80, no. 6, p. 063 604, Dec. 1, 2009 (cit. on pp. 19, 21, 23, 292, 294, 296).

[42] A. Bonnin, N. Zahzam, Y. Bidel, and A. Bresson, "Simultaneous dual-species matter-wave accelerometer", *Physical Review A*, vol. 88, no. 4, p. 043 615, Oct. 11, 2013 (cit. on pp. 19, 21, 292, 294).

[43] D. Schlippert, J. Hartwig, H. Albers, L. L. Richardson, C. Schubert, A. Roura, W. P. Schleich, W. Ertmer, and E. M. Rasel, "Quantum test of the universality of free fall", *Physical Review Letters*, vol. 112, no. 20, p. 203 002, May 22, 2014 (cit. on pp. 19, 21, 24, 292, 294, 297).

[44] H. Xue, Y. Feng, S. Chen, X. Wang, X. Yan, Z. Jiang, and Z. Zhou, "A continuous cold atomic beam interferometer", *Journal of Applied Physics*, vol. 117, no. 9, p. 094 901, Mar. 7, 2015 (cit. on pp. 19, 21, 292, 294).

[45] B. Barrett, L. Antoni-Micollier, L. Chichet, B. Battelier, P.-A. Gominet, A. Bertoldi, P. Bouyer, and A. Landragin, "Correlative methods for dual-species quantum tests of the weak equivalence principle", *New Journal of Physics*, vol. 17, no. 8, p. 085 010, 2015 (cit. on pp. 19, 21, 151, 292, 294).

[46] M. Arndt, O. Nairz, J. Vos-Andreae, C. Keller, G. van der Zouw, and A. Zeilinger, "Wave–particle duality of c60 molecules", *Nature*, vol. 401, no. 6754, pp. 680–682, Oct. 14, 1999 (cit. on pp. 19, 292).

[47] J. F. Clauser and S. Li, "Talbot-vonLau atom interferometry with cold slow potassium", *Physical Review A*, vol. 49, no. 4, R2213–R2216, Apr. 1, 1994 (cit. on pp. 19, 21, 292, 294).

[48] L. Deng, E. W. Hagley, J. Denschlag, J. E. Simsarian, M. Edwards, C. W. Clark, K. Helmerson, S. L. Rolston, and W. D. Phillips, "Temporal, matter-wave-dispersion talbot effect", *Physical Review Letters*, vol. 83, no. 26, pp. 5407–5411, Dec. 27, 1999 (cit. on pp. 19, 21, 292, 294).

[49] C. Gross, T. Zibold, E. Nicklas, J. Estève, and M. K. Oberthaler, "Nonlinear atom interferometer surpasses classical precision limit", *Nature*, vol. 464, no. 7292, pp. 1165–1169, Apr. 22, 2010 (cit. on pp. 19–21, 292–294).

[50] M. DeKieviet, D. Dubbers, C. Schmidt, D. Scholz, and U. Spinola, "^{3}He spin echo: New atomic beam technique for probing phenomena in the neV range", *Physical Review Letters*, vol. 75, no. 10, pp. 1919–1922, Sep. 4, 1995 (cit. on pp. 19, 21, 292, 294).

[51] M. Zielonkowski, J. Steiger, U. Schünemann, M. DeKieviet, and R. Grimm, “Optically induced spin precession and echo in an atomic beam”, *Physical Review A*, vol. 58, no. 5, pp. 3993–3998, Nov. 1, 1998 (cit. on pp. 19, 21, 292, 294).

[52] A. Steane, P. Szriftgiser, P. Desbiolles, and J. Dalibard, “Phase modulation of atomic de broglie waves”, *Physical Review Letters*, vol. 74, no. 25, pp. 4972–4975, Jun. 19, 1995 (cit. on pp. 19, 21, 53, 292, 294).

[53] S. B. Cahn, A. Kumarakrishnan, U. Shim, T. Sleator, P. R. Berman, and B. Dubetsky, “Time-domain de broglie wave interferometry”, *Physical Review Letters*, vol. 79, no. 5, pp. 784–787, Aug. 4, 1997 (cit. on pp. 19, 21, 292, 294).

[54] L. Cognet, V. Savalli, G. Z. K. Horvath, D. Holleville, R. Marani, N. Westbrook, C. I. Westbrook, and A. Aspect, “Atomic interference in grazing incidence diffraction from an evanescent wave mirror”, *Physical Review Letters*, vol. 81, no. 23, pp. 5044–5047, Dec. 7, 1998 (cit. on pp. 19, 21, 292, 294).

[55] M. Weel, I. Chan, S. Beattie, A. Kumarakrishnan, D. Gosset, and I. Yavin, “Effect of a magnetic field gradient and gravitational acceleration on a time-domain grating-echo interferometer”, *Physical Review A*, vol. 73, no. 6, p. 063 624, Jun. 28, 2006 (cit. on pp. 19, 21, 292, 294).

[56] M.-K. Zhou, B. Pelle, A. Hilico, and F. Pereira dos Santos, “Atomic multiwave interferometer in an optical lattice”, *Physical Review A*, vol. 88, no. 1, p. 013 604, Jul. 3, 2013 (cit. on pp. 19, 21).

[57] S. Wu, E. Su, and M. Prentiss, “Demonstration of an area-enclosing guided-atom interferometer for rotation sensing”, *Physical Review Letters*, vol. 99, no. 17, p. 173 201, Oct. 25, 2007 (cit. on pp. 19, 21).

[58] C. F. Ockeloen, R. Schmied, M. F. Riedel, and P. Treutlein, “Quantum metrology with a scanning probe atom interferometer”, *Physical Review Letters*, vol. 111, no. 14, p. 143 001, Oct. 3, 2013 (cit. on pp. 19, 21, 294).

[59] P. Cladé, E. de Mirandes, M. Cadoret, S. Guellati-Khélifa, C. Schwob, F. Nez, L. Julien, and F. Biraben, “Precise measurement of h/mRb using bloch oscillations in a vertical optical lattice: Determination of the fine-structure constant”, *Physical Review A*, vol. 74, no. 5, p. 052 109, Nov. 21, 2006 (cit. on pp. 20, 21, 23, 293, 294, 297).

[60] T. Lévèque, A. Gauguet, F. Michaud, F. Pereira Dos Santos, and A. Landragin, “Enhancing the area of a raman atom interferometer using a versatile double-diffraction technique”, *Physical Review Letters*, vol. 103, no. 8, p. 080 405, Aug. 21, 2009 (cit. on pp. 20, 141, 293).

[61] S.-w. Chiow, T. Kovachy, H.-C. Chien, and M. A. Kasevich, “$102\hbar k$ large area atom interferometers”, *Physical Review Letters*, vol. 107, no. 13, p. 130 403, Sep. 19, 2011 (cit. on pp. 20, 21, 23, 141, 142, 193–195, 293, 294, 296).

[62] S. Fray, C. A. Diez, T. W. Hänsch, and M. Weitz, “Atomic interferometer with amplitude gratings of light and its applications to atom based tests of the equivalence principle”, *Physical Review Letters*, vol. 93, no. 24, p. 240 404, Dec. 8, 2004 (cit. on pp. 20, 21, 293, 294).

[63] J. Robert, C. Miniatura, S. L. Boiteux, J. Reinhardt, V. Bocvarski, and J. Baudon, “Atomic interferometry with metastable hydrogen atoms”, *EPL (Europhysics Letters)*, vol. 16, no. 1, p. 29, 1991 (cit. on pp. 21, 294).

[64] J. P. Toennis, “Novel spectroscopies using helium atoms clusters and droplets, hinshelwood lectures”, cited in *Interferometry with atoms* [16] (cit. on pp. 21, 294).

[65] T. Schumm, S. Hofferberth, L. M. Andersson, S. Wildermuth, S. Groth, I. Bar-Joseph, J. Schmiedmayer, and P. Krüger, “Matter-wave interferometry in a double well on an atom chip”, *Nature Physics*, vol. 1, no. 1, pp. 57–62, Oct. 2005 (cit. on pp. 21, 294).

[66] T. Mazzoni, X. Zhang, R. Del Aguila, L. Salvi, N. Poli, and G. M. Tino, “Large-momentum-transfer bragg interferometer with strontium atoms”, *Physical Review A*, vol. 92, no. 5, p. 053 619, Nov. 19, 2015 (cit. on pp. 21, 294).

[67] C. C. N. Kuhn, G. D. McDonald, K. S. Hardman, S. Bennetts, P. J. Everitt, P. A. Altin, J. E. Debs, J. D. Close, and N. P. Robins, “A bose-condensed, simultaneous dual-species mach–zehnder atom interferometer”, *New Journal of Physics*, vol. 16, no. 7, p. 073 035, 2014 (cit. on pp. 21, 179, 294).

[68] L. Zhou, S. Long, B. Tang, *et al.*, “Test of equivalence principle at 10^{-8} level by a dual-species double-diffraction raman atom interferometer”, *Physical Review Letters*, vol. 115, no. 1, p. 013 004, Jul. 2, 2015 (cit. on pp. 21, 294).

[69] M. G. Tarallo, T. Mazzoni, N. Poli, D. V. Sutyrin, X. Zhang, and G. M. Tino, “Test of einstein equivalence principle for 0-spin and half-integer-spin atoms: Search for spin-gravity coupling effects”, *Physical Review Letters*, vol. 113, no. 2, p. 023 005, Jul. 8, 2014 (cit. on pp. 21, 294).

[70] C. R. Ekstrom, J. Schmiedmayer, M. S. Chapman, T. D. Hammond, and D. E. Pritchard, “Measurement of the electric polarizability of sodium with an atom interferometer”, *Physical Review A*, vol. 51, no. 5, pp. 3883–3888, May 1, 1995 (cit. on pp. 22, 62, 296).

[71] A. Miffre, M. Jacquey, M. Büchner, G. Trénec, and J. Vigué, “Measurement of the electric polarizability of lithium by atom interferometry”, *Physical Review A*, vol. 73, no. 1, p. 011 603, Jan. 30, 2006 (cit. on pp. 22, 30, 111, 296).

[72] J. Schmiedmayer, M. S. Chapman, C. R. Ekstrom, T. D. Hammond, S. Wehinger, and D. E. Pritchard, “Index of refraction of various gases for sodium matter waves”, *Physical Review Letters*, vol. 74, no. 7, pp. 1043–1047, Feb. 13, 1995 (cit. on pp. 23, 296).

[73] M. Jacquey, M. Büchner, G. Trénec, and J. Vigué, “First measurements of the index of refraction of gases for lithium atomic waves”, *Physical Review Letters*, vol. 98, no. 24, p. 240 405, Jun. 15, 2007 (cit. on pp. 23, 30, 296).

[74] J. Weiner, L. Feenstra, and J. Schmiedmayer, “Conference on atoms and molecules near surfaces (CAMS)”, *Journal of Physics: Conference Series*, vol. 19, no. 1, 2005 (cit. on pp. 23, 296).

[75] S. Lepoutre, H. Jelassi, V. P. A. Lonij, G. Trénec, M. Büchner, A. D. Cronin, and J. Vigué, “Dispersive atom interferometry phase shifts due to atom-surface interactions”, *EPL (Europhysics Letters)*, vol. 88, no. 2, p. 20 002, 2009 (cit. on pp. 23, 30, 296).

[76] F. P. d. Santos and S. Bonvalot, “Cold-atom absolute gravimetry”, in *Encyclopedia of Geodesy*, E. Grafarend, Ed., Springer International Publishing, 2016, pp. 1–6 (cit. on pp. 23, 296).

[77] J. M. McGuirk, G. T. Foster, J. B. Fixler, M. J. Snadden, and M. A. Kasevich, “Sensitive absolute-gravity gradiometry using atom interferometry”, *Physical Review A*, vol. 65, no. 3, p. 033 608, Feb. 8, 2002 (cit. on pp. 23, 296).

[78] J. Rudolph, W. Herr, C. Grzeschik, *et al.*, “A high-flux BEC source for mobile atom interferometers”, *New Journal of Physics*, vol. 17, no. 6, p. 065 001, 2015 (cit. on pp. 23, 156, 179, 296).

[79] D. N. Aguilera, H. Ahlers, B. Battelier, *et al.*, “STE-QUEST—test of the universality of free fall using cold atom interferometry”, *Classical and Quantum Gravity*, vol. 31, no. 11, p. 115 010, 2014 (cit. on p. 23).

[80] D. Aguilera, H. Ahlers, B. Battelier, *et al.*, “STE-QUEST - test of the universality of free fall using cold atom interferometry”, *ARXIV:1312.5980 [gr-qc, physics:physics, physics:quant-ph]*, Dec. 20, 2013 (cit. on pp. 24, 143, 296, 297).

[81] G. Ferrari, N. Poli, F. Sorrentino, and G. M. Tino, “Long-lived bloch oscillations with bosonic Sr atoms and application to gravity measurement at the micrometer scale”, *Physical Review Letters*, vol. 97, no. 6, p. 060 402, Aug. 9, 2006 (cit. on pp. 24, 297).

[82] F. P. Dos Santos, P. Wolf, A. Landragin, M. C. Angonin, P. Lemonde, S. Bize, A. Clairon, A. Lambrecht, B. Lamine, and S. Reynaud, “Measurement of short range forces using cold atoms”, *Proceeding of the 7th International Symposium on Frequency Standard and Metrology, ed. by L. Maleki (World Scientific)*, pp. 44–52, 2009 (cit. on pp. 24, 143, 297).

[83] A. Miffre, M. Jacquey, M. Büchner, G. Trénec, and J. Vigué, “Lithium atom interferometer using laser diffraction: Description and experiments”, *The European Physical Journal D - Atomic, Molecular, Optical and Plasma Physics*, vol. 33, no. 1, pp. 99–112, Feb. 1, 2005 (cit. on pp. 30, 37, 101).

[84] J. Gillot, S. Lepoutre, A. Gauguet, M. Büchner, and J. Vigué, "Measurement of the He-McKellar-Wilkens topological phase by atom interferometry and test of its independence with atom velocity", *Physical Review Letters*, vol. 111, no. 3, Jul. 2013 (cit. on pp. 30, 62).

[85] A. Miffre, "Expériences d'interférométrie atomique avec le lithium. mesure de précision de la polarisabilité électrique", PhD thesis, Université Paul Sabatier - Toulouse III, Jun. 23, 2005 (cit. on pp. 31, 45, 47).

[86] J. P. Toennies and K. Winkelmann, "Theoretical studies of highly expanded free jets: Influence of quantum effects and a realistic intermolecular potential", *The Journal of Chemical Physics*, vol. 66, no. 9, pp. 3965–3979, May 1, 1977 (cit. on p. 33).

[87] H. C. W. Beijerinck and N. F. Verster, "Absolute intensities and perpendicular temperatures of supersonic beams of polyatomic gases", *Physica B+C*, vol. 111, no. 2, pp. 327–352, Nov. 1, 1981 (cit. on p. 33).

[88] A. Miffre, M. Jacquey, M. Büchner, G. Trénec, and J. Vigué, "Parallel temperatures in supersonic beams: Ultracooling of light atoms seeded in a heavier carrier gas", *The Journal of Chemical Physics*, vol. 122, no. 9, p. 094 308, Mar. 1, 2005 (cit. on p. 33).

[89] M. Jacquey, A. Miffre, M. Büchner, G. Trénec, and J. Vigué, "Test of the isotopic and velocity selectivity of a lithium atom interferometer by magnetic dephasing", *EPL (Europhysics Letters)*, vol. 77, no. 2, p. 20 007, 2007 (cit. on pp. 33, 46).

[90] C. Cohen-Tannoudji, J. Dupont-Roc, G. Grynberg, and T. A. B. Kennedy, "Atom-photon interactions: Basic processes and applications", *American Journal of Physics*, vol. 61, no. 6, pp. 572–572, Jun. 1, 1993 (cit. on p. 34).

[91] A. Aspect, E. Arimondo, R. Kaiser, N. Vansteenkiste, and C. Cohen-Tannoudji, "Laser cooling below the one-photon recoil energy by velocity-selective coherent population trapping", *Physical Review Letters*, vol. 61, no. 7, pp. 826–829, Aug. 15, 1988 (cit. on p. 34).

[92] P. Meystre, E. Schumacher, and E. M. Wright, "Quantum pendellösung in atom diffraction by a light grating", *Annalen der Physik*, vol. 503, no. 1, pp. 141–148, Jan. 1, 1991 (cit. on p. 34).

[93] P. L. Kapitza and P. a. M. Dirac, "The reflection of electrons from standing light waves", *Mathematical Proceedings of the Cambridge Philosophical Society*, vol. 29, no. 2, pp. 297–300, May 1933 (cit. on p. 35).

[94] M. Büchner, R. Delhuille, A. Miffre, C. Robilliard, J. Vigué, and C. Champenois, "Diffraction phases in atom interferometers", *Physical Review A*, vol. 68, no. 1, p. 013 607, Jul. 16, 2003 (cit. on p. 35).

[95] C. Keller, J. Schmiedmayer, A. Zeilinger, T. Nonn, S. Durr, and G. Rempe, "Adiabatic following in standing-wave diffraction of atoms", *Applied Physics B-Lasers and Optics*, vol. 69, no. 4, pp. 303–309, Oct. 1999 (cit. on p. 35).

[96] F. Biraben and P. Labastie, “Balayage d’un laser a colorant continu monomode sur 150 GHz”, *Optics Communications*, vol. 41, no. 1, pp. 49–51, Mar. 1, 1982 (cit. on p. 39).

[97] T. W. Hansch and B. Couillaud, “Laser frequency stabilization by polarization spectroscopy of a reflecting reference cavity”, *Optics Communications*, vol. 35, no. 3, pp. 441–444, Dec. 1, 1980 (cit. on p. 40).

[98] S. Lepoutre, “Mesures de précision par interférométrie atomique. interaction de van der Waals et phase géométrique de He-McKellar-Wilkens”, PhD thesis, Université Paul Sabatier - Toulouse III, Oct. 21, 2011 (cit. on pp. 41, 127).

[99] I. Langmuir and K. H. Kingdon, “Thermionic effects caused by vapours of alkali metals”, *Proceedings of the Royal Society of London A: Mathematical, Physical and Engineering Sciences*, vol. 107, no. 741, pp. 61–79, Jan. 1, 1925 (cit. on p. 41).

[100] J. B. Taylor, “The reflection of beams of the alkali metals from crystals”, *Physical Review*, vol. 35, no. 4, pp. 375–380, Feb. 15, 1930 (cit. on p. 41).

[101] R. Delhuille, “Interférométrie atomique avec l’atome de lithium : Réalisation d’un interféromètre présentant un contraste et un flux élevés en vue de mesures de précision”, PhD thesis, Université Paul Sabatier - Toulouse III, Dec. 2002 (cit. on pp. 41, 74).

[102] R. Delhuille, A. Miffre, E. Lavallette, M. Büchner, C. Rizzo, G. Trénec, J. Vigué, H. J. Loesch, and J. P. Gauyacq, “Optimization of a Langmuir–Taylor detector for lithium”, *Review of Scientific Instruments*, vol. 73, no. 6, pp. 2249–2258, Jun. 1, 2002 (cit. on pp. 41, 42, 71).

[103] M. Jacquey, A. Miffre, G. Trénec, M. Büchner, J. Vigué, and A. Cronin, “Dispersion compensation in atom interferometry by a sagnac phase”, *Physical Review A*, vol. 78, no. 1, p. 013 638, Jul. 31, 2008 (cit. on p. 45).

[104] A. Miffre, M. Jacquey, M. Büchner, G. Trénec, and J. Vigué, “Vibration-induced phase noise in mach–zehnder atom interferometers”, *Applied Physics B*, vol. 84, no. 4, pp. 617–625, Jul. 27, 2006 (cit. on p. 47).

[105] J. Kerr, “Xl a new relation between electricity and light: Dielectrified media birefringent”, *Philosophical Magazine Series 4*, vol. 50, no. 332, pp. 337–348, Nov. 1, 1875 (cit. on p. 49).

[106] *The feynman lectures on physics*. Addison-Welsley, 1966 (cit. on p. 50).

[107] S. T. Cundiff and J. Ye, “Colloquium : Femtosecond optical frequency combs”, *Reviews of Modern Physics*, vol. 75, no. 1, pp. 325–342, Mar. 10, 2003 (cit. on p. 50).

[108] H. R. Carleton and W. T. Maloney, “A balanced optical heterodyne detector”, *Applied Optics*, vol. 7, no. 6, p. 1241, Jun. 1, 1968 (cit. on p. 50).

[109] H. P. Yuen and V. W. S. Chan, “Noise in homodyne and heterodyne detection”, *Optics Letters*, vol. 8, no. 3, p. 177, Mar. 1, 1983 (cit. on p. 50).

[110] G. C. Bjorklund, "Frequency-modulation spectroscopy: A new method for measuring weak absorptions and dispersions", *Optics Letters*, vol. 5, no. 1, p. 15, Jan. 1, 1980 (cit. on p. 50).

[111] W. A. Hamilton, A. G. Klein, G. I. Opat, and P. A. Timmins, "Neutron diffraction by surface acoustic waves", *Physical Review Letters*, vol. 58, no. 26, pp. 2770–2773, Jun. 29, 1987 (cit. on p. 53).

[112] J. Felber, R. Gähler, C. Rausch, and R. Golub, "Matter waves at a vibrating surface: Transition from quantum-mechanical to classical behavior", *Physical Review A*, vol. 53, no. 1, pp. 319–328, Jan. 1, 1996 (cit. on p. 53).

[113] P. Szriftgiser, D. Guéry-Odelin, M. Arndt, and J. Dalibard, "Atomic wave diffraction and interference using temporal slits", *Physical Review Letters*, vol. 77, no. 1, pp. 4–7, Jul. 1, 1996 (cit. on pp. 53, 54).

[114] S. Bernet, M. K. Oberthaler, R. Abfalterer, J. Schmiedmayer, and A. Zeilinger, "Coherent frequency shift of atomic matter waves", *Physical Review Letters*, vol. 77, no. 26, pp. 5160–5163, Dec. 23, 1996 (cit. on pp. 53, 54).

[115] J. Summhammer, K. A. Hamacher, H. Kaiser, H. Weinfurter, D. L. Jacobson, and S. A. Werner, "Multiphoton exchange amplitudes observed by neutron interferometry", *Physical Review Letters*, vol. 75, no. 18, pp. 3206–3209, Oct. 30, 1995 (cit. on p. 53).

[116] E. T. Smith, A.-A. Dhirani, D. A. Kokorowski, R. A. Rubenstein, T. D. Roberts, H. Yao, and D. E. Pritchard, "Velocity rephased longitudinal momentum coherences with differentially detuned separated oscillatory fields", *Physical Review Letters*, vol. 81, no. 10, pp. 1996–1999, Sep. 7, 1998 (cit. on p. 54).

[117] R. A. Rubenstein, A.-A. Dhirani, D. A. Kokorowski, T. D. Roberts, E. T. Smith, W. W. Smith, H. J. Bernstein, J. Lehner, S. Gupta, and D. E. Pritchard, "Search for off-diagonal density matrix elements for atoms in a supersonic beam", *Physical Review Letters*, vol. 82, no. 10, pp. 2018–2021, Mar. 8, 1999 (cit. on p. 54).

[118] P. Bouyer, S. A. Rangwala, J. H. Thywissen, Y. L. Coq, F. Gerbier, S. Richard, G. Delannoy, and A. Aspect, "Production of CW and mode-locked atom lasers", *Journal de Physique IV - Proceedings*, vol. 12, no. 5, p. 9, 2002 (cit. on p. 54).

[119] I. Bloch, T. W. Hänsch, and T. Esslinger, "Measurement of the spatial coherence of a trapped bose gas at the phase transition", *Nature*, vol. 403, no. 6766, pp. 166–170, Jan. 13, 2000 (cit. on p. 54).

[120] A. I. Frank, S. N. Balashov, I. V. Bondarenko, P. Geltenbort, P. Høghøj, S. V. Masalovich, and V. G. Nosov, "Phase modulation of a neutron wave and diffraction of ultracold neutrons on a moving grating", *Physics Letters A*, vol. 311, no. 1, pp. 6–12, May 5, 2003 (cit. on p. 54).

[121] C. Cohen-Tannoudji, B. Diu, and F. Laloë, *Mécanique quantique*, Hermann, Ed. 1973 (cit. on p. 56).

[122] P. Storey and C. Cohen-Tannoudji, “The feynman path integral approach to atomic interferometry. a tutorial”, *Journal de Physique II*, vol. 4, no. 11, pp. 1999–2027, Nov. 1994 (cit. on p. 56).

[123] *Handbook of mathematical functions*. Dover Publications, 1964 (cit. on p. 57).

[124] M. Jacquey, “Expériences d interférométrie atomique avec l’atome de lithium”, PhD thesis, Dec. 4, 2006 (cit. on p. 58).

[125] W. Li and L. E. Reichl, “Floquet scattering through a time-periodic potential”, *Physical Review B*, vol. 60, no. 23, pp. 15 732–15 741, Dec. 15, 1999 (cit. on p. 58).

[126] L. P. Eisenhart, “Enumeration of potentials for which one-particle Schroedinger equations are separable”, *Physical Review*, vol. 74, no. 1, pp. 87–89, Jul. 1, 1948 (cit. on p. 58).

[127] H. T. Koelink and R. F. Swarttouw, “A q-analogue of Graf’s addition formula for the Hahn-Exton q-bessel function”, *Journal of Approximation Theory*, vol. 81, no. 2, pp. 260–273, 1995 (cit. on p. 61).

[128] T. D. Roberts, A. D. Cronin, M. V. Tiberg, and D. E. Pritchard, “Dispersion compensation for atom interferometry”, *Physical Review Letters*, vol. 92, no. 6, p. 060 405, Feb. 12, 2004 (cit. on p. 62).

[129] W. F. Holmgren, I. Hromada, C. E. Klauss, and A. D. Cronin, “Atom beam velocity measurements using phase choppers”, *New Journal of Physics*, vol. 13, no. 11, p. 115 007, 2011 (cit. on p. 62).

[130] J. Gillot, “Expériences en interférométrie atomique: Application à la mesure des phases géométriques he-mckellar-wilkens et aharonov-casher”, PhD thesis, Université Paul Sabatier - Toulouse III, Nov. 5, 2013 (cit. on pp. 68, 127).

[131] C. A. Mead and D. G. Truhlar, “On the determination of Born–Oppenheimer nuclear motion wave functions including complications due to conical intersections and identical nuclei”, *The Journal of Chemical Physics*, vol. 70, no. 5, pp. 2284–2296, Mar. 1, 1979 (cit. on pp. 80, 81).

[132] C. Ning and H. Haken, “The geometric phase in nonlinear dissipative systems”, *Modern Physics Letters B*, vol. 06, no. 25, pp. 1541–1568, Oct. 30, 1992 (cit. on p. 80).

[133] N. A. Sinitsyn and I. Nemenman, “The Berry phase and the pump flux in stochastic chemical kinetics”, *EPL (Europhysics Letters)*, vol. 77, no. 5, p. 58 001, 2007 (cit. on p. 80).

[134] R. P. Feynman, “Space-time approach to non-relativistic quantum mechanics”, *Rev. Mod. Phys.*, vol. 20, no. 2, pp. 367–387, Apr. 1, 1948 (cit. on p. 81).

[135] J. W. Noh, A. Fougères, and L. Mandel, “Measurement of the quantum phase by photon counting”, *Physical Review Letters*, vol. 67, no. 11, pp. 1426–1429, Sep. 9, 1991 (cit. on p. 81).

[136] ——, “Operational approach to the phase of a quantum field”, *Physical Review A*, vol. 45, no. 1, pp. 424–442, Jan. 1, 1992 (cit. on p. 81).

[137] ——, "Further investigations of the operationally defined quantum phase", *Physical Review A*, vol. 46, no. 5, pp. 2840–2852, Sep. 1, 1992 (cit. on p. 81).

[138] N. Mukunda and R. Simon, "Quantum kinematic approach to the geometric phase. i. general formalism", *Annals of Physics*, vol. 228, no. 2, pp. 205–268, Dec. 1993 (cit. on p. 81).

[139] M. V. Berry, "Quantal phase factors accompanying adiabatic changes", *Proceedings of the Royal Society of London A: Mathematical, Physical and Engineering Sciences*, vol. 392, no. 1802, pp. 45–57, Mar. 8, 1984 (cit. on p. 81).

[140] S. Pancharatnam, "Partial polarisation, partial coherence and their spectral description for polychromatic light—part II", *Proceedings of the Indian Academy of Sciences - Section A*, vol. 57, no. 4, pp. 231–243, Apr. 1963 (cit. on p. 81).

[141] W. Ehrenberg and R. E. Siday, "The refractive index in electron optics and the principles of dynamics", *Proceedings of the Physical Society. Section B*, vol. 62, no. 1, p. 8, 1949 (cit. on p. 82).

[142] Y. Aharonov and D. Bohm, "Significance of electromagnetic potentials in the quantum theory", *Physical Review*, vol. 115, no. 3, pp. 485–491, Aug. 1, 1959 (cit. on p. 82).

[143] S. Pancharatnam, "Partial polarisation, partial coherence and their spectral description for polychromatic light—part I", *Proceedings of the Indian Academy of Sciences - Section A*, vol. 57, no. 4, pp. 218–230, Apr. 1963 (cit. on p. 84).

[144] M. V. Berry, "The adiabatic phase and Pancharatnam's phase for polarized light", *Journal of Modern Optics*, vol. 34, no. 11, pp. 1401–1407, Nov. 1, 1987 (cit. on p. 84).

[145] J. Lages, R. Giust, and J.-M. Vigoureux, "Geometric phase and Pancharatnam phase induced by light wave polarization", *Physica E: Low-dimensional Systems and Nanostructures*, vol. 59, pp. 6–14, 2014 (cit. on p. 84).

[146] H. G. Jerrard, "Transmission of light through birefringent and optically active media: The Poincaré sphere", *Journal of the Optical Society of America*, vol. 44, no. 8, p. 634, Aug. 1, 1954 (cit. on p. 84).

[147] H. Cartan and J. Kouneiher, *Cours de calcul différentiel*. Paris: Editions Hermann, 2007, 355 pp. (cit. on p. 84).

[148] R. Y. Chiao and Y.-S. Wu, "Manifestations of Berry's topological phase for the photon", *Physical Review Letters*, vol. 57, no. 8, pp. 933–936, Aug. 25, 1986 (cit. on p. 85).

[149] A. Tomita and R. Y. Chiao, "Observation of Berry's topological phase by use of an optical fiber", *Physical Review Letters*, vol. 57, no. 8, pp. 937–940, Aug. 25, 1986 (cit. on pp. 85, 86).

[150] R. Y. Chiao, A. Antaramian, K. M. Ganga, H. Jiao, S. R. Wilkinson, and H. Nathel, "Observation of a topological phase by means of a nonplanar Mach-Zehnder interferometer", *Physical Review Letters*, vol. 60, no. 13, pp. 1214–1217, Mar. 28, 1988 (cit. on p. 85).

[151] R. Bhandari, “Observation of non-integrable geometric phase on the Poincaré sphere”, *Physics Letters A*, vol. 133, no. 1, pp. 1–3, Oct. 31, 1988 (cit. on p. 85).

[152] T. H. Chyba, L. J. Wang, L. Mandel, and R. Simon, “Measurement of the Pancharatnam phase for a light beam”, *Optics Letters*, vol. 13, no. 7, p. 562, Jul. 1, 1988 (cit. on pp. 85, 86, 88).

[153] R. Simon, H. J. Kimble, and E. C. G. Sudarshan, “Evolving geometric phase and its dynamical manifestation as a frequency shift: An optical experiment”, *Physical Review Letters*, vol. 61, no. 1, pp. 19–22, Jul. 4, 1988 (cit. on p. 86).

[154] P. G. Kwiat and R. Y. Chiao, “Observation of a nonclassical Berry’s phase for the photon”, *Physical Review Letters*, vol. 66, no. 5, pp. 588–591, Feb. 4, 1991 (cit. on pp. 86, 87).

[155] P. Hariharan, M. Roy, P. A. Robinson, and J. W. O’Byrne, “The geometric phase”, *Journal of Modern Optics*, vol. 40, no. 5, pp. 871–877, May 1, 1993 (cit. on p. 86).

[156] H. Schmitzer, S. Klein, and W. Dultz, “Nonlinearity of Pancharatnam’s topological phase”, *Physical Review Letters*, vol. 71, no. 10, pp. 1530–1533, Sep. 6, 1993 (cit. on p. 87).

[157] Q. Li, L. Gong, Y. Gao, and Y. Chen, “Experimental observation of the nonlinearity of the Pancharatnam phase with a Michelson interferometer”, *Optics Communications*, vol. 169, no. 1, pp. 17–22, Oct. 1, 1999 (cit. on p. 87).

[158] M. V. Berry and S. Klein, “Geometric phases from stacks of crystal plates”, *Journal of Modern Optics*, vol. 43, no. 1, pp. 165–180, Jan. 1, 1996 (cit. on p. 87).

[159] T. D. Visser, T. van Dijk, H. F. Schouten, and W. Ubachs, “The Pancharatnam-Berry phase for non-cyclic polarization changes”, *Optics Express*, vol. 18, no. 10, p. 10 796, May 10, 2010 (cit. on p. 87).

[160] P. Hariharan, K. G. Larkin, and M. Roy, “The geometric phase: Interferometric observations with white light”, *Journal of Modern Optics*, vol. 41, no. 4, pp. 663–667, Apr. 1, 1994 (cit. on p. 87).

[161] P. Hariharan and P. E. Ciddor, “An achromatic phase-shifter operating on the geometric phase”, *Optics Communications*, vol. 110, no. 1, pp. 13–17, Aug. 1, 1994 (cit. on p. 87).

[162] P.-E. Dupouy, M. Büchner, P. Paquier, G. Trénec, and J. Vigué, “Interferometric measurement of the temperature dependence of an index of refraction: Application to fused silica”, *Applied Optics*, vol. 49, no. 4, p. 678, Feb. 1, 2010 (cit. on p. 91).

[163] G. Ghosh, “Dispersion-equation coefficients for the refractive index and birefringence of calcite and quartz crystals”, *Optics Communications*, vol. 163, no. 1, pp. 95–102, 1999 (cit. on p. 92).

[164] N. Vansteenkiste, “Réalisation d’un laser LNA monomode et asservi sur la transition 23s1-23p de l’hélium 4 (1083nm): Utilisation pour quelques expériences de refroidissement radiatif d’atomes d’hélium 4 métastable”, PhD thesis, Université Paris Sud - Paris XI, Oct. 3, 1989 (cit. on p. 93).

[165] S. Nakadate, “High precision retardation measurement using phase detection of Young’s fringes”, *Applied Optics*, vol. 29, no. 2, p. 242, Jan. 10, 1990 (cit. on p. 101).

[166] W. Liu, M. Liu, and S. Zhang, “Method for the measurement of phase retardation of any wave plate with high precision”, *Applied Optics*, vol. 47, no. 30, p. 5562, Oct. 20, 2008 (cit. on p. 101).

[167] J. M. Beckers, “Achromatic linear retarders”, *Applied Optics*, vol. 10, no. 4, p. 973, Apr. 1, 1971 (cit. on p. 102).

[168] J. M. Herrera-Fernandez, J. L. Vilas, L. M. Sanchez-Brea, and E. Bernabeu, “Design of superachromatic quarter-wave retarders in a broad spectral range”, *Applied Optics*, vol. 54, no. 33, p. 9758, Nov. 20, 2015 (cit. on p. 102).

[169] H. Kikuta, Y. Ohira, and K. Iwata, “Achromatic quarter-wave plates using the dispersion of form birefringence”, *Applied Optics*, vol. 36, no. 7, p. 1566, Mar. 1, 1997 (cit. on p. 102).

[170] K. Kinnstaetter, A. W. Lohmann, J. Schwider, and N. Streibl, “Accuracy of phase shifting interferometry”, *Applied Optics*, vol. 27, no. 24, p. 5082, Dec. 15, 1988 (cit. on p. 103).

[171] M. Traini, “Electric polarizability of the hydrogen atom: Classical variational approaches” (cit. on p. 106).

[172] J. Mitroy, M. S. Safronova, and C. W. Clark, “Theory and applications of atomic and ionic polarizabilities”, *Journal of Physics B: Atomic, Molecular and Optical Physics*, vol. 43, no. 20, p. 202 001, Oct. 28, 2010. arXiv: `1004.3567` (cit. on pp. 106, 111).

[173] F. L. Kien, P. Schneeweiss, and A. Rauschenbeutel, “Dynamical polarizability of atoms in arbitrary light fields: General theory and application to cesium”, *The European Physical Journal D*, vol. 67, no. 5, pp. 1–16, May 1, 2013 (cit. on p. 107).

[174] A. D. Ludlow, M. M. Boyd, J. Ye, E. Peik, and P. O. Schmidt, “Optical atomic clocks”, *Reviews of Modern Physics*, vol. 87, no. 2, pp. 637–701, Jun. 26, 2015 (cit. on p. 108).

[175] M. D. Gregoire, N. Brooks, R. Trubko, and A. D. Cronin, “Analysis of polarizability measurements made with atom interferometry”, *Atoms*, vol. 4, no. 3, p. 21, Jul. 6, 2016 (cit. on pp. 109, 111, 134).

[176] B. Arora, M. S. Safronova, and C. W. Clark, “Magic wavelengths for the np-ns transitions in alkali-metal atoms”, *Physical Review A*, vol. 76, no. 5, p. 052 509, Nov. 15, 2007 (cit. on p. 111).

[177] M. S. Safronova, U. I. Safronova, and C. W. Clark, “Magic wavelengths for optical cooling and trapping of lithium”, *Physical Review A*, vol. 86, no. 4, p. 042 505, Oct. 10, 2012 (cit. on pp. 111, 114).

[178] C. J. Sansonetti, C. E. Simien, J. D. Gillaspy, J. N. Tan, S. M. Brewer, R. C. Brown, S. Wu, and J. V. Porto, “Absolute transition frequencies and quantum interference in a frequency comb based measurement of the ^{6,7}Li D lines”, *Physical Review Letters*, vol. 107, no. 2, p. 023 001, Jul. 6, 2011 (cit. on p. 111).

[179] W. L. Wiese and J. R. Fuhr, “Accurate atomic transition probabilities for hydrogen, helium, and lithium”, *Journal of Physical and Chemical Reference Data*, vol. 38, no. 3, pp. 565–720, Sep. 1, 2009 (cit. on p. 111).

[180] W. I. McAlexander, E. R. I. Abraham, and R. G. Hulet, “Radiative lifetime of the ^{2}P state of lithium”, *Physical Review A*, vol. 54, no. 1, R5–R8, Jul. 1, 1996 (cit. on p. 111).

[181] A. Fallon and C. Sackett, “Obtaining atomic matrix elements from vector tune-out wavelengths using atom interferometry”, *Atoms*, vol. 4, no. 2, p. 12, Mar. 30, 2016 (cit. on p. 115).

[182] N. Bouloufa, A. Crubellier, and O. Dulieu, “Photoassociative molecular spectroscopy for atomic radiative lifetimes”, *Physica Scripta*, vol. 2009, p. 014 014, T134 2009 (cit. on p. 115).

[183] C. D. Herold, V. D. Vaidya, X. Li, S. L. Rolston, J. V. Porto, and M. S. Safronova, “Precision measurement of transition matrix elements via light shift cancellation”, *Physical Review Letters*, vol. 109, no. 24, p. 243 003, Dec. 14, 2012 (cit. on p. 115).

[184] W. F. Holmgren, R. Trubko, I. Hromada, and A. D. Cronin, “Measurement of a wavelength of light for which the energy shift for an atom vanishes”, *Physical Review Letters*, vol. 109, no. 24, p. 243 004, Dec. 14, 2012 (cit. on pp. 115, 134).

[185] R. H. Leonard, A. J. Fallon, C. A. Sackett, and M. S. Safronova, “High-precision measurements of the ^{87}Rb D-line tune-out wavelength”, *Physical Review A*, vol. 92, no. 5, p. 052 501, Nov. 2, 2015 (cit. on pp. 115, 134).

[186] J. Mitroy and L.-Y. Tang, “Tune-out wavelengths for metastable helium”, *Physical Review A*, vol. 88, no. 5, p. 052 515, Nov. 20, 2013 (cit. on p. 115).

[187] B. M. Henson, R. I. Khakimov, R. G. Dall, K. G. H. Baldwin, L.-Y. Tang, and A. G. Truscott, “Precision measurement for metastable helium atoms of the 413 nm tune-out wavelength at which the atomic polarizability vanishes”, *Physical Review Letters*, vol. 115, no. 4, p. 043 004, Jul. 24, 2015 (cit. on p. 115).

[188] R. Chamakhi, H. Ahlers, M. Telmini, C. Schubert, E. M. Rasel, and N. Gaaloul, “Species-selective lattice launch for precision atom interferometry”, *New Journal of Physics*, vol. 17, no. 12, p. 123 002, 2015 (cit. on p. 116).

[189] M. Saffman and T. G. Walker, “Analysis of a quantum logic device based on dipole-dipole interactions of optically trapped rydberg atoms”, *Physical Review A*, vol. 72, no. 2, p. 022 347, Aug. 31, 2005 (cit. on p. 116).

[190] H. Katori, M. Takamoto, V. G. Pal'chikov, and V. D. Ovsiannikov, "Ultrastable optical clock with neutral atoms in an engineered light shift trap", *Physical Review Letters*, vol. 91, no. 17, p. 173 005, Oct. 24, 2003 (cit. on p. 116).

[191] M. Takamoto, F.-L. Hong, R. Higashi, and H. Katori, "An optical lattice clock", *Nature*, vol. 435, no. 7040, pp. 321–324, May 19, 2005 (cit. on p. 116).

[192] R. Le Targat, X. Baillard, M. Fouché, A. Brusch, O. Tcherbakoff, G. D. Rovera, and P. Lemonde, "Accurate optical lattice clock with ^{87}Sr atoms", *Physical Review Letters*, vol. 97, no. 13, p. 130 801, Sep. 26, 2006 (cit. on p. 116).

[193] P.-L. Liu, Y. Huang, W. Bian, H. Shao, H. Guan, Y.-B. Tang, C.-B. Li, J. Mitroy, and K.-L. Gao, "Measurement of magic wavelengths for the ^{40}Ca^{+} clock transition", *Physical Review Letters*, vol. 114, no. 22, p. 223 001, Jun. 2, 2015 (cit. on p. 116).

[194] L. Li, Y. O. Dudin, and A. Kuzmich, "Entanglement between light and an optical atomic excitation", *Nature*, vol. 498, no. 7455, pp. 466–469, Jun. 27, 2013 (cit. on p. 116).

[195] J. Gillot, A. Gauguet, M. Büchner, and J. Vigué, "Optical pumping of a lithium atomic beam for atom interferometry", *The European Physical Journal D*, vol. 67, no. 12, pp. 1–11, Dec. 12, 2013 (cit. on p. 121).

[196] J. Pipin and D. M. Bishop, "Accurate variational calculations of energies of the $2\ ^2S$, $2\ ^2P$ and $3\ ^2D$ states and the dipole, quadrupole, and dipole-quadrupole polarizabilities and hyperpolarizability of the lithium atom", *Physical Review A*, vol. 45, no. 5, pp. 2736–2743, Mar. 1, 1992 (cit. on pp. 129, 130).

[197] Z.-C. Yan, M. Tambasco, and G. W. F. Drake, "Energies and oscillator strengths for lithiumlike ions", *Physical Review A*, vol. 57, no. 3, pp. 1652–1661, Mar. 1, 1998 (cit. on p. 133).

[198] U. Volz and H. Schmoranzer, "Precision lifetime measurements on alkali atoms and on helium by beam–gas–laser spectroscopy", *Physica Scripta*, vol. 1996, p. 48, T65 1996 (cit. on p. 134).

[199] R. J. Rafac and C. E. Tanner, "Measurement of the ratio of the cesium D-line transition strengths", *Physical Review A*, vol. 58, no. 2, pp. 1087–1097, Aug. 1, 1998 (cit. on p. 134).

[200] J. E. Simsarian, L. A. Orozco, G. D. Sprouse, and W. Z. Zhao, "Lifetime measurements of the 7P levels of atomic francium", *Physical Review A*, vol. 57, no. 4, pp. 2448–2458, Apr. 1, 1998 (cit. on p. 134).

[201] T. Pfau, C. Kurtsiefer, C. S. Adams, M. Sigel, and J. Mlynek, "Magneto-optical beam splitter for atoms", *Physical Review Letters*, vol. 71, no. 21, pp. 3427–3430, Nov. 22, 1993 (cit. on p. 140).

[202] H. Müntinga, H. Ahlers, M. Krutzik, *et al.*, "Interferometry with Bose-Einstein condensates in microgravity", *Physical Review Letters*, vol. 110, no. 9, p. 093 602, Feb. 25, 2013 (cit. on pp. 140, 142).

[203] R. Bouchendira, P. Cladé, S. Guellati-Khélifa, F. Nez, and F. Biraben, "New determination of the fine structure constant and test of the quantum electrodynamics", *Physical Review Letters*, vol. 106, no. 8, p. 080 801, Feb. 24, 2011 (cit. on pp. 140–143).

[204] H. Müller, S.-w. Chiow, Q. Long, S. Herrmann, and S. Chu, "Atom interferometry with up to 24-photon-momentum-transfer beam splitters", *Physical Review Letters*, vol. 100, no. 18, p. 180 405, May 8, 2008 (cit. on pp. 141, 194, 195).

[205] S.-Y. Lan, P.-C. Kuan, B. Estey, P. Haslinger, and H. Müller, "Influence of the Coriolis force in atom interferometry", *Physical Review Letters*, vol. 108, no. 9, p. 090 402, Feb. 27, 2012 (cit. on p. 141).

[206] G. D. McDonald, C. C. N. Kuhn, S. Bennetts, J. E. Debs, K. S. Hardman, M. Johnsson, J. D. Close, and N. P. Robins, "$80\hbar k$ momentum separation with Bloch oscillations in an optically guided atom interferometer", *Physical Review A*, vol. 88, no. 5, p. 053 620, Nov. 18, 2013 (cit. on pp. 141, 194).

[207] F. Sorrentino, Y.-H. Lien, G. Rosi, L. Cacciapuoti, M. Prevedelli, and G. M. Tino, "Sensitive gravity-gradiometry with atom interferometry: Progress towards an improved determination of the gravitational constant", *New Journal of Physics*, vol. 12, no. 9, p. 095 009, 2010 (cit. on p. 141).

[208] A. Sugarbaker, "Atom interferometry in a 10 m fountain", PhD thesis, Stanford University, 2014 (cit. on p. 141).

[209] T. Kovachy, P. Asenbaum, C. Overstreet, C. A. Donnelly, S. M. Dickerson, A. Sugarbaker, J. M. Hogan, and M. A. Kasevich, "Quantum superposition at the half-metre scale", *Nature*, vol. 528, no. 7583, pp. 530–533, Dec. 24, 2015 (cit. on p. 141).

[210] K.-Y. Chung, S.-w. Chiow, S. Herrmann, S. Chu, and H. Müller, "Atom interferometry tests of local lorentz invariance in gravity and electrodynamics", *Physical Review D*, vol. 80, no. 1, p. 016 002, Jul. 6, 2009 (cit. on p. 141).

[211] A. O. Jamison, J. N. Kutz, and S. Gupta, "Atomic interactions in precision interferometry using Bose-Einstein condensates", *Physical Review A*, vol. 84, no. 4, p. 043 643, Oct. 28, 2011 (cit. on p. 141).

[212] J. Grond, U. Hohenester, J. Schmiedmayer, and A. Smerzi, "Mach-Zehnder interferometry with interacting trapped Bose-Einstein condensates", *Physical Review A*, vol. 84, no. 2, p. 023 619, Aug. 16, 2011 (cit. on p. 141).

[213] S. S. Szigeti, J. E. Debs, J. J. Hope, N. P. Robins, and J. D. Close, "Why momentum width matters for atom interferometry with Bragg pulses", *New Journal of Physics*, vol. 14, no. 2, p. 023 009, Feb. 3, 2012 (cit. on pp. 141, 194).

[214] K. S. Hardman, C. C. N. Kuhn, G. D. McDonald, J. E. Debs, S. Bennetts, J. D. Close, and N. P. Robins, "Role of source coherence in atom interferometry", *Physical Review A*, vol. 89, no. 2, p. 023 626, 2014 (cit. on p. 141).

[215] S. M. Dickerson, J. M. Hogan, A. Sugarbaker, D. M. S. Johnson, and M. A. Kasevich, “Multiaxis inertial sensing with long-time point source atom interferometry”, *Physical Review Letters*, vol. 111, no. 8, p. 083 001, Aug. 19, 2013 (cit. on p. 141).

[216] T. van Zoest, N. Gaaloul, Y. Singh, *et al.*, “Bose-Einstein condensation in microgravity”, *Science*, vol. 328, no. 5985, pp. 1540–1543, Jun. 18, 2010 (cit. on p. 142).

[217] A. E. Leanhardt, T. A. Pasquini, M. Saba, A. Schirotzek, Y. Shin, D. Kielpinski, D. E. Pritchard, and W. Ketterle, “Cooling Bose-Einstein condensates below 500 picokelvin”, *Science*, vol. 301, no. 5639, pp. 1513–1515, Sep. 12, 2003 (cit. on p. 142).

[218] S. Chu, J. E. Bjorkholm, A. Ashkin, J. P. Gordon, and L. W. Hollberg, “Proposal for optically cooling atoms to temperatures of the order of 10^{-6} K”, *Optics Letters*, vol. 11, no. 2, p. 73, Feb. 1, 1986 (cit. on p. 142).

[219] L. Wang, P. Zhang, X.-Z. Chen, and Z.-Y. Ma, “Generating a picokelvin ultracold atomic ensemble in microgravity”, *Journal of Physics B: Atomic, Molecular and Optical Physics*, vol. 46, no. 19, p. 195 302, Oct. 14, 2013 (cit. on p. 142).

[220] D. M. Farkas, E. A. Salim, and J. Ramirez-Serrano, “Production of rubidium Bose-Einstein condensates at a 1 hz rate”, *ARXIV:1403.4641 [cond-mat, physics:physics]*, Mar. 18, 2014 (cit. on pp. 142, 179).

[221] S. Kohler and F. Sols, “Phase-resolution limit in the macroscopic interference between Bose-Einstein condensates”, *Physical Review A*, vol. 63, no. 5, p. 053 605, Apr. 17, 2001 (cit. on p. 142).

[222] M. Horikoshi and K. Nakagawa, “Dephasing due to atom-atom interaction in a waveguide interferometer using a Bose-Einstein condensate”, *Physical Review A*, vol. 74, no. 3, p. 031 602, Sep. 13, 2006 (cit. on p. 142).

[223] Y. Castin and R. Dum, “Bose-Einstein condensates in time dependent traps”, *Physical Review Letters*, vol. 77, no. 27, pp. 5315–5319, Dec. 30, 1996 (cit. on p. 142).

[224] R. Jannin, P. Cladé, and S. Guellati-Khélifa, “Phase shift due to atom-atom interactions in a light-pulse atom interferometer”, *Physical Review A*, vol. 92, no. 1, p. 013 616, Jul. 13, 2015 (cit. on p. 142).

[225] M. J. Snadden, J. M. McGuirk, P. Bouyer, K. G. Haritos, and M. A. Kasevich, “Measurement of the earth’s gravity gradient with an atom interferometer-based gravity gradiometer”, *Physical Review Letters*, vol. 81, no. 5, pp. 971–974, Aug. 3, 1998 (cit. on pp. 143, 151).

[226] G. D’Amico, F. Borselli, L. Cacciapuoti, M. Prevedelli, G. Rosi, F. Sorrentino, and G. M. Tino, “Bragg interferometer for gravity gradient measurements”, *Physical Review A*, vol. 93, no. 6, p. 063 628, Jun. 22, 2016 (cit. on p. 143).

[227] G. Tackmann, P. Berg, S. Abend, C. Schubert, W. Ertmer, and E. M. Rasel, “Large-area Sagnac atom interferometer with robust phase read out”, *Comptes Rendus Physique*, The Sagnac effect: 100 years later / L’effet Sagnac : 100 ans après, vol. 15, no. 10, pp. 884–897, Dec. 2014 (cit. on p. 143).

[228] J. B. Fixler, G. T. Foster, J. M. McGuirk, and M. A. Kasevich, “Atom interferometer measurement of the Newtonian constant of gravity”, *Science*, vol. 315, no. 5808, pp. 74–77, Jan. 5, 2007 (cit. on p. 143).

[229] H. Müller, S.-W. Chiow, Q. Long, C. Vo, and S. Chu, “A new photon recoil experiment: Towards a determination of the fine structure constant”, *Applied Physics B*, vol. 84, no. 4, pp. 633–642, Jul. 25, 2006 (cit. on p. 143).

[230] S. Dimopoulos, P. W. Graham, J. M. Hogan, M. A. Kasevich, and S. Rajendran, “Atomic gravitational wave interferometric sensor”, *Physical Review D*, vol. 78, no. 12, p. 122 002, Dec. 19, 2008 (cit. on p. 143).

[231] R. Kaltenbaek, M. Aspelmeyer, P. F. Barker, *et al.*, “Macroscopic quantum resonators (MAQRO): 2015 update”, *EPJ Quantum Technology*, vol. 3, no. 1, p. 5, Mar. 24, 2016 (cit. on p. 143).

[232] P. Wolf, P. Lemonde, A. Lambrecht, S. Bize, A. Landragin, and A. Clairon, “From optical lattice clocks to the measurement of forces in the casimir regime”, *Physical Review A*, vol. 75, no. 6, p. 063 608, Jun. 8, 2007 (cit. on p. 143).

[233] B. Young, M. Kasevich, and S. Chu, “Precision atom interferometry with light pulses”, in *Atom Interferometry*, P. R. Berman, Ed., San Diego: Academic Press, 1997, pp. 363–406 (cit. on p. 143).

[234] C. Champenois, M. Büchner, R. Delhuille, R. Mathevet, C. Robilliard, C. Rizzo, and J. Vigué, “Matter neutrality test using a Mach-Zehnder interferometer”, Lecture Notes in Physics, no. 570, D. S. G. Karshenboim, P. F. Bassani, P. F. S. Pavone, P. M. Inguscio, and P. T. W. Hänsch, Eds., pp. 554–563, Jan. 1, 2001 (cit. on p. 143).

[235] A. Arvanitaki, S. Dimopoulos, A. A. Geraci, J. Hogan, and M. Kasevich, “How to test atom and neutron neutrality with atom interferometry”, *Physical Review Letters*, vol. 100, no. 12, p. 120 407, Mar. 27, 2008 (cit. on pp. 143, 144).

[236] R. Foot, G. C. Joshi, H. Lew, and R. R. Volkas, “Charge quantization in the standard model and some of its extensions”, *Modern Physics Letters A*, vol. 05, no. 32, pp. 2721–2731, Dec. 30, 1990 (cit. on p. 143).

[237] C. S. Unnikrishnan and G. T. Gillies, “The electrical neutrality of atoms and of bulk matter”, *Metrologia*, vol. 41, no. 5, S125, Oct. 1, 2004 (cit. on p. 144).

[238] J. G. King, “Search for a small charge carried by molecules”, *Physical Review Letters*, vol. 5, no. 12, pp. 562–565, Dec. 15, 1960 (cit. on p. 144).

[239] A. M. Hillas and T. E. Cranshaw, “A comparison of the charges of the electron, proton and neutron”, *Nature*, vol. 184, no. 4690, pp. 892–893, Sep. 19, 1959 (cit. on pp. 144, 145).

[240] M. Marinelli and G. Morpurgo, "The electric neutrality of matter: A summary", *Physics Letters B*, vol. 137, no. 5, pp. 439–442, Apr. 5, 1984 (cit. on pp. 144, 145).

[241] H. F. Dylla and J. G. King, "Neutrality of molecules by a new method", *Physical Review A*, vol. 7, no. 4, pp. 1224–1229, Apr. 1, 1973 (cit. on pp. 144, 145).

[242] J. Baumann, R. Gähler, J. Kalus, and W. Mampe, "Experimental limit for the charge of the free neutron", *Physical Review D*, vol. 37, no. 11, pp. 3107–3112, Jun. 1, 1988 (cit. on pp. 144, 145).

[243] J. Reichel and V. Vuletic, Eds., *Atom chips*, 1 edition, Weinheim, Germany: Wiley-VCH, Mar. 14, 2011, 445 pp. (cit. on pp. 149, 157).

[244] P. A. Ruprecht, M. J. Holland, K. Burnett, and M. Edwards, "Time-dependent solution of the nonlinear schrödinger equation for Bose-condensed trapped neutral atoms", *Physical Review A*, vol. 51, no. 6, pp. 4704–4711, Jun. 1, 1995 (cit. on p. 149).

[245] R. V. Latham, *High voltage vacuum insulation: Basic concepts and technological practice*. London; San Diego: Academic Press, 1995, 568 pp. (cit. on p. 150).

[246] P. Cheinet, B. Canuel, F. P. D. Santos, A. Gauguet, F. Yver-Leduc, and A. Landragin, "Measurement of the sensitivity function in a time-domain atomic interferometer", *IEEE Transactions on Instrumentation and Measurement*, vol. 57, no. 6, pp. 1141–1148, Jun. 2008 (cit. on p. 150).

[247] J. L. Gouët, "Étude des performances d'un gravimètre atomique absolu : Sensibilité limite et exactitude préliminaire", PhD thesis, Université Paris Sud - Paris XI, Feb. 7, 2008 (cit. on p. 150).

[248] S.-w. Chiow, S. Herrmann, S. Chu, and H. Müller, "Noise-immune conjugate large-area atom interferometers", *Physical Review Letters*, vol. 103, no. 5, p. 050 402, Jul. 28, 2009 (cit. on p. 151).

[249] F. Sorrentino, A. Bertoldi, Q. Bodart, L. Cacciapuoti, M. d. Angelis, Y.-H. Lien, M. Prevedelli, G. Rosi, and G. M. Tino, "Simultaneous measurement of gravity acceleration and gravity gradient with an atom interferometer", *Applied Physics Letters*, vol. 101, no. 11, p. 114 106, Sep. 10, 2012 (cit. on p. 151).

[250] F. P. Dos Santos, "Differential phase extraction in an atom gradiometer", *Physical Review A*, vol. 91, no. 6, p. 063 615, 2015 (cit. on p. 151).

[251] H. Ammann and N. Christensen, "Delta kick cooling: A new method for cooling atoms", *Physical Review Letters*, vol. 78, no. 11, pp. 2088–2091, Mar. 17, 1997 (cit. on p. 153).

[252] J. Reichel, W. Hänsel, and T. W. Hänsch, "Atomic micromanipulation with magnetic surface traps", *Physical Review Letters*, vol. 83, no. 17, pp. 3398–3401, Oct. 25, 1999 (cit. on pp. 154, 156).

[253] T. Bergeman, G. Erez, and H. J. Metcalf, "Magnetostatic trapping fields for neutral atoms", *Physical Review A*, vol. 35, no. 4, pp. 1535–1546, Feb. 15, 1987 (cit. on pp. 154, 157).

[254] I. Bloch, M. Greiner, O. Mandel, T. W. Hänsch, and T. Esslinger, "Sympathetic cooling of 85Rb and 87Rb", *Physical Review A*, vol. 64, no. 2, p. 021 402, Jul. 10, 2001 (cit. on pp. 154, 171, 173).

[255] J. F. Barry, D. J. McCarron, E. B. Norrgard, M. H. Steinecker, and D. DeMille, "Magneto-optical trapping of a diatomic molecule", *Nature*, vol. 512, no. 7514, pp. 286–289, Aug. 21, 2014 (cit. on p. 154).

[256] H. J. Metcalf, *Laser cooling and trapping*, in collab. with P. Van der Straten, ser. Graduate texts in contemporary physics. New York: Springer, 1999, 323 pp. (cit. on p. 154).

[257] P. Meystre, *Atom optics*, 2001 edition. New York: Springer, Sep. 21, 2001, 312 pp. (cit. on p. 154).

[258] R. Williamson, P. Voytas, R. Newell, and T. Walker, "A magneto-optical trap loaded from a pyramidal funnel", *Optics Express*, vol. 3, no. 3, p. 111, Aug. 3, 1998 (cit. on p. 156).

[259] S. Wildermuth, P. Krüger, C. Becker, M. Brajdic, S. Haupt, A. Kasper, R. Folman, and J. Schmiedmayer, "Optimized magneto-optical trap for experiments with ultracold atoms near surfaces", *Physical Review A*, vol. 69, no. 3, p. 030 901, Mar. 17, 2004 (cit. on p. 156).

[260] S. Du, M. B. Squires, Y. Imai, L. Czaia, R. A. Saravanan, V. Bright, J. Reichel, T. W. Hänsch, and D. Z. Anderson, "Atom-chip Bose-Einstein condensation in a portable vacuum cell", *Physical Review A*, vol. 70, no. 5, p. 053 606, Nov. 10, 2004 (cit. on p. 156).

[261] O. Cherry, J. D. Carter, and J. D. Martin, "An atom chip for the manipulation of ultracold atoms", *Canadian Journal of Physics*, vol. 87, no. 6, pp. 633–638, Jun. 1, 2009 (cit. on p. 156).

[262] C. J. Myatt, N. R. Newbury, R. W. Ghrist, S. Loutzenhiser, and C. E. Wieman, "Multiply loaded magneto-optical trap", *Optics Letters*, vol. 21, no. 4, pp. 290–292, Feb. 15, 1996 (cit. on p. 158).

[263] D. E. Pritchard, "Cooling neutral atoms in a magnetic trap for precision spectroscopy", *Physical Review Letters*, vol. 51, no. 15, pp. 1336–1339, Oct. 10, 1983 (cit. on p. 158).

[264] G. Condon, "Bose-Einstein condensation: From finite size periodic potentials to phase space manipulations", PhD thesis, Université Paul Sabatier, Oct. 21, 2015 (cit. on p. 159).

[265] K. B. Davis, M. O. Mewes, M. R. Andrews, N. J. van Druten, D. S. Durfee, D. M. Kurn, and W. Ketterle, "Bose-Einstein condensation in a gas of sodium atoms", *Physical Review Letters*, vol. 75, no. 22, pp. 3969–3973, Nov. 27, 1995 (cit. on p. 159).

[266] J. Stuhler, P. O. Schmidt, S. Hensler, J. Werner, J. Mlynek, and T. Pfau, "Continuous loading of a magnetic trap", *Physical Review A*, vol. 64, no. 3, p. 031 405, Aug. 20, 2001 (cit. on p. 160).

[267] D. W. Sesko, T. G. Walker, and C. E. Wieman, “Behavior of neutral atoms in a spontaneous force trap”, *Journal of the Optical Society of America B*, vol. 8, no. 5, p. 946, May 1, 1991 (cit. on p. 160).

[268] W. Petrich, M. H. Anderson, J. R. Ensher, and E. A. Cornell, “Behavior of atoms in a compressed magneto-optical trap”, *Journal of the Optical Society of America B*, vol. 11, no. 8, p. 1332, Aug. 1, 1994 (cit. on p. 160).

[269] R. A. Duine and H. T. C. Stoof, “Atom–molecule coherence in Bose gases”, *Physics Reports*, vol. 396, no. 3, pp. 115–195, Jun. 2004 (cit. on p. 163).

[270] J. Walvaren, “Quantum gases - statistics and interactions”, Les Houches Predoc School lecture notes (cit. on p. 163).

[271] A. L. Marchant, S. Händel, S. A. Hopkins, T. P. Wiles, and S. L. Cornish, “Bose-Einstein condensation of 85Rb by direct evaporation in an optical dipole trap”, *Physical Review A*, vol. 85, no. 5, p. 053 647, 2012 (cit. on pp. 163, 164).

[272] H. F. Hess, “Evaporative cooling of magnetically trapped and compressed spin-polarized hydrogen”, *Physical Review B*, vol. 34, no. 5, pp. 3476–3479, Sep. 1, 1986 (cit. on p. 166).

[273] C. C. Tannoudij. (1996). Cours claude cohen-tannoudji 1996-1997, [Online]. Available: `http://www.phys.ens.fr/~cct/college-de-france/1996-97/1996-97.htm` (visited on 06/05/2016) (cit. on p. 166).

[274] K. Dieckmann, “Bose-Einstein condensation with high atom number in a deep magnetic trap”, PhD thesis, Van der Waals-Zeeman Institute, 2001 (cit. on p. 167).

[275] G. A. Bird, *Molecular gas dynamics and the direct simulation of gas flows*. Clarendon Press, 1998, 458 pp. (cit. on p. 170).

[276] P. A. Altin, N. P. Robins, R. Poldy, J. E. Debs, D. Döring, C. Figl, and J. D. Close, “Measurement of inelastic losses in a sample of ultracold 85Rb”, *Physical Review A*, vol. 81, no. 1, p. 012 713, Jan. 29, 2010 (cit. on pp. 171, 173).

[277] E. A. Burt, R. W. Ghrist, C. J. Myatt, M. J. Holland, E. A. Cornell, and C. E. Wieman, “Coherence, correlations, and collisions: What one learns about Bose-Einstein condensates from their decay”, *Physical Review Letters*, vol. 79, no. 3, pp. 337–340, Jul. 21, 1997 (cit. on p. 171).

[278] J. P. Burke, J. L. Bohn, B. D. Esry, and C. H. Greene, “Prospects for mixed-isotope Bose-Einstein condensates in rubidium”, *Physical Review Letters*, vol. 80, no. 10, pp. 2097–2100, Mar. 9, 1998 (cit. on p. 171).

[279] J. L. Roberts, N. R. Claussen, S. L. Cornish, and C. E. Wieman, “Magnetic field dependence of ultracold inelastic collisions near a Feshbach resonance”, *Physical Review Letters*, vol. 85, no. 4, pp. 728–731, Jul. 24, 2000 (cit. on p. 171).

[280] B. Yuen, “Production and oscillations of a Bose-Einstein condensate on an atom chip”, PhD thesis, Dec. 2013 (cit. on p. 174).

[281] M. Dupont-Nivet, M. Casiulis, T. Laudat, C. I. Westbrook, and S. Schwartz, "Microwave-stimulated Raman adiabatic passage in a Bose-Einstein condensate on an atom chip", *Physical Review A*, vol. 91, no. 5, p. 053 420, 2015 (cit. on p. 175).

[282] S. B. Papp, J. M. Pino, and C. E. Wieman, "Tunable miscibility in a dual-species Bose-Einstein condensate", *Physical Review Letters*, vol. 101, no. 4, p. 040 402, Jul. 24, 2008 (cit. on pp. 177, 179).

[283] P. A. Altin, G. McDonald, D. Döring, J. E. Debs, T. H. Barter, J. D. Close, N. P. Robins, S. A. Haine, T. M. Hanna, and R. P. Anderson, "Optically trapped atom interferometry using the clock transition of large 87 Rb Bose-Einstein condensates", *New Journal of Physics*, vol. 13, no. 6, p. 065 020, 2011 (cit. on p. 177).

[284] S. Dutta and E. J. Mueller, "Kinetics of Bose-Einstein condensation in a dimple potential", *Physical Review A*, vol. 91, no. 1, p. 013 601, Jan. 5, 2015 (cit. on p. 178).

[285] Z.-Y. Ma, C. J. Foot, and S. L. Cornish, "Optimized evaporative cooling using a dimple potential: An efficient route to Bose–Einstein condensation", *Journal of Physics B: Atomic, Molecular and Optical Physics*, vol. 37, no. 15, p. 3187, 2004 (cit. on p. 178).

[286] K. M. O'Hara, M. E. Gehm, S. R. Granade, and J. E. Thomas, "Scaling laws for evaporative cooling in time-dependent optical traps", *Physical Review A*, vol. 64, no. 5, p. 051 403, Oct. 12, 2001 (cit. on p. 178).

[287] J.-F. Clément, J.-P. Brantut, M. Robert-de-Saint-Vincent, R. A. Nyman, A. Aspect, T. Bourdel, and P. Bouyer, "All-optical runaway evaporation to Bose-Einstein condensation", *Physical Review A*, vol. 79, no. 6, p. 061 406, Jun. 19, 2009 (cit. on p. 179).

[288] T. Kinoshita, T. Wenger, and D. S. Weiss, "All-optical Bose-Einstein condensation using a compressible crossed dipole trap", *Physical Review A*, vol. 71, no. 1, p. 011 602, Jan. 2005 (cit. on p. 179).

[289] M. Horikoshi and K. Nakagawa, "Atom chip based fast production of Bose-Einstein Condensate", *Applied Physics B*, vol. 82, no. 3, pp. 363–366, Mar. 1, 2006 (cit. on p. 179).

[290] M. H. T. Extavour, L. J. LeBlanc, T. Schumm, B. Cieslak, S. Myrskog, A. Stummer, S. Aubin, and J. H. Thywissen, "Dual-Species Quantum Degeneracy of ^{40}K and ^{87}Rb on an Atom Chip", in *AIP Conference Proceedings*, vol. 869, AIP Publishing, Nov. 7, 2006, pp. 241–249 (cit. on p. 179).

[291] D. M. Farkas, K. M. Hudek, E. A. Salim, S. R. Segal, M. B. Squires, and D. Z. Anderson, "A compact, transportable, microchip-based system for high repetition rate production of Bose-Einstein condensates", *Applied Physics Letters*, vol. 96, no. 9, p. 093 102, Mar. 1, 2010 (cit. on p. 179).

[292] M. Ben Dahan, E. Peik, J. Reichel, Y. Castin, and C. Salomon, "Bloch oscillations of atoms in an optical potential", *Physical Review Letters*, vol. 76, no. 24, pp. 4508–4511, Jun. 10, 1996 (cit. on p. 180).

[293] Q. Niu, X.-G. Zhao, G. A. Georgakis, and M. G. Raizen, "Atomic Landau-Zener tunneling and Wannier-Stark ladders in optical potentials", *Physical Review Letters*, vol. 76, no. 24, pp. 4504–4507, Jun. 10, 1996 (cit. on p. 180).

[294] P. Cladé, S. Guellati-Khélifa, F. Nez, and F. Biraben, "Large momentum beam splitter using Bloch oscillations", *Physical Review Letters*, vol. 102, no. 24, p. 240 402, Jun. 18, 2009 (cit. on pp. 182, 194).

[295] M. D. Feit, J. A. Fleck, and A. Steiger, "Solution of the Schrödinger equation by a spectral method", *Journal of Computational Physics*, vol. 47, no. 3, pp. 412–433, Sep. 1, 1982 (cit. on p. 186).

[296] R. W. Heather, "An asymptotic wavefunction splitting procedure for propagating spatially extended wavefunctions: Application to intense field photodissociation of H_2^+", *Computer Physics Communications*, vol. 63, no. 1, pp. 446–459, Feb. 1, 1991 (cit. on p. 186).

[297] K. Posso-Trujillo, PhD thesis, Leibniz Universität Hannover, 2015 (cit. on p. 186).

[298] R. Chamaki, "Transport quantique des atomes ultras froids dans des réseaux optiques accélérés", PhD thesis, Tunis El Manar university, 2016 (cit. on p. 186).

[299] J. G. Muga, X. Chen, A. Ruschhaupt, and D. Guéry-Odelin, "Frictionless dynamics of Bose-Einstein condensates under fast trap variations", *Journal of Physics B: Atomic, Molecular and Optical Physics*, vol. 42, no. 24, p. 241 001, 2009 (cit. on p. 188).

[300] X. Chen, A. Ruschhaupt, S. Schmidt, A. del Campo, D. Guéry-Odelin, and J. G. Muga, "Fast optimal frictionless atom cooling in harmonic traps: Shortcut to adiabaticity", *Physical Review Letters*, vol. 104, no. 6, p. 063 002, Feb. 11, 2010 (cit. on p. 188).

[301] J.-F. Schaff, P. Capuzzi, G. Labeyrie, and P. Vignolo, "Shortcuts to adiabaticity for trapped ultracold gases", *New Journal of Physics*, vol. 13, no. 11, p. 113 017, 2011 (cit. on p. 188).

[302] J. H. Denschlag, J. E. Simsarian, H. Haffner, C. McKenzie, A. Browaeys, D. Cho, K. Helmerson, S. L. Rolston, and W. D. Phillips, "A Bose-Einstein condensate in an optical lattice", *Journal of Physics B-Atomic Molecular and Optical Physics*, vol. 35, no. 14, pp. 3095–3110, Jul. 28, 2002, WOS:000177512400010 (cit. on p. 188).

[303] E. Peik, M. Ben Dahan, I. Bouchoule, Y. Castin, and C. Salomon, "Bloch oscillations of atoms, adiabatic rapid passage, and monokinetic atomic beams", *Physical Review A*, vol. 55, no. 4, pp. 2989–3001, Apr. 1, 1997 (cit. on p. 188).

[304] M. Gustavsson, E. Haller, M. J. Mark, J. G. Danzl, G. Rojas-Kopeinig, and H.-C. Nägerl, "Control of interaction-induced dephasing of Bloch oscillations", *Physical Review Letters*, vol. 100, no. 8, p. 080 404, Feb. 28, 2008 (cit. on p. 189).

[305] C. J. Bordé and C. Lämmerzahl, "Atomic interferometry as two-level particle scattering by a periodic potential", *Annalen der Physik*, vol. 8, no. 1, pp. 83–110, Jan. 1, 1999 (cit. on p. 194).

[306] H. Müller, S.-w. Chiow, and S. Chu, "Atom-wave diffraction between the raman-nath and the bragg regime: Effective rabi frequency, losses, and phase shifts", *Physical Review A*, vol. 77, no. 2, p. 023 609, Feb. 6, 2008 (cit. on p. 194).

[307] K. Kotru, D. L. Butts, J. M. Kinast, and R. E. Stoner, "Large-area atom interferometry with frequency-swept Raman adiabatic passage", *Physical Review Letters*, vol. 115, no. 10, p. 103 001, Aug. 31, 2015 (cit. on p. 194).

[308] V. S. Malinovsky and P. R. Berman, "Momentum transfer using chirped standing wave fields: Bragg scattering", *Physical Review A*, vol. 68, no. 2, p. 023 610, Aug. 27, 2003 (cit. on p. 194).

[309] K. Moler, D. S. Weiss, M. Kasevich, and S. Chu, "Theoretical analysis of velocity-selective Raman transitions", *Physical Review A*, vol. 45, no. 1, pp. 342–348, Jan. 1, 1992 (cit. on p. 194).

[310] P. Cladé, T. Plisson, S. Guellati-Khélifa, F. Nez, and F. Biraben, "Theoretical analysis of a large momentum beamsplitter using Bloch oscillations", *The European Physical Journal D*, vol. 59, no. 3, pp. 349–360, Jul. 27, 2010 (cit. on p. 195).

[311] P. Cheinet, "Conception et réalisation d'un gravimètre à atomes froids", PhD thesis, Université Pierre et Marie Curie - Paris VI, Mar. 24, 2006 (cit. on pp. 197, 198, 202, 242).

[312] A. Papoulis, *Probability, random variables, and stochastic processes*. McGraw-Hill, 1991, 696 pp. (cit. on p. 202).

[313] S. Bali, K. M. O'Hara, M. E. Gehm, S. R. Granade, and J. E. Thomas, "Quantum-diffractive background gas collisions in atom-trap heating and loss", *Physical Review A*, vol. 60, no. 1, R29–R32, Jul. 1, 1999 (cit. on p. 207).

[314] J. Armijo, C. L. G. Alzar, and I. Bouchoule, "Thermal properties of AlN-based atom chips", *The European Physical Journal D*, vol. 56, no. 1, pp. 33–39, Nov. 6, 2009 (cit. on p. 229).

[315] M. T. DePue, S. Lukman Winoto, D. J. Han, and D. S. Weiss, "Transient compression of a MOT and high intensity fluorescent imaging of optically thick clouds of atoms", *Optics Communications*, vol. 180, no. 1, pp. 73–79, Jun. 1, 2000 (cit. on p. 247).

[316] P. D. Lett, R. N. Watts, C. I. Westbrook, W. D. Phillips, P. L. Gould, and H. J. Metcalf, "Observation of atoms laser cooled below the doppler limit", *Physical Review Letters*, vol. 61, no. 2, pp. 169–172, Jul. 11, 1988 (cit. on p. 247).

[317] T. M. Brzozowski, M. Maczynska, M. Zawada, J. Zachorowski, and W. Gawlik, "Time-of-flight measurement of the temperature of cold atoms for short trap-probe beam distances", *Journal of Optics B: Quantum and Semiclassical Optics*, vol. 4, no. 1, p. 62, 2002 (cit. on p. 247).

[318] J. Dalibard and C. Cohen-Tannoudji, “Laser cooling below the doppler limit by polarization gradients: Simple theoretical models”, *Journal of the Optical Society of America B*, vol. 6, no. 11, pp. 2023–2045, Nov. 1, 1989 (cit. on p. 253).

[319] C. J. Cooper, G. Hillenbrand, J. Rink, C. G. Townsend, K. Zetie, and C. J. Foot, “The temperature of atoms in a magneto-optical trap”, *EPL (Europhysics Letters)*, vol. 28, no. 6, p. 397, 1994 (cit. on p. 253).

[320] B. Décamps, J. Gillot, J. Vigué, A. Gauguet, and M. Büchner, “Observation of atom-wave beats using a kerr modulator for atom waves”, *Physical Review Letters*, vol. 116, no. 5, p. 053 004, Feb. 5, 2016 (cit. on pp. 257, 299).

[321] S. Wu, E. J. Su, and M. Prentiss, “Time domain de broglie wave interferometry along a magnetic guide”, *The European Physical Journal D - Atomic, Molecular, Optical and Plasma Physics*, vol. 35, no. 1, pp. 111–118, Aug. 2, 2005 (cit. on pp. 292, 294).

FRENCH INTRODUCTION

> She felt... how life, from being made up of little separate incidents which one lived one by one, became curled and whole like a wave which bore one up with it and threw one down with it, there, with a dash on the beach.
>
> Virginia Woolf, To the Lighthouse

Les ondes présentent un ensemble de propriétés mathématiques qui, conceptuellement, leur permettent de décrire un ensemble toujours plus large de phénomènes physiques (mécaniques, acoustiques, électromagnétiques, gravitationnels,...). Une de leurs propriétés, le principe de superposition, est particulièrement flagrante pour les ondes électromagnétiques dans le domaine visible grâce à un phénomène fondamental : l'interférence.

INTERFÉRENCES OPTIQUES

La première observation de signaux interférentiels, aujourd'hui connus sous le nom d'anneaux de Newton (voir Fig. 111), a été décrite par R. Boyle et R. Hooke au XVII^{e} siècle siècle. Les zones de faible ou de forte intensité lumineuse correspondent respectivement à une interférence destructive ou constructive issue de la superposition de deux ondes cohérentes (c.-à-d. ayant une relation de phase fixée). Ces motifs (aussi appelés franges d'interférence) peuvent être très contrastés et permettent de mesurer des perturbations à l'échelle de la longueur d'onde optique. Les interféromètres optiques se sont largement développés en partie grâce à cette très grande sensibilité. Mais ils ont aussi permis de tester certaines propriétés fondamentales des ondes électromagnétiques. Que cela soit la fameuse expérience de Fizeau en 1851 sur la viscosité supposée de l'éther, le test de l'invariance de la vitesse de la lumière par Michelson & Morley ou la récente détection d'ondes gravitationnelles par l'interféromètre LIGO, les interféromètres optiques ont été, et sont encore, des outils extrêmement sensibles pour tester des théories physiques.

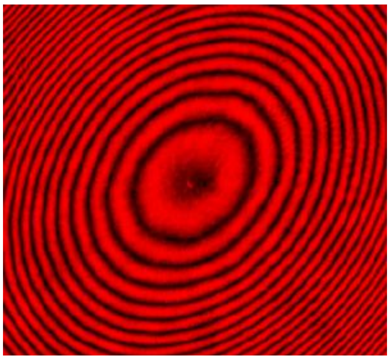

Figure 111
Anneaux de Newton obtenus avec une lentille convexe illuminée par une lumière laser. Photo sous licence libre CC BY-SA 3.0

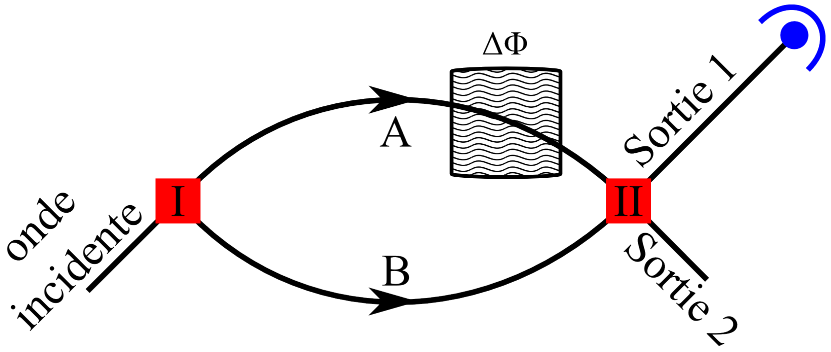

Figure 112: Schéma général d'un interféromètre.

Un interféromètre peut être résumé (voir Fig. 112) à deux chemins différents parcourus par une onde et recombinés. Pour la lumière, ces deux chemins peuvent soit correspondre à deux sources cohérentes (séparation de fronts d'onde tels que pour les fentes d'Young), à deux vecteurs d'ondes différents (séparation d'amplitude comme pour l'interféromètre de Michelson) ou à deux états de polarisation (séparation de l'état interne comme pour l'interféromètre de Fresnel-Arago). Les étapes de séparations cohérentes (I et II) sont réalisées, respectivement pour ces précédents interféromètres, par des fentes mécaniques, des interfaces air/verre et des matériaux biréfringents. L'intensité lumineuse sur chacune des deux sorties de l'interféromètre dépend de la différence de phase $\Delta\Phi$ entre les deux chemins parcourus. Par exemple, l'une des origines les plus simples de déphasage est la différence de chemin optique (provenant d'une différence de distance ou d'une différence d'indice). Cependant, d'autres phases, telles que des phases topologiques, par exemple la phase de Pancharatnam, peuvent être à l'origine d'un déphasage et ne dépendent pas exactement du chemin suivi.

INTERFÉRENCES D'ONDE DE MATIÈRE

En 1924, l'hypothèse de dualité onde-corpuscule formulée par L. de Broglie a étendu le domaine de l'interférométrie aux particules massives. En effet, l'essence de cette dualité est contenue dans la longueur d'onde de de Broglie, λ_{dB}, associée à toute particule de quantité de mouvement p:

$$\lambda_{dB} = \frac{h}{p} \simeq \frac{h}{mv}$$

où h est la constante de Plank et, à la limite non relativiste, m est la masse et v la vitesse classique. Cette hypothèse a connu sa première vérification expérimentale en 1927 lorsque C. Davisson et H. Germer ont réalisé la diffraction d'un faisceau d'électrons incidents sur un cristal métallique [1]. Peu de temps après, la diffraction d'atomes d'hélium fut réalisée par I. Estermann et O. Stern [2]. En plus d'apporter un argument solide en faveur de la mécanique quantique, cette dualité a permis d'ouvrir le champ de l'optique à la physique atomique ce qui a mené à l'essor de l'optique atomique. En effet, l'évolution des ondes électromagnétiques et des ondes atomiques sont toutes régies par l'équation de Helmoltz :

$$\nabla^2 u + k^2 u = 0 \tag{112}$$

avec $k^2 = 2mE/\hbar^2$ pour les ondes de matières et $k^2 = E^2/\left(\hbar^2 c^2\right)$ pour les ondes électromagnétiques. Cette analogie a cependant ses limites, car le vide est dispersif pour les ondes de matières alors que la théorie électromagnétique est linéaire dans le vide. Toujours est-il que les interféromètres à ondes atomiques sont devenus des outils incontournables pour l'étude des interactions entre particules ainsi que pour la caractérisation de leur structure interne.

Interféromètres à ondes de matière

Les premiers interféromètres à ondes de matière ont été réalisés avec des électrons (Marton *et al.* 1952 [3], Möllenstedt and Düker 1955 [4]) et ont bénéficié de la diffraction produite par de fines lames de cristal et du biprisme à électron. Les interféromètres à électrons ont ouvert la voie à l'holographie électronique qui permet de nos jours de sonder la structure atomique à l'échelle de l'atome et permet de cartographier les champs magnétiques et électriques. Les interféromètres à électrons ont aussi été les premiers outils démontrant des propriétés fondamentales telles que l'effet Aharonov-Bohm [5], [6] ou l'effet d'anticoïncidence (antibunching) résultant du principe d'exclusion de Pauli pour les Fermions. La publication récente de Hasselbach *et al.* [7] passe en revue l'interférométrie électronique pour de plus amples détails.

Le premier interféromètre à neutron (H. Rauch *et al.* 1974 [8]) a vu le jour grâce aux cristaux parfaits de silicone. Ces interféromètres ont démontré un grand nombre de propriétés physiques telles que la phase de Berry ou l'effet Josephson magnétique (voir le livre de Rauch [9]).

L'interféromètre à électrons de Marton ainsi que celui à neutrons de Rauch ont en commun une géométrie à bras séparés similaire à celle de l'interféromètre optique de Mach Zehnder. Cette géométrie particulièrement simple est répandue en interférométrie.

Géométrie Mach Zehnder

L'interféromètre de Mach Zehnder s'inspire de l'interféromètre optique schématisé sur la figure 113 développé à la fin du XIX$^{\text{e}}$ siècle par L. Mach et L. Zehnder. Ce type d'interféromètre sépare l'amplitude de l'onde en deux chemins séparés spatialement qui sondent des environnements différents. Ces deux chemins sont souvent appelés bras de l'interféromètre. Après réflexion sur des miroirs, les deux ondes sont recombinées sur une seconde séparatrice. Les deux sorties de la seconde séparatrice présentent des signaux complémentaires qui oscillent en fonction de la différence de phase $\Delta\Phi$ accumulée par chaque bras. Ce dispositif expérimental permet de contrôler $\Delta\Phi$ en introduisant des objets macroscopiques interagissant séparément avec chaque chemin interférométrique.

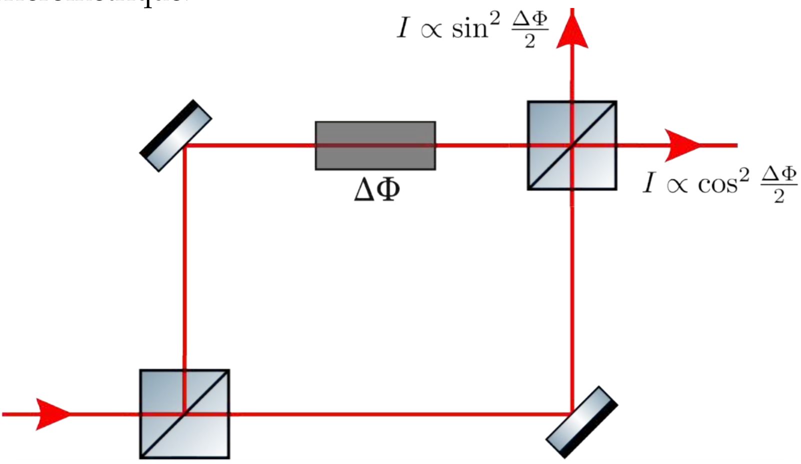

Figure 113: Mach Zehnder optique composé de deux séparatrices et deux miroirs.

Spécificités des électrons et des neutrons

Les électrons sont relativement simples à produire, mais, à cause de la répulsion de Coulomb, de larges flux ne sont accessibles qu'à haute énergie ($> 10\,\mathrm{keV}$). Des neutrons de basse énergie sont produits dans les réacteurs nucléaires qui ne sont pas très courants et pour lesquels le flux disponible est relativement faible.

Les ondes atomiques, elles, ne sont pas sujettes à des interactions à longue portée et peuvent être produites par des systèmes relativement simples. De plus, des techniques de manipulation cohérente d'atomes ont vu le jour au milieu des années 80, grâce à l'avènement des sources laser, ce qui a rendu possible le développement d'interféromètres atomiques. Ces interféromètres ont permis l'investigation de phénomènes physiques nouveaux en regard des précédents interféromètres à ondes atomiques :

- La plupart des interféromètres à neutrons et à électrons font interférer une onde de matière à une particule avec elle-même et une seule particule est présente, en moyenne, dans l'interféromètre. Ceci est une conséquence directe des flux relativement faibles ou de la forte interaction entre électrons qui peuvent mener à des déphasages indésirables. Les atomes ne sont pas soumis à ces contraintes et des effets à plusieurs particules (tel que les états comprimés en spin) font même l'objet de développements spécifiquement appliqués à l'interférométrie.
- La gamme d'états internes accessibles pour les atomes est bien plus large que pour les électrons ou les neutrons[8]. En particulier, il est possible de combiner différentes caractéristiques (comme la polarisabilité ou le moment magnétique) selon l'espèce atomique choisie. De plus, l'interaction de l'atome avec son en-

---

[8] Pour lesquels seul l'état de spin est variable.

vironnement peut être amplifiée de façon résonante ou spécifiquement supprimée, ce qui permet de contrôler la phase interférométrique précisément.

Les interféromètres atomiques ont été démontrés pour la première fois[9] en 1991 et ils sont depuis devenu un champ de recherche majeur en physique fondamentale.

INTERFÉROMÉTRIE ATOMIQUE

Passer en revue l'ensemble du champ de l'interférométrie atomique est une tâche imposante qui a été entreprise dans quatre revues [11]–[14] et deux livres [15], [16]. Dans cette partie, nous allons décrire quelques caractéristiques générales de ces expériences avec une attention particulière en ce qui concerne les aspects communs à l'interféromètre développé à Toulouse.

1991: une année prolifique

En 1991, quatre groupes différents ont publié des résultats présentant des franges d'interférence atomiques.

- O. Carnal et J. Mlynek [17] ont utilisé un jet d'hélium métastable dans une expérience de type fentes d'Young.
- D. Pritchard *et al.* [18] ont développé un interféromètre de type Mach Zehnder avec du sodium.
- M. Kasevich et S. Chu [19] ont mesuré l'accélération de la pesanteur avec un interféromètre de type Mach Zehnder utilisant une source d'atomes de sodium refroidis.
- Ch. J. Bordé et J. Helmcke *et al.* [20] ont mesuré la phase de Sagnac à l'aide d'un dispositif de franges de Ramsey sur du calcium en absorption saturée.

Ces interféromètres (Mach Zehnder, fentes d'Young et Ramsey) utilisent différents types d'éléments diffractant (structures mécaniques pour les deux premiers et réseaux optiques pour les deux derniers) ainsi que différentes sources d'atomes (jets thermiques ou nuages d'atomes froids); ils présentent déjà une large diversité. Depuis, beaucoup d'autres interféromètres ont vu le jour.

Type d'interféromètres

Un interféromètre atomique peut être produit selon différentes méthodes. L'une des plus répandues recombine des ondes atomiques ayant eu différents états d'impulsions

---

[9] La spectroscopie Ramsey d'atomes et de molécules a existé bien avant ces interféromètre et peut être considérée, à strictement parler, comme un interféromètre atomique réalisé sur l'état interne [10] (ce type d'interféromètre est similaire aux interféromètres à polarisation en optique). Cependant, l'absence de structure diffractante empêche habituellement de considérer ces expériences comme des interféromètres atomiques.

avant d'être recombinées dans le(s) même(s) état(s) afin d'obtenir des franges d'interférences. Ce type d'interféromètre comprend les analogues à la géométrie Mach Zehnder ([18], [19], [21]–[33]) qui peut séparer spatialement les deux bras par une différence de direction (ou de vitesse) de propagation. La combinaison de cette géométrie avec des états atomiques internes différents sur chaque bras interférométrique donne lieu à la configuration dite de Ramsey-Bordé ([20], [34]–[45]).

En plus de ces deux types d'interféromètres, il se trouve un certain nombre de géométries différentes qui permettent de réaliser un interféromètre atomique. Par exemple, l'interféromètre de Talbot-Lau[10] ([47], [48]) est un interféromètre qui exploite la diffraction en champs proche, généralement produite par des structures absorbantes. Ces interféromètres bénéficient habituellement de signaux de plus grande intensité, car la condition de cohérence transverse de la source n'est plus nécessaire. Des interféromètres utilisant différents états internes peuvent aussi être décrits comme des interféromètres atomiques avec par exemple, la méthode de Ramsey à champs oscillants séparés [49] ou la technique d'écho de spin ([50], [51]) qui peuvent être décrit comme un phénomène d'interférence dont chaque bras évolue dans l'espace des états internes. Ces méthodes ont été initialement développées pour la spectroscopie et sont aujourd'hui plus du domaine des horloges atomiques. Une autre méthode peut être vue comme l'équivalent temporel des franges d'interférences spatiales ; elle est généralement regroupée sous la dénomination d'interféromètre en temps ([52]–[55], [321]), car les franges d'interférences évoluent dynamiquement à un point donné de l'espace.

Enfin, certains interféromètres reposent sur des géométries confinées qui tirent parti du développement des atomes froids et des puces à atomes pour produire des signaux d'interférences avec des atomes guidés.

Processus de diffraction

Les outils d'optique atomique permettant de produire une superposition cohérente d'ondes de matière peuvent aussi être séparés en catégories avec les principalement des structures mécaniques (absorbantes) qui ont été utilisées aux débuts de l'interférométrie atomique et des réseaux optiques qui sont de nos jours un des outils les plus largement exploités. Les réseaux optiques peuvent remplir le rôle de réseau de phase et/ou de réseau absorbant. Le régime de diffraction de ces réseaux peut être subdivisé selon que le processus adresse le même état interne (diffraction de Kapitza-Dirac, de Bragg ou de Raman-Nath, voir Chap. 1) ou des états internes différents (diffraction Raman). Quelle que soit la situation, ce processus de diffraction produit une superposition cohérente d'états d'impulsion séparés par un nombre entier d'impulsions k_L des photons optiques.

Cependant, avec l'essor des sources d'atomes ultra froids, tel que les condensats de Bose-Einstein (CBE), de nouvelles techniques très sélectives en vitesse ont pu voir

---

[10] L'interféromètre à agrégats de C_{60} développé dans le groupe de M. Arndt [46] est un exemple notable d'interféromètre de Talbot-Lau. De plus, des objets de plus en plus massifs ont été utilisés par ce groupe pour démontrer la dualité onde-corpuscule sur des systèmes de plus en plus complexes.

le jour telles que les oscillations de Bloch ([59]) ou la diffraction de Bragg d'ordre multiple. Parallèlement, des interféromètres utilisant deux espèces atomiques ont pu être développés grâce à des méthodes plus complexes telle que la double diffraction Raman à quatre ondes [60].

L'on peut aussi citer d'autres méthodes, comme le Stern et Gerlach longitudinal qui couple l'état d'impulsion avec l'état interne à l'aide de gradients de champs magnétiques, ou les méthodes de diffraction en temps, telle que la réflexion sur une onde évanescente modulée ou sur des potentiels dépendants du temps (comme cela sera décrit au Chap. 2) qui permettent de produire des interféromètre en temps.

Source d'atomes

Un dernier critère permet de différencier les interféromètres atomiques : la source d'atomes. À leur début, la majorité des interféromètres atomiques utilisaient un jet d'atomes (effusif ou supersonique), éventuellement refroidi, qui produisait des flux atomiques modestes et nécessitait des détecteurs très performants. C'est une des raisons pour laquelle les premiers interféromètres atomiques utilisaient soit des alcalins, soit des atomes de gaz nobles dans un état métastable. Suite au développement des sources d'atomes froids, un nouveau domaine d'interférométrie s'est développé, bénéficiant de temps d'interaction plus longs ce qui améliora la sensibilité de ces appareils.

L'utilisation de condensats de Bose-Einstein comme source d'atomes avait été initialement rejetée, car les quelques expériences initiales avaient mis en évidence l'effet préjudiciable des interactions interatomiques sur les déphasages interférométriques. Cependant, la possibilité d'utiliser des condensats dans des états comprimés [49] ou ayant une distribution en vitesse extrêmement fine permettant l'augmentation de la séparation spatiale entre les bras atomiques [61] a renouvelé l'intérêt pour ce type de source en interférométrie atomique.

Le tableau 17 récapitule l'ensemble des interféromètres sus-cités. Cette liste ne comptabilise pas toutes les expériences d'interférométrie atomique, mais elle permet tout de même de mettre en avant le prépondérance des interféromètres à atomes froids, avec l'exemple clair du rubidium, pour les interféromètres atomiques actuels. De plus, le développement récent d'interféromètres atomiques à double espèce ne date, si ce n'est la démonstration initiale de M. Weitz *et al.* [62], que de 2013.

---

[11] Cette valeur est la seule disponible dans la littérature pour estimer la température initiale de leur nuage.

[12] Ou, de façon plus précise, Transitions Raman Sélectives en Vitesse (TRSV) qui filtrent la distribution en impulsion initiale du nuage.

Atome	Source	Diffraction	Groupe	Référence
H*	Jet thermique	Stern-Gerlach	J. Baudon	[63]
	Jet refroidi	Echo de photon	T. Hänsch	[39]
He*	Jet thermique	Mecanique	O. Carnal and J. Mylnek	[17]
	Jet refroidi	Fentes matérielles	J. P. Toennies	[64]
^{3}He	Jet refroidi	Stern-Gerlach	U. Spinola	[50]
Li	Jet thermique	Spin echo	R. Grimm	[51]
	Jet thermique	Bragg	J. Vigué	[24]
Ne*	Jet thermique	Bragg	S. A. Lee	[22]
Na	Jet thermique	Mecanique	D. E. Pritchard	[18]
	Atomes froids (30 µK)	Raman	M. Kasevich and S. Chu	[19]
	CBE	Kapitza-Dirac	W. D. Phillips	[48]
	Jet thermique	Mecanique	A. D. Cronin	[25]
Mg	Jet thermique	Ramsey	W. Ertmer	[34]
Ar*	Jet thermique	Kapitza Dirac	E. M. Rasel	[21]
K	Jet refroidi	Mécanique	S. Li	[47]
Ca	Jet thermique	Ramsey	C. J. Bordé	[20]
	Jet thermique	Ramsey	N. Ito	[35]
^{85}Rb	Jet thermique	Ramsey	A. Weis	[36]
	Atomes froids	Modulation temporelle	T. Sleator and B. Dubettsky	[53]
	Atomes froids	Echo de photon	A. Kumarakrishnan	[55]
^{87}Rb	Atomes froids	Onde évanescente	A. Aspect	[54]
	CBE	Bragg	T. Kuga	[23]
	CBE	Potentiel à double puits	J. Schmiedmayer	[65]
	CBE	Bragg, confiné	S. Wu	[26]
	Atomes froids	Echo de réseau	M. Prentiss	[321]
	Atomes froids (8 µK)	Raman[12]	W. Ertmer	[59]
	Atomes froids (3 µK)	Oscillations de Bloch	F. Biraben	[40]
	Atomes froids (0.3 µK)	Raman	P. Bouyer	[27]
	CBE	Ramsey	M. Oberthaler	[49]
	CBE	Bragg	N. P. Robins	[28]
	CBE (0.004 µK)	Multi-Bragg	M. Kasevich	[29]
	Atomes froids (2 µK)	Raman	F. P. D. Santos	[61]
	CBE	Ramsey, confiné	P. Treutlein	[58]
	Atomes froids (1.8 µK)	Raman	A. Bresson	[30]
	Atomes froids (0.3 µK)	Raman	J. Luo	[31]
	Atomes froids (3 µK)	Raman	A. Peters	[32]
	Atomes froids (4 µK)	Raman	G. N. Tino	[33]
	Atomes froids (30 µK[11])	Raman	Z. Zhou	[44]
Sr	Atomes froids (1.2 µK)	Bragg	G. M. Tino	[66]
Cs	Jet refroidi	Onde évanescente	J. Dalibard	[52]
	Jet thermique	Raman	M. Kasevich	[37]
	Atomes froids (1.5 µK)	Raman	S. Chu	[38]
	Atomes froids(1.2 µK)	Raman	A. Landragin	[41]
(^{85}Rb/^{87}Rb)	Atomes froids(6 µK)	Raman-Nath	M. Weitz	[62]
	Atomes froids(1 µK)	Raman	A. Bresson	[42]
	CBE	Bragg	N. P. Robins	[67]
	Atomes froids(6 µK)	Raman	M. Zhan	[68]
(^{39}K/^{87}Rb)	Atomes froids (30 µK)	Raman	E. M. Rasel	[43]
(^{40}K/^{87}Rb)	Atomes froids (20/3 µK)	Raman	P. Bouyer and A. Landragin	[45]
(^{87}Sr,^{88}Sr)	Atomes froids (1 µK)	Atomes confinés	G. M. Tino	[69]

Table 17

Sélection d'interféromètres atomiques classés par espèce atomique. La grande variété des méthodes de diffraction ainsi que l'importance des sources d'atomes froids sont mises en évidence par la différence entre le nombre d'interféromètres utilisant les atomes les plus légers (premier quart de tableau, expériences souvent pionnières) et le nombre d'interféromètres à base de rubidium refroidi.

MESURES DE PRÉCISION

Les interféromètres atomiques sont rapidement devenus des outils de mesure de précision en plus de leur utilité en terme d'expérience de principe. Ces vingt dernières années, ils ont fait la preuve d'une très large sensibilité et d'une grande exactitude, et ce dans de nombreux domaines. La phase interférométrique combine en effet différentes contributions avec des termes provenant notamment de l'interaction des atomes avec des potentiels externes, des trajectoires suivies par l'atome à la fois dans l'espace réel (phase dynamique) ou dans l'espace des états internes. Ces différents effets peuvent être étudiés en eux-même ou peuvent être mis à contribution pour mesurer des propriétés physiques plus fondamentales, voire pour tester les théories physiques.

Déphasage dû aux interactions

L'intérêt porté aux interféromètres atomiques provient en partie de leur très grande sensibilité à des perturbations induites par des potentiels externes. Par exemple, dans le cadre de la théorie des perturbations au premier ordre, un potentiel statique U va modifier le vecteur d'onde d'un atome, initialement k_0 en espace libre, selon la loi de conservation de l'énergie :

$$\frac{\hbar^2 k_0^2}{2m} = \frac{\hbar^2 k_p^2}{2m} + U$$

où k_p désigne le vecteur d'onde dans la zone d'interaction. L'hypothèse perturbative, $U \ll \hbar^2 k_0^2\,(2m)$, nous permet de donner une forme approchée de k_p :

$$k_p \simeq k_0 - \frac{mU}{\hbar^2 k_0}$$

Ainsi, nous pouvons exprimer le déphasage induit par l'effet de ce potentiel externe selon :

$$\phi_p = \int (k_p - k_0)\, ds = -\int \frac{U}{\hbar v} ds = -\int \frac{U}{\hbar} dt \tag{113}$$

où la modification de la trajectoire classique de l'atome, induite par l'effet du potentiel d'interaction, a été négligée et où nous avons utilisé le fait que la vitesse de groupe v est reliée au chemin parcouru s par $ds/dt = v$, t étant le temps de propagation.

Par exemple, une perturbation constante appliquée pendant $100\,\mu s$ mesuré avec une sensibilité sur la phase interférométrique de $10\,mrad$ permet de détecter des potentiels d'interaction de l'ordre de $U = 6 \times 10^{-14}\, eV$ ce qui, en regard de l'énergie cinétique des atomes (de l'ordre de quelques meV pour des atomes thermiques) montre une sensibilité relative de l'ordre de 10^{11}.

Selon l'origine du potentiel perturbatif, il est possible d'obtenir, par interférométrie atomique, des informations sur la structure atomique tels que :

- L'interaction avec un champ électromagnétique permet de procéder à des mesures de polarisabilité statique et dynamique [70], [71] (voir Chap. 4).
- L'ajout d'un gaz sur le trajet de l'un des bras interférométriques induit des déphasages et des collisions par interaction de type Van der Waals qui peuvent être décrites par un indice de réfraction effectif et mesurées par interférométrie [72], [73].
- La présence de surface proche des trajectoires atomiques peut aussi permettre d'accéder à des régimes d'interaction de type Casimir-Polder [74], [75].

Effets inertiels

Une autre contribution importante au déphasage interférométrie peut être regroupé dans la catégorie d'effets inertiels. En effet, l'équation (113) met clairement en évidence le fait que la phase interférométrique dépend des trajectoires atomiques au sein de l'interféromètre. C'est pourquoi des accéléromètres et des gyromètres atomiques ont pu voir le jour et sont même devenus des instruments sensibles, à une seconde, aux niveaux de $4 \times 10^{-8}\, m/s^2$ [31] et de $10^{-8}\, rad/s$ respectivement. Ces interféromètres permettent de mesurer, au niveau atomique, l'accélération gravitationnelle [19], [76], les gradients de gravité [77] et les rotations [37], [41].

La sensibilité de ces interféromètres augmente proportionnellement à différence d'impulsion k_{eff} entre les deux bras et avec le carré du temps interférométrique T. C'est pourquoi les développements en vue d'augmenter l'extrême sensibilité de ces appareils sont en partie dirigés vers de plus grandes séparatrices en impulsion [61] ou vers de plus long temps d'interactions. Ceci étant possible avec de grands appareils, ou des expériences en micro-gravité [27], [78], voire même avec des projets spatiaux [80].

Phases topologiques

En plus d'être des outils en physique atomique et des capteurs inertiels fins, la sensibilité à la phase de la fonction d'onde elle-même a été mise en application pour accéder à des déphasages qui ne rentrent pas dans la catégorie des phases dynamiques (telles que décrites par l'équation (113)). Les phases Aharonov-Bohm, Aharonov-Casher et phases de Berry sont quelques exemples de telles phases. Elles correspondent respectivement à une situation où les deux bras interférométriques traversent des zones où le potentiel vecteur est différent (pour des particules chargées), où le champ électrique est différent (pour des dipôles magnétiques) ou de façon plus générale, lorsque l'état atomique interne évolue selon certaines transformations cycliques (voir le Chap. 3). Cette catégorie de phases ne peut être détectée que par interférométrie, car elles ne sont pas issues d'une différence d'énergie (c.-à-d. d'une force) qui peut, elle, être détectée par la modification d'une trajectoire atomique.

Mesure de constantes fondamentales

La très grande sensibilité aux effets inertiels a été utilisée pour mesurer d'une nouvelle manière la constante de gravitation $\mathcal{G}$. L'incertitude relative sur cette constante était de 150 ppm selon le CODATA 2002 ce qui était dû à une dispersion des mesures préalablement effectuées. Utiliser l'interférométrie atomique [33] pour évaluer cette constante a permis de s'affranchir de certains effets systématiques de par la différence conceptuelle importante apportée par la mesure au niveau de l'atome libre. Une autre mesure de constante fondamentale, utilisant le caractère quantifié du nombre de photons transmis avec des séparatrices lumineuses, a permis d'évaluer la constante de structure fine α avec une très grande exactitude grâce à une mesure du rapport h/m [59].

Test de physique fondamentale

Pour finir, les interféromètres atomiques sont des outils suffisamment sensibles pour explorer de nouvelles théories physiques. Un exemple parmi la large gamme de tests fondamentaux est par exemple le panel d'expériences menées sur la décohérence. Des processus très différents ont ainsi été mis à jour tels que le couplage avec l'environnement ou la décohérence progressive lorsque les chemins sont couplés à l'état atomique interne.

Certains interféromètres atomiques sont de nos jours dédiés à des tests du principe d'équivalence [43], [80], à la recherche de déviation supposée de la loi de gravitation universelle [81], [82] ou à des tests de la neutralité de la matière (voir Chap. 5).

PLAN DE LA THÈSE

Dans ce contexte d'interférométrie atomique, le travail que j'ai effectué au sein de l'équipe de Toulouse se situe en partie dans la continuité de l'essor initial, maintenant sur le déclin, d'interféromètres à jet atomique et en partie dans le champ plus récent d'interféromètre à atomes froids pour des mesures de précision. En effet, durant mes trois années de thèse, j'ai travaillé sur l'interféromètre à jet de lithium développé à Toulouse dans les années 2000. En particulier, j'ai contribué aux expériences menées sur le battement d'ondes de matières, sur l'utilisation d'une phase topologique en interférométrie, sur une mesure de précision de la longueur d'onde d'extinction (tune-out), ainsi que sur des expériences de décohérence induite par un rayonnement de type corps noir. Parallèlement, j'ai contribué au développement d'un nouvel interféromètre utilisant une source de deux isotopes atomiques condensés. Cette nouvelle expérience s'inscrit dans la lignée des mesures mettant en jeu des interactions électromagnétiques avec en particulier l'objectif de tester la neutralité de la matière.

Assez naturellement, cette thèse sera donc divisée en deux parties :

Expériences basées sur l'interaction électromagnétique :

La première partie est dédiée aux expériences réalisées sur l'interféromètre à jet de lithium qui sera préalablement décrit dans le Chap. 1. Les chapitres suivants décriront chacun une des expériences qui, par ordre d'apparition, sont :

- **Chap 2**: Une expérience de modulation en temps utilisant un modulateur à effet Kerr, facilement transposable à d'autres systèmes, qui nous a permis de mettre en évidence la détection homodyne et hétérodyne du battement des ondes de matières modulées.
- **Chap 3**: Un déphaseur de Pancharatnam d'un nouveau genre permettant de transférer cette phase géométrique de la lumière aux atomes et ainsi de scanner la phase du signal d'interférence atomique.
- **Chap 4**: La première mesure de la longueur d'onde d'extinction du ^{7}Li dans le niveau $^2S_{1/2}\,|F=2, m_F=2\rangle$ à laquelle sa polarisabilité dynamique devient nulle.

Conception d'un nouvel interféromètre à CBE :

La deuxième partie de cette thèse décrit le travail de conception et de développement du nouveau dispositif expérimental basé sur une source d'atomes condensés contenant deux isotopes de rubidium. Les objectifs expérimentaux, en particulier en terme de performance d'un test de neutralité de la matière, ainsi que les outils théoriques nécessaires au dimensionnement de ce dispositif seront tout d'abord présentés dans le chapitre 5. Dans ce chapitre, nous discuterons des spécificités de la condensation d'un nuage de ces deux isotopes, de la problématique du transport du condensat ainsi que des premiers résultats théoriques sur la modélisation d'un interféromètre à pulses multiples de type Mach Zehnder. Puis, un chapitre beaucoup plus technique présentera à la fois le dispositif expérimental (système à vide, sources laser, sources de champs magnétiques...) ainsi que ses performances en regard des besoins pour des mesures de précision. Enfin, le dernier chapitre discutera des premiers signaux obtenus avec ce dispositif et des performances de la source d'atomes refroidis déjà obtenue.

FRENCH CONCLUSION

Ce manuscrit a présenté la majorité du travail réalisé durant ces trois dernières années au sein du groupe d'interférométrie atomique de Toulouse sous la tutelle de Alexandre Gauguet, Matthias Büchner et Jacques Vigué. Il est divisé en deux parties.

La première année et demie, j'ai travaillé sur la mise en place et l'interprétation de quelques expériences réalisées avec l'interféromètre à jet de lithium.

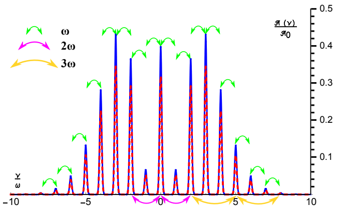

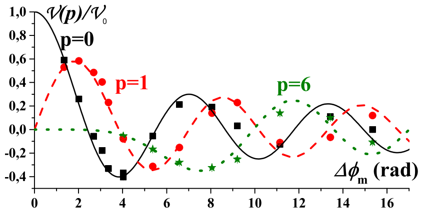

Nous avons commencé par une expérience de diffraction en temps des deux bras interférométriques à l'aide d'un modulateur de phase basé sur l'effet Kerr. Cela nous a permis de démontrer par détection homodyne et hétérodyne la présence de composantes de fréquence latérales produites dans le spectre atomique. Le dispositif expérimental avait été précédemment construit par Jonathan Gillot et mon travail a consisté à implémenter les différentes expériences afin de les confronter à un modèle théorique que nous avons développé. Le très bon accord des amplitudes et des phases de modulation avec notre modèle nous a menés à réaliser une expérience pédagogique consistant en un fax et une radio à onde de matière. Ces expériences ont été présentées dans le Chap. 2 et ont été publiées dans [320].

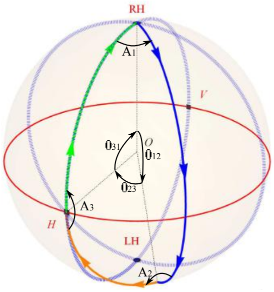

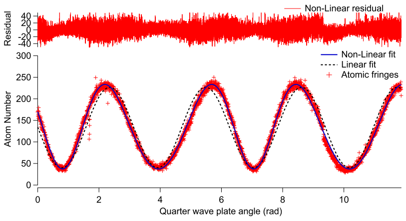

Puis, alors que nous mettions en place le système optique nécessaire à la mesure de la longueur d'onde d'extinction ("tune-out wavelength"), nous avons démontré l'applicabilité d'un déphaseur de Pancharatnam pour les ondes atomiques. Afin d'interpréter le caractère non linéaire de notre déphaseur, une analyse détaillée des différentes imperfections expérimentales a été présentée. Cette étude a été partiellement confirmée par le traitement de nos franges d'interférences obtenues à l'aide des interféromètres optiques et atomiques. Cette étude nous a permis de quantifier l'actuelle exactitude limite de ce type de système et de présenter ses intérêts potentiels lorsqu'il est appliqué à l'interférométrie atomique.

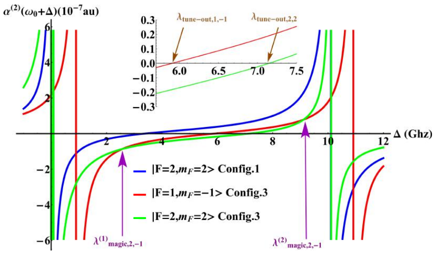

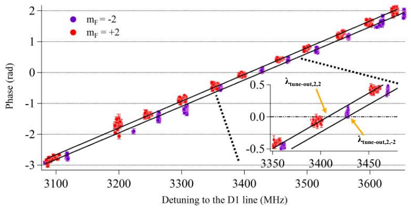

Dans le chapitre 4, nous avons présenté un modèle théorique de la polarisabilité dynamique du ^{7}Li, ainsi que le dispositif expérimental qui nous a permis de mesurer, pour la première fois, la longueur d'onde d'extinction de l'état $|F = 2, m_F = 2\rangle$:

$$\lambda_{2,2,tune-out} = 670.972097(15)[3]\text{nm}$$

Cette mesure contribue à la connaissance des longueurs d'ondes d'extinction des Alcalins avec une précision similaire à celle des autres mesures de précisions réalisées ces dernières années. Cette expérience nous a aussi amenés à remettre en question le modèle théorique utilisé qui ne prend pas en compte les effets d'ordres supérieurs avec notamment le fait que l'hyperpolarisabilité déplace la position de la longueur d'extinction linéairement avec l'intensité.

L'année et demie restante, j'ai participé, avec Julien Alibert et Alexandre Gauguet, au développement et au dimensionnement d'un nouvel interféromètre atomique.

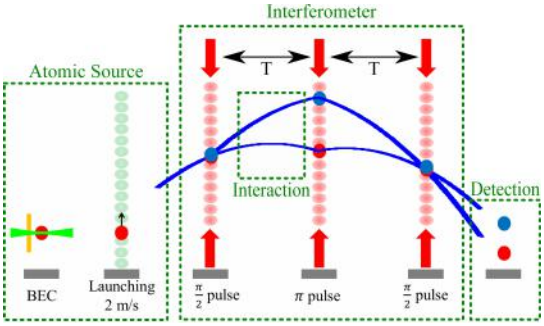

Ce nouvel interféromètre est basé sur un condensat de Bose-Einstein produit avec un large taux de répétition grâce à la combinaison d'une source d'atome intense (Piège Magnéto-Optique, PMO, 2D), d'un PMO 3D sur miroir et d'une puce à atome. Cette source est conçue pour réaliser un interféromètre atomique en fontaine bénéficiant d'une large séparation spatiale des bras atomiques grâce à des séparatrices optiques à large différence d'impulsion. En plus de permettre l'étude de l'utilisation de condensats en interférométrie, ce système a pour but de tester la neutralité de la matière à l'aide d'un déphasage de type Aharonov-Bohm scalaire. Pour cette raison, la source est conçue de façon à permettre l'utilisation de deux isotopes du rubidium ^{85}Rb/^{87}Rb afin de tester à la fois la neutralité du neutron et l'égalité des charges protonique et électronique. Ces objectifs nous ont menés à réaliser des simulations (de l'évaporation sympathique entre isotopes, du transport dans un réseau optique d'un condensat depuis une position proche de la puce à atome, etc...) et à développer des outils théoriques pour les interféromètres à séparatrices multiples. La présentation de ce travail a été réalisée dans le chapitre 5.

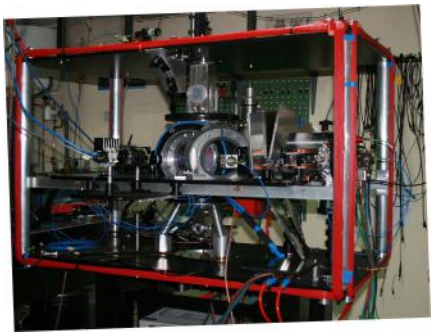

La réalisation pratique du système à vide, des sources de champs magnétiques et du système laser a aussi fait partie de mon travail de thèse. L'ensemble du processus, partir d'une salle vide, de tables optiques nues, des chambres en titane, de fil de cuivre brut, de systèmes laser et d'électronique en pièce détachée jusqu'au système fonctionnel actuel, n'a pas été particulièrement mis en avant dans cette thèse, mais a été définitivement formateur et motivant. Toutefois, certains choix techniques ainsi que les performances globales du système actuel ont été présentés avec force détails dans le chapitre 6 et donnent un bon aperçu des différentes tâches associées.

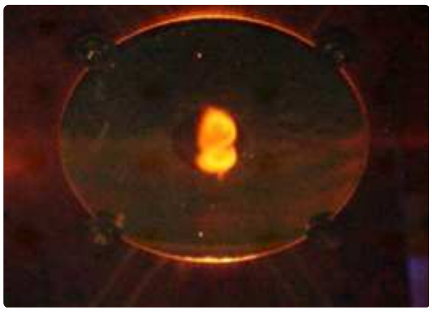

Enfin, dans le dernier chapitre, les récentes performances de ce système ont été présentées. Comme nous l'attendions, quelques milliards d'atomes sont capturés dans le PMO miroir en une seconde. Des étapes de compression, de déplacement et de mélasse nous permettent d'obtenir un nuage contenant 2×10^9 Atomes proches de la surface à une température ultra froide ($12\,\mu K$). Nous sommes en train de transférer ces atomes dans le piège magnétique et espérons poursuivre la route jusqu'au condensat de Bose très prochainement !

REMERCIEMENTS

Il est maintenant grand temps de terminer par quelques mots adressés directement à ceuxes qui ont contribué, de près ou de loin, à ce travail de thèse. C'est d'ailleurs en ce sens que ce manuscrit est dédicacé un peu vaguement, un peu pompeusement, à un « environnement ». Concept physique couramment utilisé comme voile pudique sur un magma difficilement définissable aux multiples facettes. Bien que l'exhaustivité soit un vœu pieux, je vais donc m'atteler à préciser ce que cet environnement a été pour moi ces dernières années.

Et, quitte à surprendre, j'aimerais débuter par l'expression lucide de ce contexte socioculturel qui est le prérequis quasi indispensable à cette liberté d'entreprendre, de penser et aussi (mais pas tout le temps) d'échouer qui m'a été continûment accordée. L'énergie que j'ai dû dépenser pour surmonter les obstacles à hauteur spécifique de genre, d'origine, d'orientation... me semble bien minimale aujourd'hui. C'est donc avec la volonté de rester conscient de ceux qui ne bénéficient pas de ces avantages iniques que je souhaite amorcer ce regard dans le temps. Je pense à ceux pour qui cela n'est pas aussi accessible.

Mais au-delà de ces structures et interactions à longue portée, une multitude d'individus beaucoup plus localisés ont rendu ce parcours possible. Je tiens donc à remercier Béatrice CHATEL et Jean-Marc L'HERMITE pour leur accueil au sein du Laboratoire Collisions Agrégats Réactivité de l'Université Toulouse III Paul Sabatier qu'iels ont dirigé. Laboratoire au sein duquel un grand nombre d'équipes techniques et administratives m'ont apporté une aide constante. Merci donc aux mécaniciens Laurent POLIZZI (avec des plans tout en couleur), Daniel CASTEX (toujours disponible pour une modification rapide) et Michel GIANESIN. Merci à Philippe PAQUIER pour ses conseils et travaux en électronique. Merci à Stéphane FAURE (toujours prêt à descendre en salle de manip'), à Jean-Philippe LOISEL (un bon nombre de systèmes optiques ont vu le jour grâce à toi), à Julien MAUCHAIN (pour ton aide avec COMSOL, je rêve encore de ce verre en fusion virevoltant au plafond) et à William VOLONDAT. Logistiquement parlant, je souhaite remercier Sylvie BOUKHARI, Jonathan BETHE, Carole LECINANA et bien sûr Christine SOUCASSE (toujours patiente et prête à répondre à des questions bien ignorantes). Merci Nicolas ELEFANTIS pour ton aide bibliographique.

Quant à toi, Alexandre GAUGUET, qui m'a ouvert les portes de ce laboratoire ; je tiens évidemment à te remercier pour cette chance, mais plus encore je retiendrai ton honnêteté, scientifique et humaine, ainsi que ta patience et ta pédagogie qui m'ont poussé à plus de rigueur et d'exactitude (même si ma conscience métrologique n'est que balbutiante, je sais définitivement de qui je la tiens). Ce fut cependant sous la direction officielle de David GUERY-ODELIN et de Matthias BÜCHNER que cette thèse a pu voir le jour. Merci, David, pour ton expertise, tes conseils ainsi que ton exigence scientifique. Merci, Matthias, pour tout ce temps passé à travailler sur l'interféromètre de lithium, je me rappellerai longtemps ce 17 février 2014 où, pour la première fois, une radio atomique fut entendue. Et enfin, que serait ce temps passé au LCAR sans Jacques VIGUÉ, individu hors norme qui, contrairement à l'hypothèse qu'il peut souvent formuler, ne m'a jamais fait perdre une seconde de mon temps. Si l'univers de la recherche est une grande famille, Jacques aura été pour moi un membre des plus importants.

Ce fut donc avec votre soutien et votre enseignement patient que ce travail de thèse à pu arriver à terme. Mais je ne tiens absolument pas à oublier Naceur GAALOUL qui m'a initié aux simulations numériques en m'accueillant au sein du groupe d'Ernst RASEL à Hannovre. L'excellente ambiance de ce séjour (au plaisir de partager encore un repas au Broyhanhaus) ainsi que la poursuite à distance des simulations de transport dans un réseau optique sont largement dues à ton enthousiasme scientifique. Enthousiasme qui s'est allègrement propagé à Robin CORGIER et Sina LORIANI qui ont contribué à ce travail et que j'ai eu très grand plaisir à connaître. Je te remercie aussi de ta lecture de ce manuscrit et de tes judicieuses remarques.

Cela me mène naturellement à remercier l'ensemble des membres du jury qui ont jugé ce travail. Merci Carlo RIZZO d'avoir accepté de présider à ma soutenance, merci à Christoph WESTBROOK et Frank PEREIRA DOS SANTOS pour leurs rapports détaillés. Je remercie vivement Phillipe TREUTLEIN pour son intérêt pour ce travail ainsi que pour son accueil à Bâle. Merci aussi à Caroline CHAMPENOIS pour ses remarques et sans qui une bonne part de cette expérience (dans les deux sens du terme) aurait probablement été bien différente !

Voilà pour l'environnement professionnel au sens le plus strict. Mais il est bien souvent difficile de différencier celleux qui, au courant de ma formation universitaire, m'ont apporté sur le plan scientifique de ceuxes qui m'ont permis de m'ouvrir au reste. Merci donc à mes camarades de labo : Aéla , Alex, Antonine, Bruno, Citlali, Christos, Elise, Éric (elle est où l'aiguille ?), Éric, Éric, Étienne (l'être avant le néant), François, Gabriel, Guillaume (merci d'être aussi exigeant), Hyppolite, Ibrahim, Isabelle, Julien (Le problème c'est la dette), Lionel (Miaou), Lucien, Lucile, Mareike, Maxime, Médha, Qi, Raphaël, Simon (tu l'ouvres quand ta brasserie ?). J'ai aussi une pensée pour ces ami.e.s Cachanais.e.s avec qui j'ai beaucoup partagé Cécile, Ileyk, Ivan, Jean-Louis, Marien, Rémi, Simon, Tanguy, Thibault, Tom, ainsi que celleux connu.e.s en classe préparatoire, Florent, Gautier, Jérémy, Maximilien, Sarah, Stéphane, Yannick. Restent enfin ces camarades les plus proches rencontrés depuis plus ou moins longtemps. Aton l'ingénu (merci pour ces lectures), Aurélien le gardien, Camille l'incertaine, Cédric le médecin, Donovan le calme curieux, Laurent le rigoriste (tu l'as eue), Maï la force vive, Marianne la lindy hopeuse, Thomas l'écoradical (moutmout), Xavier la force tranquille...

Enfin, à celle qui m'a supporté lors de ma rédaction et qui appréhende avec tant d'intelligence et de sensibilité la vie, je tiens à te remercier d'être ainsi. Merci, Cléo, de m'avoir laissé un peu de place auprès de Marlène.

Mes derniers remerciements vont à Marie, Théo, Max, Dominique et Régis pour qui l'émotion va au-delà des mots.